

Bimetallic Reactive Intermediates Containing Late Transition Metals

by

Amanda R. Corcos

A dissertation submitted in partial fulfillment of
the requirements for the degree of

Doctor of Philosophy
(Chemistry)

at the

University of Wisconsin–Madison

2016

Date of final oral examination: March 3, 2016.

The dissertation is approved by the following members of the Final Oral Committee:

John F. Berry, Professor, Chemistry

Thomas C. Brunold, Professor, Chemistry

Clark R. Landis, Professor, Chemistry

Jennifer M. Schomaker, Associate Professor, Chemistry

Shannon S. Stahl, Professor, Chemistry

© COPYRIGHT BY AMANDA R. CORCOS, PH.D. 2016

ALL RIGHTS RESERVED

Bimetallic Reactive Intermediates Containing Late Transition Metals

Amanda R. Corcos

Under the Supervision of Associate Professor John F. Berry

University of Wisconsin–Madison

Abstract.

The diruthenium species studied herein are equatorially supported by either the chp (6-chloro-2-hydroxypyridinate) or ap (2-anilinopyridinate) ligands. Both ligands bind to the diruthenium core in a (4,0) geometry, leaving one axial site unencumbered and available for reactivity while simultaneously sterically blocking the second axial site. Chapters 3 and 4 describe diruthenium azide and oxyanion complexes supported by the chp ligand, $\text{Ru}_2(\text{chp})_4\text{N}_3$ and $\text{Ru}_2(\text{chp})_4\text{OEO}_x$ ($E = \text{N}$ or Cl), which were investigated under photolytic conditions for their ability to generate putative diruthenium nitride and oxo intermediates, respectively. Both Ru_2N and Ru_2O species were spectroscopically characterized and subsequently studied for their capacity to transfer a single atom (N or O) to PPh_3 .

Chapters 5 and 6 describe diruthenium complexes supported by the ap ligand. Chapter 5 describes the new precursory Ru_2 complexes $[\text{Ru}_2(\text{ap})_4\text{NCMe}][\text{BF}_4]$ and $\text{Ru}_2(\text{ap})_4\text{FBF}_3$, which have the ability to undergo chemical oxidation with O-atom transfer agents *m*CPBA or PhIO to form $[\text{Ru}_2\text{O}]^+$ intermediates, which also have the ability to perform O-atom transfer. Chapter 6 describes the dimeric dumbbell complex $\{[\text{Ru}_2(\text{ap})_4]_2(\text{AgF}_2)\}[\text{BF}_4]_3$, which contains the first synthetic characterization of a coinage metal difluoride anion.

Chapters 7 and 8 describe dimeric complexes that do not contain ruthenium; rather they contain nickel and cobalt, respectively. The nickel complex $[\text{Cp}'\text{Ni}(\mu\text{-H})]_2$ ($\text{Cp}' = 1,2,3,4\text{-tetrakisopropylcyclopentadienyl}$) exhibits an unusual electronic ground state compared to other $\text{Ni}_2(\mu\text{-H})_2$ species. The cobalt catalyst $[\text{Co}_2(\text{L})_2]^{2-}$ (where $(\text{L})^{3-} = (\text{N}(o\text{-PhNC(O)}^i\text{Pr})_2)^{3-}$) is capable of both nucleophilic and electrophilic aerobic oxidation. It is determined that, upon exposure to O_2 , the dimeric catalyst breaks apart into a monomer, and that the reactive intermediate responsible for this unusual reactivity is a Co^{II} superoxide species supported by a redox non-innocent ligand $[\text{Co}(\text{L})\text{O}_2]^{1-}$.

DEDICATION

To my parents, Daniel and Kathy, for your unwavering support and belief in me, and for your unconditional love.

ACKNOWLEDGEMENTS

I would like to thank my advisor, Professor John Berry, for taking a chance on me by bringing me into the group during my first semester in graduate school. I was one of four students to join the lab within one month of each other, but because of John I never felt lost in the shuffle or that he did not have time to discuss research. On the contrary – John *always* made the time for interesting new projects, and I was fortunate to work on many of them. He never put limits on me, and he encouraged me to think outside the box and work on projects I found interesting. Thank you, John, for giving me this freedom and for believing in me as a scientist.

I would also like to thank the Berry Group, members both past and present, especially: Dr. Mandy Long, Dr. Eugenia Turov, Dr. Kasia Kornecki, Ryan Pakula, and Travis Sunderland. Mandy, Eugenia, and Kasia – thank you for being stellar lab-mates and for teaching me Schlenk techniques and how to care for all of our instruments. More importantly, thank you for teaching me about life, for continuing to be *in* my life even after you all graduated, and for being amazing friends, confidants, role models, and genuinely amazing human beings. I love all three of you, and I am truly a better person for knowing each of you. Ryan – I really do not know what I would have done without your being *literally* at my right hand for the last five-and-a-half years. You are truly one of the smartest people I have ever met, and I am so grateful for your insights, your knowledge, and your friendship – I would not have gotten through the RP without you and Anna and the proposal shields! Travis – you and Julia have been my rocks, and while I am grateful for your partnership in lab, it also means a great deal to me that we are also friends outside of work. Thank you for having me over on random weekday evenings, for including me in Frisbee golf, for being a fabulous bartender, and for going to DMB concerts with me even when no one else would or could.

While here in Madison I met many truly fabulous, smart, strong, humble, and hilarious women, who are incidentally also all chemists. To Dr. Anna Dunn and Julia Wildt (both previously mentioned), Dr. Sarah Decato, Kristine Smith, Dr. Judy Hines, Dr. Jamie Wheeler, and Dr. Ankit Pokhrel – Thank you, ladies, for being amazing friends and confidantes, for always loving and supporting me, for “talking shop” when I needed it, and for finding the time to spin, brunch, go to concerts and movies, host women-only football game-days, and enjoy delicious wine/sangria with me! In each of you I feel like I’ve finally found a friends who actually understand me, and I hope we continue our friendships after we leave Wisconsin.

My committee here at UW has been truly outstanding. I would like to thank Shannon Stahl and Clark Landis for being on my committee since Day 1 and for their fantastic insights. All of their comments and ideas related to my research projects (including the TBO and RP) were critically constructive, and this really forced me to evaluate my results and ideas. Clark was also especially patient, kind, and approachable – I have had many chats with Clark in an informal, non-committee setting, and he always made time for me and had a genuine interest in my concerns, for which I am truly thankful. I would also like to thank Thomas Brunold and Jennifer Schomaker for joining my committee for my oral defense. Thomas has been incredibly helpful in discussing calculations with me over the last few years, and his group has been even more awesome in teaching and training me in EPR, resonance Raman, and calculations. Jennifer took the time to chat with me as well, and I am grateful for her insights both in chemistry and with respect to life trajectories.

I would very much like to thank the staff within the Chemistry department for their hard work and commitment to the students. It is because of their expertise in their fields, the top-notch facilities they maintain, and their genuine interest in our research projects that we as students are

able to succeed and prosper. I would like to thank Ilia Guzei for teaching me crystallography and for his ending patience, especially when repeatedly explaining how to model different types of atom disorder. I would also like to thank Charlie Fry and Bob Shanks for their help and upkeep of the NMR and EPR facilities, Martha Vestling for maintaining the vast number of instruments in our mass spectrometry lab, and all three of them for their kindness.

Over the last three years I have had the opportunity to collaborate with many top-notch scientists, and it is because of their help and expertise that we were able to figure out some very difficult problems. Through the NSF Center for Selective C–H Functionalization (CCHF) I worked with Cora MacBeth and Omar Villanueva to characterize their unique cobalt complex. Even though the project took three years to complete, they were both incredibly positive, humble, and gracious throughout this time, something which I am very grateful for. I would especially like to thank Kyle Lancaster for his XAS expertise and collaboration, for in addition to working with me on many projects (including some which failed), his group also hosted me at Cornell during an XES run so that I could learn about it first-hand. I am truly grateful for the experience, for I learned a lot and had a great time.

Outside of the chemistry department here at UW–Madison, there are a few friends I met in college who are still instrumental in my life. Julia Kennedy-Darling and Siggy Nachtergaele are smart, delightful, supportive, chemistry rock-stars who I met on the soccer field in Hyde Park 10 years ago, and I could not imagine college classes or graduate research without either of them. Anna Hofrichter and Bridget Kiernan are humble, funny, and courageous friends who have both taken the world by storm. Even though neither of them is a scientist, they are both resolute friends who have each visited me in Madison almost every year I've been here, and not just for football game-days either! I am truly grateful for their friendship.

There are two very important teachers I'd also like to acknowledge – Doug Hunt and Greg Hillhouse. Doug was my high school chemistry teacher (and soccer coach), and he was the reason that chemistry was the first class I signed up for in college. Doug inspired me with lab demonstrations (one of which I describe in Chapter 1) and answered all of my questions, and for that I am truly grateful. Greg was my college professor, and I worked in his lab for three years as an undergraduate researcher. Greg's knowledge and love of chemistry was infectious, and he was incredibly supportive and protective of his students. I am forever grateful that I had the opportunity to know him and to learn from him.

To my family – I am truly at a loss for words to describe how thankful and grateful I am for your love and unconditional support, but I'll write a few words anyways...

To David: I love your sense of humor (even if I don't always understand it!), the joy you have when competing in the Highland games, and I am so proud of you for working your way up through Amelia's restaurant and for earning your bartending license. You are truly one of the smartest people I know, and I am so glad that, of all people, you, kiddo, are my brother.

To Caroline: We've always made the joke that we are each half of one whole person, but I could not be more proud of you for the *individual* that you are. I still can't believe you lived in Azerbaijan for almost three years and then took on both law and master's degrees! I've loved all of our international travels together, for there is no one else whose twin I'd rather be than yours.

To Mom and Dad: Thank you for being my parents, for being an active part of my life, for believing in me, for pushing me to do the things I wanted to do but didn't think I was able to do, for being my moral compass, for always having my back, and for being my role models. The only person I've ever looked up to or wanted to be is the two of you. I love you both more than words can say. I am the person I am today because of the both of you. Thank you.

TABLE OF CONTENTS

Abstract	i
Dedication	iii
Acknowledgements	iv
Table of Contents	viii
List of Figures	xiii
List of Schemes	xvii
List of Tables	xviii
List of Charts	xix

Chapter 1*Wisconsin Initiative for Science Literacy: Introduction for a General Audience*

1.1 Chemistry	1
1.2 Inorganic Chemistry	1
1.3 Design and Synthesis of New Compounds	3
1.4 Spectroscopy	4
1.5 Overview of My Thesis Work	6
References	8

Chapter 2*Introduction: Background, Motivation, and Outline.*

2.1 Background and Motivation	9
2.1.1 Importance of M-M=L Intermediates	9

2.1.2 Choice of Supporting Ligand.....	11
2.2 Outline.....	13
References.....	14

Chapter 3

A Synthetic Cycle for Nitrogen Atom Transfer Featuring a Diruthenium Nitride Intermediate

3.1 Abstract.....	19
3.2 Introduction.....	19
3.3 Results and Discussion	21
3.4 Conclusions.....	23
3.5 Acknowledgements.....	25
3.6 Supplementary Information	25
References.....	37

Chapter 4

Oxygen Atom Transfer from an $\text{Ru}_2(\text{chp})_4^+$ Oxyanion Complex via a Putative Ru–Ru=O Intermediate

4.1 Abstract.....	40
4.2 Introduction.....	41
4.3 Results and Discussion	44
4.4 Conclusions.....	56
4.5 Acknowledgements.....	56
4.6 Supplementary Information	57
References.....	73

Chapter 5

Preliminary Studies of an $[Ru_2O]^+$ Intermediate

5.1 Abstract	77
5.2 Introduction	77
5.3 Results and Discussion	79
5.4 Conclusions and Future Work	88
5.5 Supplementary Information	88
References	92

Chapter 6

Capturing the Missing $[AgF_2]^-$ Anion within an $Ru_2(III/III)$ Dimeric Dumbbell Complex

6.1 Abstract	95
6.2 Introduction	95
6.3 Results and Discussion	97
6.4 Conclusions	101
6.5 Acknowledgements	102
6.6 Supplementary Information	102
References	108

Chapter 7

An “Intermediate Spin” Nickel Hydride Complex Stemming from Delocalized $Ni_2(\mu-H)_2$ Bonding

7.1 Abstract	110
7.2 Introduction	110

7.3 Results and Discussion	112
7.4 Conclusions.....	117
7.5 Acknowledgements.....	118
7.6 Supplementary Information	118
References.....	131

Chapter 8

Oxygen Activation by Co(II) and a Redox Non-Innocent Ligand: Spectroscopic Characterization of a Radical–Co(II)–Superoxide Complex with Divergent Catalytic Reactivity

8.1 Abstract.....	136
8.2 Introduction.....	137
8.3 Results and Discussion	138
8.4 Conclusions.....	144
8.5 Acknowledgements.....	145
8.6 Supplementary Information	145
References.....	178

Appendix 1

Attempts to Characterize the $Ru_2(chp)_4NPh_3$ Intermediate in the Synthetic Cycle of Chapter 3

A1.1 Background	183
A1.2 Results and Discussion.....	183
A1.3 Supplementary Information	186
References.....	187

Appendix 2

Attempts at Additional Stoichiometric and Catalytic Reactivity with a Proposed Ru₂ Nitride Intermediate

A2.1 Background	188
A2.2 Results and Discussion.....	188
A2.3 Future Directions.....	190
A2.4 Supplementary Information	191
References.....	192

Appendix 3

Additional Attempts to Generate Ru₂O by Photolysis of a Different Ru₂-Oxyanion Complex

A3.1 Background	193
A3.2 Results and Conclusions	193
A3.3 Supplementary Information	195
References.....	196

Appendix 4

Characterization of an Unusual Cu₂O₂ Species

A4.1 Background	197
A4.2 Results and Conclusions	198
References.....	199

LIST OF FIGURES

Figure 1.1 Periodic table of the elements.....	2
Figure 1.2 Photograph of different ruthenium complexes in solution	3
Figure 1.3 Proposed bimetallic complexes with a metal-metal, metal-ligand multiple bond.....	6
Figure 1.4 Drawings of diruthenium complexes with equatorially-bound chp and ap ligands	7
Figure 1.5 Formation of diruthenium nitride from diruthenium azide	8
Figure 2.1 Drawings of proposed metal-metal, metal-ligand multiply bonded species, specifically (a) M ₂ -carbene, (b) M ₂ -nitrene, (c) M ₂ -nitride, and (d) M ₂ -oxo complexes.....	10
Figure 2.2 Possible regioisomers for binding an asymmetric ligand to an M ₂ core	11
Figure 2.3 Both the chp and ap ligands bind to the Ru ₂ center to form the (4,0) isomer	12
Figure 2.4 Examples of other dimeric nickel systems	12
Figure 2.5 Formation, characterization, and reactivity of cobalt catalyst studied in this work	13
Figure 3.1 Thermal ellipsoid plot of Ru ₂ (chp) ₄ N ₃ (4).....	21
Figure S3.1 EPR spectrum for Ru ₂ (chp) ₄ N ₃ (4) recorded at 6 K.....	30
Figure S3.2 EPR spectrum and simulation for Ru ₂ (chp) ₄ N (6) recorded at 6 K	31
Figure S3.3.a ³¹ P{ ¹ H} NMR spectrum for [H ₂ NPPh ₃]Cl formation.....	32
Figure S3.3.b ³¹ P{ ¹ H} NMR spectrum after addition of authentic sample of [H ₂ NPPh ₃]Cl.....	32
Figure S3.4.a UV-Vis data for confirmation that 5 is Ru ₂ (chp) ₄ Cl	33
Figure S3.4.b Calibration curve data used to determine yield of 5 as quantitative	33
Figure S3.5 Thermal ellipsoid plot of Ru ₂ (chp) ₄ Cl (5).....	34
Figure S3.6 Thermogravimetric analysis data for Ru ₂ (chp) ₄ N ₃ (4).....	35
Figure 4.1 Thermal ellipsoid plot of Ru ₂ (chp) ₄ ONO ₂ (4).....	45
Figure 4.2 Thermal ellipsoid plot of Ru ₂ (chp) ₄ OCIO ₃ (5).....	45
Figure 4.3 UV-Vis data for compounds 3-5 in CH ₂ Cl ₂	47

Figure 4.4 Cyclic voltammograms for Ru ₂ ^{5/4+} couple for 3-5 versus Fc/Fc ⁺	48
Figure 4.5 MALDI-TOF mass spectra for 4 and 4*	50
Figure 4.6 EPR spectrum and simulation for 4 recorded at 10 K	52
Figure 4.7 EPR spectrum of 4 recorded at 10 K after 16 hr frozen photolysis at 254 nm	53
Figure 4.8 GC-MS headspace analysis for formation of N ¹⁸ O ₂ · (<i>m/z</i> = 50) after photolysis of 4* at room temperature under N ₂ for 4 h using 350 nm wavelength	54
Figure 4.9 Yield of OPPh ₃ after exposure to different oxygen atom sources, both with and without exposure to photolytic conditions	55
Figure S4.1 MALDI-TOF mass spectrum of 2 with simulation	62
Figure S4.2 MALDI-TOF mass spectrum of 5 with simulation	63
Figure S4.3 EPR spectrum and simulation for 2 recorded at 15 K	64
Figure S4.4 EPR spectrum and simulation for 5 recorded at 10 K	65
Figure S4.5 ³¹ P{ ¹ H} NMR for formation of OPPh ₃ after photolysis of 4 , both with and without addition of authentic sample of OPPh ₃	66
Figure S4.6 ESI mass spectrum for reaction mixture of 4 , PPh ₃ , and PPnCl post room temperature photolysis, showing formation of OPPh ₃ (<i>m/z</i> = 279)	67
Figure S4.7 ESI mass spectrum for reaction mixture of 4* , PPh ₃ , and PPnCl post room temperature photolysis, showing formation of ¹⁸ OPPh ₃ (<i>m/z</i> = 281)	68
Figure S4.8 GC-MS headspace analysis for formation of ¹⁸ O ₂ · (<i>m/z</i> = 36) after photolysis of 4* at room temperature under N ₂ for 4 h using 350 nm wavelength	69
Figure S4.9 IR data for AgNO ₃ compared to AgN ¹⁸ O ₃	70
Figure S4.10 IR data for 4 and 4*	71
Figure 5.1 Thermal ellipsoid plot of [Ru ₂ (ap) ₄ NCMe][BF ₄] (2)	81
Figure 5.2 Thermal ellipsoid plot of Ru ₂ (ap) ₄ FBF ₃ (3)	81
Figure 5.3 EPR spectra and simulations for 2 and 3	83
Figure 5.4 UV-Vis spectrum of 3 after aliquot additions of <i>m</i> CPBA	84

Figure 5.5 EPR data for 3 after oxidation with <i>m</i> CPBA or PhIO	85
Figure 5.6 Overlay of EPR data for oxidation reactions of 3 with <i>m</i> CPBA or PhIO	86
Figure 5.7 Resonance Raman data for [4][BF₄] after oxidation with 1 equiv. of <i>m</i> CPBA	87
Figure 6.1 Number of known two-coordinate coinage metal dihalogen complexes	96
Figure 6.2 Thermal ellipsoid plot of $\{[\text{Ru}_2(\text{ap})_4]_2[\text{AgF}_2]\}[\text{BF}_4]_3$ ({2} $[\text{BF}_4]_3$).....	98
Figure 6.3 Cyclic voltammogram for {2} $[\text{BF}_4]_3$ versus Fc/Fc ⁺	100
Figure S6.1 MALDI-TOF mass spectrum for {2} $[\text{BF}_4]_3$ with simulation	105
Figure S6.2 Electronic absorption spectrum for {2} $[\text{BF}_4]_3$	106
Figure 7.1 Thermal ellipsoid plot of $[\text{Cp}'\text{Ni}(\mu\text{-H})_2$ (1)	113
Figure 7.2 Temperature depends of the χT product between 1.8 and 270 K for 1	114
Figure 7.3 Molecular orbital analysis of 1	115
Figure S7.1 ¹ H NMR of 1 in C ₆ D ₆	124
Figure S7.2 UV-Vis spectrum of 1 in pentane.....	125
Figure S7.3 CASSCF orbital contributions for $[\text{Ni}(\mu\text{-H})_2]^{2+}$ and Cp_2^{2-}	126
Figure S7.4 Temperature depends of χ between 1.8 and 270 K for 1	127
Figure 8.1 Preparation of [2]²⁻ and [3]¹⁻ from [1]²⁻ , with thermal ellipsoid plot of [2]²⁻	139
Figure 8.2.a Experimental EPR data and simulations for [2]²⁻ and [3]¹⁻	141
Figure 8.2.b Co KBeta XES main lines of [1]²⁻ – [3]¹⁻	141
Figure 8.2.c Co K-edge XANES of [1]²⁻ – [3]¹⁻	141
Figure 8.2.d Overlay of TDDFT-calculated Co K-edge XANES pre-edge peaks for [3]¹⁻	141
Figure 8.3 Molecular orbital interactions for [3]¹⁻	143
Figure S8.1 Ellipsoid plot of [2]²⁻ (different orientation)	156
Figure S8.2 Plot of asymmetric unit of (Et ₄ N) ₂ [2]	156

Figure S8.3 Plot of asymmetric unit of (Et ₄ N) ₂ [2]	156
Figure S8.4 UV-Vis absorption spectrum before and after addition of O ₂ to (Et ₄ N) ₂ [1]	157
Figure S8.5 MALDI-TOF mass spectra for (Et ₄ N)[^{16/18} 3].....	158
Figure S8.6 Liquid-cell IR difference spectrum upon isotopic labeling of (Et ₄ N)[3]	159
Figure S8.7 Overlay of Fourier-transformed EXAFS for [2] ²⁻ and [3] ¹⁻	160
Figure S8.8 EXAFS and fits for [3] ¹⁻	161
Figure S8.9 Experimental rising edge inflection point energies for [1] ²⁻ –[3] ¹⁻	163
Figure S8.10 Correlation of experimental Co K pre-edge XAS energies to transition energies calculated by TDDFT	164
Figure S8.11 Spin densities of [2] ²⁻ and [3] ¹⁻	165
Figure S8.12 Molecular orbitals for [2] ²⁻	166
Figure S8.13 Molecular orbitals for [3] ¹⁻	167
Figure S8.14 Natural orbitals from a SORCI calculation on [3] ¹⁻	168
Figure S8.15 Molecular orbitals for [3b] ¹⁻	169
Figure S8.16 Cyclic voltammogram and UV-Vis absorption spectrum for (Et ₄ N) ₂ [2].....	170
Figure A1.1 Thermal ellipsoid plot of [Ru ₂ (chp) ₄ NHPPPh ₃][BF ₄] (3).....	184
Figure A1.2 Thermal ellipsoid plot of Ru ₂ (chp) ₄ NHPPPh ₃ (4)	185
Figure A2.1 Headspace analysis by GC-MS after photolysis of Ru ₂ (chp) ₄ ¹⁵ NN ₂ in solution at room temperature	189
Figure A2.2 Yield and identification of products generated after performing catalytic reaction shown in Scheme A2.1	190
Figure A2.3 Proposed mechanism for catalytic nitrogen atom transfer via a nitride or nitrene intermediate.....	191
Figure A3.1 Thermal ellipsoid plot of Ru ₂ (ap) ₄ ONO ₂ (2).....	194
Figure A3.2 Compiled EPR data for 2 before and after prolonged photolysis under frozen conditions using 254 nm bulbs	195

Figure A4.1 Resonance Raman data collected at room temperature in THF for complex [('Bu ₃ tacn)Cu ^I (NCMe)][PF ₆]	199
--	-----

LIST OF SCHEMES

Scheme 3.1 Intramolecular nitride insertion into aryl C-H bonds	18
Scheme 3.2 Synthetic cycle for intermolecular N atom transfer	22
Scheme 4.1 Synthetic scheme for photolysis of Ru ₂ azides η ¹ -O-coordinated oxanions to form terminal nitrides and oxo, respectively	42
Scheme 4.2 Formation of nitrate complex 2 from chloride precursor 1 and oxanion complexes 4 and 5 from chloride precursor 3	44
Scheme 4.3 Possible products upon exposing nitrate complexes to photolytic conditions	51
Scheme 5.1 Spin states for Ru ₂ core both before and after photolytic or chemical oxidation	78
Scheme 5.2 Drawings of chp and ap ligands	79
Scheme 5.3 Formation of 2 and 3 from 1	80
Scheme 5.4 Proposed formation of intermediate [Ru ₂ (ap) ₄ O][BF ₄] ([4] [BF ₄] upon oxidation of 3 with <i>m</i> CPBA	84
Scheme 5.5 Proposed <i>S</i> = 1/2 species from oxidations of 3 with either <i>m</i> CPBA or PhIO	86
Scheme 6.1 Examples of equatorial- and axial-bridged Ru ₂ dimeric dumbbell complexes	97
Scheme 6.2 Synthetic formation of { 2 } [BF ₄] ₃ from Ru ₂ (ap) ₄ Cl (1)	98
Scheme 6.3 Observed Ru ₂ -based redox features for { 2 } [BF ₄] ₃	101
Scheme 6.4 Equilibrium for { 2 } ³⁺ as derived from cyclic voltammetry	101
Scheme 8.1 Catalytic aerobic deformylation of 2-PPA by (Et ₄ N) ₂ [1]	138
Scheme A1.1 Proposed formation of 2 from 1 and subsequent formation of Ru ₂ (chp) ₄ Cl	183
Scheme A1.2 Synthetic formation of unexpected product 3 (instead of 2)	184
Scheme A1.3 Formation of 4 from 3 , rather than 2	185

Scheme A2.1 Formation of $\text{Ru}_2(\text{chp})_4^{15}\text{NN}_2$ from $\text{Ru}_2(\text{chp})_4\text{Cl}$ (2)	188
Scheme A2.2 Possible dimerization products and their corresponding masses	189
Scheme A2.3 Conditions and proposed products for catalytic nitrogen atom transfer	190
Scheme A3.1 Synthetic formation of 2 from 1	194
Scheme A4.1 Synthetic scheme for Cu metalation of ${}^t\text{Bu}_3\text{tacn}$ to form 1 , followed by oxygenation to form bridging peroxide species 2	197

LIST OF TABLES

Table S3.1 Crystal data for $\text{Ru}_2(\text{chp})_4\text{N}_3$ (4) and $\text{Ru}_2(\text{chp})_4\text{Cl}$ (5)	34
Table 4.1 Selected crystallographic bond lengths and angles for 4 and 5	46
Table 4.2 <i>E</i> values for $\text{Ru}_2^{5/4+}$ couple for 1-5 versus Fc/Fc^+	49
Table 4.3 EPR spectral simulation parameters for 2 , 4 , and 5	52
Table S4.1 Crystal data of $\text{Ru}_2(\text{chp})_4\text{ONO}_2$ (4) and $\text{Ru}_2(\text{chp})_4\text{OCIO}_3$ (5)	72
Table 6.1 Selected bond distances for comparable Ru_2^{5+} and Ru_2^{6+} structures	99
Table S6.1 Crystal data for $\{\textbf{2}\}[\text{BF}_4]_3$	107
Table S7.1 Crystal data for 1 and 2	128
Table S7.2 Selected bond distances for 1 , 2 , and reported $[\text{Cp}'\text{Ni}(\mu\text{-X})]_2$ complexes	129
Table S7.3 Total energies from DFT calculations on 1 and CASSCF/CASPT2 calculations on $\text{Cp}_2\text{Ni}_2(\mu\text{-H})_2$	130
Table S8.1 EXAFS fitting parameters	162
Table S8.2 Crystal data for $(\text{Et}_4\text{N})_2[\textbf{2}]$	171
Table S8.3 Selected experimental and calculated bond lengths and angles for $[\textbf{2}]^{2-}$, $[\textbf{3}]^{1-}$, and $[\textbf{3b}]^{1-}$	172
Table S8.4 Relative energies of ground states for $[\textbf{3}]^{1-}$ and $[\textbf{3b}]^{1-}$	173

Table S8.5 Spin multiplicities and energies of 15 electronic states of $[\mathbf{3}]^{1-}$ calculated via SORCI using a CAS(17,11) reference.....	174
Table A1.1 Selected bond lengths and angles for 3 and 4	186

LIST OF CHARTS

Chart 4.1 Coordination modes and oxidation states for bimetallic oxo complexes.....	41
Chart 4.2 Compounds discussed in this chapter	43
Chart 7.1 $\text{Ni}_2(\mu\text{-H})_2$ Complexes	111

Chapter 1

Wisconsin Initiative for Science Literacy: Introduction for a General Audience.

1.1 Chemistry.

You may have taken a general chemistry class in high school or even college. What are some of the things you remember? Perhaps using a Bunsen burner or a hot plate? Watching a reaction change color? One of the things I best remember was when my high school chemistry teacher splashed three clear, colorless liquids on a blackboard and asked us to identify them. The acetone quickly evaporated, the ethanol caught fire when lit with a match, and the water did neither of these things. I was interested and excited that we could differentiate seemingly identical compounds based on their physical properties. This is the very essence of chemistry, of studying the properties and composition of different compounds and correlating them to physical and electronic structure. Chemistry is used to describe the world around us, and it often acts as a “bridge” between the natural sciences, including biology and physics.¹

1.2 Inorganic Chemistry.

There are many subdivisions of chemistry, and maybe you know of some: organic chemistry, theoretical chemistry, nuclear chemistry, biochemistry, and inorganic chemistry, to name a few. Many people are familiar with organic chemistry, as it is a required course to attend medical school and is often associated with the pharmaceutical industry, which designs and prepares drugs to treat disease. If you have not heard of organic chemistry, you most certainly have interacted with organic matter, like medicine and food. The term “inorganic”, if you look at

its etymology, should then describe any and all things that are not organic. Inorganic chemistry is most often associated with the materials we use in technology, like batteries, cell phones, and cars – things that are not “natural” but are “man-made”. This, however, is misleading. Salt, sand, minerals, gemstones, gas, and water are all “natural” and are not organic – they are inorganic!

Many inorganic complexes contain a metal, and these are most often a transition metal. The transition metals occupy a significant amount of space on the periodic table (Figure 1.1). You may have heard of some of these transition metals, like iron or zinc, as they are biologically important – iron is in your blood and zinc is an antioxidant that helps your immune system. There is also a wide range in the number of transition metal atoms that we can use at any one time. For example, an inorganic complex may consist of a single titanium atom supported by many ligands (described in the next section), or it can consist of a surface of thousands of titanium atoms bound together with only oxygen atoms. There are also many more options, including using multiple different metals.

Periodic Table of the Elements

Normal boiling points are in °C.
SP = Triple Point
Pressure is listed if not 1 atm.
Allotrope is listed if more than one allotrope.

Legend:

- Alkali Metal
- Alkaline Earth
- Transition Metal
- Basic Metal
- Semimetal
- Nonmetal
- Halogens
- Noble Gas
- Lanthanide
- Actinide

© 2014 Todd Helmenstine
sciencerefacts.org

Figure 1.1 Periodic table of the elements.² Transition metals are yellow.

1.3 Design and Synthesis of New Compounds.

In the laboratory we use an assortment of metals depending on the goal we are trying to achieve. We can also “customize” them for our specific purpose by altering their oxidation state and the ligands that support them. The oxidation state of a metal indicates how many electrons it has, and it represents the number of electrons that metal can still gain or lose. Ligands are ions or molecules that bind to the metal center. They are usually made of carbon and hydrogen atoms, and can often include nitrogen, oxygen, and other atoms. A ligand is like the skeleton of a building: it is part of the framework that supports the larger structure and affects its design, use, and utility. For example, Figure 1.2 shows multiple test tubes, each filled with a colored solution. Each solution contains ruthenium: the color difference is due to the different supporting ligands and subsequent oxidation state of each metal center.

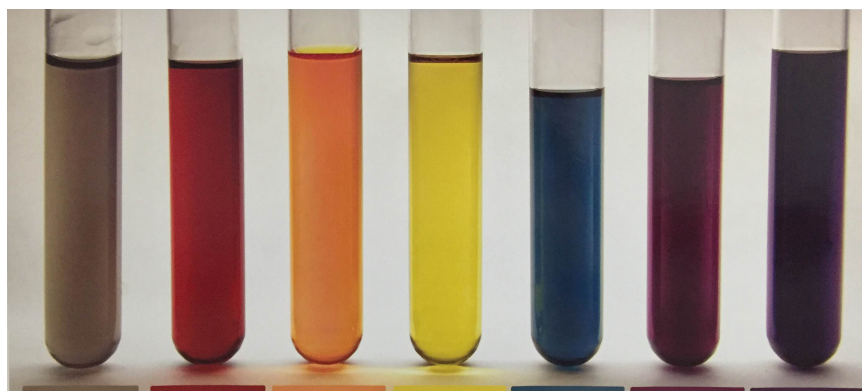


Figure 1.2 Photograph of different ruthenium complexes in solution. The color of any metal-based complex can change based on the metal’s oxidation state and its supporting ligands.

Designing and synthesizing a new compound in the lab is very much like buying a new car. There are many important questions to ask, including but not limited to: Why are you buying a new car? What were the limitations of the previous car? Were there any positive aspects of your old car you would like the new one to have? Is a car commercially available or do you need

to custom order it? And, significantly, how much is a new car going to *cost*? All of these questions must also be asked and answered when designing a new compound, which I have had the opportunity to do many times in my research project. Most often I use the same metal, but I change the number and type of ligands that support it.

There are many different ways to synthesize compounds, and the method I use to make them depends on their properties. Sometimes we can simply dissolve two reagents in solution and stir them together to form a new complex. Other times we are required to heat the reaction to form the new complex. If a complex is air- or water-sensitive, then we prepare and store them in an oxygen-free, dry environment like a glovebox. Many of the compounds I study are extremely sensitive to oxygen and water, and some are also temperature-sensitive! Storing these samples requires liquid nitrogen, which, at 77 K (-196 °C or -321 °F), freezes or suspends the samples so they no longer react or decompose on their own.

1.4 Spectroscopy.

After we design and synthesize a new compound, we need to prove that we did in fact generate the intended complex. If we do not confirm the identity of the complex, if we assume it to be “A” but it is really “X”, then we will misinterpret all of the resulting data and mis-assign the properties of the complex. It is a little bit like the old prank where someone replaces the salt in a salt-shaker with sugar: both white powders look the same, but if you use sugar to flavor your food instead of the intended salt, then the food will taste will terrible. So how can you tell the difference between the white powder of sugar and salt? You can taste it – you know that salt is bitter and sugar is sweet, so whichever flavor you taste will tell you what the powder is. Tasting complexes, however, is NOT an option in the laboratory. I repeat: DO NOT TASTE reagents in

the lab!! The vast majority of chemicals we work with are highly toxic and therefore poisonous, if not also carcinogenic. How, then, do we tell compounds apart? How to do we study their properties? We can observe how the compound interacts with electromagnetic radiation. This is called spectroscopy, and it is critical to use multiple different methods of spectroscopy to investigate new compounds.

Some of the most common methods of spectroscopy include nuclear magnetic resonance (NMR), electron paramagnetic resonance (EPR), infrared (IR), resonance Raman, and ultra violet and visible absorption (UV-Vis), and X-ray crystallography (XRD). NMR is extremely powerful, for it provides information about the connectivity of atoms by using radio frequencies to excite specific nuclei. One of the limitations of NMR is that the molecules under study, for the most part, need to be diamagnetic, meaning that they must have an even, paired number of electrons. EPR is similar to NMR, but it is used to investigate paramagnetic complexes, which are species with unpaired electrons. IR and resonance Raman provide information about the vibrational stretches and connectivity of atoms. XRD utilizes X-ray beams that are then diffracted by the atoms in the complex under study. It is one of the most powerful techniques, for with it we can attain a 3-D image of the molecule and determine the bond lengths, angles, and charge of the complex. XRD is limited in scope, however, for it can only be used with single crystals – powders and liquids cannot be studied – and it only provides information about that one crystal, not the bulk sample of material. It is important to recognize that each technique has its strengths and weakness, and only after using multiple techniques can we get a more-complete picture of the molecules under study.

1.5 Overview of My Thesis Work.

So far I have given you a few clues about my research: I modify the oxidation state and supporting ligands on inorganic compounds which are often air-, water-, and temperature sensitive, and I use some very specific spectroscopies to investigate and characterize them. Let's get into the nitty-gritty now.

While I worked on many projects, the vast majority of my research centered on studying discrete complexes that had a metal-metal bond and a metal-ligand multiple bond (Figure 1.3). These types of complexes have been identified as reactive intermediates in catalytic cycles to make new bonds with carbon, nitrogen, and oxygen. Why do we care about a reactive intermediate? We care because, for a long time, the relevant species were only postulated – there was no proof. If we can characterize these species and show that they are mechanistically relevant to catalysis, then we can better optimize the catalytic cycle to be more efficient, cost-effective, and potentially broaden the applicability of the cycle.

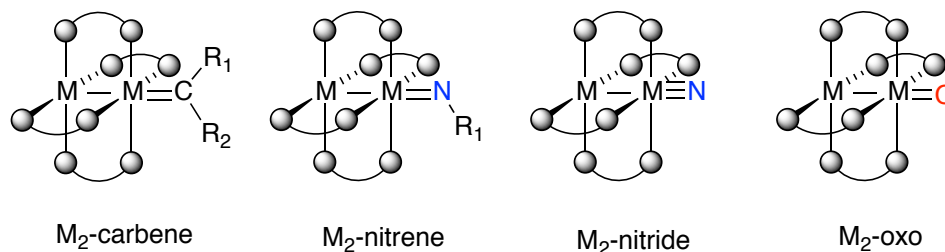


Figure 1.3 Proposed bimetallic complexes with a metal-metal, metal-ligand multiple bond.

The specific systems I studied use two ruthenium atoms bound to one another and supported by four equatorial ligands which form a paddlewheel-type structure (Figure 1.4). The two equatorial ligands I used are named “chp” and “ap”, and they both bind to the Ru₂ core in a (4,0) geometry. This means that, for chp, all of the O atoms of the ligand bind to one ruthenium

atom while all of the N atoms bind to the other ruthenium. The ap ligand has two nitrogen atoms which can bind to the ruthenium core, but they have different properties: one nitrogen atom is in a ring while the other is not. Here, all of the N atoms of the ring bind to one ruthenium atom, while the N atom not in the ring binds to the other. By using these ligands I can block one end of the ruthenium unit while leaving the other end free and available to form the metal-ligand bond mentioned previously.

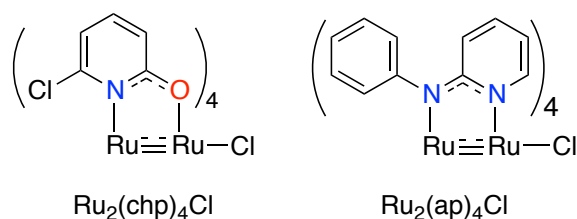


Figure 1.4 Drawings of diruthenium complexes with equatorially-bound chp and ap ligands.

After synthesizing these complexes I can then systematically change the axial ligand to be a nitride “N” atom or oxo “O” atom precursor, like azide or nitrate, respectively, or I can switch to have an ion that does not bind to the diruthenium core. I can then either expose these complexes to light to break specific bonds, or I can use a chemical oxidant that will transfer a single atom to the available diruthenium axial site. For example, Figure 1.5 shows a diruthenium azide complex I made from a chloride precursor ($\text{Ru}_2(\text{chp})_4\text{Cl}$ from Figure 1.4), and after I expose it to light in a frozen matrix, then the $\text{N}=\text{N}$ bond breaks and I am left with (and can investigate!) the diruthenium nitride species, which now has a metal-metal bond and a metal-ligand multiple bond.

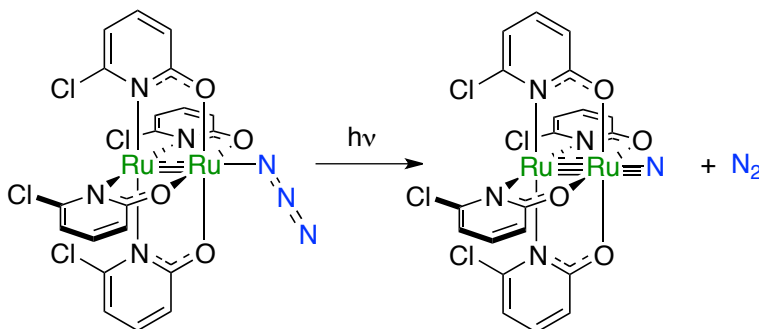


Figure 1.5 Formation of diruthenium nitride from diruthenium azide.

Once generated, these complexes (with a metal-metal bond and a metal-ligand bond) are extremely reactive. Remember when I said I have to store some of them in liquid nitrogen? If I warm these complexes even to -78°C (from being frozen at -196°C) then they react and can no longer be studied. And this helps explain the limited number of spectroscopies I can use to probe and characterize these sensitive materials, for some spectroscopies are solution-phase measurements (UV-Vis), some require solid-state crystalline materials (XRD), and some require diamagnetic materials (NMR). The reactive intermediates I study do not meet any of these requirements, so I often use EPR, resonance Raman, and I collaborate with scientists who have access to other non-standard spectroscopies that are housed at national labs. Thank you, government funding (especially the National Science Foundation and Department of Energy) !

I hope that I've shown you that chemistry, and inorganic chemistry in particular, is exciting, accessible, and relevant. Thank you for reading!

References.

- (1) Brown, T. L.; Lemay, H. E.; Bursten, B. E.; Lemay, H. *Chemistry: The Central Science*. Prentice Hall. 8th ed. 2000.
- (2) <http://sciencenotes.org/printable-periodic-table/>

Chapter 2

Introduction: Background, Motivation, and Outline.

2.1 Background and Motivation.

2.1.1 Importance of M–M=L Intermediates. Metal-metal bonded complexes have been used and studied in the context of catalysis since the 1970s.¹ For example, Rh₂ species like Rh₂(OAc)₄ are well known to decompose diazo-complexes for use in carbene-transfer reactions, including C-H functionalization.²⁻⁴ The key Rh₂-carbene⁵⁻⁷ and -nitrene⁸⁻¹¹ intermediates in these reactions are thought to contain a metal-metal bond and a metal-ligand multiply bonded fragment (Figure 2.1.a and b, respectively).¹² It has also been proposed that metal-metal, metal-ligand multiply bonded species like Ru₂-oxo complexes (Figure 2.1.d) are crucial intermediates for catalytic water oxidation¹³ and sulfur oxygenation.¹⁴ Our group identified this commonality, that many proposed, catalytically-relevant bimetallic intermediates are thought to contain both a metal-metal bond and a metal-ligand multiply bonded species. As no such complexes had been previously studied, our group set out to synthesize and spectroscopically characterize all of the species in Figure 2.1. In addition to the proposed M₂-carbene,¹⁵ -nitrene, and -oxo intermediates, we also set out to study M₂-nitride complexes (Figure 2.1.c), which should exhibit a similar coordination motif and could possibly be used to discover new catalytic transformations.

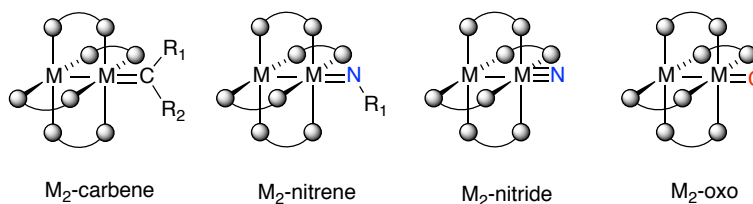


Figure 2.1 Drawings of proposed metal-metal, metal-ligand multiply bonded species, specifically (a) M₂-carbene, (b) M₂-nitrene, and (c) M₂-nitride, and (d) M₂-oxo complexes.

The first target from Figure 2.1 that we aimed to synthesize and characterize was an Ru₂-nitride since it seemed to be an accessible target: mononuclear azide species are known to lose N₂ under photolytic conditions to generate nitrides¹⁶ and it is possible to trap unstable metal nitrides using cryogenic photolytic techniques.¹⁷ Our group prepared and characterized this intermediate by first synthesizing an Ru₂-azide species¹⁸ and subjecting it to photolysis under frozen conditions.¹⁹ Upon further exploration of this system, it was determined that the resulting terminal nitride is extremely electrophilic, and due to its proximity to the supporting ligand the nitride atom inserts into a ligand C-H bond.^{20,21} The resulting species is stable and does not continue to react. One of the goals of the work presented here is to characterize a new Ru₂N species that is capable of intermolecular reactivity.²²

Complexes containing a terminal oxygen atom, which is electronically equivalent to a carbene or nitrene, are also of interest. Many examples of mononuclear Ru=O complexes have been prepared and characterized,²³⁻³² and some have also been used for catalytic purposes including water oxidation.^{33,34} To date, no proposed Ru₂O intermediate has ever been observed. Some of the work presented here includes efforts to synthesize and characterize two new Ru–Ru=O species, each in a different oxidation state. Different methodologies (photolytic³⁵ and

chemical oxidation) are used to generate these Ru_2O species depending on their desired oxidation state. Efforts are also made to explore the utility of this species in O-atom transfer.

2.1.2 Choice of Supporting Ligand. While the metal center(s) employed in any homogeneous system are critically chosen, the supporting ligands play an enormous role too. In previous studies from our lab of paddlewheel-type Ru_2 complexes, the Ru_2 core has been supported by four symmetric ligands, such as the diphenylformamidinate (DPhF^-) ligand.³⁶ If, instead, an unsymmetric ligand is used, then there are four possible regioisomers ((4,0), (3,1), (2,2) cis, or (2,2) trans) that can form around the bimetallic core (Figure 2.2).¹

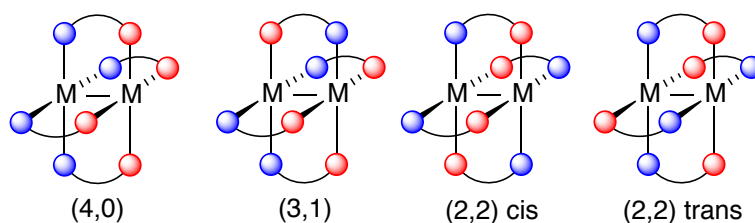


Figure 2.2 Possible regioisomers for binding an asymmetric ligand to an M_2 core.

In the paddlewheel-type diruthenium complexes studied here, the ligands chp (chp = 6-chloro-2-hydroxypyridinate) and ap (ap = 2-anilinopyridinate) were chosen specifically because they preferentially bind to the Ru_2 core to form the (4,0) isomer (Figure 2.3).^{37,38} In this way, one axially site is blocked from any potential reactivity, and the other site may bind an axial ligand. Complexes with either the chp or ap ligand are studied here because, while these ligands provide similar steric protections around the Ru_2 core, they have different electronic properties.³⁹ The chp ligand is an (N,O) donor while the ap ligand is an (N,N) donor, so while they both electronically stabilize the Ru_2 core better than an (O,O) donor like acetate (OAc^-), the increased basicity of the ap ligand enables it to stabilize the Ru_2 core in higher oxidation states than the chp ligand.⁴⁰

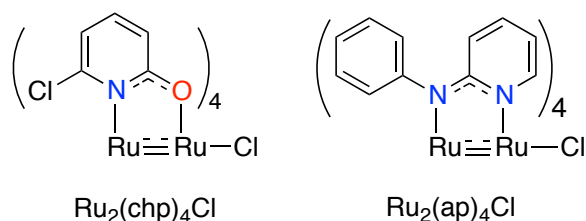


Figure 2.3 Both the chp and ap ligands bind to the Ru_2 center to form the (4,0) isomer.

The other two bimetallic systems presented in this work do not have a formal metal-metal interaction, but they do owe their properties to unique supporting ligands. The nickel complex studied here is $[\text{Cp}'\text{Ni}(\mu\text{-H})]_2$. Previous examples of bridging nickel hydride complexes with cyclopentadienyl ligands are polymeric clusters⁴¹⁻⁴³ or are dimeric complexes with either a diamagnetic⁴⁴⁻⁵¹ or antiferromagnetically-coupled⁵²⁻⁵⁵ electronic ground state. In the examples where dimeric NiCp' complexes have bridging halogen⁵⁶ or chalcogen ligands,⁵⁷⁻⁵⁹ then they exhibit either paramagnetic (high spin) or diamagnetic ground states, respectively. Thus, the nickel complex described here exhibits an unusual electronic ground state due to the effects of both the supporting Cp' and bridging hydride ligands.

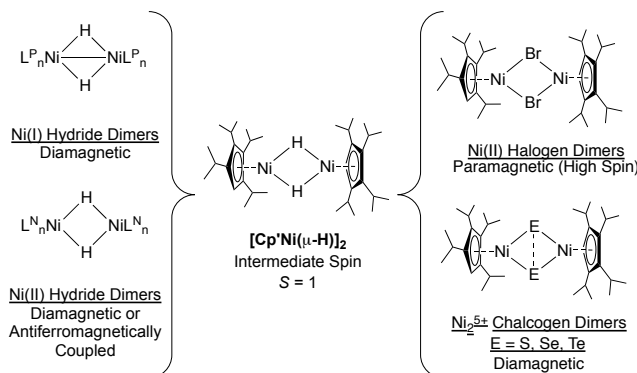


Figure 2.4 Examples of other dimeric nickel systems.

The last system presented here, a bimetallic cobalt system, is capable of performing both nucleophilic and electrophilic aerobic oxidation reactions. Not only is this divergent reactivity unusual, but this system is unique among Co compounds in that it performs this reactivity without the addition of a sacrificial co-reductant.⁶⁰⁻⁶⁴ This is due to the redox non-innocent nature of the supporting ligand L ($(L)^{3-} = (N(o\text{-PhNC(O)}^i\text{Pr})_2)^{3-}$) (Figure 2.5).

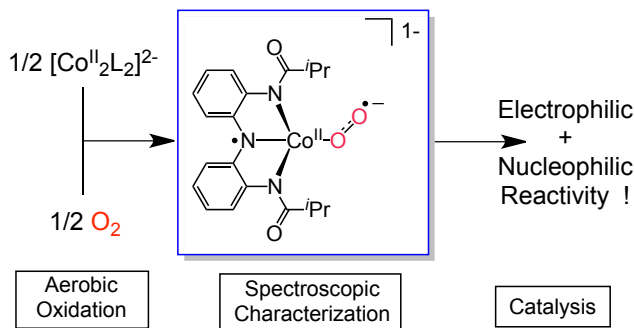


Figure 2.5 Formation, characterization, and reactivity of cobalt catalyst studied in this work.

2.2 Outline.

Chapters 3 and 4 describe our efforts to utilize photolytic (frozen and solution phase) methods to generate reactive intermediates capable of N-atom or O-atom transfer, respectively. In both cases the complexes capable of this reactivity are supported by the chp ligand. Chapter 3 characterizes an Ru_2 -azide complex which loses N_2 to form a terminal Ru_2 -nitride and subsequently transfers this N atom to a phosphine. Similarly, Chapter 4 characterizes two Ru_2 -oxanion complexes (-nitrate and -perchlorate), of which the Ru_2 -nitrate complex loses NO_2^{\cdot} upon photolysis to generate an Ru_2 -oxo species, which subsequently transfers its O atom to a phosphine.

Chapter 5 continues on our theme of single-atom transfer to a phosphine. This time we utilize the ap ligand. We also switch to O-atom transfer agents to prepare the novel $[\text{Ru}_2\text{O}]^+$

species, which is reactive and can transfer its oxygen atom to a phosphine. In our efforts to prepare appropriate starting Ru₂ complexes for this chemistry, we serendipitously synthesized a Ru₂ dimeric dumbbell complex containing the [AgF₂]⁻ ion. This complex and its importance are described in Chapter 6.

Chapters 7 and 8 describe our characterization of reactive, dimeric complexes that do not contain ruthenium. Chapter 7 describes a very sensitive bridging nickel hydride complex with an unusual electronic ground state, which we were able to determine with the help of our collaborators. Elizabeth Hillard and Rodolphe Clérac (University of Bordeaux) collected and interpreted magnetic susceptibility data, and Ivan Infante (University of the Basque Country) performed advanced calculations on our unique system. Chapter 8 describes our collaboration with Professor Cora MacBeth, Omar Villanueva, and Savita Sharma from Emory University, as well as Professor Kyle Lancaster and Richard Walroth from Cornell University. The MacBeth group developed a new dimeric cobalt complex that is capable of both nucleophilic and electrophilic catalytic reactivity. We were able to fully characterize the relevant reactive intermediate responsible for this unusual reactivity, which is a Co(II) superoxide complex with a redox non-innocent ligand. The Lancaster group collected XAS data to further corroborate our experimental and calculated characterizations of the catalyst.

References.

- (1) Cotton, F. A.; Murillo, C. A.; Walton, R. A. *Multiple Bonds Between Metal Atoms*; 3rd ed.; Springer Science and Business Media, Inc.: New York, 2005.
- (2) Doyle, M. P. *J. Org. Chem.* **2006**, *71*, 9253.
- (3) Davies, H. M. *Angew. Chem. Int. Ed.* **2006**, *45*, 6422.

- (4) Paulissen, R.; Reimlinger, H.; Hayez, E.; Hubert, A. J.; Teyssie, P. *Tetrahedron Lett.* **1973**, *14*, 2233.
- (5) Yates, P. *J. Am. Chem. Soc.* **1952**, *74*, 5376.
- (6) Doyle, M. P.; Duffy, R.; Ratnikov, M.; Zhou, L. *Chem. Rev.* **2010**, *110*, 704.
- (7) Nakamura, E.; Yoshikai, N.; Yamanaka, M. *J. Am. Chem. Soc.* **2002**, *124*, 7181.
- (8) Varela-Alvarez, A.; Yang, T.; Jennings, H.; Kornecki, K. P.; Macmillan, S. N.; Lancaster, K. M.; Mack, J. B. C.; Du Bois, J.; Berry, J. F.; Musaev, D. G. *J. Am. Chem. Soc.* **2016**, *138*, 2327.
- (9) Zalatan, D. N.; Du Bois, J. *J. Am. Chem. Soc.* **2009**, *131*, 7558.
- (10) Perry, R. H.; Cahill III, T. J.; Roizen, J. L.; Du Bois, J.; Zare, R. N. *Proc. Natl. Acad. Sci. U.S.A.* **2012**, *109*, 18295.
- (11) Kornecki, K. P.; Berry, J. F. *Chem. Eur. J.* **2011**, *17*, 5827.
- (12) Berry, J. F. *Dalton Trans.* **2012**, *41*, 700.
- (13) Goberna-Ferrón, S.; Peña, B.; Soriano-López, J.; Carbó, J. J.; Zhao, H.; Poblet, J. M.; Dunbar, K. R.; Galán-Mascarós, J. R. *J. Catalysis* **2014**, *315*, 25.
- (14) Villalobos, L.; Barker Paredes, J. E.; Cao, Z.; Ren, T. *Inorg. Chem.* **2013**, *52*, 12545.
- (15) Kornecki, K. P.; Briones, J. F.; Boyarskikh, V.; Fullilove, F.; Autschbach, J.; Schrote, K. E.; Lancaster, K. M.; Davies, H. M.; Berry, J. F. *Science* **2013**, *342*, 351.
- (16) Meyer, K.; Bill, E.; Mienert, B.; Weyhermuller, T.; Wieghardt, K. *J. Am. Chem. Soc.* **1999**, *121*, 4859.
- (17) Berry, J. F.; Bill, E.; Bothe, E.; George, S. D.; Mienert, B.; Neese, F.; Wieghardt, K. *Science* **2006**, *312*, 1937.
- (18) Chen, W.-Z.; De Silva, V.; Lin, C.; Abellard, J.; Marcus, D. M.; Ren, T. *J. Cluster Sci.* **2005**, *16*, 151.
- (19) Pap, J. S.; DeBeer George, S.; Berry, J. F. *Angew. Chem. Int. Ed.* **2008**, *47*, 10102.
- (20) Long, A. K. M.; Yu, R. P.; Timmer, G. H.; Berry, J. F. *J. Am. Chem. Soc.* **2010**, *132*, 12228.
- (21) Long, A. K. M.; Timmer, G. H.; Pap, J. S.; Snyder, J. L.; Yu, R. P.; Berry, J. F. *J. Am. Chem. Soc.* **2011**, *133*, 13138.

- (22) Corcos, A. R.; Long, A. K. M.; Guzei, I. A.; Berry, J. F. *Eur. J. Inorg. Chem.* **2013**, 2013, 3808.
- (23) Che, C.-M.; Wong, K.-Y.; Mak, T. C. W. *J. Chem. Soc., Chem. Commun.* **1985**, 546.
- (24) Che, C.-M.; Wong, K.-Y.; Mak, T. C. W. *J. Chem. Soc., Chem. Commun.* **1985**, 988.
- (25) Che, C. M.; Lai, T. F.; Wong, K. Y. *Inorg. Chem.* **1987**, 26, 2289.
- (26) Che, C.-M.; Tang, W.-T.; Lee, W.-O.; Wong, W.-T.; Lai, T.-F. *J. Chem. Soc., Dalton Trans.* **1989**, 2011.
- (27) Dengel, A. C.; Griffith, W. P.; O'Mahoney, C. A.; Williams, D. J. *J. Chem. Soc., Chem. Commun.* **1989**, 1720.
- (28) Nagao, H.; Nishimura, H.; Kitanaka, Y.; Howell, F. S.; Mukaida, M.; Kakihana, H. *Inorg. Chem.* **1990**, 29, 1693.
- (29) Power, J. M.; Evertz, K.; Henling, L.; Marsh, R.; Schaefer, W. P.; Labinger, J. A.; Bercaw, J. E. *Inorg. Chem.* **1990**, 29, 5058.
- (30) Wong, K.-Y.; Che, C.-M.; Yip, W.-H.; Wang, R.-J.; Mak, T. C. W. *J. Chem. Soc., Dalton Trans.* **1992**, 1417.
- (31) de Souza, V. R.; Nunes, G. S.; Rocha, R. C.; Toma, H. E. *Inorg. Chim. Acta* **2003**, 348, 50.
- (32) Man, W.-L.; Lam, W. W. Y.; Wong, W.-Y.; Lau, T.-C. *J. Am. Chem. Soc.* **2006**, 128, 14669.
- (33) Rodriguez, M.; Romero, I.; Sens, C.; Llobet, A. *J. Molec. Catal. A* **2006**, 251, 215.
- (34) Hirahara, M.; Ertem, M. Z.; Komi, M.; Yamazaki, H.; Cramer, C. J.; Yagi, M. *Inorg. Chem.* **2013**, 52, 6354.
- (35) Corcos, A. R.; Pap, J. S.; Yang, T.; Berry, J. F. *In Preparation*.
- (36) Bear, J. L.; Han, B.; Huang, S.; Kadish, K. M. *Inorg. Chem.* **1996**, 35, 3012.
- (37) Chakravarty, A. R.; Cotton, F. A.; Tocher, D. A. *Inorg. Chem.* **1985**, 24, 1263.
- (38) Chakravarty, A. R.; Cotton, F. A.; Tocher, D. A. *Inorg. Chem.* **1985**, 24, 172.
- (39) Chakravarty, A. R.; Cotton, F. A.; Tocher, D. A.; Tocher, J. H. *Polyhedron* **1985**, 4, 1475.

- (40) Cotton, F. A.; Yokochi, A. *Inorg. Chem.* **1997**, *36*, 567.
- (41) Müller, J.; Dorner, H.; Huttner, G.; Lorenz, H. *Angew. Chem. Int. Ed.* **1973**, *12*, 1005.
- (42) Paquette, M. S.; Dahl, L. F. *J. Am. Chem. Soc.* **1980**, *102*, 6621.
- (43) Pasynkiewicz, S.; Buchowicz, W.; Pietrzykowski, A.; Głowiak, T. *J. Organomet. Chem.* **1997**, *536-537*, 249.
- (44) Jonas, K.; Wilke, G. *Angew. Chem. Int. Ed.* **1970**, *9*, 312.
- (45) Barnett, B. L.; Kruger, C.; Tsay, Y.-H.; Summerville, R. H.; Hoffmann, R. *Chem. Ber.* **1977**, *110*, 3900.
- (46) Vicic, D. A.; Jones, W. D. *J. Am. Chem. Soc.* **1997**, *119*, 10855.
- (47) Fryzuk, M. D.; Clentsmith, G. K. B.; Leznoff, D. B.; Rettig, S. J.; Geib, S. J. *Inorg. Chim. Acta* **1997**, *265*, 169.
- (48) Bach, I.; Goddard, R.; Kopiske, C.; Seevogel, K.; Pörschke, K.-R. *Organometallics* **1999**, *18*, 10.
- (49) Crestani, M. G.; Muñoz-Hernández, M.; Arévalo, A.; Acosta-Ramírez, A.; García, J. J. *J. Am. Chem. Soc.* **2005**, *127*, 18066.
- (50) Li, T.; García, J. J.; Brennessel, W. W.; Jones, W. D. *Organometallics* **2010**, *29*, 2430.
- (51) Cornella, J.; Gómez-Bengoa, E.; Martin, R. *J. Am. Chem. Soc.* **2013**, *135*, 1997.
- (52) Pfirrmann, S.; Limberg, C.; Ziemer, B. *Dalton Trans.* **2008**, 6689.
- (53) Pfirrmann, S.; Limberg, C.; Herwig, C.; Knispel, C.; Braun, B.; Bill, E.; Stösser, R. *J. Am. Chem. Soc.* **2010**, *132*, 13684.
- (54) Matsumoto, T.; Nagahama, T.; Cho, J.; Hizume, T.; Suzuki, M.; Ogo, S. *Angew. Chem. Int. Ed.* **2011**, *50*, 10578.
- (55) Dong, Q.; Zhao, Y.; Su, Y.; Su, J.-H.; Wu, B.; Yang, X.-J. *Inorg. Chem.* **2012**, *51*, 13162.
- (56) Weismann, D.; Saurenz, D.; Boese, R.; Bläser, D.; Wolmershäuser, G.; Sun, Y.; Sitzmann, H. *Organometallics* **2011**, *30*, 6351.
- (57) Sitzmann, H.; Saurenz, D.; Wolmershäuser, G.; Klein, A.; Boese, R. *Organometallics* **2001**, *20*, 700.

- (58) Yao, S. A.; Lancaster, K. M.; Götz, A. W.; DeBeer, S.; Berry, J. F. *Chem. Eur. J.* **2012**, *18*, 9179.
- (59) Yao, S. A.; Martin-Diaconescu, V.; Infante, I.; Lancaster, K. M.; Gotz, A. W.; DeBeer, S.; Berry, J. F. *J. Am. Chem. Soc.* **2015**, *137*, 4993.
- (60) Schultz, M. J.; Sigman, M. S. *Tetrahedron* **2006**, *62*, 8227.
- (61) Sharma, V. B.; Jain, S. L.; Sain, B. *Tetrahedron Lett.* **2003**, *44*, 383.
- (62) Bailey, C. L.; Drago, R. S. *Coord. Chem. Rev.* **1987**, *79*, 321.
- (63) Smith, T. D.; Pilbrow, J. R. *Coord. Chem. Rev.* **1981**, *39*, 295.
- (64) Mandal, A. K.; Iqbal, J. *Tetrahedron* **1997**, *53*.

Chapter 3

A Synthetic Cycle for Nitrogen Atom Transfer Featuring a Diruthenium Nitride Intermediate

This chapter has been published:

Reprinted with permission from Amanda R. Corcos, Amanda Kae Musch Long, Ilia A. Guzei, and John F. Berry. *Eur. J. Inorg. Chem.* **2013**, 2013 (22-23), 3808-3811.

Copyright 2013 John Wiley & Sons, Inc.

Contributions: A. K. M. Long designed and characterized complex **4**. I. A. Guzei provided crystallographic assistance. All other work was performed by A. R. Corcos.

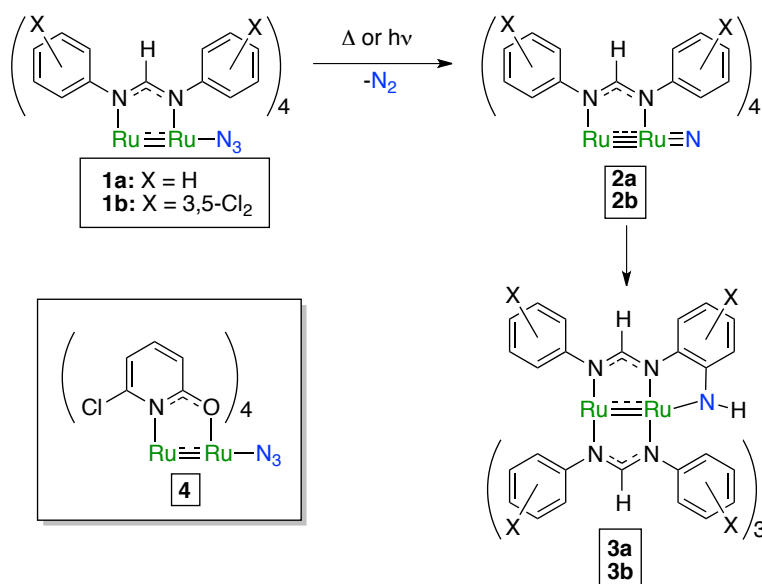
3.1 Abstract.

A new Ru₂-azide complex, Ru₂(chp)₄N₃ (**4**, chp = 6-chloro-2-hydroxypyridinate), was investigated under photolytic conditions to study the chemical reactivity of the corresponding Ru₂-nitride species Ru₂(chp)₄N (**6**) towards intermolecular N atom transfer to triphenylphosphine (PPh₃). Photolysis of a dichloromethane solution of **4** at $\lambda > 350$ nm leads to a characteristic color change from purple to magenta. Upon acidic workup, triphenylphosphinimine chloride ([H₂NPPh₃]Cl) is produced and Ru₂(chp)₄Cl (**5**), the precursor to **4**, is regenerated. The first stoichiometric cycle for intermolecular N atom transfer from an Ru₂-nitride is thus presented.

3.2 Introduction.

The preparation and reactivity of transition metal terminal nitride compounds has long been of interest in inorganic chemistry.¹⁻³ Recently, the electrophilic character of late transition metal nitrides, and in particular some early metal nitrides, has been exploited. These studies resulted in a rich N atom transfer chemistry to phosphines,⁴⁻⁶ CO,^{7,8} isocyanates,⁹ H₂,¹⁰ and other nucleophiles,¹¹⁻¹⁸ as well as N atom insertion into Si-H¹⁹ and C-H bonds.^{20-24,25-28} In particular,

we have studied the unstable Ru_2 -nitride complex $\text{Ru}_2(\text{DPhF})_4\text{N}$ (**2a**, $\text{DPhF} = N,N'$ -diphenylformamidinate) and its 3,5-dichlorophenyl analogue, $\text{Ru}_2(\text{D}(3,5\text{-Cl}_2)\text{PhF})_4\text{N}$ (**2b**), generated by photolytic²⁹ or thermolytic²⁵ methods from the known Ru_2 -azide complexes **1a/b**, reported in 2005 by Ren and coworkers.³⁰ Interestingly, we found these nitride compounds to undergo intramolecular N atom insertion into the aryl C–H bonds of the supporting diaryl formamidinate ligands to form complexes **3a/3b**²⁶ (Scheme 3.1).



Scheme 3.1 Intramolecular nitride insertion into aryl C–H bonds.

Because of the unusually facile intramolecular reactivity of nitride compounds **2a/2b**, which is even observed below room temperature, it seemed plausible that related compounds could promote intermolecular N atom transfer if an Ru_2 -nitride could be produced that was devoid of aryl rings in proximity of the axial nitride position. We have taken advantage of the wide variety of bridging ligands known to support Ru_2 paddlewheel complexes to design the new Ru_2 -azide complex $\text{Ru}_2(\text{chp})_4\text{N}_3$ (**4**, $\text{chp} = 6\text{-chloro-2-hydroxypyridinate}$) (Figure 3.1) which, unlike our previous examples highlighting intramolecular C–H functionalization, has the

potential to achieve intermolecular N atom transfer. Herein we report the first example of intermolecular N atom transfer from an Ru₂-nitride and full recovery of the Ru₂(chp)₄Cl molecule (**5**), which is the direct synthetic precursor to **4**. We therefore establish a closed cycle for intermolecular N atom transfer.

3.3 Results and Discussion.

The purple Ru₂-azide complex **4** was prepared directly from the room temperature reaction of the known chloride precursor **5**³¹ with sodium azide in a mixture of dichloromethane and methanol over the course of 96 hours. We note that insufficient reaction time leads reliably to isolation of a product mixture containing both **4** and **5**. Removing the solvent in vacuo and washing the residue with diethyl ether produced a purple solid that was recrystallized from dichloromethane and hexanes to yield dark purple X-ray quality crystals of **4**.

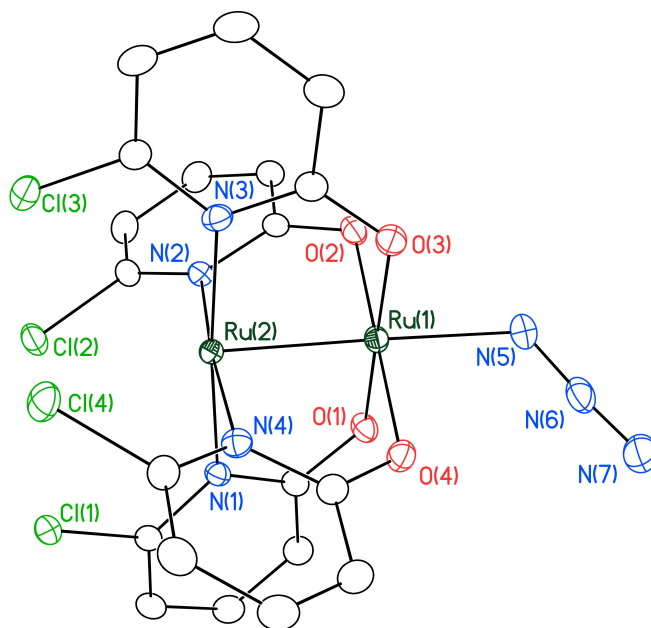


Figure 3.1 Thermal ellipsoid plot of Ru₂(chp)₄N₃ (**4**) with ellipsoids drawn at the 50% probability level. Hydrogen atoms are omitted for clarity.

In the X-ray crystal structure of **4** (Figure 3.1), the Ru₂ core is surrounded by four monoanionic chp ligands bridging the metal centers of the Ru₂⁵⁺ unit to yield a classical paddlewheel-type structure having an Ru–Ru bond distance of 2.2907(2) Å. As in its chloro precursor **5**, the four chp ligands in **4** are oriented so as to produce the (4,0) isomer of this complex. As such, one Ru center is bound equatorially by only the N-donors of each bridging hydroxypyridinate (Ru–N bond lengths range from 2.091 to 2.097 Å) and the other Ru center is bound equatorially by only the ligand O-atom (Ru–O bond lengths range from 1.990 to 2.005 Å). Thus, the chloro-substituted position of each of the four bridging ligands is arranged to surround the N-ligated Ru axial site and block it from reactivity. The monoanionic N₃[−] azide ligand therefore binds only at the exposed, non-skirted O-ligated Ru axial position. The Ru–N₃ bond distance is 2.116(2) Å, and the Ru–N–N angle of 123.5(2)° contrasts with the ~180° binding of azide in compounds **1a/b**. The linear azide binding in the formamidinate compounds is likely a result of steric congestion caused by the aryl rings. The azide in **4**, however, is sterically unhindered, which suggests that intermolecular N atom transfer reactions may be facile upon conversion of **4** to the corresponding nitride.

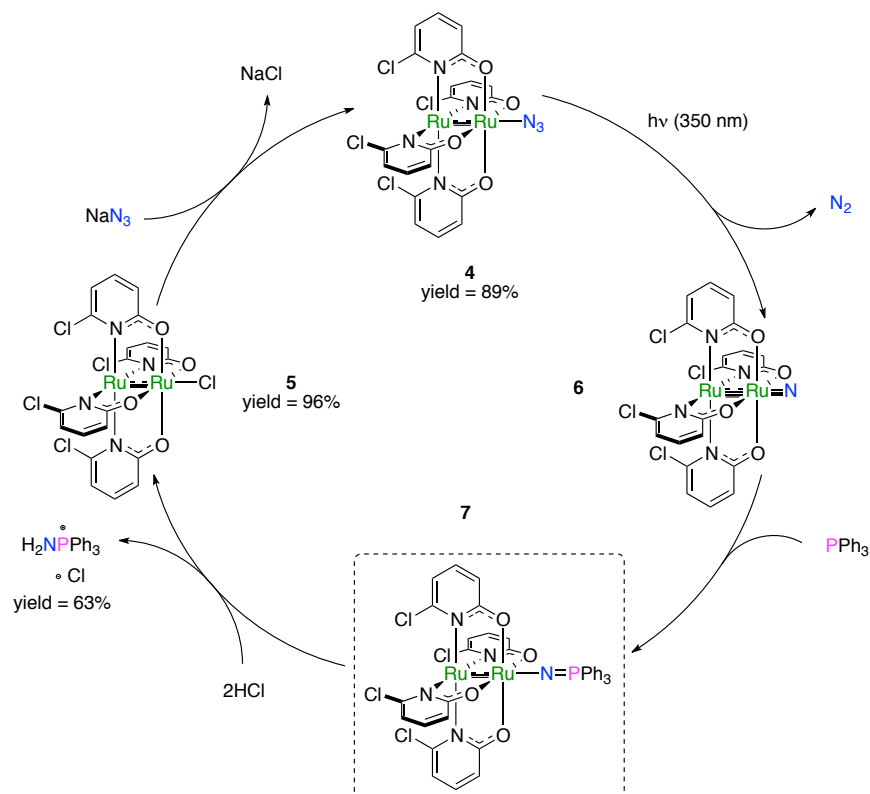
Photolytic conversion of **4** to the corresponding Ru₂-nitride, Ru₂(chp)₄N (**6**), has been established by MALDI-TOF mass spectrometry studies in which the molecular fragment corresponding to the nitride ($m/z = 730.1$ amu) increases as the laser power is increased. We hypothesized that irradiation of **4** in solution would allow formation of **6** as a fleeting intermediate that could be trapped in a frozen matrix. EPR spectroscopy was used to monitor the photolysis of a dichloromethane solution of **4** frozen in liquid nitrogen. After 8 h of photolysis at 350 nm, we found that the EPR signal for the starting azide species, which initially displays a rhombic $S = 3/2$ signal (with effective g values of $g_1 = 4.38$, $g_2 = 3.975$, $g_3 = 1.95$) (Figure S3.1),

disappears nearly completely, and a new species with a rhombic $S = 1/2$ signal evolves ($g_1 = 2.35$, $g_2 = 2.155$, $g_3 = 1.97$) (Figure S3.2). We note that the EPR spectrum of $\text{Ru}_2(\text{DPhF})_4\text{N}$ (**2a**) also indicates an $S = 1/2$ ground state²⁹ but is axial rather than rhombic, suggestive of a difference in electronic configuration between **6** and **2a**.

To test our new Ru_2 -nitride complex for intermolecular reactivity, we subsequently attempted to trap **6** with an organic substrate to form a more stable intermediate. A dichloromethane solution of **4**, PPh_3 , and bis(triphenylphosphine)iminium chloride (PPNCl , an internal standard for calibration by ^{31}P NMR spectroscopy) was photolyzed at 350 nm at room temperature for 2 h and then subjected to acidic workup. Analysis by $^{31}\text{P}\{^1\text{H}\}$ NMR spectroscopy indicated the formation of the intermolecular N atom transfer product $[\text{H}_2\text{NPPH}_3]\text{Cl}$ (signal at $\delta = 35.91$ ppm) in 63% yield, and the identity of this product was confirmed by doping the sample with an authentic sample of $[\text{H}_2\text{NPPH}_3]\text{Cl}$ (Figure S3.3). Additionally, the remaining dichloromethane solution was analyzed to ascertain the identity of the Ru-containing reaction product. A UV-Vis spectrum of this solution is indistinguishable from that of $\text{Ru}_2(\text{chp})_4\text{Cl}$ (**5**) (Figure S3.4.a), and the yield of this product (96%) was determined by UV-Vis using a calibration curve based on genuine samples of **5** (Figure S3.4.b). Furthermore, when a sample of the reaction solution was layered with hexanes dark purple crystals grew, which were shown by X-ray crystallography to be $\text{Ru}_2(\text{chp})_4\text{Cl} \cdot 2\text{CH}_2\text{Cl}_2$ (**5**· $2\text{CH}_2\text{Cl}_2$) (Figure S3.5).

Thus, the original Ru_2 -chloride precursor **5** used in the N atom transfer reaction seen here was successfully regenerated. We have therefore completed a synthetic cycle for the conversion of PPh_3 to $[\text{H}_2\text{NPPH}_3]\text{Cl}$, as shown in Scheme 3.2. Compound **4** is formed from **5** by metathesis with sodium azide, and **4** may be photolyzed to yield the reactive nitride intermediate **6**. PPh_3

traps **6** to presumably yield the proposed intermediate **7**,³² which reacts with HCl (g) to yield [H₂NPPh₃]Cl and reform compound **5**.



Scheme 3.2 Synthetic cycle for intermolecular N atom transfer. The dotted box around **7** indicates that it is a proposed structure.

3.4 Conclusions.

Through this study we report a novel Ru₂-azide system wherein photochemically induced N atom transfer is engineered to be both intermolecular and quantifiable in the formation of [H₂NPPh₃]Cl from PPh₃. It should be noted that intermolecular reactivity of other late transition-metal nitrides is often hampered by nitride dimerization, which yields N₂,^{10,23,33} or perhaps reaction with solvent, as Basolo reported, by formation of chloroamines through reaction of electrophilic nitrenes with chloride in solution.³⁴ We suggest (and have now shown – see

Appendix 2) that such an alternate pathway may be responsible for the decreased yield of $[\text{H}_2\text{NPPH}_3]\text{Cl}$ produced through this cycle. On-going efforts to increase this yield include altering the workup methodology as well as designing new supporting ligands and exploring a larger substrate scope. This work completes the first synthetic cycle for intermolecular N atom transfer using an Ru_2N species and implicates Ru_2N as a reactive species with potential for other N atom transfer reactions.

3.5 Acknowledgments.

We thank the U.S. Department of Energy, Chemical Sciences, Geosciences, and Biosciences Division, Office of Basic Energy Sciences, Office of Science (DE-FG02-10ER16204) and the Petroleum Research Fund (50690-ND3) for their support of this work. A.R.C. thanks the National Science Foundation for Graduate Research Fellowship (DGE-0718123).

3.6 Supplementary Information.

Materials and Methods. All syntheses were conducted under a dry N_2 atmosphere using Schlenk line techniques; product workup and isolation were achieved under ambient conditions. Dichloromethane and methanol were dried over CaH_2 and MgO , respectively, and distilled before use. Toluene, hexanes, and ether were obtained from a Vacuum Atmospheres Solvent System and degassed prior to use. All materials were commercially available and used as received, unless otherwise noted. $\text{Ru}_2(\text{chp})_4\text{Cl}$ (**5**) was prepared from $\text{Ru}_2(\text{OAc})_4\text{Cl}$ ³⁵ via modifications to published procedure.³¹ Photolysis of both frozen and room temperature samples

of **4** was performed in a Rayonet RPR-200 photochemical reactor with light from 350 nm mercury vapor lamps.

Ru₂(chp)₄N₃ (**4**). *Ru₂(chp)₄Cl* (**5**) (315.25 mg, 0.419 mmol) and NaN₃ (2.72 g, 41.85 mmol) were added to a 200 mL Schlenk flask along with a mixture of dry dichloromethane (100 mL) and anhydrous methanol (12 mL) and stirred for 96 h under static, dry nitrogen. The suspension was then filtered through a fine frit, the filtrate solvent was removed in vacuo, and the product was washed with ether and hexanes and collected (280 mg, 88%). MW: 758.26 g/mol. MALDI-TOF (m/z): ([M - N₃]⁺) 716. IR (ATR): 3092 w, 2028 s (N₃), 1608 m, 1593 s, 1529 s, 1437 s, 1429 m, 1387 m, 1345 s, 1324 w, 1231 m, 1014 s, 931 w, 920 w, 795 m, 787 m, 668 s. (**4**·2CH₂Cl₂) (C₂₂H₁₆N₇Cl₈O₄Ru₂): calcd. C 28.47, H 1.74, N 10.56; found C 28.74, H 1.69, N 9.93 (the N content is routinely low for samples of **4**, which we attribute to partial decomposition of the azide group during sample shipment). Its instability under ambient conditions is attested by thermal gravimetric analysis (see Figure S3.6).

[*H₂NPPh₃*]*Cl*. Compound **4** (10.08 mg, 0.01329 mmol), PPh₃ (recrystallized from hot ethanol) (9.92 mg, 0.01318 mmol), and PPnCl (7.63 mg, 0.01329 mmol) (for use as an internal standard) were combined with dry dichloromethane (100 mL) in a 100 mL Schlenk tube. The headspace was evacuated and the clear, dark purple mixture was photolyzed for two hours at room temperature to yield a clear magenta product. Gaseous HCl was then bubbled into the solution for 10 seconds, which subsequently turned pink. A 4 mL aliquot was then removed, the solvent was removed in vacuo, and the residue was dissolved in CDCl₃ for analysis via ¹H and ³¹P NMR. The remaining organic solution was set to crystallize by slow diffusion with hexanes and yielded

purple crystals of the $\text{Ru}_2(\text{chp})_4\text{Cl}\cdot 2\text{CH}_2\text{Cl}_2$ (**5** $\cdot 2\text{CH}_2\text{Cl}_2$) starting material. Yield ($\text{H}_2\text{NPPH}_3\text{Cl}$): 63%. MW: 313.76. ^{31}P NMR (CDCl_3): δ 35.91 (s). Yield ($\text{Ru}_2(\text{chp})_4\text{Cl}$): 96% by UV-Vis.

$\text{Ru}_2(\text{chp})_4\text{Cl}$ MW: 751.71 g/mol. MALDI-TOF (m/z): ($[\text{M}]^+$) 751, ($[\text{M} - \text{Cl}]^+$) 716.

Ru₂(chp)₄Cl (**5**). $\text{Ru}_2(\text{OAc})_4\text{Cl}$ (520 mg, 1.10 mmol), anhydrous LiCl (660 mg, 15.57 mmol) and Hchp ligand (recrystallized from hot hexanes) (1.23 g, 9.50 mmol) were added to a 200 mL Schlenk flask, followed by the addition of dry, degassed toluene (100 mL). A Soxhlet extractor containing a cellulose thimble filled with 3 g of anhydrous K_2CO_3 was then fitted onto the Schlenk flask along with a condenser. The mixture was heated to reflux at 150°C for 72 hours under dry N_2 flow. The purple precipitate (**5**) was collected by filtration, dissolved in dichloromethane, and filtered again to remove excess LiCl salt. The filtrate was then removed *in vacuo*, washed with hexanes, and collected. Yield: 0.76 g (92%). MW: 751.71 g/mol. MALDI-TOF (m/z): ($[\text{M}]^+$) 751, ($[\text{M} - \text{Cl}]^+$) 716. IR (ATR): 3082 w, 1591 w, 1529 s, 1430 w, 1387 s, 1339 w, 1265 m, 1167 w, 1073 s, 1014 s, 934 s, 788 s, 718 s, 697 s.

Physical Measurements. ^1H and ^{31}P NMR spectra were recorded at an operating frequency of 300 or 400 MHz on Bruker spectrometers in the deuterated solvent noted. The ^1H spectra were referenced to TMS at 0 ppm, and the ^{31}P NMR spectra were properly referenced to the corresponding ^1H NMR spectra. Chemical shifts are reported in parts per million. Matrix-assisted laser desorption/ionization (MALDI) mass spectrometry data were obtained using an anthracene matrix on a Bruker Reflex II mass spectrometer in positive ion detection mode. IR spectra were taken on a Bruker Tensor 27 spectrometer using an ATR adapter (no matrix). Elemental analysis was done at Midwest Microlab, LLC in Indianapolis, IN, USA.

EPR Spectroscopy. EPR data were acquired on a Bruker ELEXSYS E500 EPR spectrometer equipped with a Varian E102 microwave bridge interfaced with a Linux system. An Oxford Instruments ESR-900 continuous-flow helium cryostat and an Oxford Instruments 3120 temperature controller were used to control the sample temperature. A Hewlett-Packard 432A power meter was used for microwave power calibration, with measurement conditions as follows: for **4** 9.3833 GHz, 4.000 G modulation amplitude, 4000 G center field, 8000 G sweep width, 2.00 mW power, 60 dB gain, 327.68 ms time constant, and 6K; for **6** 9.3779 GHz, 5.000 G modulation amplitude, 4000 G center field, 8000 G sweep width, 2.00 power, 60 dB gain, 327.68 mw time constant, and 6K.

X-Ray Crystallography Data Collection and Structure Determination. Crystallographic data were measured at the Molecular Structure Laboratory of the Chemistry Department of the University of Wisconsin – Madison. Suitable crystals of **4** and **5** were selected under oil and ambient conditions. For **4**, a black block shaped crystal with dimensions 0.40 x 0.30 x 0.20 mm³ was selected. For **5**, a violet block shaped crystal with dimensions 0.33 x 0.28 x 0.181 mm³ was selected. The crystal was attached to the tip of a MiTeGen MicroMount©, mounted in a stream of cold nitrogen at 100(1) K, and centered in the X-ray beam using a video monitoring system. The crystal evaluation and data collection were performed on a Bruker Quazar SMART APEX-II diffractometer with Mo K α (λ = 0.71073 Å) radiation. The data were collected using a routine to survey the reciprocal space to the extent of a full sphere to a resolution of 0.70 Å and were indexed by the APEX program.³⁶ The structures were solved via direct methods and refined by iterative cycles of least-squares refinement on F² followed by difference Fourier synthesis. All hydrogen atoms were included in the final structure factor calculation at idealized positions and

were allowed to ride on the neighboring atoms with relative isotropic displacement coefficients. Absorption corrections were based on a fitted function to the empirical transmission surface as sampled by multiple equivalent measurements.³⁷ The systematic absences in the diffraction data were uniquely consistent for the space group $P2_1/c$ for **4** and $Pbca$ for **5**, yielding chemically reasonable and computationally stable results of refinement, and both structures were solved using direct methods using XS software.^{38,39} For **5**, the unit cell contains 16 dichloromethane molecules, which have been treated as a diffuse contribution to the overall scattering without specific atom positions by SQUEEZE/PLATON.⁴⁰

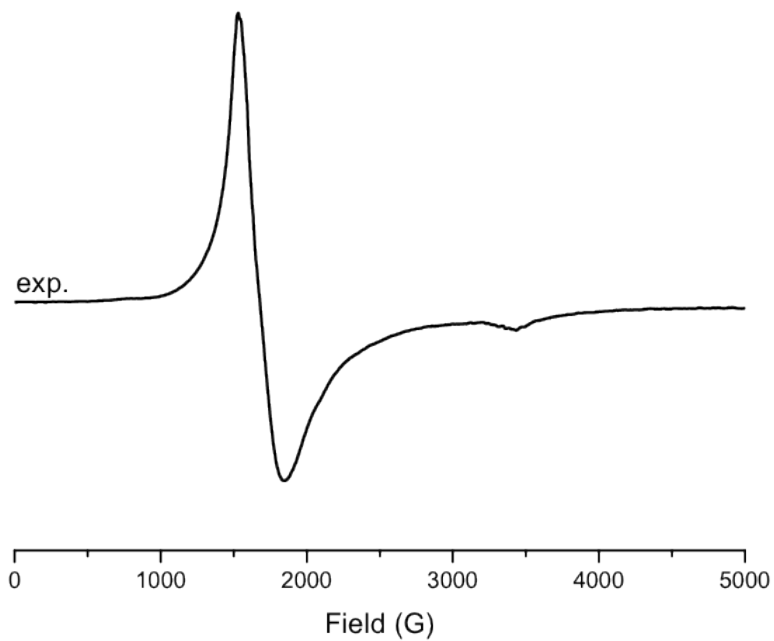


Figure S3.1 EPR data for $\text{Ru}_2(\text{chp})_4\text{N}_3$ (**4**) recorded at 6K.

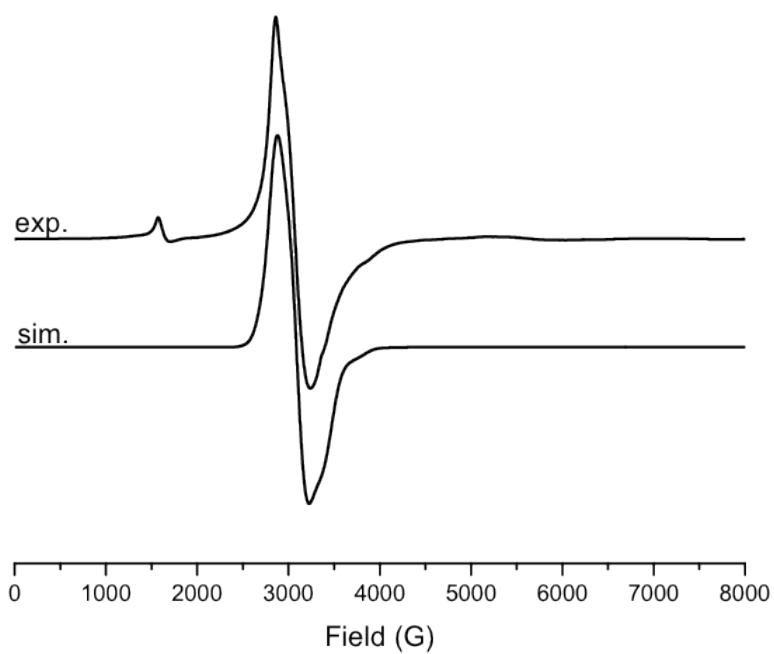


Figure S3.2 EPR data and simulation for $\text{Ru}_2(\text{chp})_4\text{N}$ (**6**) at recorded 6K. The signal at $g = 4$ is due to residual $\text{Ru}_2(\text{chp})_4\text{N}_3$ (**4**) in the sample.

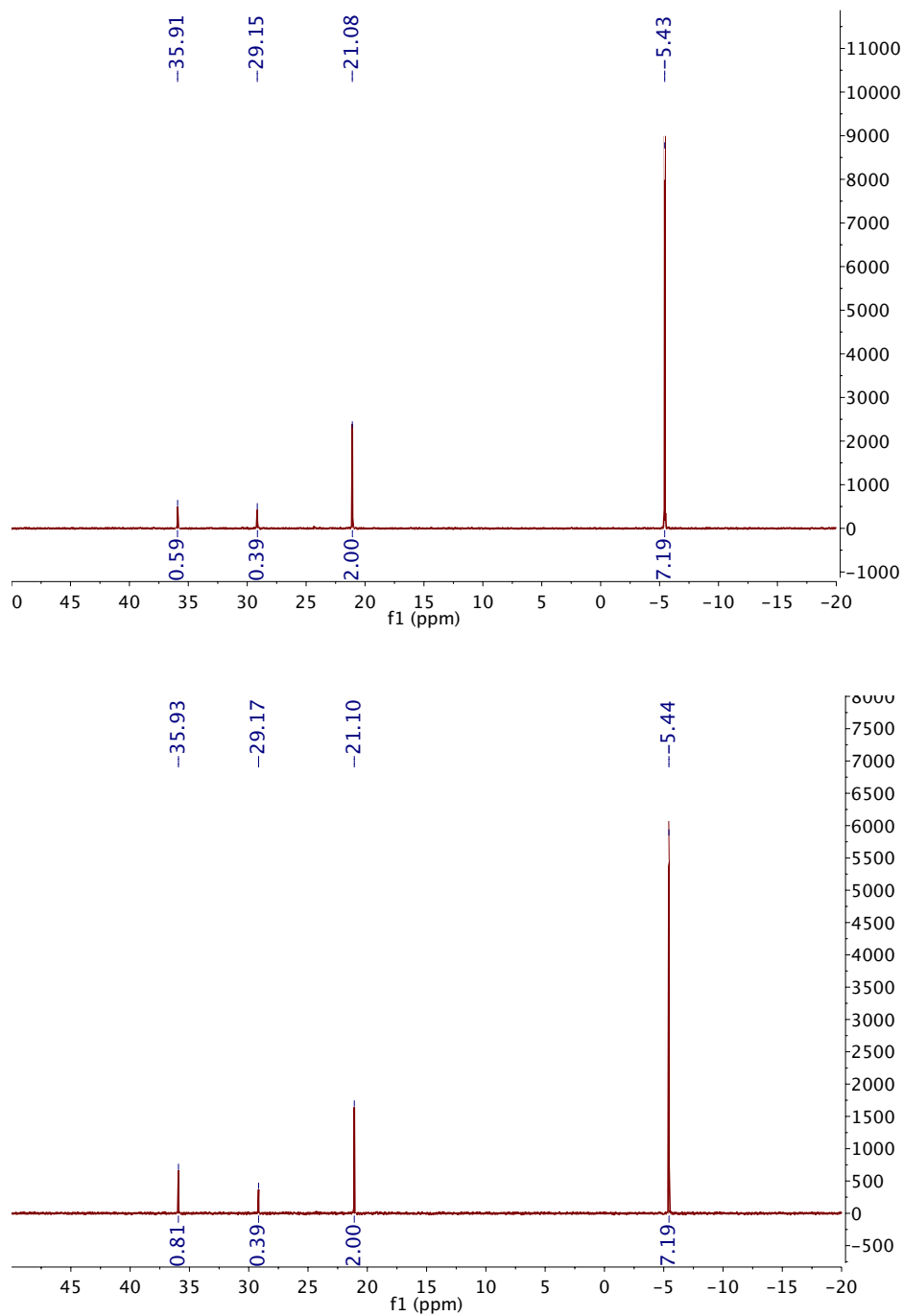


Figure S3.3 (a) $^{31}\text{P}\{^1\text{H}\}$ NMR spectrum for $[\text{H}_2\text{NPPh}_3]\text{Cl}$ formation, and
(b) $^{31}\text{P}\{^1\text{H}\}$ NMR spectrum after addition of authentic sample of $[\text{H}_2\text{NPPh}_3]\text{Cl}$.

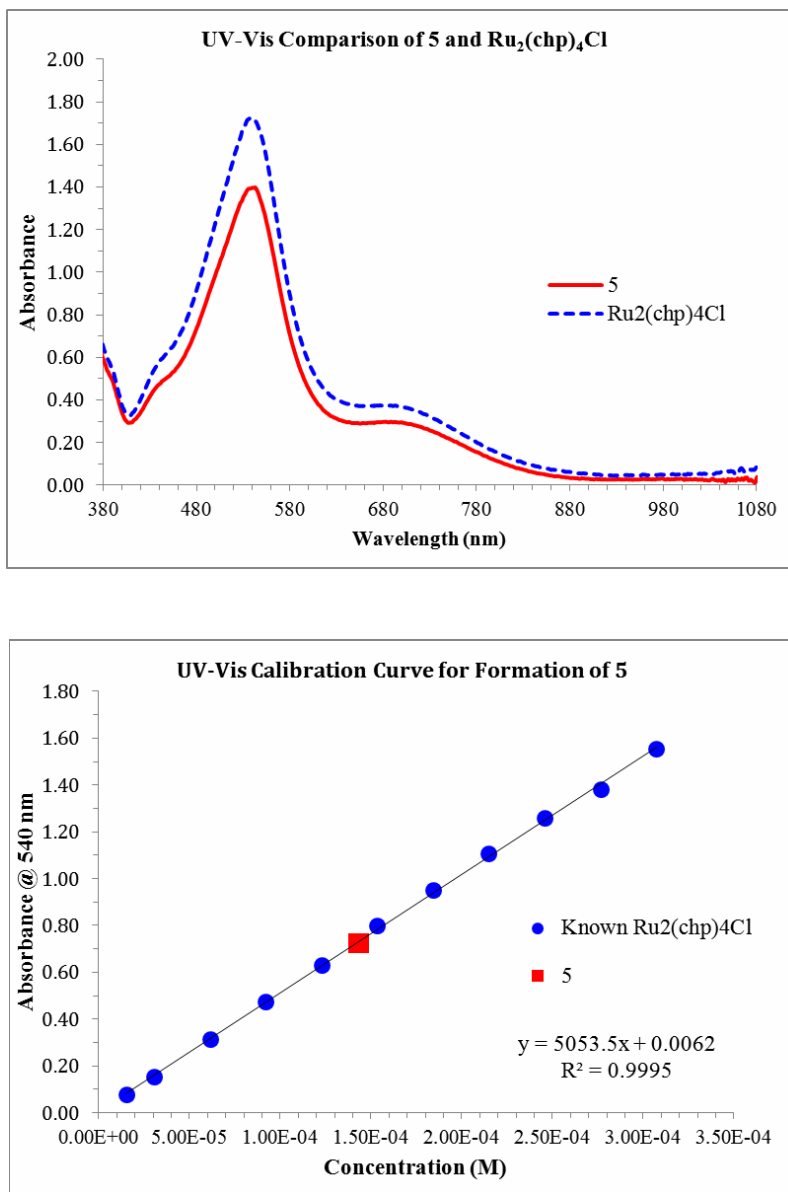


Figure S3.4 (a) UV-Vis data for confirmation that **5** is Ru₂(chp)₄Cl, and
(b) calibration curve data used to determine the yield of **5** as quantitative.

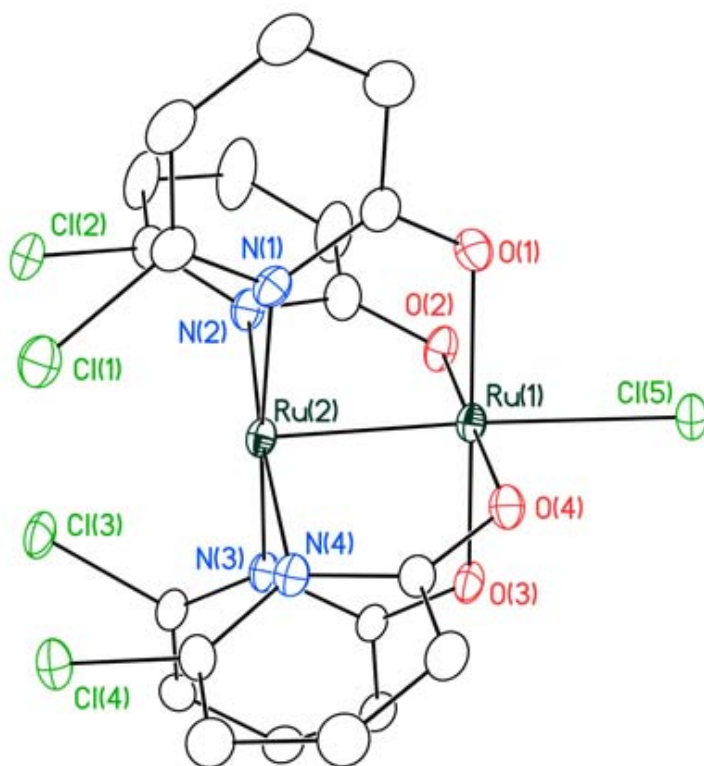


Figure S3.5 Thermal ellipsoid plot of $\text{Ru}_2(\text{chp})_4\text{Cl}$ (**5**) with ellipsoids drawn at the 30% probability level. Hydrogen atoms are omitted for clarity.

Sample: AKML 102-001 Ru2(chp)4N3
Size: 5.1570 mg
Comment: AKML 102-001 Ru2(chp)4N3

TGA

File: C:\...\Long\AKML 102-001 Ru2(chp)4N3.001
Operator: AKML
Run Date: 01-Apr-2011 08:21
Instrument: TGA Q500 V6.7 Build 203

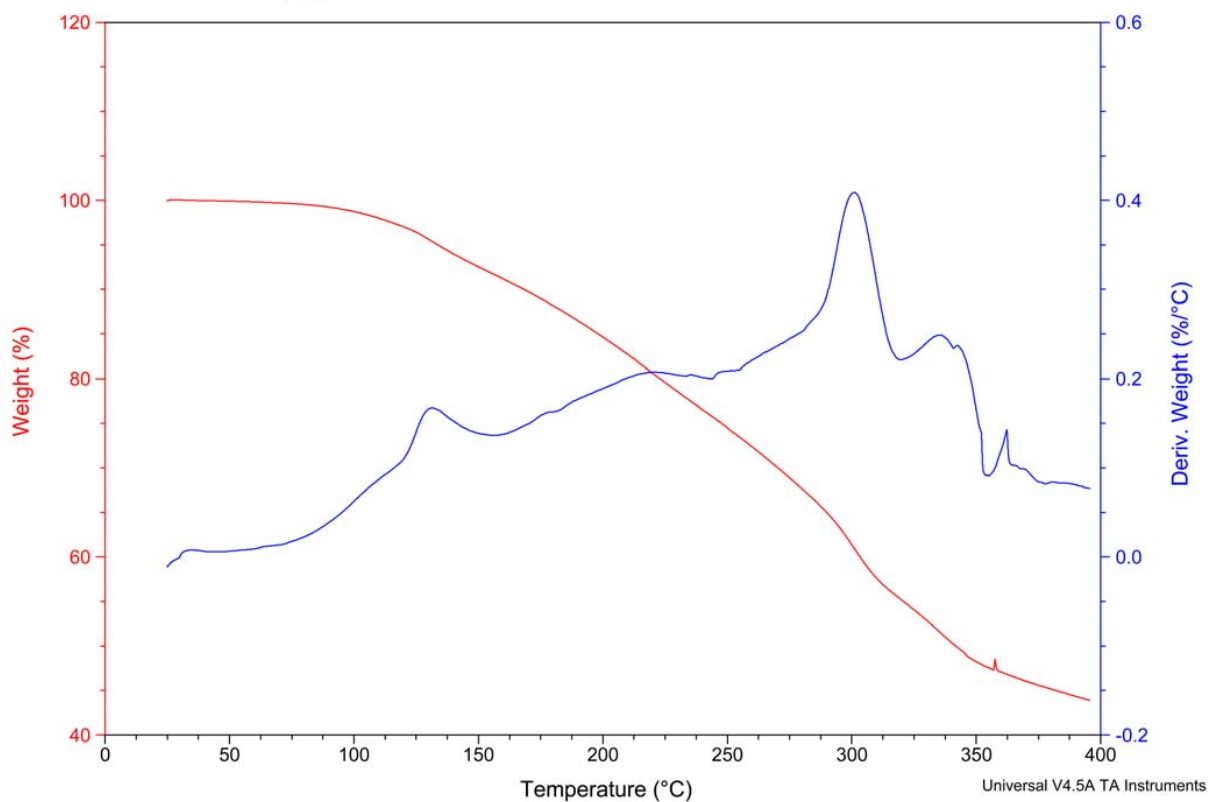


Figure S3.6 Thermogravimetric analysis data for **4**. Included is the percent mass loss as temperature is increased, as well as the derivative weight change, to show that **4** is not a stable compound.

Table S3.1 Crystal data for **4** and **5**.

Identification code	4	5
Empirical formula	C ₂₀ H ₁₂ Cl ₄ N ₇ O ₄ Ru ₂	C ₂₀ H ₁₂ Cl ₅ N ₄ O ₄ Ru ₂
Formula weight	758.31	751.73
Temperature	100(2) K	100(1) K
Wavelength	0.71073 Å	0.71073 Å
Crystal system	Monoclinic	Orthorhombic
Space group	<i>P</i> 2 ₁ / <i>c</i>	<i>P</i> <i>b c a</i>
Unit cell dimensions	a = 10.8755(3) Å	a = 19.535(4) Å
	b = 11.8291(3) Å	b = 12.827(3) Å
	c = 19.2576(5) Å	c = 24.586(5) Å
	α = 90°	α = 90°
	β = 99.783(2) °	β = 90°
Volume	γ = 90°	γ = 90°
	2441.4(1) Å ³	6161(2) Å ³
Z	4	8
Density (calculated)	2.063 g/cm ³	1.621 g/cm ³
Crystal size	0.40 x 0.30 x 0.20 mm ³	0.33 x 0.28 x 0.181 mm ³
Data / restraints / parameters	7157 / 0 / 334	109497 / 0 / 316
Goodness-of-fit on F ²	1.023	1.189
Final R ^{a,b} indices [I>2σ(I)]	R ₁ = 0.0237, wR ₂ = 0.0551	R ₁ = 0.0393, wR ₂ = 0.0913
R indices (all data)	R ₁ = 0.0276, wR ₂ = 0.0570	R ₁ = 0.0454, wR ₂ = 0.0934

^aR₁ = 3||F₀| - |F_c||/3|F₀|; ^bwR₂ = |[3[w(F₀² - F_c²)²] / 3[w(F₀²)²]]1/2, w = 1/σ² (F₀²) + (aP)² + bP, where P = [max(0 or F₀²) + 2(F_c²)]/3.

References.

- (1) Nugent, W. A.; Mayer, J. M. *Metal-Ligand Multiple Bonds*, John Wiley & Sons, New York, **1988**.
- (2) Eikey, R. A.; Abu-Omar, M. M. *Coord. Chem. Rev.* **2003**, *243*, 83.
- (3) Berry, J. F. *Comments Inorg. Chem.* **2009**, *30*, 28.
- (4) Huynh, M. H. V.; Meyer, T. J.; Jameson, D. L. *Inorg. Chem.* **2005**, *44*, 3657.
- (5) Scepianiak, J. J.; Fulton, M. D.; Bontchev, R. P.; Duesler, E. N.; Kirk, M. L.; Smith, J. M. *J. Am. Chem. Soc.* **2008**, *130*, 10515.
- (6) Scepianiak, J. J.; Margarit, C. G.; Harvey, J. N.; Smith, J. M. *Inorg. Chem.* **2011**, *50*, 9508.
- (7) Silvia, J. S.; Cummins, C. C. *J. Am. Chem. Soc.* **2008**, *131*, 446.
- (8) Tran, B. L.; Pink, M.; Gao, X.; Park, H.; Mindiola, D. J. *J. Am. Chem. Soc.* **2010**, *132*, 1458.
- (9) Scepianiak, J. J.; Bontchev, R. P.; Johnson, D. L.; Smith, J. M. *Angew. Chem. Int. Ed.* **2011**, *50*, 6630.
- (10) Schöffel, J.; Rogachev, A. Y.; DeBeer George, S.; Burger, P. *Angew. Chem. Int. Ed.* **2009**, *48*, 4734.
- (11) Crevier, T. J.; Mayer, J. M. *J. Am. Chem. Soc.* **1998**, *120*, 5595.
- (12) Crevier, T. J.; Mayer, J. M. *Angew. Chem. Int. Ed.* **1998**, *37*, 1891.
- (13) Brown, S. N. *J. Am. Chem. Soc.* **1999**, *121*, 9752.
- (14) Huynh, M. H. V.; White, P. S.; Meyer, T. J. *Inorg. Chem.* **2000**, *39*, 2825.
- (15) Maestri, A. G.; Cherry, K. S.; Toboni, J. J.; Brown, S. N. *J. Am. Chem. Soc.* **2001**, *123*, 7459.
- (16) Crevier, T. J.; Bennett, B. K.; Soper, J. D.; Bowman, J. A.; Dehestani, A.; Hrovat, D. A.; Lovell, S.; Kaminsky, W.; Mayer, J. M. *J. Am. Chem. Soc.* **2001**, *123*, 1059.
- (17) Huynh, M. H. V.; Meyer, T. J.; Hiskey, M. A.; Jameson, D. L. *J. Am. Chem. Soc.* **2004**, *126*, 3608.

- (18) Wu, A.; Dehestani, A.; Saganic, E.; Crevier, T. J.; Kaminsky, W.; Cohen, D. E.; Mayer, J. M. *Inorg. Chim. Acta* **2006**, 359, 2842.
- (19) Sieh, D.; Schöffel, J.; Burger, P. *Dalton Trans.* **2011**, 40, 9512.
- (20) Schlangen, M.; Neugebauer, J.; Reiher, M.; Schroder, D.; Lopez, J. P.; Haryono, M.; Heinemann, F. W.; Grohmann, A.; Schwarz, H. *J. Am. Chem. Soc.* **2008**, 130, 4285.
- (21) Hojilla Atienza, C. C.; Bowman, A. C.; Lobkovsky, E.; Chirik, P. J. *J. Am. Chem. Soc.* **2010**, 132, 16343.
- (22) Thomson, R. K.; Cantat, T.; Scott, B. L.; Morris, D. E.; Batista, E. R.; Kiplinger, J. L. *Nature Chem.* **2010**, 2, 723.
- (23) Schöffel, J.; Šušnjar, N.; Nüchel, S.; Sieh, D.; Burger, P. *Eur. J. Inorg. Chem.* **2010**, 2010, 4911.
- (24) Man, W.-L.; Lam, W. W. Y.; Kwong, H.-K.; Yiu, S.-M.; Lau, T.-C. *Angew. Chem. Int. Ed.* **2012**, 51, 9101.
- (25) Long, A. K. M.; Yu, R. P.; Timmer, G. H.; Berry, J. F. *J. Am. Chem. Soc.* **2010**, 132, 12228.
- (26) Long, A. K. M.; Timmer, G. H.; Pap, J. S.; Snyder, J. L.; Yu, R. P.; Berry, J. F. *J. Am. Chem. Soc.* **2011**, 133, 13138.
- (27) Berry, J. F. *Dalton Trans.* **2012**, 41, 700.
- (28) Timmer, G. H.; Berry, J. F. *Chem. Sci.* **2012**, 3, 3038.
- (29) Pap, J. S.; DeBeer George, S.; Berry, J. F. *Angew. Chem. Int. Ed. Engl.* **2008**, 47, 10102.
- (30) Chen, W. Z.; De Silva, V.; Lin, C.; Abellard, J.; Marcus, D. M.; Ren, T. *J. Cluster Sci.* **2005**, 16, 151.
- (31) Chakravarty, A. R.; Cotton, F. A.; Tocher, D. A. *Inorg. Chem.* **1985**, 24, 1263.
- (32) We note that an Fe analog of **7** has been crystallographically characterized. See Ref. 5.
- (33) Betley, T. A.; Peters, J. C. *J. Am. Chem. Soc.* **2004**, 126, 6252.
- (34) Lane, B. C.; McDonald, J. W.; Basolo, F.; Pearson, R. G. *J. Am. Chem. Soc.* **1972**, 94, 3786.
- (35) Mitchell, R. W.; Spencer, A.; Wilkinson, G. *J. Chem. Soc., Dalton Trans.* **1973**, 846.

- (36) *SMART*; Bruker-AXS: Madison, WI. 2009.
- (37) *SADABS*; Bruker-AXS: Madison, WI. 2012.
- (38) Sheldrick, G. M. *Acta Cryst. A* **2008**, *64*, 112.
- (39) Dolomanov, O. V.; Bourhis, L. J.; Gildea, R. J.; Howard, J. A. K.; Puschmann, H. J. *Appl. Cryst.* **2009**, *42*, 339.
- (40) <http://www.cryst.chem.uu.nl/platon/>.

Chapter 4

Oxygen Atom Transfer from an $Ru_2(chp)_4^+$ Oxyanion Complex via a Putative Ru–Ru=O Intermediate

This chapter is in preparation:

Amanda R. Corcos, József S. Pap, Tzuhsiung Yang, and John F. Berry.

Contributions: J. Pap synthesized complex **2**. T. Yang initially prepared **4**. All other work was performed by A. R. Corcos.

4.1 Abstract.

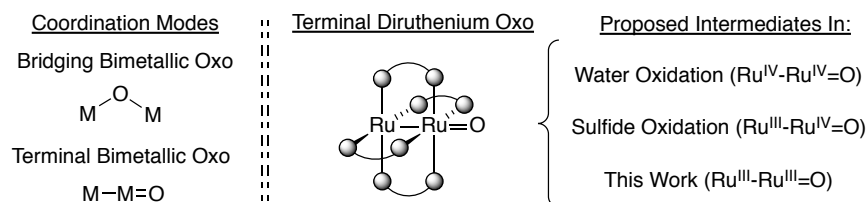
Ruthenium oxo complexes are important reactive intermediates in catalytic oxidations. To explore a novel synthetic oxidative route via potential Ru=O intermediates using decomposition of oxyanions, the complexes $[Ru_2(DPhF)_4][NO_3]$ (**2**, DPhF = diphenylformamidinate), $Ru_2(chp)_4ONO_2$ (**4**, chp = 6-chloro-2-hydroxypyridinate), and $Ru_2(chp)_4OCIO_3$ (**5**) were prepared, characterized, and investigated. IR spectroscopic and X-ray crystallographic data indicate that the nitrate anion does not bind to the Ru_2 center in **2**, while nitrate and perchlorate are weakly bound to the Ru_2 centers in **4** and **5**, respectively. MALDI-TOF mass spectra were recorded for **2**, **4**, and **5**, but only in the case of **4** are signals observed with m/z of 733 amu, consistent with the formation of the $[Ru_2(chp)_4O]^+$ ion. This signal shifts to 735 amu in **4*** (**4** containing ^{18}O -labeled nitrate). Compound **4** was further investigated by photolysis in frozen (77 K) and fluid (room temperature) solution. EPR spectroscopy indicates that frozen photolysis of **4** for 16 h produces NO_2^{\bullet} , implying the co-formation EPR-silent $Ru_2(chp)_4O$ (**6**). Formation of NO_2^{\bullet} is further confirmed by GC-MS headspace analysis after room temperature photolysis of **4** in fluid solution. Room temperature photolysis in the presence of the O-atom acceptor PPh_3 is accompanied by nearly quantitative formation of $OPPh_3$, and the

analogous experiment with **4*** yields $^{18}\text{OPPh}_3$. We propose that O-atom transfer from **4** occurs via an electrophilic Ru–Ru=O intermediate.

4.2 Introduction.

Metal terminal oxo species are well established as reactive intermediates for numerous biological and synthetic oxidation reactions,¹⁻⁶ for which correlation between electronic structure and reactivity have played a key role.⁷⁻¹⁰ In the presence of two metal centers, the oxo ligand generally favors a bridging coordination mode, i.e. M–O–M (Chart 1, left, above), which is less reactive than the terminal M=O mode. An interesting thought experiment is to consider whether compounds can be prepared in which the M–O–M connectivity is rearranged to support a metal-metal bond and a terminal oxo ligand, as in M–M=O (Chart 4.1, left, below). We recently described the first examples of such transition metal bimetallic terminal oxo species and found them to display very unusual reactivity.¹¹⁻¹³ Additionally, intermediates with a putative linear Ru–Ru=O structure have been proposed as intermediates in catalytic sulfide oxygenation¹⁴ and water oxidation.¹⁵ As shown in Chart 4.1, these intermediates are supported by bridging carboxylates on the Ru₂ unit in [Ru₂O]⁵⁺ and [Ru₂O]⁶⁺ oxidation states, respectively.

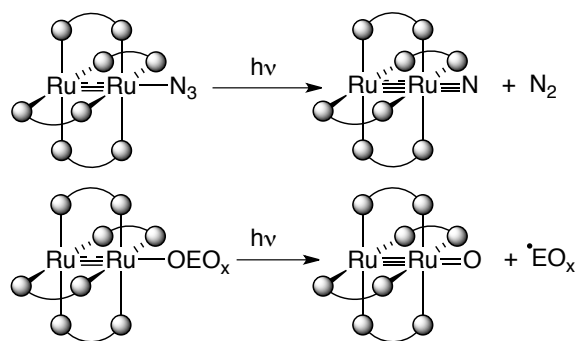
Chart 4. 1 Coordination modes and oxidation states for bimetallic oxo complexes.



Mononuclear Ru=O complexes are well-known, and a number of synthetic methods have been developed to access them. For example, chemical¹⁶⁻²⁰ and electrochemical²¹ oxidations of

Ru–OH₂ species are known, as are oxidation of Ru complexes with O-atom transfer reagents such as peroxides,^{22,23} PhIO,²⁴ NaOCl,²⁵ and even RuO₄.²⁶ Chemical reduction of dioxo Ru complexes^{23,27,28} and RuO₄[−] are also known to yield Ru=O species.²⁹ Of particular relevance to our work is the elimination of nitrite ion from an O=Ru–ONO₂ complex to produce a dioxo Ru species,³⁰ and disproportionation of nitrite to form both Ru=O and Ru–NO complexes.³¹

Our group has gained access to reactive Ru₂ nitride intermediates containing a linear Ru–Ru≡N structure via photolysis of azide precursors^{32–35} (Scheme 4.1) and, as such, we decided to explore similar methodologies for generating reactive Ru–Ru=O intermediates. Newcomb and coworkers have reported the use of flash photolysis to generate highly reactive metal oxo species by photolytic cleavage of complexes with O-coordinated oxyanions.^{36–38} We therefore decided to test whether Ru₂-nitrate and -perchlorate complexes could undergo photolytic reactions, possibly via an Ru–Ru=O intermediate.

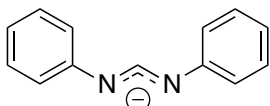
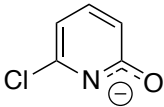


Scheme 4.1 Synthetic scheme for photolysis of Ru₂ azides and η^1 -O-coordinated oxyanions to form Ru₂ terminal nitrides and oxos, respectively.

To date, only two discrete Ru₂ compounds bearing axial oxyanionic ligands are known: Ru₂(DMBA)₄(ONO₂)₂ (DMBA = *N,N'*-dimethylbenzamidinate),³⁹ which contains two η^1 -coordinated nitrate ligands, and Ru₂(OAc)₄(ONO₂)(H₂O),⁴⁰ which forms polymeric chains upon loss of the aquo ligand. We are instead keen to explore whether a discrete, anhydrous mono-

oxyanion complex with an Ru–Ru–O–EO_x structure could be prepared. As such we turned to the DPhF (DPhF = *N,N'*-diphenylformamidinate) and chp (chp = 6-chloro-2-hydroxypyridinate) ligands, as their steric bulk near the axial coordination site should eliminate the possibility of forming polymeric chains and only one oxyanionic ligand should bind to the Ru₂ core based on charge balance. The compounds discussed herein are given in Chart 4.2.

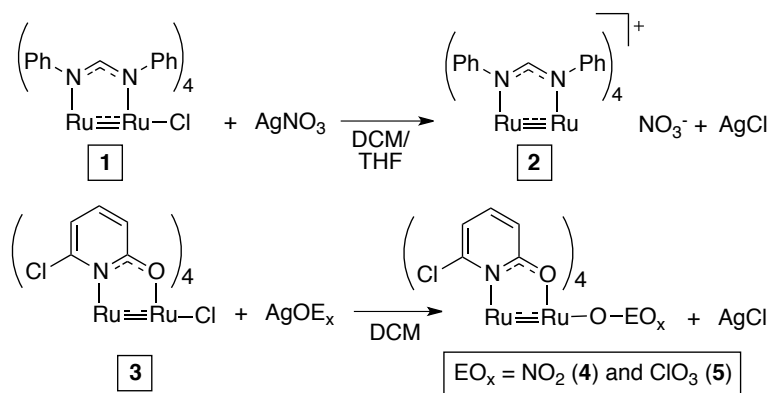
Chart 4.2 Compounds discussed in this chapter.

Entry	Complex	Ligands
1	Ru ₂ (DPhF) ₄ Cl	 DPhF
2	[Ru ₂ (DPhF) ₄][NO ₃]	
3	Ru ₂ (chp) ₄ Cl	 chp
4	Ru ₂ (chp) ₄ ONO ₂	
5	Ru ₂ (chp) ₄ OCLO ₃	

4.3 Results and Discussion.

Synthesis and IR Spectroscopic Characterization. Compounds **2**, **4**, and **5** were prepared from the chloride precursors **1** and **3** by metathesis with the appropriate Ag⁺ salts (AgNO₃ for **2** and **4**; AgClO₄ for **5**) as seen in Scheme 4.2. The IR spectrum for **2** displays a signal at 1773 cm⁻¹, which is well within the characteristic range of 1700-1800 cm⁻¹ for free nitrate anions.^{41,42} Furthermore, the MALDI-TOF mass spectrum of **2** shows an isotopic envelope indicative of the free [Ru₂(DPhF)₄]⁺ core (Figure S4.1), and the crystal structure of **2** consists of well-separated [Ru₂(DPhF)₄]⁺ cations and NO₃⁻ anions.⁴³ The steric bulk of the DPhF phenyl rings therefore prevents NO₃⁻ coordination. In contrast, the IR spectra of **4** and **5** display signals consistent with

O-coordinated nitrate and perchlorate ligands⁴² (1278 cm^{-1} [$\nu_{\text{asym}}(\text{ONO})$] for **4**; $\nu_3 = 1154, 1134, 1025\text{ cm}^{-1}$, and $\nu_4 = 894\text{ cm}^{-1}$ for **5**).



Scheme 4.2 Formation of nitrate complex **2** from chloride precursor **1** and oxyanion complexes **4** and **5** from chloride precursor **3**.

Crystallography. Compounds **4** and **5** have been characterized by X-ray crystallography (Figures 4.1 and 4.2 and Tables S4.1). As with the chloride precursor **3**⁴⁴ and azide analog $\text{Ru}_2(\text{chp})_4\text{N}_3$,³⁵ the equatorial chp ligands in **4** and **5** are bound in an orientation so as to form the (4,0) isomer, and this allows for the oxyanionic ligand to bind only to the exposed Ru axial site.

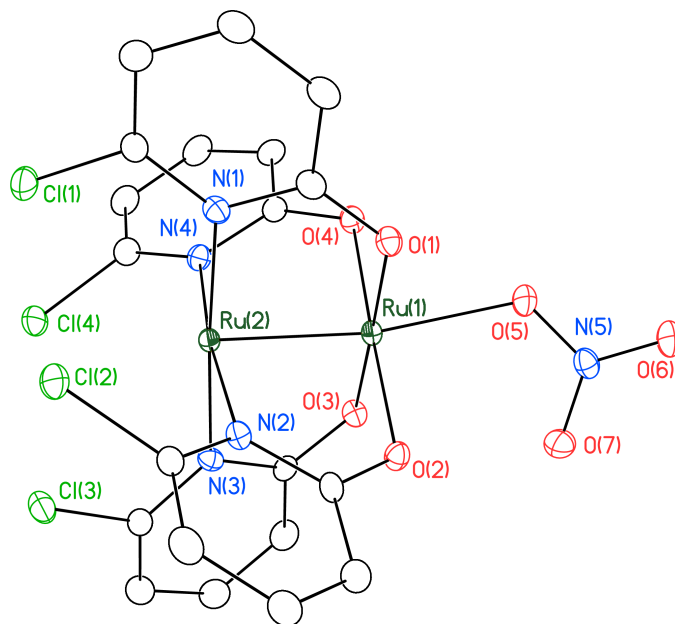


Figure 4.1 Thermal ellipsoid plot of $4 \cdot 2\text{CH}_2\text{Cl}_2$ with ellipsoids drawn at the 50% probability level. Hydrogen atoms and molecules of solvation omitted for clarity.

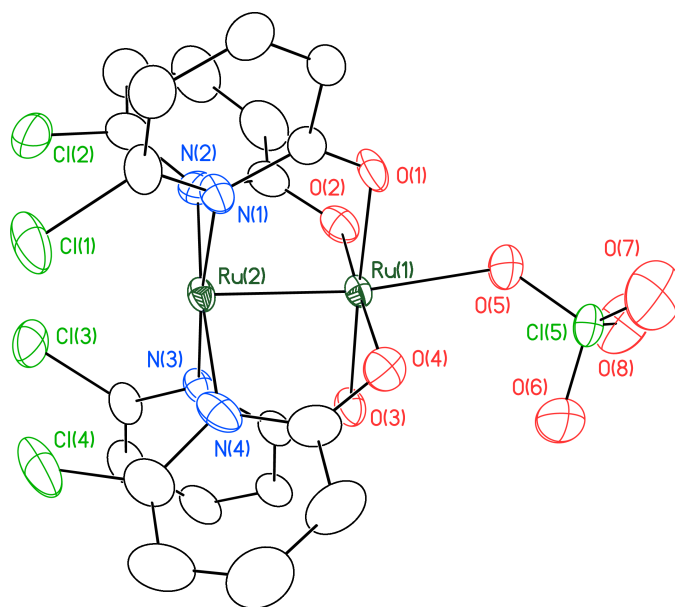


Figure 4.2 Thermal ellipsoid plot of $5 \cdot 2\text{CH}_2\text{Cl}_2$ with ellipsoids drawn at the 50% probability level. Hydrogen atoms and molecules of solvation omitted for clarity.

The Ru–Ru distances in **4** and **5** (2.2633(3) Å and 2.2540(7) Å,⁴⁵ respectively, listed in Table 1) are in accord with all other previously characterized Ru₂⁵⁺ oxypyridinate complexes.⁴⁶ The Ru(2)–Ru(1)–O(5) bond angle in **4** deviates from linearity to 170.07(7)° and that in **5** deviates to 170.9(2)°, likely due to crystal packing effects. At 1.221(3) Å and 1.236(3) Å, the nitrate N–O distances (N(5)–O(6) and N(5)–O(7), respectively) in **4** are slightly shorter than, but in line with, those of an unbound nitrate anion (1.241(2) Å).⁴⁷ At 1.306(3) Å, the O(5)–N(5) distance is significantly longer, causing the nitrate anion to lose 3-fold symmetry due to the Ru(1)–O(5) interaction. The O(6)–N(5)–O(7) angle is 122.1(3)°, and when combined with the other O–N–O angles (118.4(3)° and 119.4(2)°) sum to 359.9°, indicating a planar nitrate group, which is oriented parallel to the Ru–Ru bond. The perchlorate anion in **5** exhibits O–Cl–O angles that range from 107.0(3)°–112.8(4)°, which are close to the idealized geometry of 109.5° for a tetrahedral anion. The O(5)–Cl(5) distance is slightly elongated at 1.464(4) Å compared to the other O–Cl bond distances of 1.370(5) Å, 1.392(5) Å, and 1.445(6) Å.

Table 4.1 Selected crystallographic bond lengths and angles for **4** and **5**. E = N for **4**, Cl for **5**.

Compound	4	5
Ru(1)–Ru(2) Å	2.2633(3)	2.2540(7)
Ru(1)–O(5) Å	2.200(2)	2.249(4)
O(5)–E(5) Å	1.306(3)	1.464(4)
E(5)–O(6) Å	1.221(3)	1.445(6)
E(5)–O(7) Å	1.236(3)	1.370(5)
E(5)–O(8) Å	–	1.392(5)
Ru(2)–Ru(1)–O(5) (°)	170.07(6)	170.9(2)

UV-Vis Spectroscopy. The most intense absorption feature for compounds **3-5** shifts from 529 to 532 to 542 nm and increases in intensity as the coordinating strength of the anion increases (**5** < **4** < **3**) (Figure 4.3). Though this feature has not been definitively assigned to an electronic transition, the variation in intensity observed here suggests that it has significant LMCT character involving the axial ligand. The secondary feature in the spectrum also shifts from 666 to 678 to 689 nm in the same manner (**5** < **4** < **3**), but the intensity of this feature remains relatively consistent throughout the series.

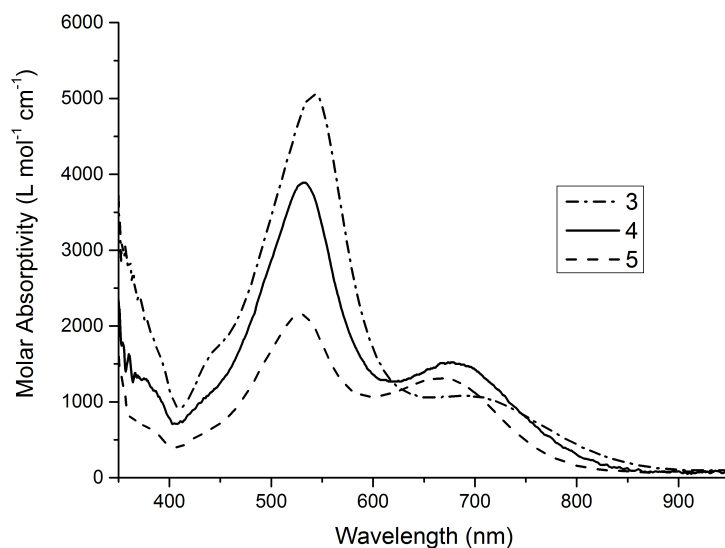


Figure 4.3 UV-Vis for compounds **3-5** in CH₂Cl₂. The spectrum for **3** was previously reported⁴⁴ but is included here for direct comparison.

Cyclic Voltammetry. Cyclic voltammograms of **4** and **5** were recorded under two distinct sets of conditions. Solutions of the compounds in CH₂Cl₂ with 0.1 M NBu₄PF₆ electrolyte were initially examined, followed by a solution of **4** in 0.1 M NBu₄NO₃ and **5** in 0.1 M NBu₄ClO₄. These varying conditions give us insight into the binding of NO₃[−] and ClO₄[−] anions to the [Ru₂(chp)₄]⁺ core in solution. In analyzing these data, we can consider two limiting cases. If, first, the NO₃[−] and ClO₄[−] anions dissociate completely from **4** and **5** in CH₂Cl₂, then we would

expect both compounds to have identical CV traces in 0.1 M NBu₄PF₆. If, on the other hand, we assume that NO₃[−] and ClO₄[−] do not dissociate at all from **4** or **5** in solution, then we would expect the CV traces of **4** and **5** to be identical in NBu₄PF₆ and NBu₄NO₃/NBu₄ClO₄ electrolytes. The data shown in Figure 4.4 (see also Table 4.2) show us clearly that neither of these limiting cases reflects reality. The fact that the CVs of **4** and **5** in NBu₄PF₆ appear distinct indicates that these solutions do not simply contain free [Ru₂(chp)₄]⁺ cations. However, the fact that the redox potentials change when the electrolyte is changed to NBu₄NO₃ or NBu₄ClO₄ indicates that both **4** and **5** undergo the following equilibrium in solution:

$$\text{Ru}_2(\text{chp})_4\text{A} \rightleftharpoons [\text{Ru}_2(\text{chp})_4]^+ + \text{A}^-$$

Addition of excess A[−] shifts this equilibrium to the left. This is clearly a fast equilibrium relative to the timescale of the electrochemical measurement since we do not observe distinct waves that may be assigned to Ru₂(chp)₄A and [Ru₂(chp)₄]⁺. We therefore cannot determine from this data the relative amounts of Ru₂(chp)₄A and [Ru₂(chp)₄]⁺ in solution.

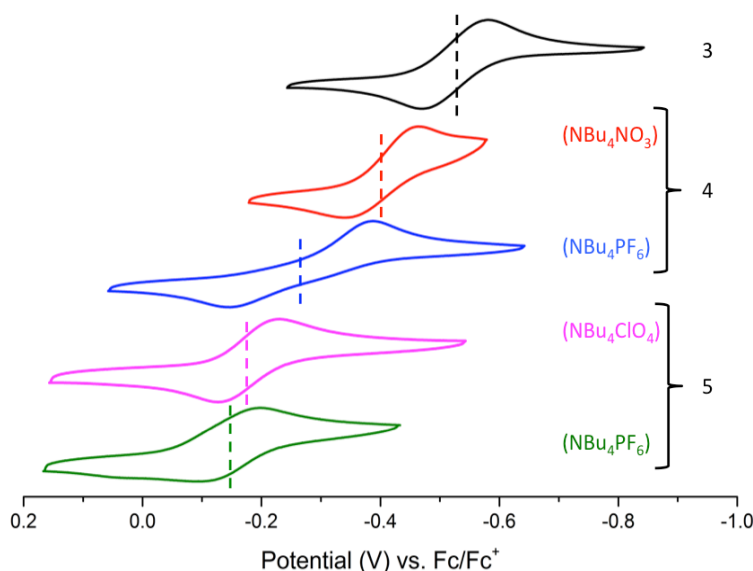


Figure 4.4 Cyclic voltammograms of Ru₂^{5/4+} couple for **3-5** versus Fc/Fc⁺. *E*_{1/2} for each species is marked with a dashed vertical line.

Table 4.2 E values for $\text{Ru}_2^{5/4+}$ couple for **1-5** vs. Fc/Fc^+ in CH_2Cl_2 with scan rate = 100 mV/s.

Electrolyte is 0.1 M. * Indicates quasi-reversible. # Previously reported against SCE⁴⁸ and converted here to be against Fc/Fc^+ .⁴⁹ ‡ Previously reported against Ag/AgCl ⁵⁰ and re-measured here for direct comparison.

Compound	Electrolyte	$E_{1/2}$ (V)	E_c (V)	E_a (V)
1		—	-1.1 [#]	—
2	NBu ₄ PF ₆	-0.687	—	—
3	NBu ₄ PF ₆	-0.525 [‡]	-0.581	—0.469
4	NBu ₄ NO ₃	-0.401 [*]	-0.465	-0.338
4	NBu ₄ PF ₆	-0.267 [*]	-0.388	-0.146
5	NBu ₄ ClO ₄	-0.179 [*]	-0.230	-0.127
5	NBu ₄ PF ₆	-0.145 [*]	-0.197	-0.094

Photolysis Screening by Mass Spectrometry. The most prominent set of signals for **4** and **5** in MALDI-TOF mass spectrometry experiments corresponds to the $\text{Ru}_2(\text{chp})_4^+$ core, with the isotopic distribution centered around $m/z = 717$ amu (Figure 4.5 for **4**; Figure S4.2 for **5**), indicating facile loss of the axially-bound oxyanions. Mass spectra of $\text{Ru}_2(\text{II/III})$ -azide complexes show similar behavior.³² Increased laser power can be used to test for photolytic reaction pathways. In the case of **4**, there is a weak Ru_2 signal centered at $m/z = 733$ amu, which is consistent with an $[\text{Ru}_2(\text{chp})_4\text{O}]^+$ ion, suggesting to us that an Ru_2O species could be formed upon photolysis of **4**. To further support this hypothesis, we used labeled ^{18}O -nitrate ($\text{N}^{18}\text{O}_3^-$) to form $\text{Ru}_2(\text{chp})_4^{18}\text{ON}^{18}\text{O}_2$ (**4***), and we found that this feature in the mass spectrum shifts to

$m/z = 735$ amu (Figure 4.5), clearly indicating that the axial O atom in the $[\text{Ru}_2(\text{chp})_4\text{O}]^+$ ion derives from nitrate. The $m/z = 733$ amu feature is barely discernable in the spectra of **5**, suggesting to us that perchlorate may not be as suitable a precursor for the formation of an Ru_2O intermediate. Therefore only **4** was investigated further.

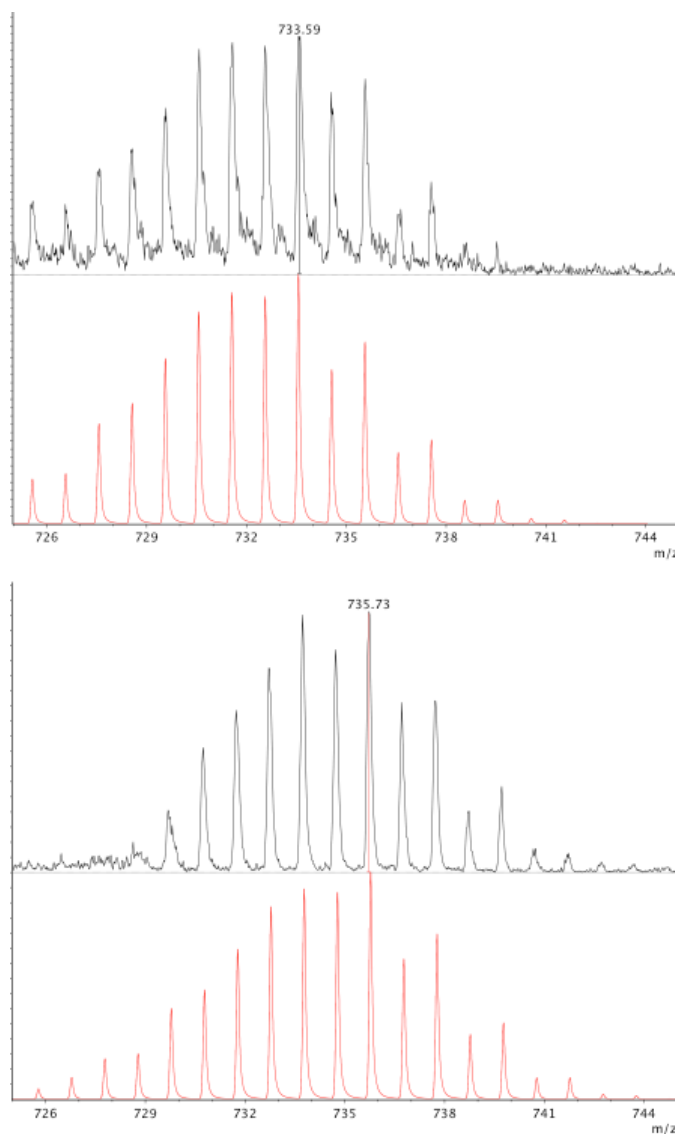
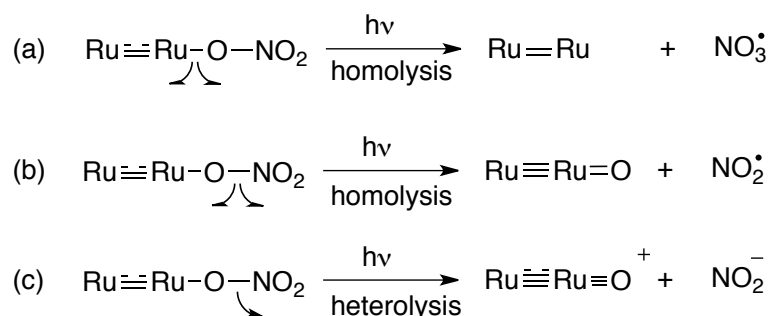


Figure 4.5 MALDI-TOF mass spectrum for **4** (black, top). Simulation (red) indicates isotope pattern at $m/z = 733$ amu is due to $[\text{Ru}_2(\text{chp})_4\text{O}]^+$. Upon isotopic labeling, MALDI-TOF mass spectrum for **4*** (black, below) shifts by 2 units, as confirmed by simulation (red, bottom).

In photolysis experiments of **4** there are two possible sites at which bonds could break homolytically: (a) the Ru–ONO₂ bond or (b) the RuO–NO₂ bond (Scheme 4.3). Previous studies have indicated that either is possible.^{36,37,51,52} Free nitrate is known to eliminate either ³P O or O[−] upon UV irradiation at ~300 nm.^{53,54} Heterolytic O–NO₂ bond cleavage is another possible pathway (pathway c in Scheme 3), which has been demonstrated for perchlorate compounds.^{36,37} Upon homolysis (pathway b), the resulting radical species NO₂[•] should be EPR active, unlike its Ru₂O counterpart Ru₂(chp)₄O (**6**), which has a ground state of *S* = 0 or 1.⁵⁵ Heterolysis (pathway c), on the other hand, would give rise to an EPR-active Ru₂O⁺ species. Thus, EPR spectroscopy may be used to assess the likely mechanism of photolysis for **4**.



Scheme 4.3 Possible products upon exposing nitrate complexes to photolytic conditions.

Photolysis of 4 in Frozen Solution at 77 K and in Fluid Solution at Room Temperature.

The EPR spectra of **2**, **4**, and **5** (Figures S4.3, 4.6, and S4.4, respectively) were measured at 10 or 15 K in a frozen solution of dichloromethane. The spectrum of **4** displays an axial signal with effective *g* values of 3.86 and 1.95, consistent with an *S* = 3/2 ground state with *D* >> *hν* (Table 4.3). This prominent EPR signal can be used to assess the efficacy of photolysis of **4** in frozen solution.

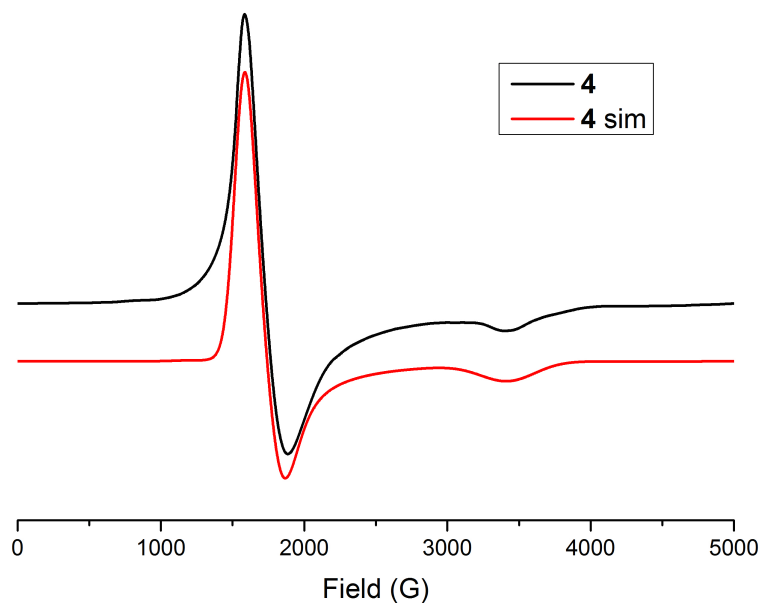


Figure 4.6 EPR spectrum and simulation of **4** recorded at 10 K.

Table 4.3 EPR spectral simulations for **2**, **4**, and **5**.

Compound	2	4	5
g_{\perp}	2.125	2.01	2.00
g_{\parallel}	1.94	1.95	1.93
E/D	0.006	0.035	0.033
HStrain	850, 350, 450	1200, 900, 1200	1550, 850, 1100

Exposure of a frozen dichloromethane solution of **4** to 350 nm wavelength light at 77 K for 8 h yielded no change in the intensity of the EPR signal of **4**. Switching to 254 nm light and photolyzing for 16 h at 77 K yielded the EPR spectrum shown in Figure 4.7. There is a slight decrease in the signal intensity from the $S = 3/2$ signal of **4** and, more significantly, a new feature in the $g = 2$ region grows in, which exists as an isotropic 1:1:1 triplet, clearly indicating hyperfine coupling involving an $I = 1$ ^{14}N nucleus. This feature compares favorably to known literature values for NO_2^{\bullet} as compared to those of NO_3^{\bullet} (Figure 4.7, inset).⁵⁶⁻⁵⁸ The presence of

NO_2^\bullet suggests that photolysis of **4** proceeds via homolytic cleavage of the O(5)–N(5) nitrate bond (pathway b in Scheme 4.3).

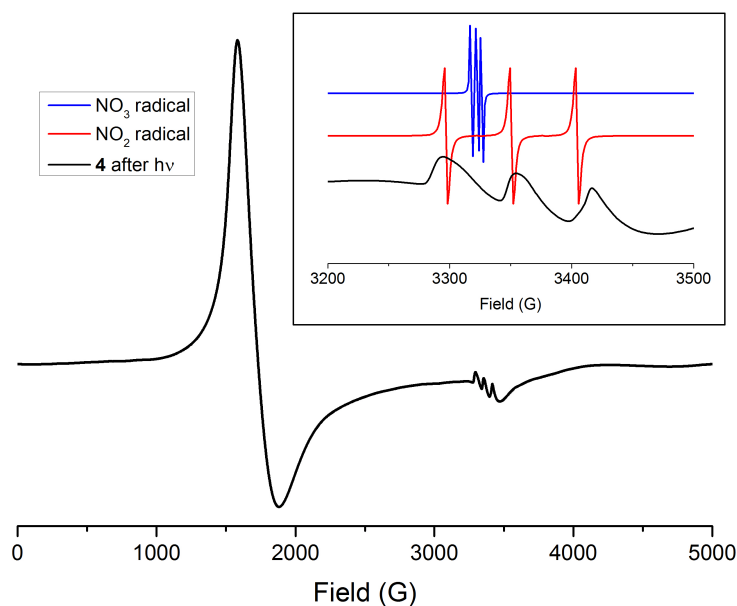


Figure 4.7 EPR spectrum of **4** in CH_2Cl_2 taken at 10 K after 16 hr of frozen photolysis at 254 nm. Inset: simulations⁵⁶⁻⁵⁸ of NO_3^\bullet (blue, above) and NO_2^\bullet (red, middle) compared to **4** after frozen photolysis (black, below).

Photolysis experiments were further performed on fluid solutions of **4** in CH_2Cl_2 at room temperature under N_2 . Under these conditions, photolysis is complete in a shorter time period of 4 h using 350 nm wavelength light. Using the isotopically-enhanced analog **4***, GC-MS analysis of the headspace of the reaction confirms formation of $\text{N}^{18}\text{O}_2^\bullet$ ($m/z = 50$) in significant quantities (Figure 4.8), further supporting the homolytic cleavage mechanism.

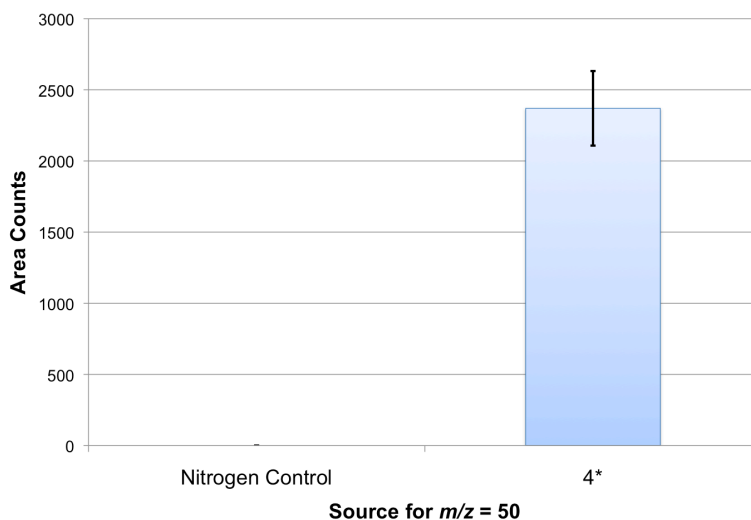


Figure 4.8 GC-MS headspace analysis for formation of $\text{N}^{18}\text{O}_2^\bullet$ ($m/z = 50$) after photolysis of **4*** at room temperature under N_2 for 4 h using 350 nm wavelength. As compared to the counts for $m/z = 50$ amu for the N_2 control, $\text{N}^{18}\text{O}_2^\bullet$ is clearly formed under reaction conditions.

Oxygen Atom Transfer via Room Temperature Photolysis of 4. Room temperature fluid solution photolytic experiments were also performed in the presence of an excess of the well-known oxygen atom acceptor PPh_3 and monitored for the formation of oxygen atom transfer products. A CH_2Cl_2 solution of **4**, PPh_3 (20 eq. vs. **4**), and bis(triphenylphosphine)iminium chloride (PPNCl , an internal standard for calibration by ^{31}P NMR spectroscopy, 1 eq. vs **4**), was photolyzed for 4 h using 350 nm light at room temperature under N_2 . Analysis by $^{31}\text{P}\{^1\text{H}\}$ NMR spectroscopy indicated the formation of the intermolecular oxygen atom transfer product OPPh_3 (signal at $\delta = 29$ ppm, Figure S4.5) in high yield (Figure 4.9). The identity of this product was confirmed by doping with an authentic sample of OPPh_3 (Figure S4.6).

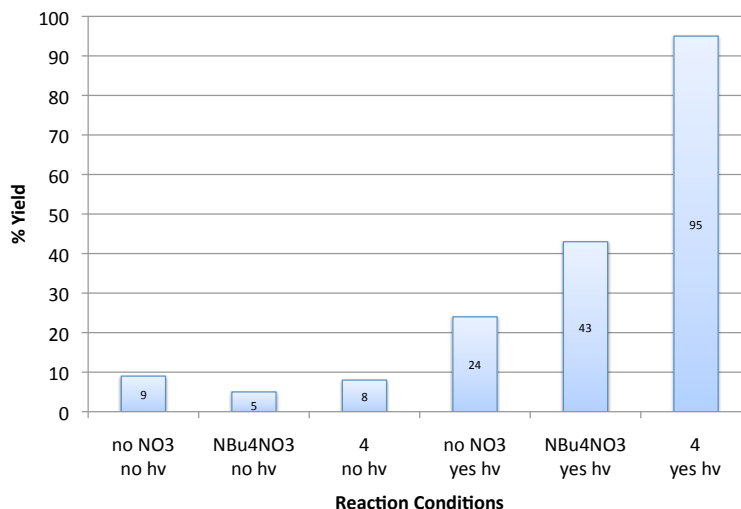


Figure 4.9 Yield of OPPh₃ after exposure to different oxygen atom sources, both with and without exposure to photolytic conditions.

Though we suspect photolytic formation of the Ru–Ru=O intermediate **6** in this reaction, there are multiple theoretical sources for the oxygen atom in OPPh₃. For example, it could be that unbound nitrate promotes oxygen atom transfer. To test this possibility, photolysis of NBu₄NO₃ was performed under identical conditions as previously expressed. OPPh₃ is indeed generated, but only in half the yield as when **4** was used (Figure 4.9). Therefore, OPPh₃ can be formed from free NO₃[−] anion but is formed more efficiently from **4**. It is also conceivable that O₂, resulting from two Ru₂O intermediates reacting together, could be the oxygen atom source in formation of OPPh₃. After photolysis of **4*** in CH₂Cl₂ at room temperature, analysis of the headspace by GCMS indicates that ¹⁸O₂ is not formed (Figure S4.8). We therefore propose that the intermediate Ru–Ru=O is responsible for oxygen atom transfer in this system.

4.4 Conclusions.

Whereas the $[\text{Ru}_2(\text{DPhF})_4]^+$ core is not sterically accessible to bind non-linear anions as ligands, the $[\text{Ru}_2(\text{chp})_4]^+$ core does support the formation of discrete, mono-oxyanion complexes with η^1 -nitrate and -perchlorate anions. The ability of these compounds to undergo photolysis with the aim of generating a reactive Ru–Ru=O intermediate was studied. Mass spectrometry and EPR data suggest that photolysis of **4** proceeds to generate Ru–Ru=O species **6** and NO_2^\bullet . Room temperature photolysis of **4** allows for oxygen atom transfer to PPh_3 to form OPPh_3 , which is observed by ^{31}P NMR and confirmed by mass spectral data using **4**^{*}. We therefore propose that PPh_3 is directly oxidized by reactive intermediate **6**. This work demonstrates for the first time that the generation of a reactive Ru_2 -oxo species from an oxyanion complexes can be achieved in a synthetically meaningful way. Further exploitation of these reaction conditions, along with efforts to stabilize and characterize the putative intermediate Ru–Ru=O are underway in our lab.

4.5 Acknowledgements.

We thank the U.S. Department of Energy, Chemical Sciences, Geosciences, and Biosciences Division, Office of Basic Energy Sciences, Office of Science (DE-FG02-10ER16204). A.R.C. thanks the National Science Foundation for a Graduate Research Fellowship (DGE-0718123). NMR and EPR facilities at UW-Madison are supported by the NSF (CHE-1048642 and CHE-0741901, respectively), and mass spectrometry instruments are funded by NIH (1S10 OD020022-1 and NCRR 1S10RR024601-01). We thank Dr. Ilia Guzei for crystallographic insights and Dr. Linghong Zhang for assistance with GC-MS measurements.

4.6 Supplementary Information.

Materials and Methods. All syntheses were conducted under a dry N₂ atmosphere using Schlenk line techniques unless otherwise noted; product workup and isolation were achieved in air. Dichloromethane was dried with CaH₂ and distilled before use. Hexanes were obtained from a Vacuum Atmospheres Solvent System and degassed prior to use. All materials were commercially available and used as received, unless otherwise noted. Compounds **1**^{48,59} and **3**^{35,44} were prepared according to literature procedures. Photolysis of frozen samples of **4** were performed in a Rayonet RPR-200 photochemical reactor with light from 254 and 350 nm mercury vapor lamps.

[Ru₂(DPhF)₄][NO₃] (2). Ru₂(DPhF)₄Cl (200 mg, 0.196 mmol, 1 eq.) was dissolved in CH₂Cl₂ and added to a suspension of AgNO₃ (500 mg, 2.94 mmol, 15 eq.) in 3 mL of THF in air. The color of the mixture changed from green to purple-blue almost instantaneously and was allowed to continue stirring at RT overnight. The solids were filtered off and the remaining solution was left to evaporate slowly to yield dark-purple crystals of the product. Yield: 180 mg, 87.7%. MW: 1045.10 g mol⁻¹. MALDI-TOF (m/z): ([M – NO₃]⁺) 984. IR (ATR): 3053, 1773 [ν_{sym} NO₃], 1591, 1520, 1486, 1449, 1364, 1349, 1314, 1214, 1175, 1156, 1078, 1027, 936, 827, 761, 693, 668, 658, 619. UV-Vis (CH₂Cl₂): λ_{max}(ε) = 437 (4250), 527 (5950), 681 (7170 mol⁻¹ L cm⁻¹). [C₅₂H₄₄N₉O₃Ru₂·CH₂Cl₂·2H₂O]: calcd. C 54.59, H 4.32, N 10.81; found C 54.31, H 3.88, N 11.37. Crystals suitable for X-ray diffraction were grown via slow evaporation from a concentrated solution of CH₂Cl₂ at RT.

Ru₂(chp)₄ONO₂ (**4**). Ru₂(chp)₄Cl (200.0 mg, 0.266 mmol, 1 eq.) and AgNO₃ (54.6 mg, 0.321 mmol, 1.2 eq.) were dissolved in 30 mL of freshly distilled CH₂Cl₂ and allowed to stir for 96 h at RT under inert N₂. A white precipitate (AgCl) formed. The reaction mixture was filtered through a fine sintered glass frit. Excess CH₂Cl₂ was washed through the frit until it was no longer colored. The filtrate was removed under reduced pressure, and the resulting purple solid was washed with hexanes and collected. Yield: 195.5 mg, 94.4%. MW: 778.29 g mol⁻¹. MALDI-TOF (m/z): ([M – NO₂]⁺) 733, ([M – ONO₂]⁺) 717. IR (ATR): 3108, 2964, 1596, 1534, 1465, 1434, 1390, 1350, 1278 [ν_{asym} (ONO)], 1262, 1181, 1085, 1011, 964, 942, 931, 866, 795, 789, 724, 630 cm⁻¹. UV-Vis (CH₂Cl₂): λ_{max} (ϵ) = 532 (3890), 678 (1520 mol⁻¹ L cm⁻¹). [C₂₀H₁₂Cl₄N₅O₇Ru₂]: calcd. C 30.86, H 1.55, N 8.99; found C 30.64, H 1.44, N 8.81. Crystals suitable for X-ray diffraction were grown from the saturated solution of CH₂Cl₂ at -80 °C.

Ru₂(chp)₄OCIO₃ (**5**). Ru₂(chp)₄Cl (200.0 mg, 0.266 mmol, 1 eq.) and AgClO₄ (66.7 mg, 0.322 mmol, 1.2 eq.) were dissolved in 30 mL of freshly distilled CH₂Cl₂ and allowed to stir for 96 h at RT under inert N₂. A white precipitate (AgCl) formed. The reaction mixture was filtered through a fine sintered glass frit. Excess CH₂Cl₂ was washed through the frit until it was no longer colored. The filtrate was removed under reduced pressure, and the resulting purple solid was washed with hexanes and collected. Yield: 205.3 mg, 94.6%. MW: 815.74 g mol⁻¹. MALDI-TOF (m/z): ([M – ClO₃]⁺) 733, ([M – OCIO₃]⁺) 717. IR (ATR): 3107, 1596, 1536, 1433, 1391, 1337, 1263, 1154 [ν_3], 1134 [ν_3], 1075, 1025 [ν_3], 1013, 932, 894 [ν_4], 790, 723, 705, 668, 632, 610 cm⁻¹. UV-Vis (CH₂Cl₂): λ_{max} (ϵ) = 529 (2150), 666 (1310 mol⁻¹ L cm⁻¹). [C₂₀H₁₂Cl₅N₄O₈Ru₂]: calcd. C 29.45, H 1.48, N 6.87; found C 29.20, H 1.68, N 6.26. Crystals suitable for X-ray diffraction were grown from a saturated solution of CH₂Cl₂ layered with hexanes at RT.

$AgN^{18}O_3$. 0.1 g $HN^{18}O_3$, 0.1 g $H_2^{18}O$, and Ag powder and a stir bar were added to a vial that was subsequently capped. This heterogeneous mixture was stirred at 50 °C in air for 48 hrs; periodically the mixture was manually rotated and the solvent mixture forced to the bottom of the vial as it had crept up the walls of the vial. A white solid became visible along with the excess Ag powder when the solvent was on the walls of the vial. The solvent was then decanted away from the heterogeneous mixture (with a pipette) into a new vial and allowed to evaporate, leaving a crystalline product, which was heated under vacuum at 50 °C overnight. Yield: 126.8 mg (76.5%). IR (ATR): 1676, 1657 [$\nu_{\text{asym}}(^{18}ON^{18}O)$], 1293 [$\nu_{\text{sym}}(^{18}ON^{18}O)$], 792 [$\nu(N^{18}O)$], 694 cm^{-1} .

$Ru_2(chp)_4^{18}ON^{18}O_2$ (**4***). $AgN^{18}O_3$ was ground into fine powder and then used in an identical procedure as **4**. Yield: 141.2 mg, 67.7%. MW: 784.29 g mol^{-1} . MALDI-TOF (m/z): ($[M - N^{18}O_2]^+$) 735. IR (ATR): 3108, 2964, 1596, 1534, 1465, 1434, 1390, 1350, 1253 [$\nu_{\text{asym}}(^{18}ON^{18}O)$], 1262, 1181, 1085, 1011, 942, 931, 866, 795, 789, 724, 630 cm^{-1} .

Physical Measurements. Matrix-assisted laser desorption/ionization (MALDI) time-of-flight (TOF) mass spectrometry data were obtained using an anthracene matrix on a Bruker ULTRAFLEX® III mass spectrometer equipped with a SmartBeam® laser in positive ion detection mode. ESI mass spectrometry data was collected on a Thermo Q Exactive Plus™ mass spectrometer and GC-MS data were collected on a Shimadzu GCMS-QP2010 Ultra. UV-Vis spectra were obtained using a StellarNet Miniature BLUE-wave UV-Vis dip probe with a Tungsten-Krypton light source and a 10 mm path length tip. IR spectra were taken on a Bruker Tensor 27 spectrometer using an ATR adapter (no matrix). Cyclic voltammograms were taken on

a BASi Potentiostat using Epsilon software in CH_2Cl_2 solutions with 0.1 M electrolyte and 1.0 mM substrate. The electrodes were as follows: glassy carbon (working), Pt wire (auxiliary) and Ag/Ag^+ in CH_3CN (reference). The potentials were referenced versus the ferrocene/ferrocenium redox couple by externally added ferrocene. Elemental analysis was performed by Midwest Microlab, LLC in Indianapolis, IN, USA.

EPR Spectroscopy. EPR data were acquired on a Bruker ELEXSYS E500 EPR spectrometer equipped with a Varian E102 microwave bridge interfaced with a Linux system. An Oxford Instruments ESR-900 continuous-flow helium flow cryostat and an Oxford Instruments 3120 temperature controller were used to control the sample temperature. A Hewlett-Packard 432A power meter was used for microwave power calibration, with measurement conditions as follows: for **2** – 9.3762 GHz, 4 G modulation amplitude, 2500 G center field, 5000 G sweep width, 5.024 mW power, 55 dB gain, 327.68 ms time constant, 10 ms conversion time, and 15 K; for **4** – 9.3765 GHz, 4 G modulation amplitude, 2500 G center field, 5000 G sweep width, 5.024 mW power, 60 dB gain, 655.36 ms time constant, 10 ms conversion time, and 10 K; for **4**- $\text{hv}/\text{NO}_2^{\bullet}$ – 9.3765 GHz, 4 G modulation amplitude, 2500 G center field, 5000 G sweep width, 5.024 mW power, 60 dB gain, 655.36 ms time constant, 10 ms conversion time, and 10 K; for **5** – 9.3832 GHz, 4 G modulation amplitude, 2500 G center field, 5000 G sweep width, 5.024 mW power, 55 dB gain, 655.36 ms time constant, 10 ms conversion time, and 10 K. Spectral simulations were performed using EasySpin.⁶⁰

X-ray Crystallographic Data Collection and Structure Determination. Crystallographic data were measured at the Molecular Structure Laboratory of the Chemistry Department of the

University of Wisconsin–Madison. Suitable crystals of **4** and **5** were selected under oil and ambient conditions. For **4**, a purple block shaped crystal with dimensions 0.728 x 0.374 x 0.216 mm³ was selected, and for **5** a purple plate crystal with dimensions 0.166 x 0.155 x 0.094 mm³ was chosen. The crystals were attached to the tip of a MiTeGen MicroMount©, mounted in a stream of cold nitrogen at 100(1) K, and centered in the X-ray beam using a video monitoring system. The crystal evaluation and data collection were performed on a Bruker Quazar SMART APEX-II diffractometer with Mo-K α ($\lambda = 0.71073$ Å) radiation. The data were collected using a routine to survey the reciprocal space to the extent of a full sphere to a resolution of 0.70 Å for **4** and 0.80 Å for **5** and were indexed by the APEX program.⁶¹ The structures were solved via direct methods and refined by iterative cycles of least-squares refinement on F² followed by difference Fourier synthesis. All hydrogen atoms were included in the final structure factor calculation at idealized positions and were allowed to ride on the neighboring atoms with relative isotropic displacement coefficients. Absorption corrections were based on a fitted function to the empirical transmission surface as sampled by multiple equivalent measurements.^{62,63} The systematic absences in the diffraction data were uniquely consistent with the space groups $P2_1/c$ for **4** and $P2_1/n$ for **5**, yielding chemically reasonable and computationally stable results of refinement, and both structures were solved using direct methods using XS software.⁶⁴ Compound **4** is a pseudo-merohedral twin with a twin component ratio of 54:46. The twin components are related by a 180° rotation about [1 0 0]. Compound **5** is a non-merohedral twin with a twin component ratio of 60:40. The twin components are related by 180° a rotation about [0 0 1].

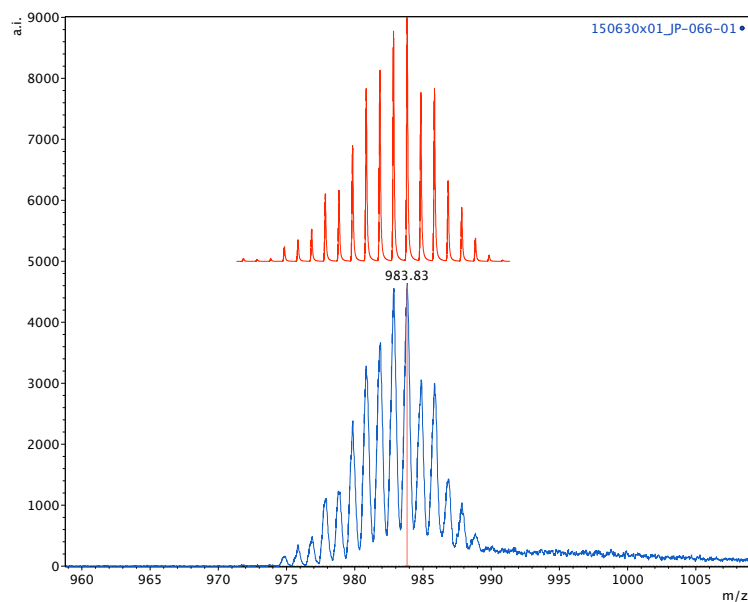


Figure S4.1 MALDI-TOF mass spectrum for **2** (below). Simulation (top) indicates major isotope pattern at $m/z = 984$ is consistent with $[\text{Ru}_2(\text{DPhF})_4]^+$ unit without an axial ligand.

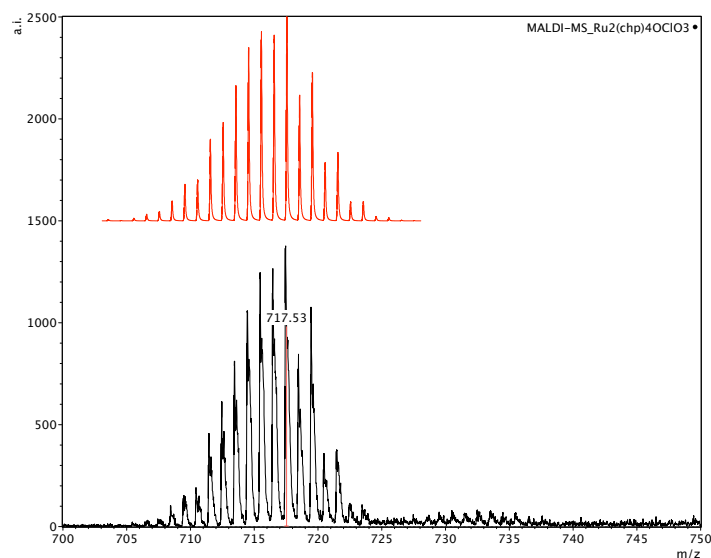


Figure S4.2 MALDI-TOF mass spectrum for **5** (below). Simulation (top) indicates major isotope pattern at $m/z = 717$ is consistent with $[\text{Ru}_2(\text{chp})_4]^+$. The signal for $[\text{Ru}_2(\text{chp})_4\text{O}]^+$ (at $m/z = 733$) is barely discernable.

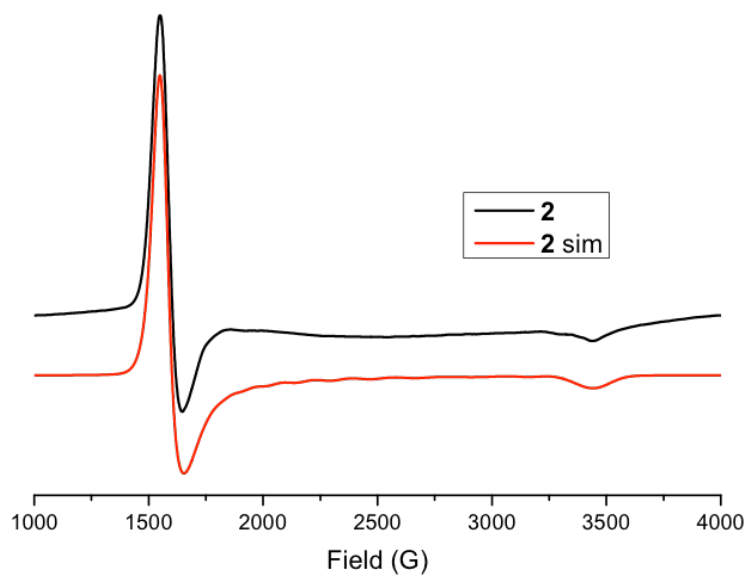


Figure S4.3 EPR spectrum and simulation for $[\text{Ru}_2(\text{DPhF})_4][\text{NO}_3]$ (**2**) at 15 K.

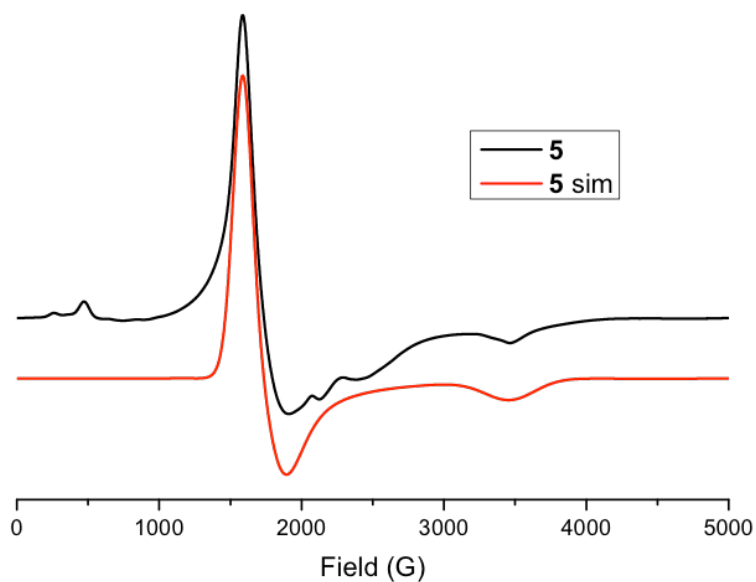


Figure S4.4 EPR spectrum and simulation for $\text{Ru}_2(\text{chp})_4\text{OClO}_3$ (**5**) at 10 K. The features at ~ 500 G and $\sim 2020 - 2500$ G, presumably due to oligomerization or aggregated species, are not included in the simulation.

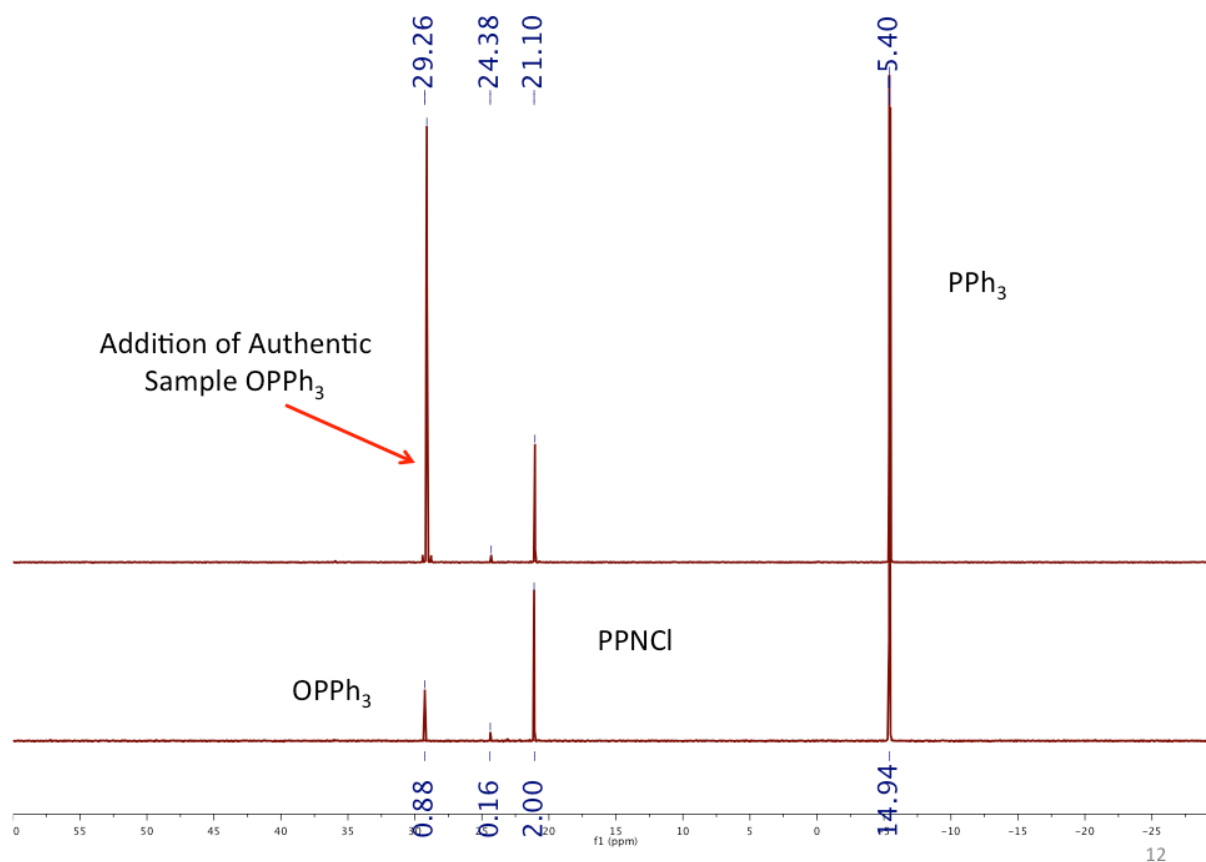


Figure S4.5 (bottom) $^{31}\text{P}\{^1\text{H}\}$ NMR for formation of OPPh_3 after photolysis of **4**, excess PPh_3 , and PPNCl (internal standard) in a dichloromethane solution for 4 hrs at room temperature under N_2 using 350 nm light. Upon doping with authentic sample of OPPh_3 (top), the intensity of this feature at $\delta = 29$ increases.

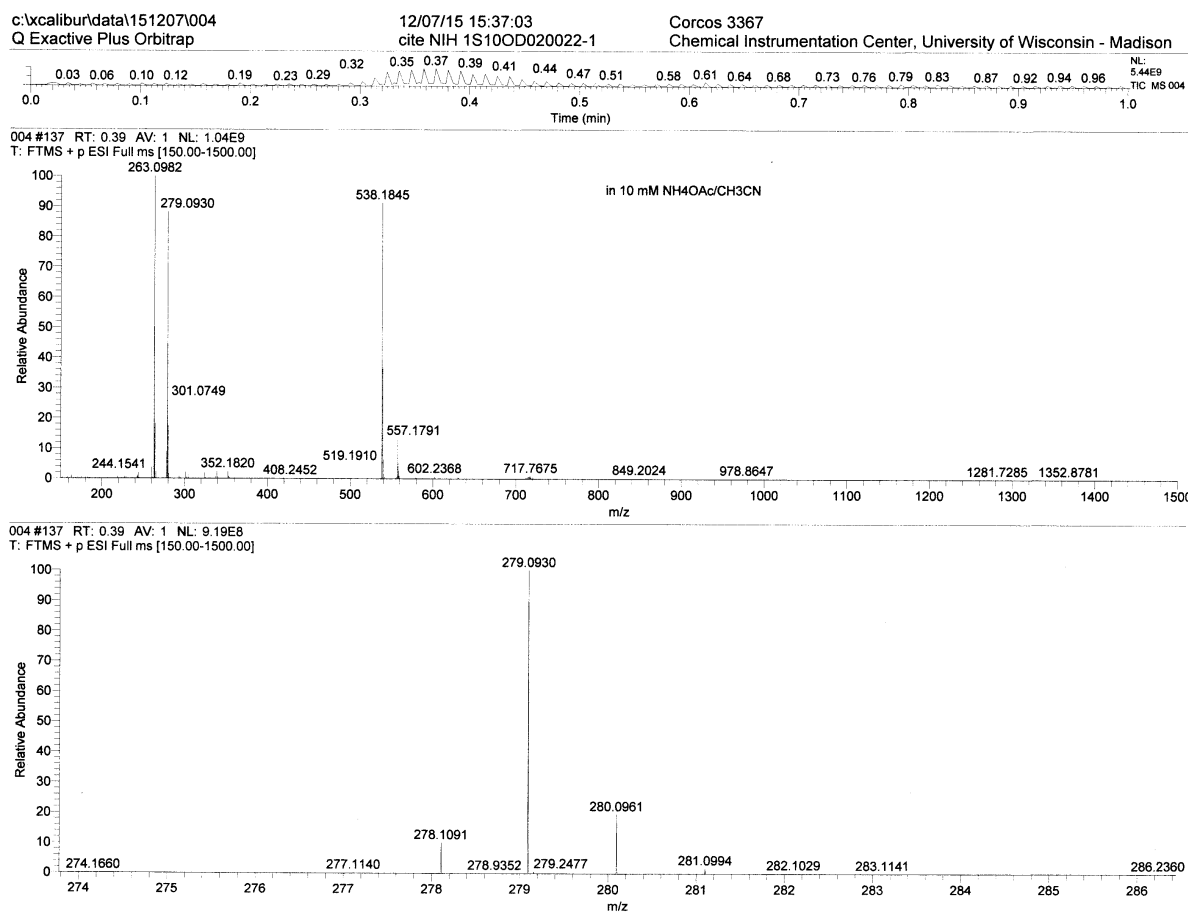


Figure S4.6 ESI mass spectrum for reaction mixture of **4**, PPh₃, and PPnCl post room temperature photolysis, showing formation of OPPh₃ ($m/z = 279$).

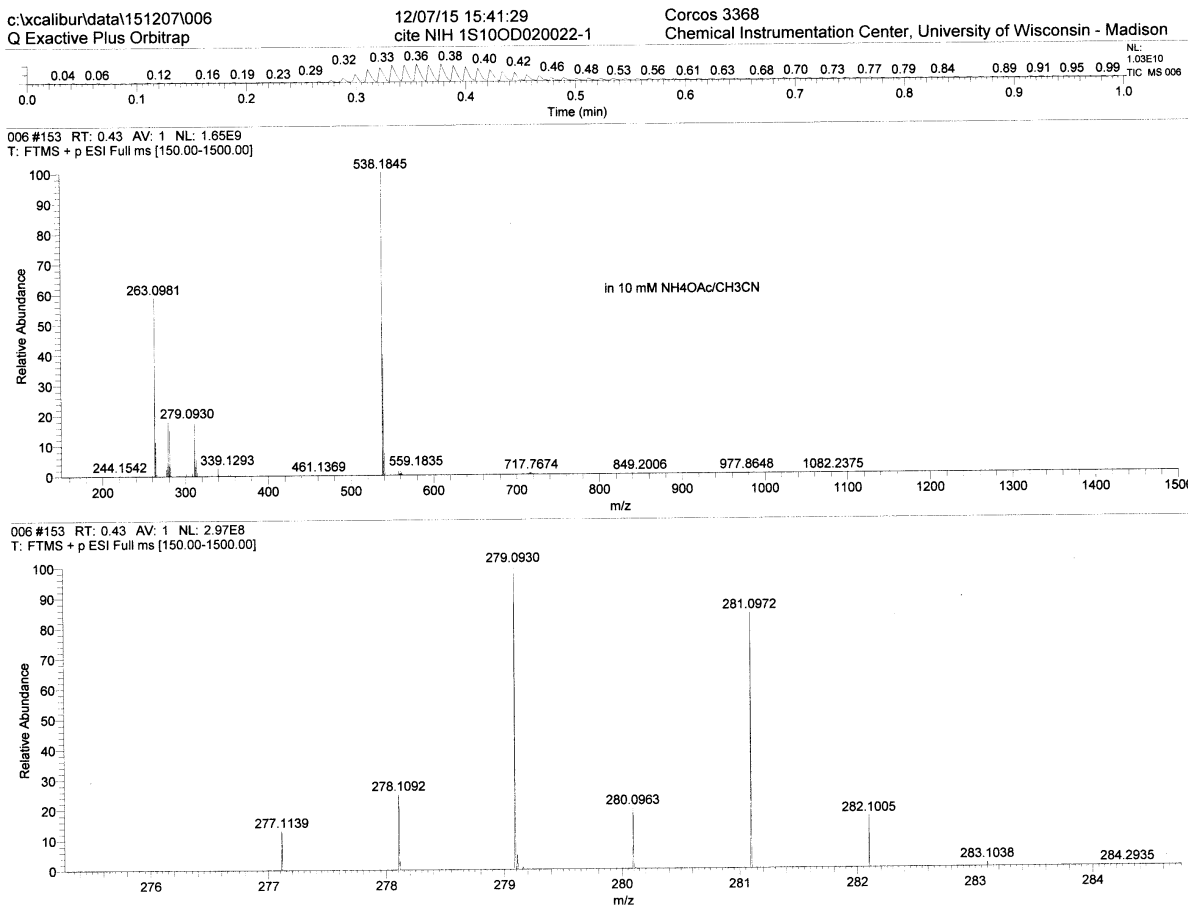


Figure S4.7 ESI mass spectrum for reaction mixture of **4***, PPh₃, and PPnCl post room temperature photolysis, showing formation of ¹⁸OPPh₃ (*m/z* = 281).

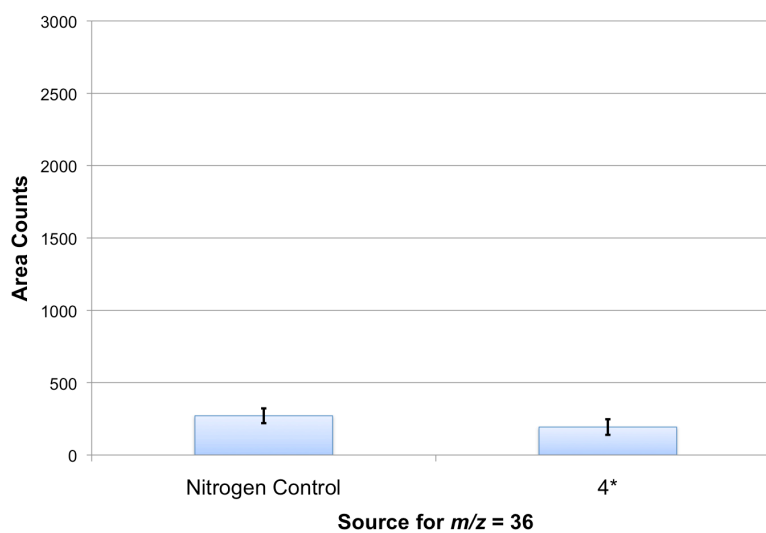


Figure S4.8 GC-MS headspace analysis for formation of $^{18}\text{O}_2$ ($m/z = 36$) after photolysis of **4*** at room temperature under N_2 for 4 h using 350 nm wavelength. As compared to the counts for $m/z = 36$ for the N_2 control, formation of $^{18}\text{O}_2$ is not statistically significant.

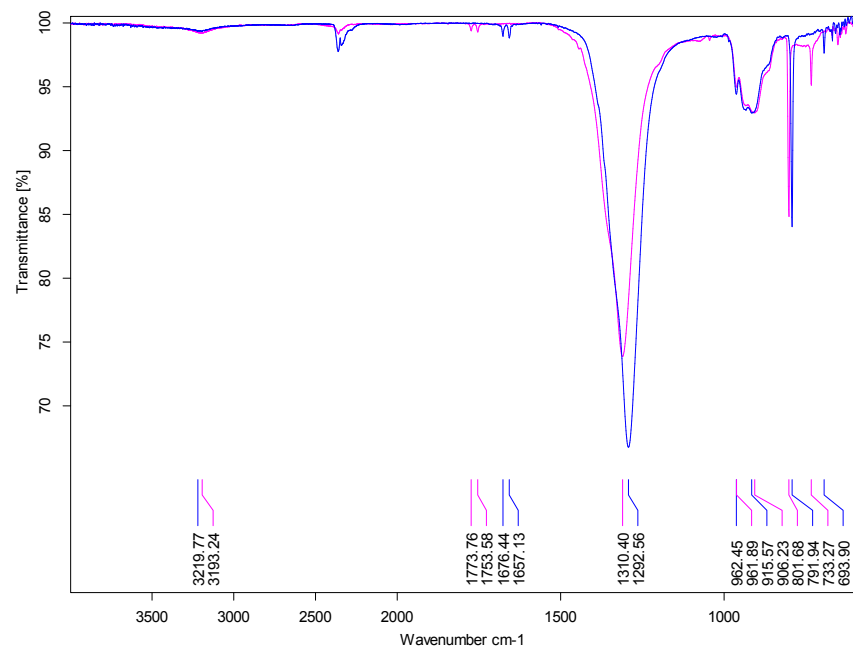


Figure S4.9 IR data for AgNO₃ (pink) compared to AgN¹⁸O₃ (blue), indicative of an isotopic shift upon using ¹⁸O.

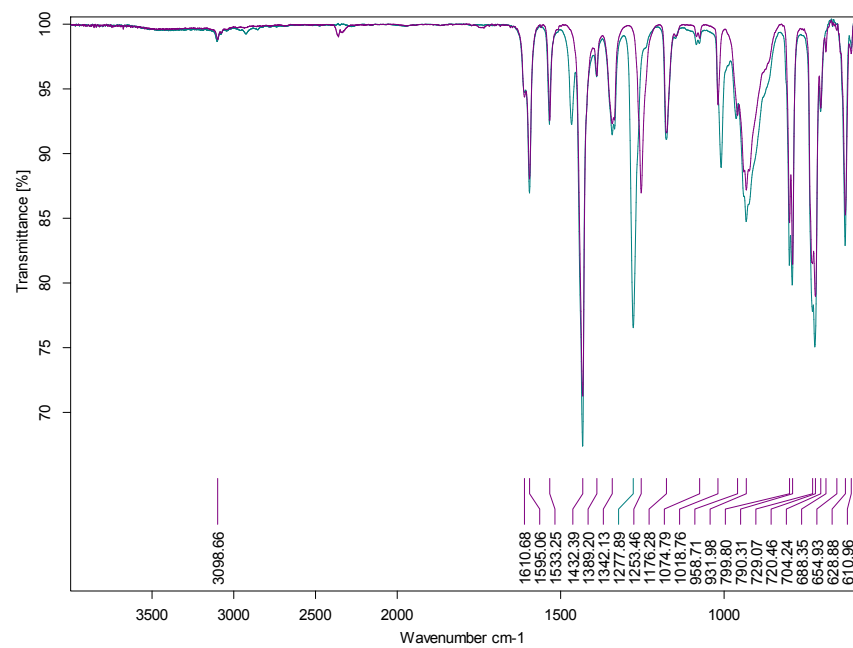


Figure S4.10 IR data of **4** (purple) and **4*** (green), showing that the -ONO_2 bound to the Ru_2^{5+} core in **4** is isotopically shifted in **4***, from 1278 cm^{-1} to 1253 cm^{-1} .

Table S4.1 Crystal Data for **4·2CH₂Cl₂** and **5·2CH₂Cl₂**.

Identification code	4·2CH₂Cl₂	5·2CH₂Cl₂
Empirical formula	Ru ₂ C ₂₂ H ₁₆ Cl ₈ N ₅ O ₇	Ru ₂ C ₂₂ H ₁₆ Cl ₉ N ₄ O ₈
Formula weight	948.14	985.58
Temperature	100(1) K	100(1) K
Wavelength	0.71073 Å	0.71073 Å
Crystal system	Monoclinic	Monoclinic
Space group	<i>P</i> 2 ₁ / <i>c</i>	<i>P</i> 2 ₁ / <i>n</i>
Unit cell dimensions	a = 17.2028(13) Å b = 15.4349(11) Å c = 11.5463(8) Å α = 90° β = 90.050(3)° γ = 90°	a = 11.5392(6) Å b = 16.7038(9) Å c = 16.6387(9) Å α = 90° β = 93.965(3)° γ = 90°
Volume	3065.8(4) Å ³	3199.4(3) Å ³
Z	4	4
Density (calculated)	2.054 g/cm ³	2.046 g/cm ³
Crystal size	0.728 x 0.374 x 0.216 mm ³	0.166 x 0.155 x 0.094 mm ³
Data / restraints / parameters	9327 / 21 / 409	6580 / 132 / 468
Goodness-of-fit on <i>F</i> ²	1.075	1.058
Final <i>R</i> ^{a,b} indices [<i>I</i> > 2σ(<i>I</i>)]	<i>R</i> ₁ = 0.0258, <i>wR</i> ₂ = 0.0667	<i>R</i> ₁ = 0.0473, <i>wR</i> ₂ = 0.1021
<i>R</i> indices (all data)	<i>R</i> ₁ = 0.0271, <i>wR</i> ₂ = 0.0683	<i>R</i> ₁ = 0.0617, <i>wR</i> ₂ = 0.1122

^a*R*₁ = Σ||*F*₀| - |*F*_c||/Σ|*F*₀|; ^b*wR*₂ = [Σ[w(*F*₀² - *F*_c²)²] / Σ[w(*F*₀²)²]]^{1/2}, w = 1/σ² (*F*₀²) + (aP)² + bP, where P = [max(0 or *F*₀²) + 2(*F*_c²)]/3.

References.

- (1) Nugent, W. A.; Mayer, J. M. *Metal-Ligand Multiple Bonds*; John Wiley & Sons: New York, 1988.
- (2) Yin, G. *Coord. Chem. Rev.* **2010**, *254*, 1826.
- (3) Winkler, J. R.; Gray, H. B. In *Molecular Electronic Structures of Transition Metal Complexes I*; Mingos, D. M. P., Day, P., Dahl, J. P., Eds.; Springer Berlin Heidelberg: 2012; Vol. 142, p 17.
- (4) Ray, K.; Heims, F.; Pfaff, F. F. *Eur. J. Inorg. Chem.* **2013**, *2013*, 3784.
- (5) Chen, Z.; Yin, G. *Chem. Soc. Rev.* **2015**, *44*, 1083.
- (6) Ray, K.; Heims, F.; Schwalbe, M.; Nam, W. *Curr. Opin. Chem. Biol.* **2015**, *25*, 159.
- (7) Yamaguchi, K.; Takahara, Y.; Fueno, T. In *Applied Quantum Chemistry*; Smith, V., Jr., Schaefer, H., III, Morokuma, K., Eds.; Springer Netherlands: 1986, p 155.
- (8) Decker, A.; Rohde, J.-U.; Que, L.; Solomon, E. I. *J. Am. Chem. Soc.* **2004**, *126*, 5378.
- (9) Decker, A.; Solomon, E. I. *Curr. Opin. Chem. Biol.* **2005**, *9*, 152.
- (10) Song, W. J.; Seo, M. S.; DeBeer George, S.; Ohta, T.; Song, R.; Kang, M.-J.; Tosha, T.; Kitagawa, T.; Solomon, E. I.; Nam, W. *J. Am. Chem. Soc.* **2007**, *129*, 1268.
- (11) Nippe, M.; Goodman, S. M.; Fry, C. G.; Berry, J. F. *J. Am. Chem. Soc.* **2011**, *133*, 2856.
- (12) Brogden, D. W.; Turov, Y.; Nippe, M.; Li Manni, G.; Hillard, E. A.; Clérac, R.; Gagliardi, L.; Berry, J. F. *Inorg. Chem.* **2014**, *53*, 4777.
- (13) Brogden, D. W.; Berry, J. F. *Chem. Commun.* **2015**, *51*, 9153.
- (14) Villalobos, L.; Barker Paredes, J. E.; Cao, Z.; Ren, T. *Inorg. Chem.* **2013**, *52*, 12545.
- (15) Goberna-Ferrón, S.; Peña, B.; Soriano-López, J.; Carbó, J. J.; Zhao, H.; Poblet, J. M.; Dunbar, K. R.; Galán-Mascarós, J. R. *J. Catal.* **2014**, *315*, 25.
- (16) Moyer, B. A.; Meyer, T. J. *J. Am. Chem. Soc.* **1978**, *100*, 3601.
- (17) Moyer, B. A.; Meyer, T. J. *Inorg. Chem.* **1981**, *20*, 436.
- (18) Huynh, M. H. V.; Meyer, T. J. *Chem. Rev.* **2007**, *107*, 5004.
- (19) Warren, J. J.; Tronic, T. A.; Mayer, J. M. *Chem. Rev.* **2010**, *110*, 6961.

- (20) Gagliardi, C. J.; Westlake, B. C.; Kent, C. A.; Paul, J. J.; Papanikolas, J. M.; Meyer, T. J. *Coord. Chem. Rev.* **2010**, *254*, 2459.
- (21) Che, C. M.; Tang, W. T.; Wong, W. T.; Lai, T. F. *J. Am. Chem. Soc.* **1989**, *111*, 9048.
- (22) Che, C.-M.; Tang, W.-T.; Lee, W.-O.; Wong, W.-T.; Lai, T.-F. *J. Chem. Soc., Dalton Trans.* **1989**, 2011.
- (23) Che, C. M.; Lai, T. F.; Wong, K. Y. *Inorg. Chem.* **1987**, *26*, 2289.
- (24) de Souza, V. R.; Nunes, G. S.; Rocha, R. C.; Toma, H. E. *Inorg. Chim. Acta* **2003**, *348*, 50.
- (25) Nagao, H.; Nishimura, H.; Kitanaka, Y.; Howell, F. S.; Mukaida, M.; Kakihana, H. *Inorg. Chem.* **1990**, *29*, 1693.
- (26) Power, J. M.; Evertz, K.; Henling, L.; Marsh, R.; Schaefer, W. P.; Labinger, J. A.; Bercaw, J. E. *Inorg. Chem.* **1990**, *29*, 5058.
- (27) Che, C.-M.; Wong, K.-Y.; Mak, T. C. W. *J. Chem. Soc., Chem. Commun.* **1985**, 546.
- (28) Che, C.-M.; Wong, K.-Y.; Mak, T. C. W. *J. Chem. Soc., Chem. Commun.* **1985**, 988.
- (29) Dengel, A. C.; Griffith, W. P.; O'Mahoney, C. A.; Williams, D. J. *J. Chem. Soc., Chem. Commun.* **1989**, 1720.
- (30) Man, W.-L.; Lam, W. W. Y.; Wong, W.-Y.; Lau, T.-C. *J. Am. Chem. Soc.* **2006**, *128*, 14669.
- (31) Wong, K.-Y.; Che, C.-M.; Yip, W.-H.; Wang, R.-J.; Mak, T. C. W. *J. Chem. Soc., Dalton Trans.* **1992**, 1417.
- (32) Pap, J. S.; DeBeer George, S.; Berry, J. F. *Angew. Chem. Int. Ed.* **2008**, *47*, 10102.
- (33) Long, A. K. M.; Yu, R. P.; Timmer, G. H.; Berry, J. F. *J. Am. Chem. Soc.* **2010**, *132*, 12228.
- (34) Long, A. K. M.; Timmer, G. H.; Pap, J. S.; Snyder, J. L.; Yu, R. P.; Berry, J. F. *J. Am. Chem. Soc.* **2011**, *133*, 13138.
- (35) Corcos, A. R.; Long, A. K. M.; Guzei, I. A.; Berry, J. F. *Eur. J. Inorg. Chem.* **2013**, *2013*, 3808.
- (36) Harischandra, D. N.; Zhang, R.; Newcomb, M. *J. Am. Chem. Soc.* **2005**, *127*, 13776.
- (37) Zhang, R.; Newcomb, M. *Acc. Chem. Res.* **2008**, *41*, 468.

- (38) Zhang, R.; Vanover, E.; Luo, W.; Newcomb, M. *Dalton Trans.* **2014**, 43, 8749.
- (39) Xu, G.-L.; Jablonski, C. G.; Ren, T. *Inorg. Chim. Acta* **2003**, 343, 387.
- (40) Dunlop, K.; Wang, R.; Stanley Cameron, T.; Aquino, M. A. S. *J. Mol. Struct.* **2014**, 1058, 122.
- (41) Lever, A. B. P.; Mantovani, E.; Ramaswamy, B. S. *Can. J. Chem.* **1971**, 49, 1957.
- (42) Nakamoto, K. *Infrared and Raman Spectra of Inorganic and Coordination Compounds. Part B: Applications in Coordination, Organometallic, and Bioinorganic Chemistry*; 5th ed.; John Wiley & Sons: New York, 1997.
- (43) Crystallographic data for [Ru₂(DPhF)₄](NO₃): space group = *C2/c*; unit cell dimensions *a* = 14.028 Å; *b* = 13.571 Å; *c* = 23.189 Å; β = 91.33°; Vol = 4413.60 Å³.
- (44) Chakravarty, A. R.; Cotton, F. A.; Tocher, D. A. *Inorg. Chem.* **1985**, 24, 1263.
- (45) Bond distances and angles for minor component (8.82%) of another Ru(1) atom not reported here.
- (46) Based on a search of the Cambridge Structural Database.
- (47) Cherin, P.; Hamilton, W. C.; Post, B. *Acta Cryst.* **1967**, 23, 455.
- (48) Bear, J. L.; Han, B.; Huang, S.; Kadish, K. M. *Inorg. Chem.* **1996**, 35, 3012.
- (49) Connelly, N. G.; Geiger, W. E. *Chemical Reviews* **1996**, 96, 877.
- (50) Chakravarty, A. R.; Cotton, F. A.; Tocher, D. A.; Tocher, J. H. *Polyhedron* **1985**, 4, 1475.
- (51) Berry, J. F.; Bill, E.; Bothe, E.; George, S. D.; Mienert, B.; Neese, F.; Wieghardt, K. *Science* **2006**, 312, 1937.
- (52) Chen, T.-H.; Asiri, N.; Kwong, K. W.; Malone, J.; Zhang, R. *Chem. Commun.* **2015**, 51, 9949.
- (53) Rotlevi, E.; Treinin, A. *J. Phys. Chem.* **1965**, 69, 2645.
- (54) Svoboda, O.; Kubelová, L.; Slaviček, P. *J. Phys. Chem. A* **2013**, 117, 12868.
- (55) The corresponding Ru–Ru≡N complex has been shown unambiguously to have an *S* = 1/2 ground state with an unpaired electron in the Ru–Ru δ^* orbital,³²⁻³⁴ the addition of one more electron upon changing N to O can therefore either fill the δ^* level yielding a

diamagnetic ground state, or (upon orbital rearrangement) the π^* orbitals may contain two unpaired electrons, yielding a paramagnetic $S = 1$ ground state.

- (56) Atkins, P. W.; Symons, M. C. R. *J. Chem. Soc.* **1962**, 4794.
- (57) Livingston, R.; Zeldes, H. *J. Chem. Phys.* **1964**, *41*, 4011.
- (58) Wertz, J. E.; Bolton, J. R. In *Electron Spin Resonance: Elementary Theory and Practical Applications*; Chapman and Hall: New York, 1986, p 164.
- (59) Lin, C.; Ren, T.; Valente, E. J.; Zubkowski, J. D.; Smith, E. T. *Chem. Lett.* **1997**, *26*, 753.
- (60) Stoll, S.; Schweiger, A. *J. Magn. Reson.* **2006**, *178*, 42.
- (61) APEX2. 2014.11-0.
- (62) SADABS. 2014/5.
- (63) TWINABS. 2012/1.
- (64) XS. 2013/1.

Chapter 5

Preliminary Studies of an $[Ru_2O]^+$ Intermediate

5.1 Abstract.

O-atom transfer was utilized in an attempt to generate an Ru_2O species in the +7 oxidation state. O-atom transfer with either *m*CPBA or PhIO was attempted. UV-Vis data show isosbestic points for conversion of $Ru_2(ap)_4BF_3$ (**3**, *ap* = 2-anilinopyridine) upon *m*CPBA addition to the proposed $[Ru_2(ap)_4O][BF_4]$ (**[4][BF₄]**), indicating conversion to a single new species. EPR data indicate a change in spin state, from an $S = 3/2$ complex to $S = 1/2$, upon addition of the O-atom transfer reagent. The EPR data for oxidation with *m*CPBA show two new $S = 1/2$ signals, while oxidation with PhIO gives one new $S = 1/2$ signal. Initial substrate reactivity indicates that proposed intermediate **[4][BF₄]** reacts with PPh_3 to form $OPPh_3$.

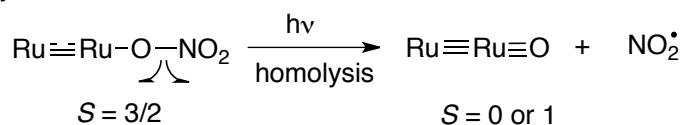
5.2 Introduction.

In our previous studies of Ru_2 intermediates, we relied on photolytic methods to generate nitrides from azides,¹⁻⁴ and we also exposed an Ru_2 oxyanion to photolytic conditions to generate an Ru_2 -oxo species.⁵ Due to the less-than-desirable conversion of the oxyanion to the oxo species, we were not able to completely characterize the putative Ru_2O intermediate. Here we present our attempts to generate an $Ru-Ru=O$ species, using the more reliable synthetic method of chemical oxidation using O-atom transfer to the metal center with *m*CPBA or PhIO. These methods have proved useful for generating monometallic $Ru=O$ species,⁶⁻¹⁵ and we have utilized

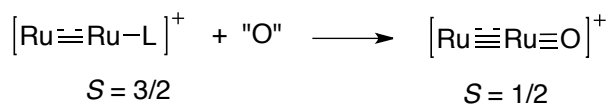
them in our lab to synthesize the first examples of metal-metal bonded compounds with a terminal oxo ligand in the form of M–M=O species with M = Mo or W.^{16,17}

There are many advantages to chemical oxidation methodologies using O-atom transfer agents compared to photolytic methodologies with oxyanions. With chemical oxidation, we can monitor reaction progress with UV-Vis spectroscopy and easily determine the temperature range for which the intermediate is stable. Additionally the reaction is quick: it is not necessary to irradiate a sample for 16 h and continually add liquid nitrogen to keep the reactive intermediate stable. For our oxyanion studies, the associated Ru₂O intermediate was difficult to study since the Ru₂ core underwent a one-electron oxidation from Ru₂⁵⁺ to Ru₂⁶⁺, which is EPR silent, and we could not characterize it by NMR spectroscopy since the intermediate was only stable while frozen in solution. With chemical oxidation, our starting Ru₂ core should undergo a two-electron oxidation, from Ru₂⁵⁺ to Ru₂⁷⁺, which we expect will result in an EPR active product. Thus the synthesis of the desired Ru₂O⁽⁺⁾ intermediate is easier to both generate and spectroscopically characterize if we use chemical oxidation methodologies rather than photolytic ones.

Photolytic Oxidation:



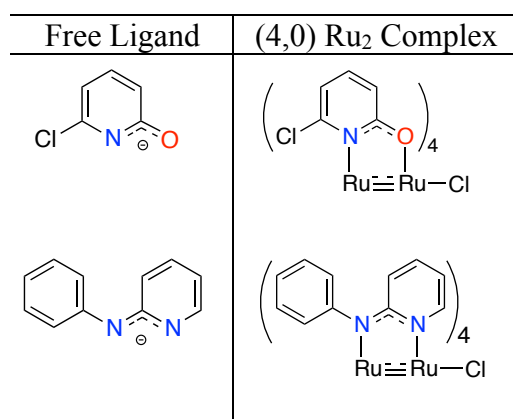
Chemical Oxidation:



Scheme 5.1 Spin states for Ru₂ core both before and after photolytic or chemical oxidation.

For these studies we also changed the equatorial supporting ligands around the Ru₂ core from chp (6-chloro-2-hydroxypyridinate) to ap (2-anilinopyridinate). Like the chp ligand used

previously,^{4,5,18} the ap ligand binds to the Ru₂ core in a (4,0) geometry,¹⁹ allowing the axial site of one Ru center to remain sterically unencumbered while the other is blocked. Additionally, the N,N donors such as ap better stabilize higher Ru₂ oxidation states than can N,O donors, like the chp ligand.²⁰ For example, when undergoing metathesis with silver salts, Ru₂(chp)₄⁺ complexes may be exposed to multiple equivalents of Ag⁺ and remain in the Ru₂⁵⁺ oxidation state, but if Ru₂(ap)₄⁺ complexes are exposed to more than one equivalent then the excess silver will oxidize the metal center to the Ru₂⁶⁺ oxidation state. Both oxidation states can be air stable for ap-supported Ru₂ complexes.

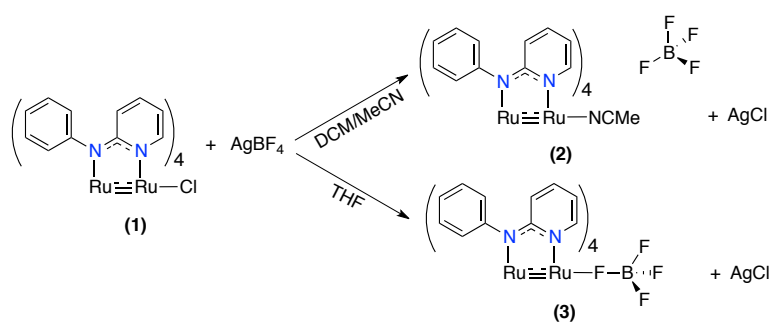


Scheme 5.2 Drawings of chp and ap ligands; both form (4,0) isomers when bound to Ru₂ core.

5.3 Results and Discussion.

Formation and Characterization of Precursors 2 and 3. As previously discussed, Ru₂(ap)₄Cl (**1**) has only one sterically-unencumbered axial site for reactivity, as the other site is blocked by multiple phenyl rings. The available site originally contains a Cl⁻ ligand that must be removed prior to oxidation attempts. **1** can therefore be exposed to one equivalent of AgBF₄ in a salt metathesis reaction and, depending on the solvents utilized for the reaction, different products are formed (Scheme 5.3). For example, when the salt metathesis is performed in a

mixture of CH_2Cl_2 and MeCN, the original dark green solution of **1** turns dark brown, resulting in the product $[\text{Ru}_2(\text{ap})_4\text{NCMe}][\text{BF}_4]$ (**2**), and in THF the dark green solution turns bright green, resulting in the formation of $\text{Ru}_2(\text{ap})_4\text{FBF}_3$ (**3**). The identities of these new compounds are confirmed by X-ray crystallography: crystals of both **2** and **3** are readily formed upon layering the filtered reaction mixtures with hexanes and subsequent slow diffusion (Figures 5.1 and 5.2). In **2** the coordinating MeCN solvent was anticipated to bind to the available axial Ru_2 site; in **3** it was surprising to see that BF_4^- binds preferentially over THF.



Scheme 5.3 Formation of **2** and **3** from **1**. The resulting product is solvent-dependent.

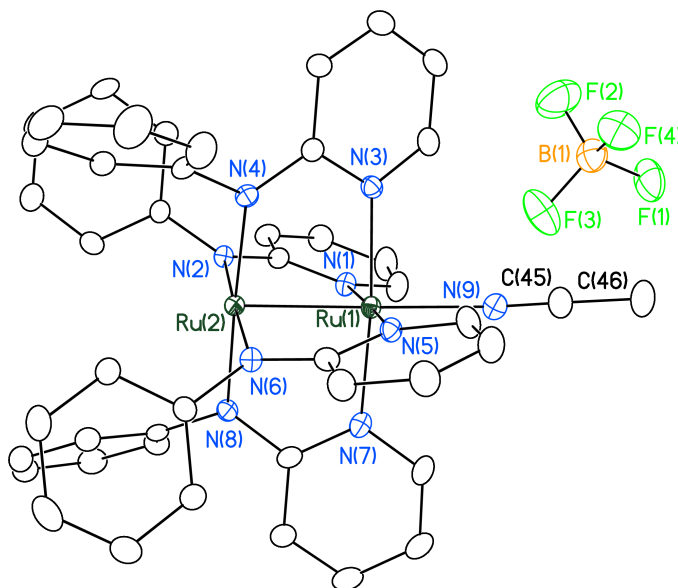


Figure 5.1 Thermal ellipsoid plot of $[\text{Ru}_2(\text{ap})_4\text{NCMe}][\text{BF}_4] \cdot 2\text{CH}_2\text{Cl}_2$ (**2**· $2\text{CH}_2\text{Cl}_2$) with ellipsoids drawn at the 50% probability level. Hydrogen atoms and molecules of solvation omitted for clarity. Selected bond distances and angles: $\text{Ru}(1)\text{--Ru}(2) = 2.3620(4) \text{ \AA}$, $\text{Ru}(1)\text{--N}(9) = 2.177(4) \text{ \AA}$, $\text{N}(9)\text{--C}(45) = 1.145(6) \text{ \AA}$, $\text{C}(45)\text{--C}(46) = 1.445(7) \text{ \AA}$, $\text{Ru}(2)\text{--Ru}(1)\text{--N}(9) = 177.7(1)^\circ$, $\text{Ru}(1)\text{--N}(9)\text{--C}(45) = 174.1(4)^\circ$, $\text{N}(9)\text{--C}(45)\text{--C}(46) = 178.9(5)^\circ$.

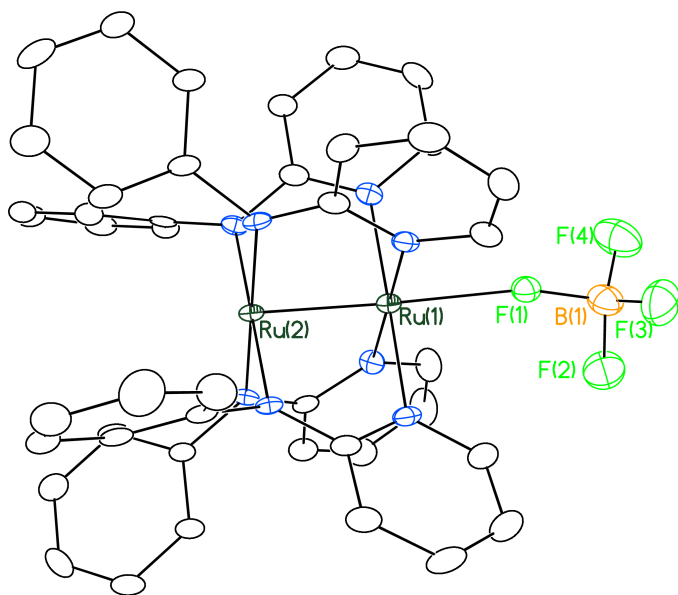


Figure 5.2 Thermal ellipsoid plot of $\text{Ru}_2(\text{ap})_4\text{FBF}_3$ (**3**) with ellipsoids drawn at the 50% probability level. Hydrogen atoms omitted for clarity. Selected bond distances and angles:

$\text{Ru(1)–Ru(2)} = 2.2579(3) \text{ \AA}$, $\text{Ru(1)–F(1)} = 2.296(2) \text{ \AA}$, $\text{F(1)–B(1)} = 1.441(4) \text{ \AA}$, $\text{F(2)–B(1)} = 1.365(4) \text{ \AA}$, $\text{F(3)–B(1)} = 1.364(4) \text{ \AA}$, $\text{F(4)–B(1)} = 1.369(4) \text{ \AA}$, $\text{Ru(2)–Ru(1)–F(1)} = 178.16(4)^\circ$, $\text{Ru(1)–F(1)–B(1)} = 164.1(2)^\circ$. F–B–F angles range from $106.1(3)^\circ$ to $112.1(3)^\circ$.

Both **2** and **3** maintain their (4,0) geometry upon conversion from **1**. The Ru(2)–Ru(1) distance in **2** at $2.3620(4) \text{ \AA}$ is rather long for an Ru_2^{5+} complex, while the Ru(2)–Ru(1) distance in **3** is rather short at $2.2579(3) \text{ \AA}$.^{21,22} Both complexes have nearly linear Ru(2)–Ru(1)-axial ligand angles at $177.7(1)^\circ$ and $178.16(4)^\circ$, respectively. Additionally, for **3**, the F(1)–B(1) distance is elongated compared to the other F(2-4)–B(1) distances due to its additional coordination to the Ru_2 center.

Compounds **2** and **3** can interconvert. Upon removal of the solvent under vacuum, a brown solution of **2** yields a bright green solid (**3**). Additionally, when a CH_2Cl_2 solution of **3** is exposed to MeCN, it turns dark brown (**2**). Compound **2** can therefore only be isolated in the solid state in crystalline form; isolation as a powder generates only **3**. Both **2** and **3** have nearly identical EPR spectroscopic fingerprints, which are shown in Figure 5.3; both **2** (left) and **3** (right) have $S = 3/2$ signals that are modeled with nearly identical axial features.

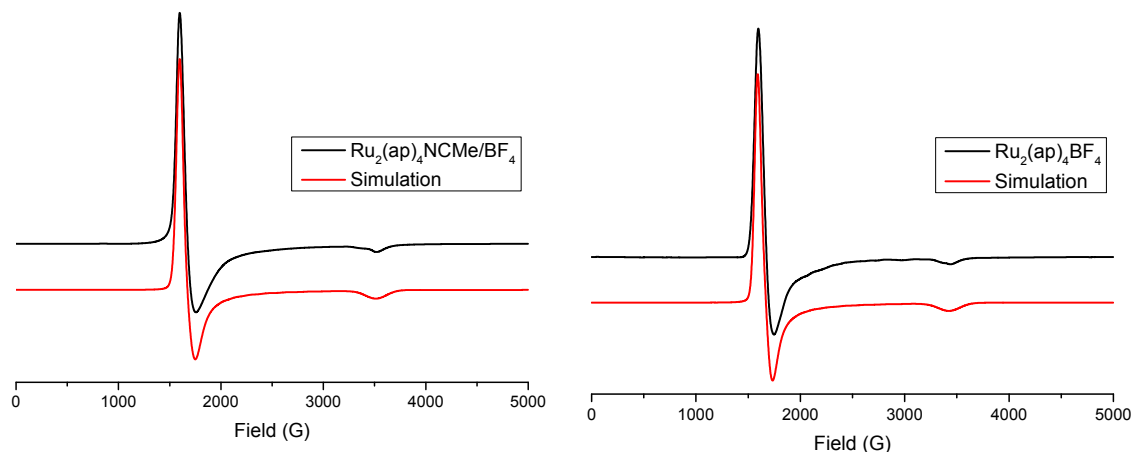
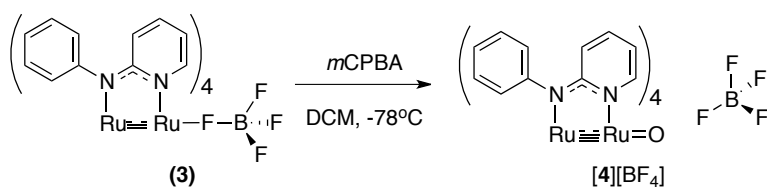


Figure 5.3 EPR data of **2** and **3** in frozen CH_2Cl_2 at 10 K. Simulation parameters for **2**: $g_{\perp} = 2.04$, $g_{\parallel} = 1.90$, $E/D = 0.017$, $\text{HStrain} = [750, 370, 625]$. Simulation parameters for **3**: $g_{\perp} = 2.05$, $g_{\parallel} = 1.95$, $E/D = 0.018$, $\text{HStrain} = [600, 350, 650]$.

Oxidation of 3 with O-atom transfer agents mCPBA and PhIO. Initial attempts at oxidation of **3** to form $[\text{Ru}_2(\text{ap})_4\text{O}][\text{BF}_4]$ (**4**) were conducted with *m*CPBA (Scheme 5.4). The oxidation reaction was conducted at $-78\text{ }^{\circ}\text{C}$ and followed by UV-Vis spectroscopy (Figure 4). Compound **3** was first dissolved in CH_2Cl_2 (green trace, Figure 5.4) and one-quarter equivalent aliquots of *m*CPBA were subsequently added. After addition of one equivalent of oxidant the solution turned dark hot pink from the initial bright green, and upon further addition of *m*CPBA the UV-Vis spectrum did not continue to change (pink trace), as indicated by the inset graph of Figure 5.4. The isosbestic behavior in the oxidation of **3** to **4** indicates this is a direct and clean conversion without any intermediate steps.



Scheme 5.4 Proposed formation of intermediate $[\text{Ru}_2(\text{ap})_4\text{O}][\text{BF}_4]$ (**[4][BF₄]**) upon oxidation of **3** with *m*CPBA.

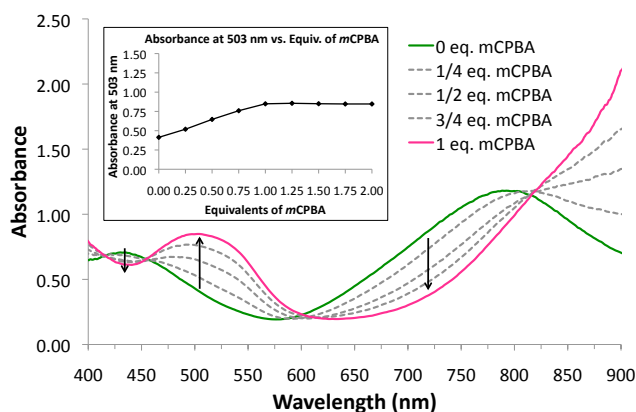


Figure 5.4 UV-Vis spectrum of **3** at -78°C (green) and after aliquot additions of *m*CPBA to form **[4][BF₄]** (pink). Inset: Graph of absorption versus aliquots of *m*CPBA. Only one equivalent of oxidant is needed.

Following UV-Vis spectroscopy, EPR spectroscopy was utilized to confirm a change in the oxidation state of the Ru_2 core upon exposure to *m*CPBA. Indeed, the starting $S = 3/2$ signal for **3** completely disappears, and a new $S = 1/2$ signal is present (Figure 5.5, left). In fact, there are at least two $S = 1/2$ features for this sample. This was surprising, as UV-Vis data initially indicated to us that this was a clean conversion, meaning there should be only one product. We therefore also attempted oxidation of **3** with PhIO (Figure 5.5, right). The reaction did not proceed at -78°C as it did for *m*CPBA, most likely due to the poor solubility of PhIO in CH_2Cl_2 . Upon warming to 0°C there was a color change from the bright green of **3** to red-brown, and

EPR spectroscopy indicates this color change is accompanied by a change in spin state, from $S = 3/2$ to $S = 1/2$, with a small amount of unreacted **3** remaining (Figure 5, right). This time one major $S = 1/2$ signal is observed.

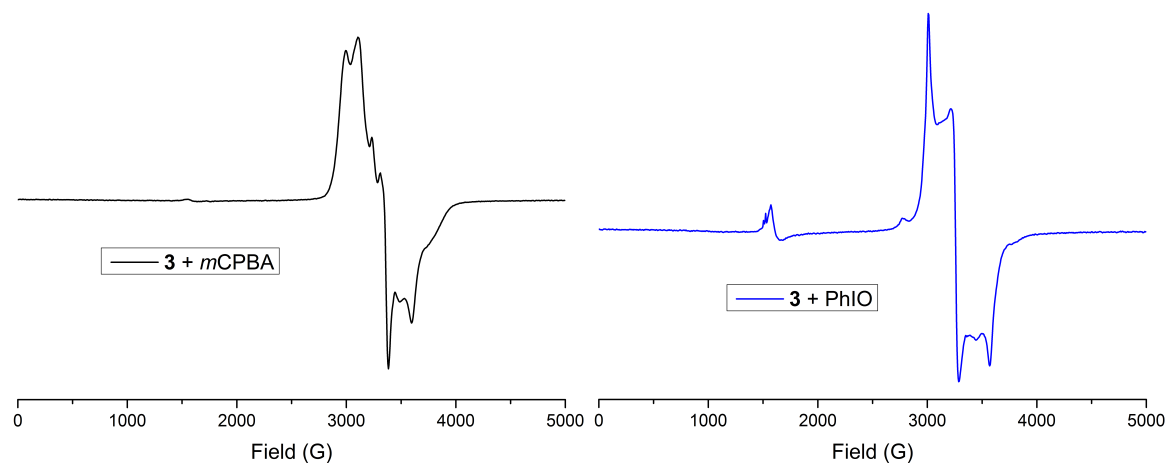


Figure 5.5 EPR data for **3** after oxidation with *m*CPBA (left) or PhIO (right).

When we overlay the EPR signals that result from both oxidation reactions, we see that one set of features is present in both samples (Figure 5.6). We propose that this set of features is due to **[4][BF₄]**, the Ru–Ru=O complex. To rationalize the second set of EPR features in the *m*CPBA reaction, we suggest an equilibrium between both $[\text{Ru}_2\text{O}]^+$ and $[\text{Ru}_2\text{OH}]^{2+}$ species (Scheme 5.5). PhIO, on the other hand, generates PhI as a by-product, which cannot protonate the $[\text{Ru}_2\text{O}]^+$ species. Thus the second set of $S = 1/2$ features which is present in the *m*CPBA reaction but not in the PhIO reaction could be the $[\text{Ru}_2\text{OH}]^{2+}$ complex. This proposal is consistent with the UV-Vis data seen above, for the starting material **3** can cleanly convert to **[4][BF₄]**, which subsequently undergoes protonation by the acid.

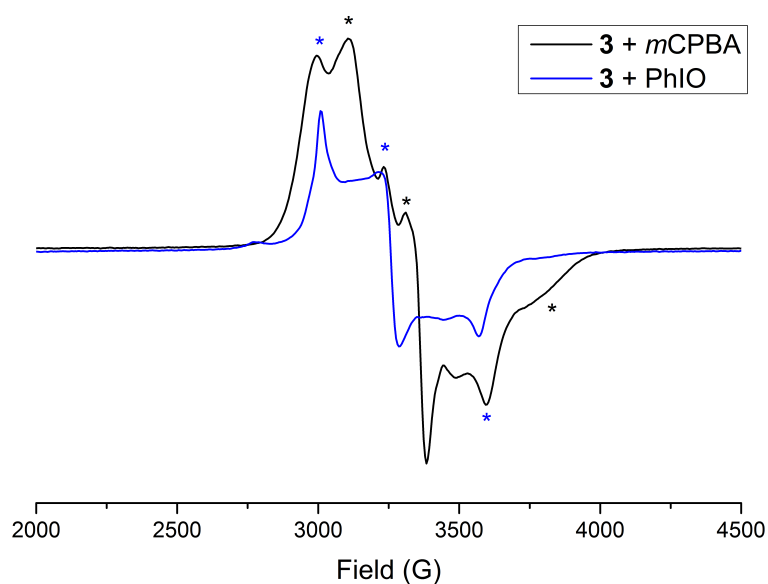
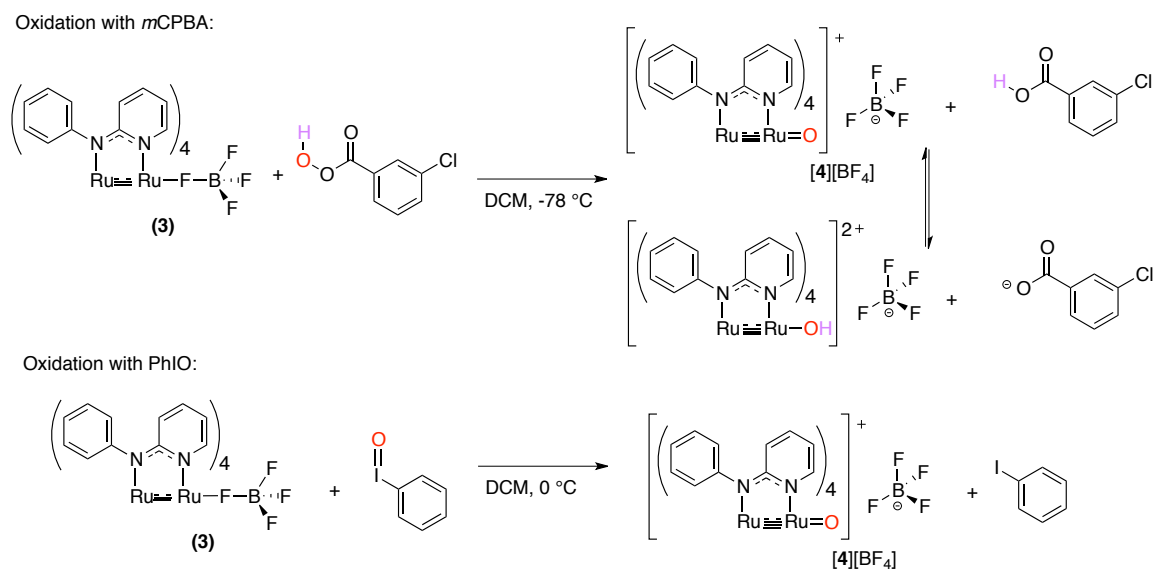


Figure 5.6 Overlay of EPR data for oxidation reactions of **3** with *m*CPBA and PhIO. Blue * symbols indicates the $S = 1/2$ signal that appears in both oxidations, while the black * symbols indicate the $S = 1/2$ species that is also only present after oxidation with *m*CPBA.



Scheme 5.5 Proposed $S = 1/2$ species resulting from oxidation of **3** with either *m*CPBA or PhIO.

Vibrational data for our proposed oxidation product $[4][BF_4]$ are also necessary to show that we do indeed have coordination of the oxygen atom to the Ru_2 center. In our previous studies, we noticed that the $Ru\equiv N$ vibrational stretch for $Ru_2(DPhF)_4N$ was intermediate between that for mononuclear $Ru\equiv N$ and surface $Ru-N$ vibrational stretches.¹ Figure 5.7 shows preliminary resonance Raman data collected after oxidation of **3** with *m*CPBA collected on the same sample characterized by UV-Vis (Figure 5.4). Boxed in red are features due to the Ru_2 sample and not solvent. Studies are on-going to determine if one of these features is due to the $Ru=O$ stretch.

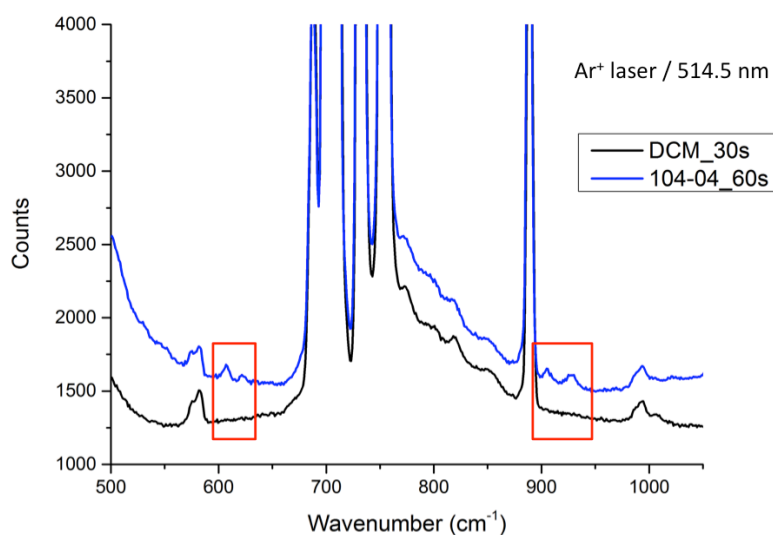


Figure 5.7 Resonance Raman data for $[4][BF_4]$ after oxidation with 1 equivalent of *m*CPBA. The regions which are boxed are red show the features due to the reaction mixture and not solvent.

Our previous N-atom⁴ and O-atom⁵ transfer studies have both utilized PPh_3 as a trapping agent due to its ease of use and study. We have therefore performed an initial trapping study using PPh_3 by adding it to a solution of $[4][BF_4]$ prepared from *m*CPBA at $-78\text{ }^\circ\text{C}$. A $^{31}\text{P}\{^1\text{H}\}$ NMR spectrum was taken after these materials were allowed to stir for 30 minutes at $-78\text{ }^\circ\text{C}$ and indicates a 20% conversion to $OPPh_3$ from PPh_3 . Additional studies will determine the reaction

conditions necessary to attain complete conversion, including the time and temperature of reaction.

5.4 Conclusions and Future Work.

Here we have shown that chemical oxidation of an Ru_2^{5+} core with an O-atom transfer agent generates a new $[\text{Ru}_2\text{O}]^{7+}$ complex. Unlike photolysis of Ru_2 -oxyanion complexes, here we can attain complete conversion of the starting species. Efforts are on-going to confirm and fully characterize this proposed Ru_2O species. Future studies will use trifluoromethanesulfonate instead of tetrafluoroborate as the non-coordinating anion since, unlike BF_4^- , triflate does not have the tendency to decompose (BF_4^- can lose F^-). Additionally, we will use PhIO as our oxidant, for this reagent gives cleaner conversion to our $S = 1/2$ species, and it can be labeled with ^{18}O for the vibrational studies. We will attempt to convert $[\text{Ru}_2\text{O}]^+$ to $[\text{Ru}_2\text{OH}]^{2+}$ with addition of acid (*mCBA*) in order to test our hypothesis of the identity of the second $S = 1/2$ species that results from the reaction of **3** with *mCPBA*. The substrate scope for O-atom transfer from $[\text{Ru}_2\text{O}]^+$ will also be expanded upon, and we are working with a collaborator to attain XAS data to structurally characterize the $\text{Ru}-\text{Ru}=\text{O}$ and $\text{Ru}-\text{Ru}=\text{OH}$ products.

5.5 Supplementary Information.

Materials and Methods. All syntheses were conducted under a dry N_2 atmosphere using Schlenk line techniques; product workup and isolation were achieved under ambient conditions. Dichloromethane (CH_2Cl_2) was dried with CaH_2 and distilled before use. Tetrahydrofuran (THF), acetonitrile (MeCN) and hexanes were obtained from a Vacuum Atmospheres Solvent System and degassed prior to use. $\text{Ru}_2(\text{ap})_4\text{Cl}$ (**1**)¹⁹ and PhIO^{23} were prepared according to

literature procedure. *m*CPBA was purified prior to use. All other materials were commercially available and used as received, unless otherwise noted.

[Ru₂(ap)₄NCMe][BF₄] (2). Ru₂(ap)₄Cl (53.3 mg, 0.0582 mmol, 1 eq.) and AgBF₄ (11.5 mg, 0.0591 mmol, 1.01 eq.) were dissolved in 10 mL of freshly distilled CH₂Cl₂ and 2 mL of dry MeCN and allowed to stir for 24 h at RT under inert N₂. A white precipitate (AgCl) formed; color change from forest green to dark brown. The reaction mixture was filtered through a fine sintered glass frit. The filtrate was removed under reduced pressure, and the resulting solid was washed with hexanes and collected. Crystals suitable for X-ray diffraction were grown from the reaction mixture solution and layered with hexanes at RT under N₂.

Ru₂(ap)₄FBF₃ (3). Ru₂(ap)₄Cl (349.8 mg, 0.3825 mmol, 1 eq.) and AgBF₄ (77.5 mg, 0.3981 mmol, 1.04 eq.) were dissolved in 25 mL of dry THF and allowed to stir for 2 hr at RT under inert N₂. A white precipitate (AgCl) formed. Color change from forest green to bright green. The reaction mixture was filtered through a medium sintered glass frit containing celite. The filtrate was then concentrated down, and hexanes were added to crash out the compound, which was collected on a medium porosity frit. Yield: 312.2 mg, 84.5%. MW: 965.75 g mol⁻¹. MALDI-TOF (*m/z*): ([M – BF₃]⁺) 899. IR (ATR): 3063 (w), 2957 (w), 2874 (w), 1602 (s), 1589 (s), 1542 (m), 1472 (s), 1433 (s), 1359 (s), 1289 (s), 1259 (w), 1229 (m), 1219 (s), 1161 (w), 1146 (m), 1116 (w), 1069 (m), 1022 (w), 999 (m), 925 (w), 917 (m), 892 (m), 865 (s), 759 (s), 736 (m), 699 (s), 675 (w), 654 (w), 645 (w) cm⁻¹. [4·C₄H₈O₁: C₄₈H₄₄B₁F₄N₈O₁Ru₂]: calcd. C 55.55, H 4.27, N 10.80; found C 55.62, H 4.37, N 10.64. Crystals suitable for X-ray diffraction were grown from a dry THF solution layered with hexanes at RT under N₂.

$[Ru_2(ap)_4O][BF_4]$ (**4**). Attempted route 1: **3** (48.0 mg, 0.0497 mmol, 1 eq.) was dissolved in 10 mL of CH_2Cl_2 and cooled to $-78\text{ }^\circ\text{C}$. *m*CPBA (14.6 mg, 0.0846 mmol, 1.7 eq.) is dissolved in 2 mL of CH_2Cl_2 in a separate flask. The *m*CPBA solution is slowly transferred via cannula into the flask containing **3**; the reaction mixture changes color from bright green to brown to finally hot dark pink. The reaction was allowed to stir at $-78\text{ }^\circ\text{C}$ for 30 minutes to ensure there was no further color change.

Attempted route 2: **3** (38.4 mg, 0.0397 mmol, 1 eq.) is dissolved in 10 mL of CH_2Cl_2 and cooled to $-78\text{ }^\circ\text{C}$. PhIO (14.6 mg, 0.0664 mmol, 1.7 eq.) is suspended in 15 mL of CH_2Cl_2 in a separate flask and also cooled to $-78\text{ }^\circ\text{C}$. The Ru_2 solution is slowly transferred via cannula into the flask containing PhIO. The reaction was allowed to stir at $-78\text{ }^\circ\text{C}$ for 30 minutes to ensure there was no color change; rather, the green solution remains green, and insoluble white powder (PhIO) can be seen. The reaction mixture was then warmed to $-40\text{ }^\circ\text{C}$ for 30 minutes, and there was still no visible color change. Upon warming to $0\text{ }^\circ\text{C}$ there was a rapid color change from bright green to dark red-brown. The reaction was allowed to stir at $-78\text{ }^\circ\text{C}$ for 30 minutes to ensure there was no further color change.

Physical Measurements. Matrix-assisted laser desorption/ionization (MALDI) time-of-flight (TOF) mass spectrometry data were obtained using an anthracene matrix on a Bruker ULTRAFLEX® III mass spectrometer equipped with a SmartBeam® laser in positive ion detection mode. UV-Vis spectra were obtained using a StellarNet Miniature BLUE-wave UV-Vis dip probe with a Tungsten-Krypton light source and a 10 mm path length tip. IR spectra were

taken on a Bruker Tensor 27 spectrometer using an ATR adapter (no matrix). Elemental analysis was done at Midwest Microlab, LLC in Indianapolis, IN, USA.

X-ray Crystallography. Crystallographic data were measured at the Molecular Structure Laboratory of the Chemistry Department of the University of Wisconsin – Madison. Suitable crystals of **2** and **3** were selected under oil and ambient conditions. For **2**, a brown plate shaped crystal with dimensions 0.236 x 0.042 x 0.040 mm³ was selected, and for **3** a green plate crystal with dimensions 0.142 x 0.098 x 0.048 mm³ was chosen. The crystals were attached to the tip of a MiTeGen MicroMount®, mounted in a stream of cold nitrogen at 100(1) K, and centered in the X-ray beam using a video monitoring system. The crystal evaluation and data collection were performed on a Bruker Quazar SMART APEX-II diffractometer with Mo-K α (λ = 0.71073 Å) radiation. The data were collected using a routine to survey the reciprocal space and indexed by the APEX program.²⁴ The structures were solved via direct methods and refined by iterative cycles of least-squares refinement on F² followed by difference Fourier synthesis. All hydrogen atoms were included in the final structure factor calculation at idealized positions and were allowed to ride on the neighboring atoms with relative isotropic displacement coefficients. Absorption corrections were based on a fitted function to the empirical transmission surface as sampled by multiple equivalent measurements.²⁵ The systematic absences in the diffraction data were uniquely consistent with the space groups *P*-1 for both **2** and **3**, yielding chemically reasonable and computationally stable results of refinement, and both structures were solved using direct methods using XS software.²⁶ Highly disordered THF solvent molecules were present in the structure of **3**. The diffusely diffracting species totaled to 158 electrons (approximately 3.95 molecules of THF) and were treated with SQUEEZE.²⁷

EPR Spectroscopy. EPR data were acquired on a Varian Line spectrometer equipped with a Varian E102 microwave bridge interfaced with a Linux system. An Oxford Instruments ESR-900 continuous-flow helium flow cryostat and an Oxford Instruments 3120 temperature controller were used to control the sample temperature. A Hewlett-Packard 432A power meter was used for microwave power calibration, with measurement conditions as follows: for **2** – 9.3761 GHz, 4 G modulation amplitude, 2500 G center field, 5000 G sweep width, 1.262 mW power, 50 dB gain, 655.36 ms time constant, 10.0 ms conversion time, and 10 K; for **3** – 9.3802 GHz, 4 G modulation amplitude, 2500 G center field, 5000 G sweep width, 1.262 mW power, 50 dB gain, 655.36 ms time constant, 10.0 ms conversion time, and 10 K; for **3 + mCPBA** – 9.3794 GHz, 4 G modulation amplitude, 2500 G center field, 5000 G sweep width, 0.5024 mW power, 50 dB gain, 20.48 ms time constant, 20.48 ms conversion time, and 10 K; for **3 + PhIO** – 9.3826 GHz, 4 G modulation amplitude, 2500 G center field, 5000 G sweep width, 0.5024 mW power, 60 dB gain, 20.48 ms time constant, 20.48 ms conversion time, and 10 K. Spectral simulations were performed using EasySpin software.²⁸

References.

- (1) Pap, J. S.; DeBeer George, S.; Berry, J. F. *Angew. Chem. Int. Ed.* **2008**, 47, 10102.
- (2) Long, A. K. M.; Yu, R. P.; Timmer, G. H.; Berry, J. F. *J. Am. Chem. Soc.* **2010**, 132, 12228.
- (3) Long, A. K. M.; Timmer, G. H.; Pap, J. S.; Snyder, J. L.; Yu, R. P.; Berry, J. F. *J. Am. Chem. Soc.* **2011**, 133, 13138.
- (4) Corcos, A. R.; Long, A. K. M.; Guzei, I. A.; Berry, J. F. *Eur. J. Inorg. Chem.* **2013**, 2013, 3808.
- (5) Corcos, A. R.; Pap, J. S.; Yang, T.; Berry, J. F. *In Preparation*.

- (6) Che, C.-M.; Wong, K.-Y.; Mak, T. C. W. *J. Chem.Soc. Chem. Commun.* **1985**, 546.
- (7) Che, C.-M.; Wong, K.-Y.; Mak, T. C. W. *J. Chem. Soc., Chem.Comm.* **1985**, 988.
- (8) Che, C. M.; Lai, T. F.; Wong, K. Y. *Inorg. Chem.* **1987**, 26, 2289.
- (9) Che, C.-M.; Tang, W.-T.; Lee, W.-O.; Wong, W.-T.; Lai, T.-F. *J. Chem. Soc., Dalton Trans.* **1989**, 2011.
- (10) Dengel, A. C.; Griffith, W. P.; O'Mahoney, C. A.; Williams, D. J. *J. Chem. Soc., Chem. Commun.* **1989**, 1720.
- (11) Nagao, H.; Nishimura, H.; Kitanaka, Y.; Howell, F. S.; Mukaida, M.; Kakihana, H. *Inorg. Chem.* **1990**, 29, 1693.
- (12) Power, J. M.; Evertz, K.; Henling, L.; Marsh, R.; Schaefer, W. P.; Labinger, J. A.; Bercaw, J. E. *Inorg. Chem.* **1990**, 29, 5058.
- (13) Wong, K.-Y.; Che, C.-M.; Yip, W.-H.; Wang, R.-J.; Mak, T. C. W. *J. Chem. Soc., Dalton Trans.* **1992**, 1417.
- (14) de Souza, V. R.; Nunes, G. S.; Rocha, R. C.; Toma, H. E. *Inorg. Chim. Acta* **2003**, 348, 50.
- (15) Man, W.-L.; Lam, W. W. Y.; Wong, W.-Y.; Lau, T.-C. *J. Am. Chem. Soc.* **2006**, 128, 14669.
- (16) Nippe, M.; Goodman, S. M.; Fry, C. G.; Berry, J. F. *J. Am. Chem. Soc.* **2011**, 133, 2856.
- (17) Brogden, D. W.; Turov, Y.; Nippe, M.; Li Manni, G.; Hillard, E. A.; Clérac, R.; Gagliardi, L.; Berry, J. F. *Inorg. Chem.* **2014**, 53, 4777.
- (18) Chakravarty, A. R.; Cotton, F. A.; Tocher, D. A. *Inorg. Chem.* **1985**, 24, 1263.
- (19) Chakravarty, A. R.; Cotton, F. A.; Tocher, D. A. *Inorg. Chem.* **1985**, 24, 172.
- (20) Cotton, F. A.; Yokochi, A. *Inorg. Chem.* **1997**, 36, 567.
- (21) Based on a search of the Cambridge Structural Database.
- (22) Cotton, F. A.; Murillo, C. A.; Walton, R. A. *Multiple Bonds Between Metal Atoms*; 3rd ed.; Springer Science and Business Media, Inc.: New York, 2005.
- (23) Martinand-Lurin, E.; Gruber, R.; Retailleau, P.; Fleurat-Lessard, P.; Dauban, P. *J. Org. Chem.* **2015**, 80, 1414.

- (24) APEX2. 2014.11-0.
- (25) SADABS. 2014/5.
- (26) XS. 2013/1.
- (27) <http://www.cryst.chem.uu.nl/platon/>.
- (28) Stoll, S.; Schweiger, A. *J. Magn. Reson.* **2006**, *178*, 42-55.

Chapter 6

Capturing the Missing $[\text{AgF}_2]^-$ Anion within an $\text{Ru}_2(\text{III/III})$ Dimeric Dumbbell Complex

This chapter has been published:

Reprinted with permission from Amanda R. Corcos and John F. Berry.
Dalton Trans. **2016**, 45, 2386-2389. Copyright 2016 The Royal Society of Chemistry.

6.1 Abstract.

The complex $\{[\text{Ru}_2(\text{ap})_4]_2[\text{AgF}_2]\}[\text{BF}_4]_3$ (**2**)[BF_4]₃, ap = 2-anilinopyridine), containing the $[\text{AgF}_2]^-$ anion ligated to two $[\text{Ru}_2]^{6+}$ cores, is prepared, characterized, and compared to dimeric dumbbell-type structures, monomeric Ru_2 structures, as well as the known set of dihalo coinage-metalate anions. X-ray crystallography indicates that the Ru–Ru and Ru–F distances are rather short, 2.2835(3) Å and 2.054(1) Å, while the Ag–F distance of 2.274(1) Å is longer than that calculated for the free/un-ligated anion. Cyclic voltammetry in dichloromethane indicates that, while some of **2**³⁺ breaks apart into an $[\text{Ru}_2(\text{ap})_4\text{F}]^+$ (**3**)⁺ monomer in solution, the remaining dimer has a single reversible two-electron redox feature for the $\text{Ru}_2^{6/5+}$ couple that is at a lower potential than that of **3**⁺. This is one of the few examples of a ligated dihalo coinage-metalate, and it is the first example of a coinage metal difluoride anion, either free or ligated.

6.2 Introduction.

The coinage metals are unique from other metals in that they exhibit an inverse trend in bond strength with the halogens upon complexation.¹ This trend is best demonstrated by the plummeting solubility of the silver halides from F to Cl to Br to I. In coordination chemistry, a common structural motif for the coinage metals in the +1 oxidation state is the linear, two

coordinate $D_{\infty h}$ mode.² When bound to two halides, coinage metal complexes can form discrete $[X-M-X]^-$ anions or these anions can be trapped by coordination to other metals in linear $M'-[X-M-X]-M'$ multimetallic complexes.³ $[CuX_2]^-$ and $[AgX_2]^-$ ions have a relative stability of $I^- > Br^- > Cl^-$,² and currently there are no examples of $[F-M-F]^-$ ions for any of the coinage metals (Figure 6.1), either as the free complex anion or when ligated to additional metals,³ most likely due to the weakness of the coinage metal M-F bond.

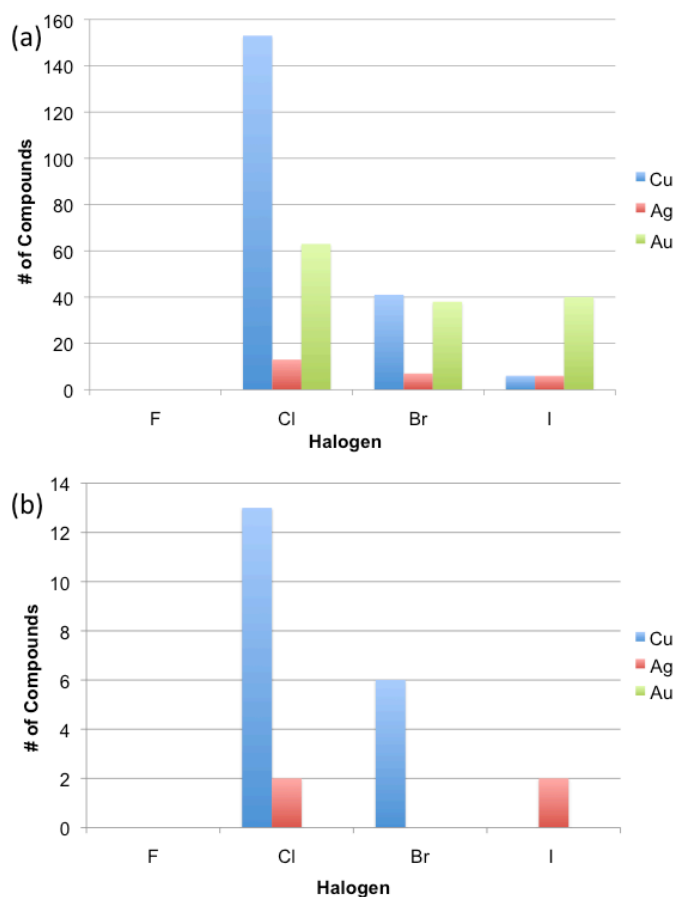
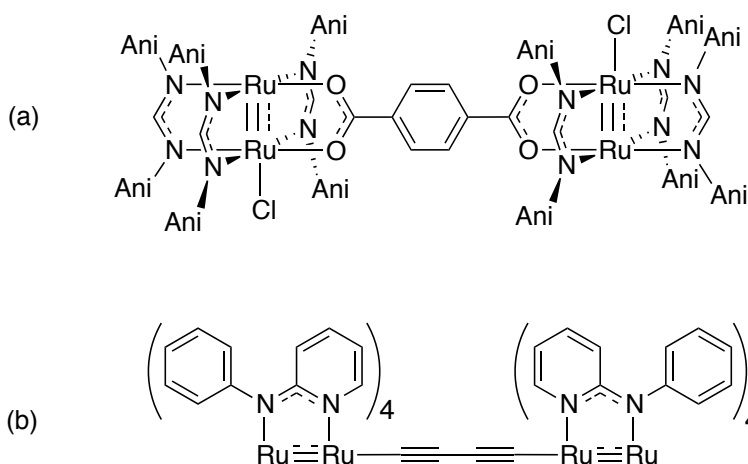


Figure 6.1 Number of known two-coordinate coinage metal dihalogen complexes, both as the (a) free complex anion and (b) ligated to additional metals.³

The ability of the metal-metal bonded Ru_2^{n+} unit to stabilize multiple oxidation states with $n = 4, 5, 6$ has inspired the deliberate synthesis of compounds with two or more Ru_2 units

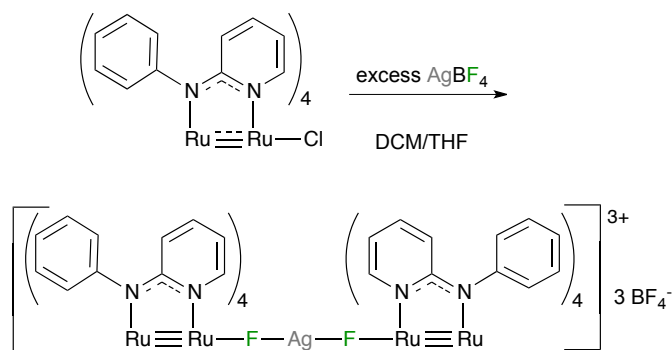
linked together through their equatorial or axial sites (Scheme 6.1).⁴⁻¹⁵ To our knowledge, all of the currently reported bridging units between Ru₂ centers are organic linkers. Herein we present the first example of a tri-cationic dimeric Ru₂⁶⁺ complex bound by an inorganic tri-atomic linker – the missing [AgF₂][−] ion – and explore its electronic properties.



Scheme 6.1 Examples of (a) equatorial-⁸ and (b) axial-bridged⁵ Ru₂ dimeric dumbbell complexes.

6.3 Results and Discussion.

Upon reacting the anilinopyridinate complex Ru₂(ap)₄Cl (**1**) with an excess of AgBF₄ in a mixture of dry dichloromethane and tetrahydrofuran at room temperature, the solution quickly changes color from green to scarlet red, and after stirring overnight a precipitate (presumably Ag/AgCl) forms. After filtration, concentration, and layering with dry hexanes, red block crystals of {[Ru₂(ap)₄][AgF₂]}[BF₄]₃ (**2**) were obtained in good (> 80%) yield (Scheme 6.2, Figure 6.2). It appears the excess Ag(I) in solution oxidizes the Ru₂ center, and the F[−] ion is abstracted from the excess BF₄[−] in solution, which is not an uncommon occurrence.^{16,17}



Scheme 6.2 Synthetic formation of $\{2\}[\text{BF}_4]_3$ from $\text{Ru}_2(\text{ap})_4\text{Cl}$ (**1**).

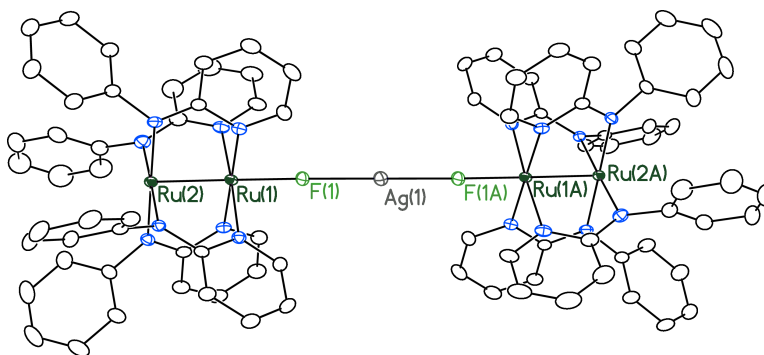


Figure 6.2 Thermal ellipsoid plot of $\{[\text{Ru}_2(\text{ap})_4]_2[\text{AgF}_2]\}[\text{BF}_4]_3 \cdot 3\text{CH}_2\text{Cl}_2$ ($\{2\}[\text{BF}_4]_3 \cdot 3\text{CH}_2\text{Cl}_2$) with ellipsoids drawn at the 50% probability level. Hydrogen atoms, molecules of solvation, and BF_4 counter ions omitted for clarity.

Unlike formation of $[\text{Ru}_2(\text{ap})_4\text{F}][\text{PF}_6]$ (**3**)[PF_6]), which occurs upon reaction of **1** with excess AgPF_6 in dry dichloromethane,¹⁸ X-ray crystallography unambiguously confirms that the $[\text{AgF}_2]^-$ ion is present in $\{2\}[\text{BF}_4]_3$. The complex crystallizes in the $P-1$ space group with dichloromethane (but not tetrahydrofuran) in the lattice. The Ru–Ru bond distance of 2.2835(3) Å in $\{2\}^{3+}$ is slightly shorter than that in other Ru_2^{6+} species but is still elongated as compared to Ru_2^{5+} species (Table 6.1),⁹ which is consistent with a local $\sigma^2\pi^4\delta^2\pi^{*2}$ electron configuration for each Ru_2 unit (further supported by the paramagnetism of the complex).¹⁸ Due to the smaller size

of fluoride versus chloride,¹⁹ it is not surprising that the axial Ru–F bond distance of 2.054(1) Å in $\{2\}^{3+}$ is shorter than the axial Ru–Cl bond distance in $[\text{Ru}_2(\text{ap})_4\text{Cl}]^+$.¹⁸ However, it is surprising that the Ru–F bond distance in $\{2\}^{3+}$ is significantly shorter by 0.05 Å than that in $[\mathbf{3}][\text{PF}_6]$, a complex with the same connectivity and metal oxidation state as $\{2\}^{3+}$; this effect is likely an electrostatic effect due to the higher positive charge in $\{2\}^{3+}$ versus $[\mathbf{3}]^+$. Additionally, the Ru–F bond distance in $\{2\}^{3+}$ is almost identical to that in $\text{Ru}_2(\text{ap})_4\text{F}$ (**3**), its reduced analog. The equatorial anilinopyridine ligands in $\{2\}^{3+}$ maintain their (4,0) isomeric connectivity to the Ru_2 core as in **1**, and the N(pyridine)–Ru bond distances in $\{2\}^{3+}$ are demonstrably shorter than the N(amine)–Ru bond distances, as expected.^{18,20} The Ru(2)–Ru(1)–F bond angle, 179.15(4)°, is almost linear.

Table 6.1. Selected bond distances for comparable Ru_2^{5+} and Ru_2^{6+} structures.

Compound	Ru_2 Ox. State	Ru–Ru (Å)	Ru–X (Å)	Ru–Ru–X (°)	Ref.
$\text{Ru}_2(\text{ap})_4\text{Cl}$ (1)	5+	2.275(3)	2.437(7)	180.00(0)	20
$\text{Ru}_2(\text{ap})_4\text{F}$ (3)	5+	2.2785(6)	2.058(3)	179.8(1)	19
$[\text{Ru}_2(\text{ap})_4\text{Cl}][\text{FeCl}_4]$	6+	2.301(1)	2.419(2)	179.84(6)	18
$[\text{Ru}_2(\text{ap})_4\text{F}][\text{PF}_6]$ ($[\mathbf{3}][\text{PF}_6]$)	6+	2.296(1)	2.104(2)	N/A	18
$\{[\text{Ru}_2(\text{ap})_4]_2(\text{AgF}_2)\}[\text{BF}_4]_3$ ($\{2\}[\text{BF}_4]_3$)	6+	2.2835(3)	2.054(1)	179.15(4)	This work

Due to Ag residing on a crystallographic inversion center, the distances between Ag(1)–F(1/1A) are identical at 2.274(1) Å. This distance is significantly longer than the calculated Ag–F distance of 2.060 Å for the free/unbound $[\text{AgF}_2]^-$ moiety²¹ (there are no crystallographic examples of this free anion),³ which is expected and in accord with other M–X distances when compared between the free $[\text{MX}_2]^-$ anions and the ligated $\text{M}'\text{--}[\text{X--M--X}]\text{--M}'$ unit. For example, the average Cu–Cl distance in $[\text{CuCl}_2]^-$ increases from 2.092 Å to 2.121 Å, the Ag–Cl distance in $[\text{AgCl}_2]^-$ increases from 2.337 Å to 2.417 Å, and the Cu–Br distance in $[\text{CuBr}_2]^-$ increases from 2.217 Å to 2.252 Å upon ligation.³

The major peak in the MALDI-TOF mass spectrum for $\{2\}[\text{BF}_4]_3$ occurs at $m/z = 899$, which is not indicative of the dimeric unit but rather the $[\mathbf{3}]^+$ moiety (Figure S6.1). The electronic

spectrum of $\{2\}[\text{BF}_4]_3$ is more similar to that of $[3][\text{PF}_6]$ than it is to that of **1**, having features at 489 and 925 nm, with a shoulder at 390 nm (Figure S6.2).

Cyclic voltammetry experiments in dichloromethane show multiple reversible features (Figure 6.3). The $E_{1/2}$ value for feature **A** is at 0.091 V, while that for **B** occurs at -0.200 V, and **C** occurs at -0.978 V versus Fc/Fc^+ . The $E_{1/2}$ values for **A** and **C** are consistent with the $\text{Ru}_2^{6/5+}$ and $\text{Ru}_2^{5/4+}$ redox couples of $[3][\text{PF}_6]$,²² and this similarity suggests that $\{2\}[\text{BF}_4]_3$ partially breaks apart in solution to release $[3]^+$. Feature **B**, the $E_{1/2}$ for the $\text{Ru}_2^{6/5+}$ couple in $\{2\}[\text{BF}_4]_3$ which remains intact in solution, exhibits more than twice the current of the monomeric species. This is due to the dimeric nature of $\{2\}^{3+}$, in which there are two $E_{1/2}$ $\text{Ru}_2^{6/5+}$ redox events that occur concurrently (Scheme 6.3). This is similar to voltammograms of symmetric dumbbell-type structures in which the Ru_2 units are connected through the equatorial ligands,¹¹ and it indicates that the two Ru_2 units in $\{2\}^{3+}$ do not influence each other's redox properties.

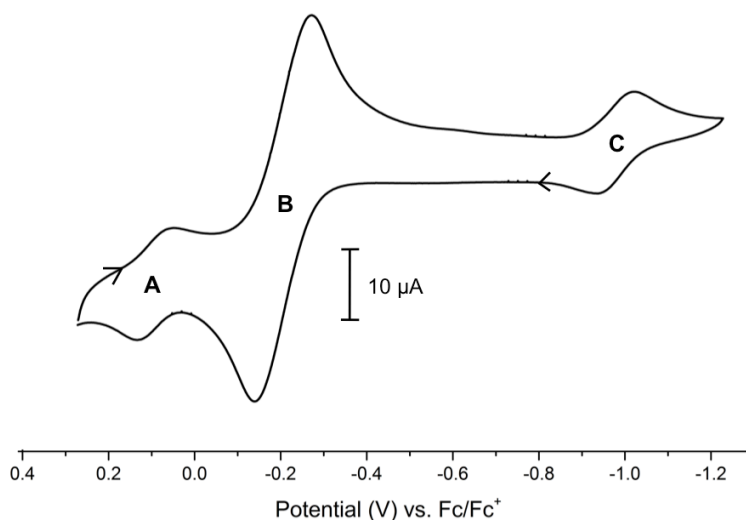
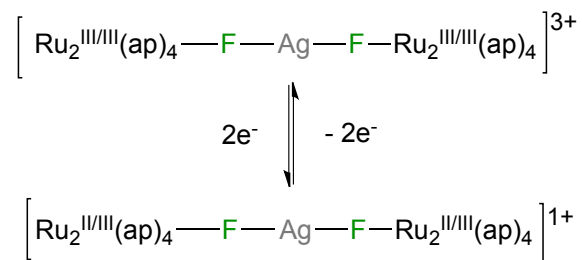
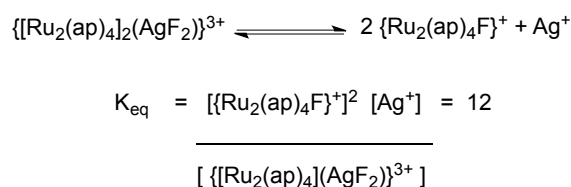


Figure 6.3 Cyclic voltammogram for $\{2\}[\text{BF}_4]_3$ in CH_2Cl_2 (1 mM) with NBu_4BF_4 (0.1 M) versus Fc/Fc^+ . Feature **B** at -0.200 V is due to two concurrent $\text{Ru}_2^{6/5+}$ events in $\{2\}^{3+}$ while features **A** and **C** are Ru_2 redox features for monomeric $[\text{Ru}_2(\text{ap})_4\text{F}]^+$ ($[3]^+$).



Scheme 6.3 Observed Ru₂-based redox feature for {**2**}[BF₄]₃.

As previously discussed, {**2**}³⁺ has a significantly shorter axial Ru–F bond than [**3**]⁺ which allows for better electron donation into the Ru–Ru bond and stabilization of higher oxidation states. It is therefore harder to reduce the Ru₂⁶⁺ core in {**2**}³⁺ than [**3**]⁺, despite the higher cationic charge of the former complex. From the peak currents in the cyclic voltammetry data it is possible to calculate an equilibrium constant for {**2**}³⁺ breaking apart into monomeric [**3**]⁺ in dichloromethane solution (Scheme 6.4). Under the assumption that the free [Ag]⁺ concentration is equal to that of [**3**]⁺ in solution, the *K*_{eq} for this equilibrium is 12, which indicates that the dumbbell structure is metastable in solution.



Scheme 6.4 Equilibrium for {**2**}³⁺ as derived from cyclic voltammetry.

6.4 Conclusions.

We have presented here an unusual example of an [Ru₂]⁶⁺ dumbbell-type dimer, {**2**}[BF₄]₃, bridged by the heretofore unknown [F–Ag–F][–] inorganic linker. While {**2**}³⁺

dissociates in solution, the dimeric species exhibits a less accessible reduction potential as compared to the monomer, and both $\text{Ru}_2^{6/5+}$ couples occur concurrently. More significantly, this is the first example of a complex containing a two-coordinate, linear coinage metal difluoride anion.

6.5 Acknowledgements.

We thank the U.S. Department of Energy, Chemical Sciences, Geosciences, and Biosciences Division, Office of Basic Energy Sciences, Office of Science (DE-FG02-10ER16204) for their support of this work. A.R.C. thanks the National Science Foundation for a Graduate Research Fellowship (DGE-0718123). The purchase of the ULTRAFLEX® III was partially funded by NIH (NCRR 1S10RR024601-01) to the Department of Chemistry. We thank Brian Dolinar for crystallographic insights.

6.6 Supplementary Information.

Materials and Methods. All syntheses were conducted under a dry N_2 atmosphere in an MBraun glovebox; product workup and isolation were achieved under ambient conditions. Dichloromethane (CH_2Cl_2) was dried with CaH_2 and distilled before use. Tetrahydrofuran (THF) and hexanes were obtained from a Vacuum Atmospheres Solvent System and degassed prior to use. All materials were commercially available and used as received, unless otherwise noted. The compound $\text{Ru}_2(\text{ap})_4\text{Cl}$ was prepared according to a literature procedure,²⁰ and the Hap ligand was purified by sublimation prior to use.

$\{[Ru_2(ap)_4]_2[AgF_2]\}[BF_4]_3$ (**2**) $[BF_4]_3$. $Ru_2(ap)_4Cl$ (150 mg, 0.164 mmol, 1.00 eq.) and $AgBF_4$ (82.5 mg, 0.423 mmol, 2.58 eq.) were dissolved in 12 mL of freshly distilled CH_2Cl_2 and 4 mL THF. The solution changed color from forest green to scarlet red and formation of a gray precipitate (presumably $Ag/AgCl$) was observed almost instantly. The reaction mixture was allowed to stir overnight at RT under N_2 . The reaction mixture was then filtered through a fine frit. After concentrating the CH_2Cl_2 /THF solution, the filtrate was layered with hexanes and allowed to crystallize by slow diffusion at RT. Yield: 146.4 mg, 82.5%. MW: 2164.18 $g\ mol^{-1}$. MALDI-TOF (m/z): 898 $[M - Ag(Ru_2(ap)_4F)(BF_4)_3]^+$. IR (ATR) ν/cm^{-1} : 1598 (s), 1482 (s), 1462 (s), 1425 (s), 1340 (m), 1287 (m), 1259 (m), 1208 (s), 1164 (m), 1057 (s), 1023 (m), 963 (m), 923 (m), 868 (s), 837 (w), 764 (s), 729 (s), 699 (s), 653 (w). UV-Vis in CH_2Cl_2 $\lambda = 390\ nm$ (sh), 489 nm, 925 nm. Anal. for $[C_{88}H_{72}AgB_3F_{14}N_{16}Ru_4] \cdot CH_2Cl_2$: calcd. C 47.53, H 3.32, N 9.96; found C 47.73, H 3.77, N 9.51.

Physical Measurements. Matrix-assisted laser desorption/ionization (MALDI) time-of-flight (TOF) mass spectrometry data were obtained using an anthracene matrix on a Bruker ULTRAFLEX® III mass spectrometer equipped with a SmartBeam® laser in positive ion detection mode. UV-Vis spectra were obtained using a StellarNet Miniature BLUE-wave UV-Vis dip probe with a Tungsten-Krypton light source and a 10 mm path length tip. IR spectra were taken on a Bruker Tensor 27 spectrometer using an ATR adapter (no matrix). Cyclic voltammograms were taken on a BASi Potentiostat using Epsilon software in CH_2Cl_2 solutions with 0.1 M NBu_4BF_4 and 1.0 mM substrate. The electrodes were as follows: glassy carbon (working), Pt wire (auxiliary) and Ag/Ag^+ in CH_3CN (reference). The potentials were referenced

versus the ferrocene/ferrocenium redox couple, by externally added ferrocene. Elemental analysis was performed at Midwest Microlab, LLC in Indianapolis, IN, USA.

X-ray Crystallography. Crystallographic data were measured at the Molecular Structure Laboratory of the Chemistry Department of the University of Wisconsin–Madison. Suitable crystals of $\{\mathbf{2}\}[\text{BF}_4]_3 \cdot 3\text{CH}_2\text{Cl}_2$ were selected under oil and ambient conditions. For $\{\mathbf{2}\}[\text{BF}_4]_3 \cdot 3\text{CH}_2\text{Cl}_2$, a red plate shaped crystal with dimensions 0.219 x 0.079 x 0.068 mm was selected. The crystal was attached to the tip of a MiTeGen MicroMount[®], mounted in a stream of cold nitrogen at 100(1) K, and centered in the X-ray beam using a video monitoring system. The crystal evaluation and data collection were performed on a Bruker Quazar SMART APEX-II diffractometer with Mo-K α ($\lambda = 0.71073 \text{ \AA}$) radiation. The data were collected using a routine to survey the reciprocal and were indexed by the SMART program.²³ The structures were solved via direct methods and refined by iterative cycles of least-squares refinement on F^2 followed by difference Fourier synthesis.^{24,25} All hydrogen atoms were included in the final structure factor calculation at idealized positions and were allowed to ride on the neighboring atoms with relative isotropic displacement coefficients. Absorption corrections were based on a fitted function to the empirical transmission surface as sampled by multiple equivalent measurements.³ The space group $P\bar{1}$ was chosen for refinement of the structure of $\{\mathbf{2}\}[\text{BF}_4]_3 \cdot 3\text{CH}_2\text{Cl}_2$ on the basis of intensity statistics indicating a centrosymmetric structure, and this choice yields a chemically reasonable and computationally stable refinement.²⁶

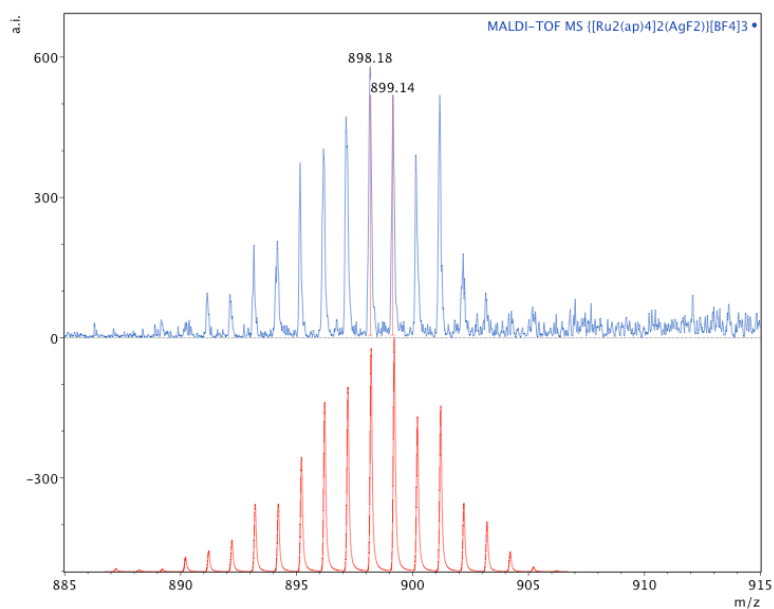


Figure S6.1 Mass spectrum for $\{2\}[\text{BF}_4]_3$. This data (top, simulation below) indicates the complex flies as $[\text{Ru}_2(\text{ap})_4\text{F}]^+$.

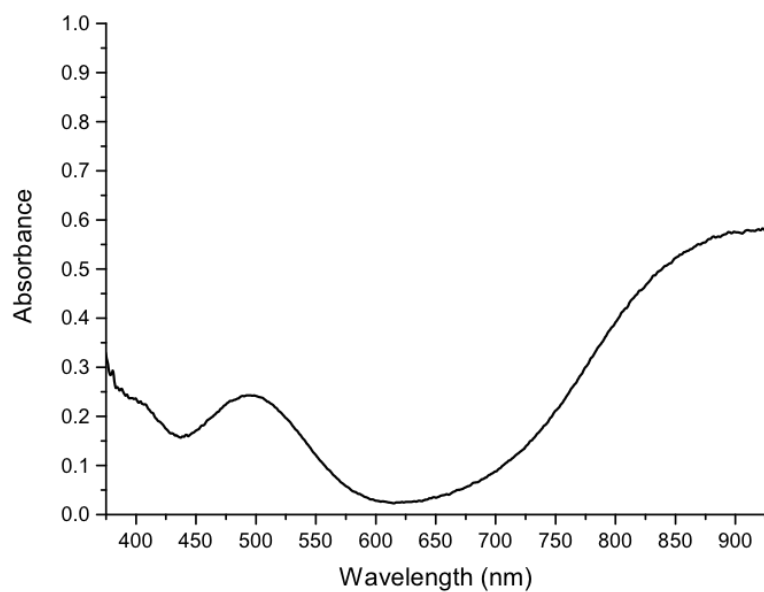


Figure S6.2 Electronic absorption spectrum for $\{2\}[\text{BF}_4]_3$ in CH_2Cl_2 .

Table S6.1. Summary of X-ray crystallographic data for **{2}[BF₄]₃•3CH₂Cl₂**

Compound	{2}[BF₄]₃•3CH₂Cl₂
Formula	C ₉₁ H ₇₈ Ag ₁ B ₃ Cl ₆ F ₁₄ N ₁₆ Ru ₄
Formula Weight g/mol	2418.97
Temperature (K)	100(1)
Crystal system	Triclinic
Space Group	<i>P</i> -1
<i>a</i> , Å	9.9382(4)
<i>b</i> , Å	12.7219(5)
<i>c</i> , Å	18.5759(8)
<i>α</i> °	87.507(2)
<i>β</i> °	88.869(2)
<i>γ</i> °	82.265(2)
<i>V</i> , Å ³	2324.8(2)
<i>Z</i>	1
Density (calculated)	1.728 g/cm ³
Crystal size	0.219 x 0.079 x 0.068 mm ³
Data / restraints / parameters	13265 / 296 / 662
Goodness-of-fit on <i>F</i> ²	1.094
<i>R</i> 1 ^a , <i>wR</i> 2 ^b (<i>I</i> < 2σ(<i>I</i>))	0.0330, 0.0786
<i>R</i> 1 ^a , <i>wR</i> 2 ^b (all data)	0.0411, 0.0823

^a*R*1 = Σ||*F*_o| - |*F*_c|| / Σ|*F*_o|. ^b*wR*2 = [Σ[w(*F*_o² - *F*_c²)²] / Σ[w(*F*_o²)²]]^{1/2}, *w* = 1/σ²(*F*_o²) + (*aP*)² + *bP*, where *P* = [max(0 or *F*_o²) + 2(*F*_c²)]/3.

References.

- (1) Greenwood, N. N.; Earnshaw, A. *Chemistry of the Elements*; 2nd ed.; Butterworth Heinemann: Oxford, 1997.
- (2) Cotton, F. A.; Wilkinson, G. *Advanced Inorganic Chemistry*; 5 ed.; John Wiley & Sons: New York, 1988.
- (3) Based on a search of the Cambridge Structural Database.
- (4) Cotton, F. A.; Labella, L.; Shang, M. *Inorg. Chem.* **1992**, *31*, 2385.
- (5) Ren, T.; Zou, G.; Alvarez, J. C. *Chem. Commun.* **2000**, 1197.
- (6) Hurst, S. K.; Ren, T. *J. Organomet. Chem.* **2003**, *670*, 188.
- (7) Xu, G.-L.; Zou, G.; Ni, Y.-H.; DeRosa, M. C.; Crutchley, R. J.; Ren, T. *J. Am. Chem. Soc.* **2003**, *125*, 10057.
- (8) Angaridis, P.; Berry, J. F.; Cotton, F. A.; Lei, P.; Lin, C.; Murillo, C. A.; Villagran, D. *Inorg. Chem. Commun.* **2004**, *7*, 9.
- (9) Cotton, F. A.; Murillo, C. A.; Walton, R. A. *Multiple Bonds Between Metal Atoms*; 3rd ed.; Springer Science and Business Media, Inc.: New York, 2005.
- (10) Barral, M. C.; Gallo, T.; Herrero, S.; Jimenez-Aparicio, R.; Torres, M. R.; Urbanos, F. A. *Inorg. Chem.* **2006**, *45*, 3639.
- (11) Chen, W.-Z.; Ren, T. *Inorg. Chem.* **2006**, *45*, 9175.
- (12) Kennon, B. S.; Miller, J. S. *Inorg. Chem.* **2010**, *49*, 5542.
- (13) Ying, J.-W.; Liu, I. P.-C.; Xi, B.; Song, Y.; Campana, C.; Zuo, J.-L.; Ren, T. *Angew. Chem. Int. Ed.* **2010**, *49*, 954.
- (14) Boyd, D. A.; Fanwick, P. E.; Ren, T. *Inorg. Chim. Acta* **2011**, *370*, 192.
- (15) Young, M. D.; Zhang, Q.; Zhou, H.-C. *Inorg. Chim. Acta* **2015**, *424*, 216.
- (16) Crabtree, R. H.; Hlatky, G. G.; Holt, E. M. *J. Am. Chem. Soc.* **1983**, *105*, 7302.
- (17) Thomas, R. R.; Chebolu, V.; Sen, A. *J. Am. Chem. Soc.* **1986**, *108*, 4096.
- (18) Cotton, F. A.; Yokochi, A. *Inorg. Chem.* **1997**, *36*, 567.
- (19) Xu, G.-L.; Cordova, A.; Ren, T. *J. Cluster Sci.* **2004**, *15*, 413.

- (20) Chakravarty, A. R.; Cotton, F. A.; Tocher, D. A. *Inorg. Chem.* **1985**, *24*, 172.
- (21) Seth, M.; Cooke, F.; Schwerdtfeger, P.; Heully, J.-L.; Pelissier, M. *J. Chem. Phys.* **1998**, *109*, 3935.
- (22) The $\text{Ru}_2^{6/5+}$ couples for complex $[\mathbf{3}]^+$ were previously recorded in THF with NBu_4PF_6 . See Ref. 19.
- (23) *SMART*; Bruker-AXS: Madison, WI, 2009.
- (24) Sheldrick, G. M. *Acta Cryst.* **2008**, *A64*, 112.
- (25) Dolomanov, O. V.; Bourhis, L. J.; Gildea, R. J.; Howard, J. A. K.; H., P. *J. Appl. Cryst.* **2009**, *42*, 339.
- (26) Sheldrick, G. M. *CELL_NOW*. University of Gottingen, Germany, 2008.

Chapter 7

An “Intermediate Spin” Nickel Hydride Complex Stemming from Delocalized Ni₂(μ-H)₂ Bonding

This chapter has been published:

Reprinted with permission from Shu A. Yao,^{a,‡} Amanda R. Corcos,^{a,‡} Ivan Infante,^b Elizabeth A. Hillard,^{c,d} Rodolphe Clérac,^{c,d} and John F. Berry^a. *J. Am. Chem. Soc.* **2014**, *136*, 13538-13541.
Copyright 2014 American Chemical Society

^a Department of Chemistry, University of Wisconsin – Madison, Madison, 1101 University Ave, Madison, Wisconsin 53706 (USA)

^b Kimika Fakultatea, Euskal Herriko Unibertsitatea, and Donostia International Physics Center (DIPC), P. K. 1072, 20080 Donostia, Euskadi (Spain)

^c CNRS, CRPP, UPR 8641, 33600 Pessac (France)

^d Univ. Bordeaux, CRPP, UPR 8641, 33600 Pessac (France)

Contributions: [‡] These authors contributed equally. S. A. Yao first synthesized complex **1**. I. Infante and J. F. Berry performed CASSCF and DFT calculations, respectively. E. A. Hillard and R. Clérac collected and modeled magnetic data. All other work was performed by A. R. Corcos.

7.1 Abstract.

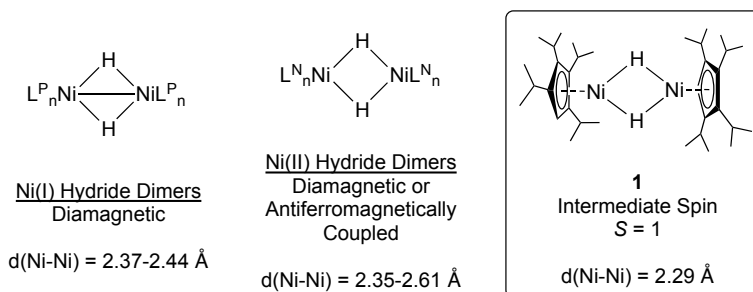
The nickel hydride complex [Cp'Ni(μ-H)]₂ (**1**, Cp' = 1,2,3,4-tetraisopropylcyclopentadienyl) is found to have a strikingly short Ni–Ni distance of 2.28638(3) Å. Variable temperature and variable field magnetic susceptibility measurements indicate an unexpected triplet ground state for **1** with a large zero-field splitting of +90 K (63 cm⁻¹). Electronic structure calculations (DFT and CASSCF/CASPT2) explain this ground state as arising from half occupation of two nearly degenerate Ni–Ni π* orbitals.

7.2 Introduction.

Nickel hydride compounds are prominent in synthetic¹⁻¹⁴ and biological¹⁵⁻¹⁹ catalysis. The diamond-shaped Ni₂(μ-H)₂ core is an important structural motif (Chart 1),^{20-27,28-31} and it can

be supported by a variety of P- or N-donor ligands (denoted L^P or L^N , respectively) that strongly influence its electronic structure. Binuclear $[L^P\text{Ni}(\mu\text{-H})_2]$ compounds, where L^P is a neutral chelating diphosphine, are diamagnetic due to the presence of a Ni(I)–Ni(I) bond with typical Ni–Ni bond lengths of 2.41 Å.²⁰⁻²⁷ Here, the local Ni(I) spin states (i.e., $S_{\text{Ni}} = 1/2$) strongly couple together antiferromagnetically to yield a singlet $S_G = 0$ ground spin state for the complex ($\chi T = 0 \text{ cm}^3 \text{ K mol}^{-1}$; here χ is the molar magnetic susceptibility and T is temperature). In contrast, $\text{Ni}_2(\mu\text{-H})_2$ complexes supported by anionic or neutral L^N ligands contain Ni(II) ions that display either a local low-spin ($S_{\text{Ni}} = 0$) or high spin ($S_{\text{Ni}} = 1$) configuration depending on their geometry.²⁸⁻³¹ In complexes with $S_{\text{Ni}} = 1$, weak antiferromagnetic exchange coupling occurs between the two ions leading to an $S_G = 0$ ground spin state for the complex. However, as the exchange coupling is small, at room temperature (rt) the two Ni(II) ions appear uncoupled from each other, leading to a total χT value of $\sim 2.0 \text{ cm}^3 \text{ K mol}^{-1}$, i.e., the sum of the two metal ion site magnetic moments. We report here the first $\text{Ni}_2(\mu\text{-H})_2$ binuclear complex bearing cyclopentadienyl (Cp) ligands. It has magnetic properties midway between those of known compounds ($\chi T \approx 1.0 \text{ cm}^3 \text{ K mol}^{-1}$) which indicates an unexpected “intermediate spin” $S_G = 1$ ground state and thus represents a new and unexpected electronic state available to $\text{Ni}_2(\mu\text{-H})_2$ compounds.

Chart 7.1 $\text{Ni}_2(\mu\text{-H})_2$ Complexes.



7.3 Results and Discussion.

Known Ni hydride complexes supported only by Cp ligands are polynuclear clusters, e.g., (CpNi)₄H₃.³²⁻³⁵ By utilizing the bulky 1,2,3,4-tetraisopropylcyclopentadienyl (Cp') ligand, first reported by Sitzmann,³⁶ it was possible to synthesize the binuclear complex [Cp'Ni(μ-H)]₂, **1**, as a dark orange-red species. It was prepared at -17 °C by mixing NaCp' and NiBr₂·DME in THF, followed by addition of NaH, removal of solvent, and extraction into pentane. The first step of the reaction is identical to the method reported by Sitzmann et al. to prepare [Cp'Ni(μ-Br)]₂ (**2**).³⁷ Thus, **2** is likely an intermediate in the formation of **1**. Compound **1** is soluble in THF, pentane, benzene, and toluene and is extremely sensitive to water, which causes a striking color change to dark forest green, attributable to an unidentified hydrolysis product.

In the crystal structure of **1**, the molecules initially appeared to be of Cp'Ni–NiCp' having an unsupported Ni–Ni bond. We were, however, able to locate bridging hydride ligands in the positions shown in Figure 7.1, in agreement with mass spectral data indicating that **1** is a dihydride (*m/z* = 584.26). The Ni···Ni distance in **1**, 2.28638(3) Å, is shorter than in any other binuclear Ni(II) complex except for the Ni=Ni (double bond) distance of 2.28 Å in [C(SiMe₃)(PMes₃)₂]₂Ni₂Cl₂.³⁸ The Ni···Ni distance in **1** is significantly longer than the calculated Ni≡Ni (triple bond) distance of 2.06 Å for the hypothetical [CpNi]₂ molecule,³⁹ but similar to the Co–Co distance of 2.249(1) Å in Cp*₂Co₂(μ-H)₃.⁴⁰ Despite the inherent uncertainty of the H atom positions derived from X-ray data, we may infer a planar Ni₂(μ-H)₂ core from the C₅···Ni–Ni angles of ~178°, where C₅ denotes the Cp' centroid. For the series of known [Cp'Ni(μ-X)]₂ compounds (X = Br, S, Se, Te, and OAr (Ar = 2,6-dimethylphenyl)), Ni···Ni separations > 3.0 Å indicate little direct Ni–Ni bonding.^{37,41-43} The [Cp'Ni(μ-CO)]₂ complex with Ni–Ni = 2.39 Å is

proposed to have a Ni(I)–Ni(I) bond,⁴⁴ and therefore the possibility of direct Ni–Ni orbital overlap may also be considered for **1**.

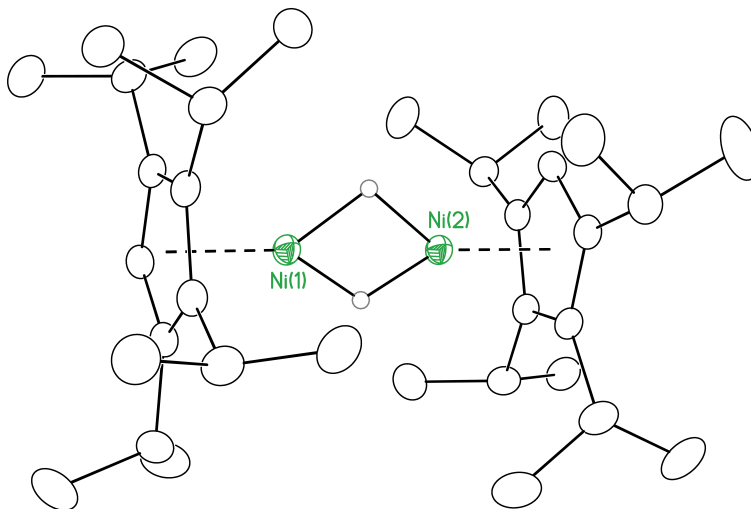


Figure 7.1 Crystal structure of **1** with thermal ellipsoids shown at the 50% probability level. All H atoms, except for the bridging hydride ligands, are omitted for clarity.

The ^1H NMR spectrum of **1** shows four major paramagnetically shifted signals at 10, 13, 14, and 20 ppm (Figure S7.1), attributed to the isopropyl methyl resonances as discussed in an NMR investigation of **2**.⁴⁵ Compound **1** displays an intense band in its absorption spectrum at 505 nm ($\epsilon = 11,000 \text{ cm}^{-1} \text{ M}^{-1}$, Figure S7.2) which is somewhat lower in energy than in the case of other $[\text{Cp}'\text{Ni}(\mu\text{-X})_2]$ compounds.

Magnetic susceptibility measurements on **1** revealed a χT product of $1.08 \text{ cm}^3 \text{ K mol}^{-1}$ at room temperature that plummets below 50 K. We tested two possible causes for the observed magnetic behavior: intracomplex antiferromagnetic coupling between the two $S_{\text{Ni}} = 1$ Ni(II) spin centers, which would yield a singlet $S_{\text{G}} = 0$ ground spin state, or a large magnetic anisotropy of the system as a whole, with an unexpected triplet ground state ($S_{\text{G}} = 1$). The room temperature

χT product is far from the expected value for two non-interacting $S_{\text{Ni}} = 1$ Ni(II) centers ($2.0 \text{ cm}^3 \text{ K mol}^{-1}$ for $g = 2$), casting doubt on the antiferromagnetic coupling interpretation. The data were nevertheless fitted to a model using the isotropic $S_{\text{Ni}} = 1$ spin dimer Heisenberg Hamiltonian: $H = -2JS_1 \cdot S_2$, where J is the Ni–Ni magnetic interaction and $S_1 = S_2 = S_{\text{Ni}} = 1$.⁴⁶ Although the data fit this model well from a mathematical standpoint (Figure 7.2, blue line), giving $J/k_B = -8.4(7)$ K, the resulting $g = 1.50(5)$ makes little physical sense, as g values greater than 2.00 are seen in Ni(II)–Cp complexes.^{37,47–50} Furthermore, a simulation^{51,52} of an $S_1 = S_2 = 1$ spin dimer using the parameters found from the χT versus T fit is inconsistent with the field-dependent magnetization (M) data; the simulation only begins to show an increase in M at very high field (> 6 T, Figure 7.2, inset, blue line).

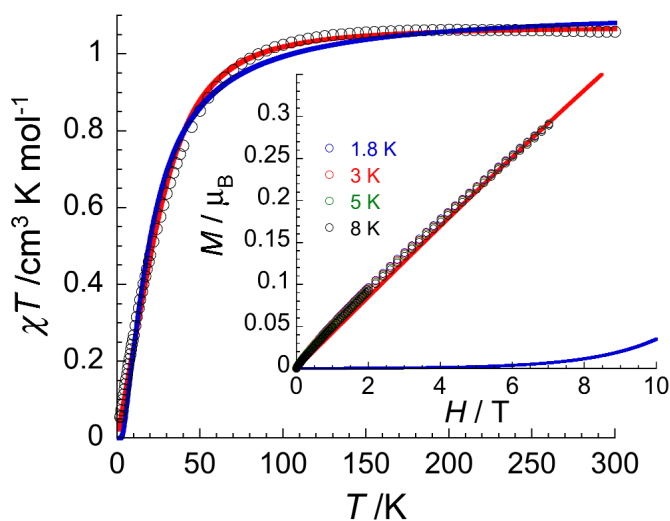


Figure 7.2 Temperature dependence of the χT product (χ is the magnetic susceptibility equal to M/H per mole of **1** at 1000 Oe) between 1.8 and 270 K for a polycrystalline sample of **1**. Solid lines are the fits using an $S_{\text{Ni}} = 1$ spin dimer model (see text, blue line) and the $S_{\text{G}} = 1$ ZFS model (see text, red line); Inset: M vs H data with numerical simulations using the parameters: (i) $S_1 = S_2 = 1$, $g = 1.50$ and $J/k_B = -8.4$ (blue line) and (ii) $S_{\text{G}} = 1$, $g = 2.07$ and $D/k_B = +90$ K (red line).

We therefore tested the unprecedented possibility of an $S_G = 1$ ground spin state for the $\text{Ni}_2(\mu\text{-H})_2$ core by fitting the χT data using a model that includes axial zero-field splitting (ZFS) based on the Hamiltonian: $\mathbf{H} = D \cdot S_z^2$, where D is the axial ZFS parameter and $S_z = 1$.⁵³ This model gave a more reasonable g value of 2.07(5) and $D/k_B = +90(5)$ K (+63(3) cm^{-1}) (Figure 7.2, red line). Moreover, the simulation of the M vs H data with these g and D/k_B values is in excellent agreement with the experimental data (Figure 7.2, inset, red line). Thus, the magnetic data clearly indicate a novel triplet ground state for **1**.

To examine the electronic basis for the unusual magnetic spin state of **1**, we utilized a molecular orbital analysis. Here we take the Ni–Ni vector as the z axis in a molecular coordinate system with the $\text{Ni}_2(\mu\text{-H})_2$ core occupying the yz plane. The typical $[\text{Cp}'\text{Ni}]^+$ orbital ordering of $d_{xy}, d_{x^2-y^2} < d_z^2 \ll d_{xz}, d_{yz}$, shown in the column (a) of Figure 7.3, is split by Ni–Ni orbital overlap to yield Ni_2 orbitals of σ, π , and δ symmetry in a $[\text{Cp}'\text{Ni}\cdots\text{NiCp}']^{2+}$ pair (Figure 7.3.b).

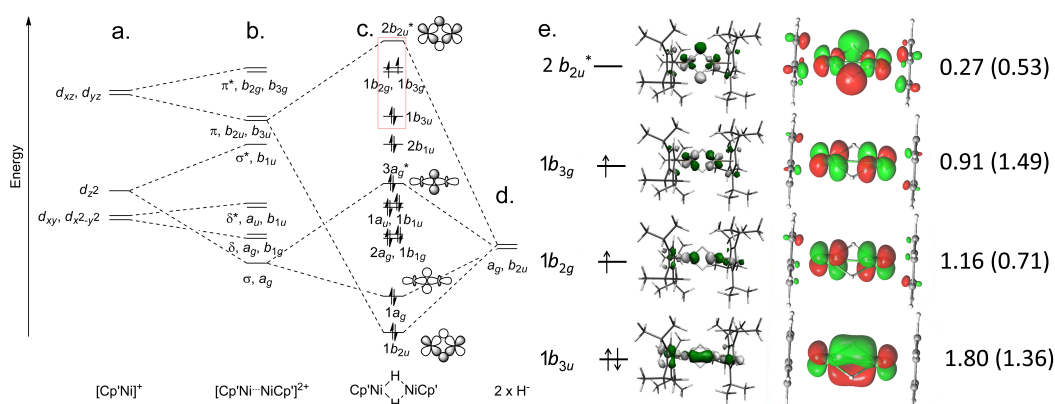


Figure 7.3 (a – d) Molecular orbital analysis of **1** assuming D_{2h} symmetry with the $\text{Ni}_2(\mu\text{-H})_2$ core occupying the yz plane. (e) Frontier orbitals of **1**, in detail from the red boxed region in (c). The green/gray orbitals are derived from DFT/B3LYP/TZVP calculations, and those in green/red derive from CASSCF calculations. The numbers listed next to each CASSCF orbital are the occupation numbers for the triplet (singlet) state.

To consider bonding between the Ni₂ unit and the two hydride ligands (in *D*_{2h} symmetry), the a_g H 1s combination (Figure 3d) is best suited to interact with the Ni–Ni σ bonding a_g combination of Ni d_{z²} orbitals. This interaction will lead to a low-energy orbital that has bonding character between all four of the core atoms (1a_g) as well as a higher energy orbital that has Ni–Ni bonding character but Ni–H antibonding character (3a_g*). The H 1s combination of b_{2u} symmetry can only interact with the Ni–Ni π-bonding b_{2u} combination in which the d_{yz} orbitals lie in the plane with the H atoms. Thus, a low energy Ni₂(μ-H)₂ bonding orbital, 1b_{2u}, will be formed as well as a high-energy antibonding combination, 2b_{2u}*, which is raised in energy above the Ni₂ π* orbitals. Filling the resulting orbital manifold, given in column (c) of Figure 7.3, with the 20 electrons of the [Ni₂H₂]²⁺ unit leads immediately to an explanation for the triplet ground state for **1** due to the filling of electrons up to the Ni–Ni π* orbitals of b_{2g} and b_{3g} symmetry. Since these b_{2g} and b_{3g} orbitals cannot interact with the H atoms, they remain quasi-degenerate. Thus, placing two electrons into these orbitals leads to the overall ³B_{1g} ground state.

The results of density functional theory (DFT) and *ab initio* CASSCF/CASPT2 calculations on **1** are consistent with the above orbital analysis. Of primary interest are the frontier orbitals: 1b_{3u}, 1b_{2g}, 1b_{3g}, and 2b_{2u}*. These orbitals are depicted in Figure 7.3.e, where the occupied 1b_{3u} orbital can clearly be seen to have Ni–Ni π bonding character. The SOMOs 1b_{2g} and 1b_{3g} are Ni–Ni π* orbitals, and they are indeed quasi-degenerate, having a calculated splitting of only 57 cm⁻¹ (82 K). The LUMO, 2b_{2u}*, is, as expected, the Ni₂(μ-H)₂ antibonding orbital that would have Ni–Ni π bonding character if the hydride ligands were not present. The antibonding interaction with the hydride ligands has raised this orbital by roughly 1000 cm⁻¹ above 1b_{3u}. The computed ground state wave function of **1** at the CASSCF/CASPT2 level was found to be composed of 70% |1b_{3u}²1b_{2g}¹1b_{3g}¹2b_{2u}⁰> and 12% |1b_{3u}¹1b_{2g}¹1b_{3g}²2b_{2u}⁰> character.

This multi-reference character leads to the following occupation numbers

$|1b_{3u}^{1.80}1b_{2g}^{1.16}1b_{3g}^{0.91}2b_{2u}^{0.27}\rangle$, which suggests significant static electron correlation among these four orbitals, in agreement with the near-degeneracy seen in the DFT results. This aspect is further reflected in the position of the corresponding singlet 1A_g state lying at only 900 cm^{-1} above the ground state. The 1A_g state has stronger multi-reference character: 48% $|1b_{3u}^21b_{2g}^01b_{3g}^22b_{2u}^0\rangle + 16\% |1b_{3u}^01b_{2g}^21b_{3g}^22b_{2u}^0\rangle + 8\% |1b_{3u}^21b_{2g}^21b_{3g}^02b_{2u}^0\rangle$, plus other minor contributions; the occupation numbers are $|1b_{3u}^{1.36}1b_{2g}^{0.71}1b_{3g}^{1.49}2b_{2u}^{0.53}\rangle$. Mulliken spin-density analysis of the $^3B_{1g}$ state shows that 0.98 electrons are localized on each Ni center, suggesting that the spin density is distributed equally across both Ni atoms as expected for the half-occupation of the two Ni–Ni π^* orbitals.

For the $1b_{3u}$ Ni–Ni π bonding orbital, the corresponding π antibonding orbitals ($1b_{2g}$ and $1b_{3g}$) are each half-filled. Therefore, there is a net 0.5 π bonding interaction in one plane that is counterbalanced by 0.5 π^* antibonding interaction in an orthogonal plane, and it makes little sense to discuss any localized Ni–Ni bonding in **1**. However, we note that the $Ni_2(\mu-H)_2$ bonding orbital $1b_{2u}$ is doubly occupied, when its antibonding counterpart $2b_{2u}^*$ is nearly empty (occupancy of 0.27 electrons). Thus, we may describe a four-center bond that holds together the $Ni_2(\mu-H)_2$ core, which is reflected in calculated Ni–Ni bond orders of 0.5–0.8.

7.4 Conclusion.

In summary, we report the first example of a diamond core $Ni_2(\mu-H)_2$ complex supported by cyclopentadienyl ligands. This dinuclear complex displays a short Ni–Ni distance of 2.29 \AA that results in the four frontier orbitals of the molecule being within 1000 cm^{-1} of each other. This near-degeneracy leads to a triplet ground spin state for the molecule and a low-lying singlet

excited state. The two unpaired electrons in the d_{xz} and d_{yz} orbitals provide a strong, cylindrically symmetric spin distribution, leading to strong axial magnetic anisotropy manifested in axial ZFS on the order of 60 cm^{-1} . It is somewhat similar to the case of metal–metal bonded $\text{Ru}_2(\text{II},\text{II})$ compounds with two half-occupied π^* orbitals, which also have large ($> 100\text{ cm}^{-1}$) axial ZFS.^{54,55} These features could be useful design principles for preparing molecules with high magnetic anisotropy.

7.5 Acknowledgements.

Dedicated to Prof. Larry F. Dahl on the occasion of his 85th birthday. We thank the following funding agencies for their support of this work: NSF CHE-1041748 (J.F.B.), NSF DGE-0718123 (A.R.C.), DOE DE-FG02-10ER16204 (J.F.B.), NIH NCRR 1S10RR024601-01 (mass spec.), CNRS, the Univ. Bordeaux the Aquitaine Region and the ANR (R.C., E.H.).

7.6 Supplementary Information.

Materials and Methods. All operations were carried out using standard Schlenk and glovebox techniques under an N_2 atmosphere unless otherwise stated. Solvents diethyl ether (Et_2O), acetonitrile (CH_3CN), and hexanes were purified using a Vacuum Atmospheres solvent purification system. THF and anhydrous pentane (purchased from Sigma-Aldrich) were each distilled over CaH_2 , degassed, and passed through a plug of activated alumina prior to use. $\text{NiBr}_2\cdot\text{DME}$ and NaH were purchased from Sigma-Aldrich and used as received. 1,2,3,4-tetraisopropylcyclopentadiene was prepared according to a literature procedure⁵⁶ and deprotonated with sodium amide.³⁷

$[Cp'Ni(\mu-H)]_2$ (**1**). NaCp' (61.7 mg, 0.241 mmol), NaH (18.4 mg, 0.767 mmol), and NiBr₂·DME (74.6 mg, 0.242 mmol) were each separately dissolved or suspended in 6 mL of THF and cooled to -17 °C in a dry ice/ethylene glycol bath. The NaCp' solution was first slowly added to the NiBr₂·DME suspension and allowed to stir for 30 minutes, during which time the suspension turned deep reddish-brown in color. The NaH suspension was subsequently added dropwise, and the resulting mixture was stirred at -17 °C for an additional 30 minutes and then warmed to room temperature and stirred for 22 hours; this resulted in the red-brown solution turning very dark brown in color. The solvent was removed in vacuo and the orange-red residue was extracted with pentane and filtered through a fine frit. After removing some of the solvent to form a saturated solution, the filtrate was placed in a -80 °C freezer and allowed to crystallize. Isolated yield: 56.2 mg (39.7%). $[Cp'Ni(\mu-H)]_2$ (**1**) UV-Vis (pentane): λ_{max} (ϵ) = 471 nm (7200), 505.5 nm (11000). MALDI-TOF MS m/z (calc.) 584.24; (found) 584.26. ¹H NMR (C₆D₆, δ , ppm): 10.09 (s, br), 13.19 (s, br), 13.96 (s, br), 19.77 (s, br). Elemental Analysis for C₃₄H₆₀Ni₂ (calc) C 69.66, H 10.31; (found) C 69.92, H 10.02.

Physical Measurement. ¹H NMR spectra were recorded at an operating frequency of 300 MHz on Bruker spectrometers in deuterated benzene. Chemical shifts are reported in parts per million. Matrix-assisted laser desorption/ionization (MALDI) time-of flight (TOF) mass spectrometry data was obtained using an anthracene matrix on a Bruker ULTRAFLEX[®] III mass spectrometer equipped with a SmartBeam[®] laser. UV-Vis- spectra were obtained using a StellarNet Miniature BLUE-wave UV-Vis dip probe with a Tungsten-Krypton light source and a 10 mm path length tip. Elemental analysis was done by Midwest Microlab, LLC in Indiana, USA. Magnetic susceptibility measurements were obtained using a Quantum Design MPMS-XL SQUID

magnetometer. The measurements were performed on a freshly filtered polycrystalline sample of **1** (11.8 mg) introduced in a sealed polyethylene bag ($3 \times 0.5 \times 0.02$ cm). The dc measurements were conducted from 340 to 1.8 K at 1000 Oe and from 0 to 7 T at 1.8, 3, 5 and 8 K. A M vs H measurement was performed at 100 K to confirm the absence of ferromagnetic impurities.

X-ray Crystallography. Crystallographic data were measured at the Molecular Structure Laboratory of the Chemistry Department of the University of Wisconsin-Madison. Crystals were selected under oil at room temperature and attached to the tip of a MiTeGen MicroMount. The crystals were mounted in a stream of cold nitrogen at 100 K and centered in the X-ray beam using a video monitoring system. The crystal evaluation and data collection were performed on a Bruker Quazar SMART APEX-II diffractometer with Mo $K\alpha$ ($\lambda = 0.71073$ Å) radiation. The data were collected using a routine to survey reciprocal space and were indexed by the SMART program. The structures were solved using direct methods and refined by least-squares refinement on F^2 followed by difference Fourier synthesis. All hydrogen atoms, except for the hydride positions on complex **1**, were included in the final structure factor calculation at idealized positions and allowed to ride on the neighboring atoms with relative isotropic displacement coefficients. The positions and (isotropic) thermal parameters of the hydride ligands in **1** were allowed to refine freely.

Magnetic Susceptibility Measurements. The theoretical expressions of the magnetic susceptibility can be estimated by applying the van Vleck equation in the weak field approximation for the $S = 1$ spin dimer model (see text):

$$\chi_{(\text{dimer})} = \frac{Ng^2\mu_B^2}{k_B T} \frac{2\exp(2x) + 10\exp(6x)}{1 + 3\exp(2x) + 5\exp(6x)} \quad \text{Eq. 1}$$

where $x = J/k_B T$.

The analytical expression for the $S = 1$ ZFS model (see text) is:

$$\chi = (2M_{xy} + M_z)/3H \quad \text{Eq. 2}$$

$$M_{xy} = \frac{Ng\mu_B G}{\sqrt{D^2/4 + G^2}} \left[\frac{2\sinh\left(\frac{\sqrt{D^2/4 + G^2}}{k_B T}\right)}{2\cosh\left(\frac{\sqrt{D^2/4 + G^2}}{k_B T}\right) + \exp\left(-\frac{D}{2k_B T}\right)} \right] \text{ and}$$

with:

$$M_z = Ng\mu_B \left[\frac{2\sinh\left(\frac{G}{k_B T}\right)}{2\cosh\left(\frac{G}{k_B T}\right) + \exp\left(\frac{D}{k_B T}\right)} \right]$$

where $G = g\mu_B H$.

Computational Details. The molecular structure of **1** was optimized in singlet and triplet states using the crystal structure as a starting point using density functional theory (DFT) using the BP86^{57,58} functional and a TZVP⁵⁹⁻⁶¹ basis. These geometries were used for single-point calculations using the hybrid B3LYP⁶²⁻⁶⁴ functional. The ORCA program⁶⁵ was used for all DFT calculations. For CASSCF calculations, the Cp' ligand was truncated to Cp and an initial geometry optimization was performed with the PBE exchange-correlation functional and a triple-

zeta TZ2P basis set using the ADF suite of programs.⁶⁶ This geometry was used for a complete active space (CAS) SCF calculation⁶⁷⁻⁶⁹ followed by a second-order perturbation theory (CASPT2) calculation.^{70,71} Scalar relativistic effects were included using the Douglas-Kroll-Hess Hamiltonian and a relativistic ANO-RCC basis set of VTZP quality,^{72,73} as implemented in the MOLCAS 7.6 package.⁷⁴ Spin-orbit coupling was included using the complete active space interaction (CASSI) method, which employs an effective one-electron spin-orbit (SO) Hamiltonian based on the mean field approximation of the two electronic part.⁷⁵ This approach has been successful in studying many metal-metal bonded systems.⁷⁶⁻⁸⁰

To choose the most suitable active space for CASSCF calculations we first imposed C_{2h} symmetry on **1** and divided the system into two fragments, a $[\text{Ni}(\mu\text{-H})]_2^{2+}$ fragment and a Cp_2^{2-} fragment. This division is purely arbitrary and is applied only for describing how we selected the CAS. The ideal active space of the $[\text{Ni}(\mu\text{-H})]_2^{2+}$ fragment would be composed of 14 molecular orbitals (MOs): 12 result from a linear combination of the 4s and five 3d orbitals localized on each of the nickel atoms, and the remaining two MOs from the 1s orbitals of the two hydrogen atoms. The active space for $[\text{Ni}(\mu\text{-H})]_2^{2+}$ would also contain a total of 20 electrons: 10 valence electrons from each nickel atom (electronic configuration $3d^8 4s^2$), plus one electron from each hydrogen 1s orbital, minus two electrons (in order to satisfy the oxidation state of the fragment). In total we would have a CAS of (20e/14o) from which we remove two filled Ni–H bonding orbitals that are very low in energy that derive from H 1s overlap with the Ni 4s and $3d_z^2$ orbitals. Additionally, for the Cp_2^{2-} fragment, the most important valence orbitals are those with the electrons delocalized on the out-of-plane 2p orbitals bearing one nodal plane (8e/4o) since these MOs are most suitable to interact with the valence $[\text{Ni}(\mu\text{-H})]_2^{2+}$ orbitals. The final active

space of $(16e/12o) + (8e/4o) = (24e/16o)$ is computationally affordable and thus has been chosen for this work.

At the CASPT2 step we have also included the semi-valence 3s and 3p orbitals from the Ni atoms and the 2s and the remaining 2p orbitals on each carbon atom, for a total of 88 electrons correlated in all the virtual space. We have calculated five excited states for each irreducible representation, i.e. a total of 20 transition energies for the singlet and 20 transition energies for the triplet. The basis-set employed on each atom is a triple-zeta ANO-RCC-VTZP contracted to $(6s5p3d2f1g)$ for Ni, $(3s2p1d)$ for H, and $(4s3p2d1f)$ for C.⁸¹ All CASSCF/CASPT2 computations have been carried out using the MOLCAS 7.6 package.⁷⁴

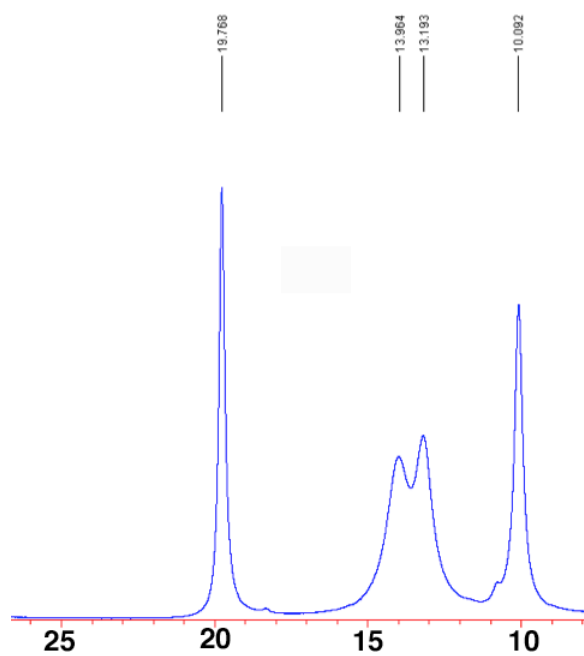


Figure S7.1 ^1H NMR spectrum of **1** in C_6D_6 . The diamagnetic region (not shown) contains only solvent signals not relevant to **1**.

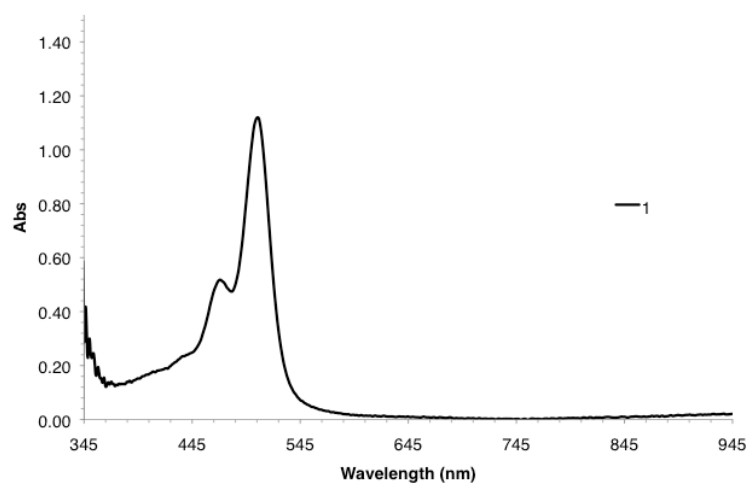


Figure S7.2 UV-Vis spectrum of $[\text{Cp}'\text{Ni}(\mu\text{-H})]_2$ (**1**) in pentane.

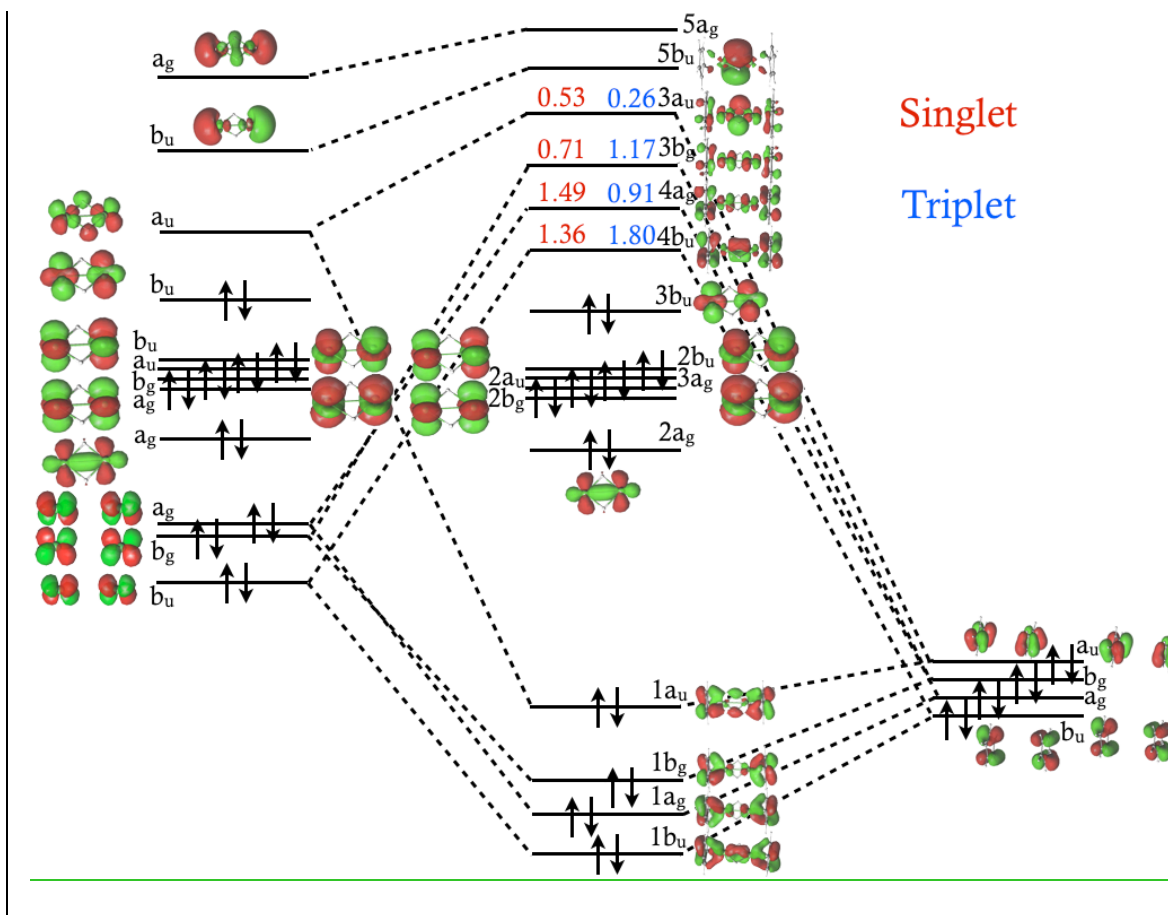


Figure S7.3 CASSCF orbital contributions for $[\text{Ni}(\mu\text{-H})]_2^{2+}$ fragment (left) and Cp_2^{2-} fragment (right). In the center is shown the complete bonding manifold.

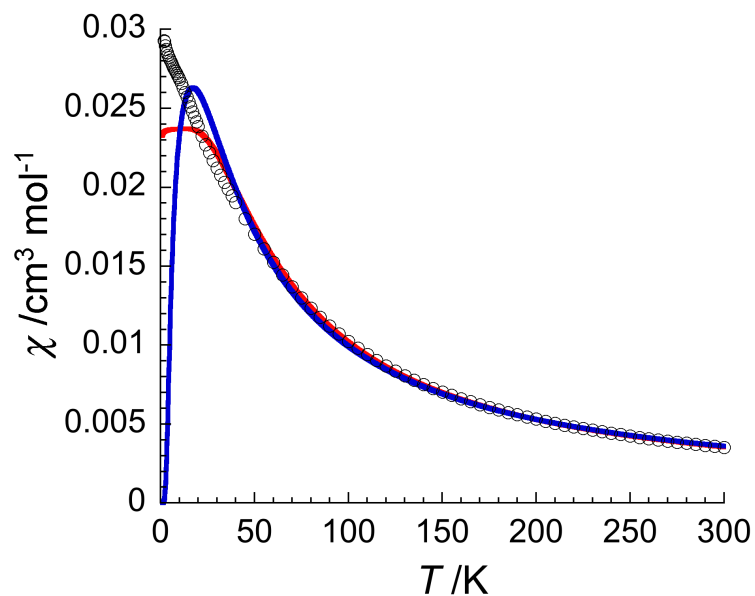


Figure S7.4 Temperature dependence of χ (χ is the magnetic susceptibility equal to M/H per mole of **1** at 1000 Oe) between 1.8 and 270 K for polycrystalline sample of **1**. Solid lines are the fits using $S_{\text{Ni}} = 1$ spin dimer model (see text, blue line) and the $S_{\text{G}} = 1$ ZFS model (see text, red line).

Table S7.1 Summary of X-ray crystallographic data for complexes **1** and **2**.

Compound	1	2
Formula	C ₃₄ H ₆₀ Ni ₂	C ₃₄ H ₅₈ Br ₂ Ni ₂
Formula Weight g/mol	586.24	744.04
Temperature (K)	100(1)	100(1)
Crystal system	Monoclinic	Triclinic
Space Group	<i>P</i> 2 ₁ /n	<i>P</i> -1
<i>a</i> , Å	13.6471(2)	12.5016(3)
<i>b</i> , Å	15.0512(3)	18.0745(4)
<i>c</i> , Å	16.2264(3)	20.0716(5)
<i>α</i> °	90	72.074(1)
<i>β</i> °	99.0936(9)	88.776(1)
<i>γ</i> °	90	84.763(1)
<i>V</i> , Å ³	3291.1(1)	4297.1(2)
<i>Z</i>	4	5
<i>R</i> ¹ ^a , <i>wR</i> ² ^b (<i>I</i> < 2σ(<i>I</i>))	0.0330, 0.0900	0.0350, 0.0633
<i>R</i> ¹ ^a , <i>wR</i> ² ^b (all data)	0.0353, 0.0922	0.0804, 0.0689

^a $R1 = \sum ||F_o| - |F_c|| / \sum |F_o|$. ^b $wR2 = [\sum [w(F_o^2 - F_c^2)^2] / \sum [w(F_o^2)^2]]^{1/2}$, $w = 1/\sigma^2(F_o^2) + (aP)^2 + bP$, where $P = [\max(0 \text{ or } F_o^2) + 2(F_c^2)]/3$.

Table S7.2 Selected bond distances for complex **1**, **2**, and those of previously reported [Cp'Ni(μ -X)]₂ complexes.^{37,41-44} The geometry for **1** is computed at the DFT/BP86/TZVP level of theory.

Formula	[Cp'Ni(μ -H)] ₂ (1)	1 (DFT)	[Cp'Ni(μ -Br)] ₂ (2)	[Cp'Ni(μ -S)] ₂	[Cp'Ni(μ -Se)] ₂	[Cp'Ni(μ -Te)] ₂	[Cp'Ni(μ -CO)] ₂	Cp'Ni ₂ (OAr) ₂
Ni-C ₅ plane, Å	1.74068(2), 1.73856(2)	1.779	1.7920[4]	1.725(2)	1.728(2)	1.736[2]	1.74	1.828
Ni···Ni, Å	2.28638(3)	2.33	3.4661[2]	3.225(1)	3.438(3)	3.771(3)	2.387(4)	3.134[1]
Ni-X, Å	1.34765[2], 1.43382[2]	1.61	2.4451[4]	2.137[1]	2.254[2]	2.440[2]	1.84(2), 1.86(2)	1.984[2]
X···X, Å	1.57915(2)	2.21	3.4066[4]	2.806(1)	2.915(3)	3.115(3)	NA	NA
Ni-X-Ni, °	105.741(1), 116.0501(9)	92.5	90.58[2]	97.96(2)	99.40(1)	100.44(2)	80.1(8)	104.4[2]
X-Ni-X, °	68.709(1), 69.4976(9)	86.4	87.88[1]	82.04(2)	80.60(1)	79.86(2)	99.9(8)	75.4(1)
Ref.	This work	This work	This work	41, 43	41, 42, 43	41, 43	44	37

Table S7.3 Total energies, in Hartrees, from DFT calculations on **1** and CASSCF/CASPT2 calculations on $\text{Cp}_2\text{Ni}_2(\mu\text{-H})_2$.

Singlet State:	BP86	−4349.332273282906
	B3LYP	−4347.724836177746
	B3LYP BS(1,1)	−4347.726202199910
	CASSCF	−3423.84040505
	CASPT2	−3426.50373281
Triplet State:	BP86	−4349.336828865834
	B3LYP	−4347.729488370999
	CASSCF	−3423.84498403
	CASPT2	−3426.50447369

References.

- (1) Kokes, R. J.; Emmett, P. H. *J. Am. Chem. Soc.* **1959**, *81*, 5032.
- (2) Svoboda, P.; Sedimayer, P.; Hetflejš, J. *Collect. Czech. Chem. Commun.* **1973**, *38*, 1783.
- (3) Iyer, S.; Varghese, J. P. *J. Chem. Soc., Chem. Commun.* **1995**, 465.
- (4) Henderson, R. A. *J. Chem. Res.* **2002**, *2002*, 407.
- (5) Chen, W.; Shimada, S.; Tanaka, M.; Kobayashi, Y.; Saigo, K. *J. Am. Chem. Soc.* **2004**, *126*, 8072.
- (6) Clement, N. D.; Cavell, K. J.; Jones, C.; Elsevier, C. J. *Angew. Chem. Int. Ed.* **2004**, *43*, 1277.
- (7) Steinke, T.; Gemel, C.; Cokoja, M.; Winter, M.; Fischer, R. A. *Angew. Chem. Int. Ed.* **2004**, *43*, 2299.
- (8) Kogut, E.; Zeller, A.; Warren, T. H.; Strassner, T. *J. Am. Chem. Soc.* **2004**, *126*, 11984.
- (9) Liang, L.-C.; Chien, P.-S.; Lee, P.-Y. *Organometallics* **2008**, *27*, 3082.
- (10) Yang, J. Y.; Bullock, R. M.; Shaw, W. J.; Twamley, B.; Frazee, K.; DuBois, M. R.; DuBois, D. L. *J. Am. Chem. Soc.* **2009**, *131*, 5935.
- (11) Chakraborty, S.; Krause, J. A.; Guan, H. *Organometallics* **2009**, *28*, 582.
- (12) Tran, B. L.; Pink, M.; Mindiola, D. J. *Organometallics* **2009**, *28*, 2234.
- (13) DuBois, D. L.; Bullock, R. M. *Eur. J. Inorg. Chem.* **2011**, *2011*, 1017.
- (14) Alonso, F.; Riente, P.; Yus, M. *Acc. Chem. Res.* **2011**, *44*, 379.
- (15) Volbeda, A.; Charon, M.-H.; Piras, C.; Hatchikian, E. C.; Frey, M.; Fontecilla-Camps, J. C. *Nature* **1995**, *373*, 580.
- (16) Volbeda, A.; Garcin, E.; Piras, C.; de Lacey, A. L.; Fernandez, V. M.; Hatchikian, E. C.; Frey, M.; Fontecilla-Camps, J. C. *J. Am. Chem. Soc.* **1996**, *118*, 12989.
- (17) Pardo, A.; De Lacey, A. L.; Fernández, V. M.; Fan, H.-J.; Fan, Y.; Hall, M. B. *J Biol Inorg. Chem.* **2006**, *11*, 286.
- (18) Barton, B. E.; Whaley, C. M.; Rauchfuss, T. B.; Gray, D. L. *J. Am. Chem. Soc.* **2009**, *131*, 6942.

- (19) Barton, B. E.; Rauchfuss, T. B. *J. Am. Chem. Soc.* **2010**, *132*, 14877.
- (20) Jonas, K.; Wilke, G. *Angew. Chem. Int. Ed.* **1970**, *9*, 312.
- (21) Barnett, B. L.; Kruger, C.; Tsay, Y.-H.; Summerville, R. H.; Hoffmann, R. *Chem. Ber.* **1977**, *110*, 3900.
- (22) Vicic, D. A.; Jones, W. D. *J. Am. Chem. Soc.* **1997**, *119*, 10855.
- (23) Fryzuk, M. D.; Clentsmith, G. K. B.; Leznoff, D. B.; Rettig, S. J.; Geib, S. J. *Inorg. Chim. Acta* **1997**, *265*, 169.
- (24) Bach, I.; Goddard, R.; Kopiske, C.; Seevogel, K.; Pörschke, K.-R. *Organometallics* **1999**, *18*, 10.
- (25) Crestani, M. G.; Muñoz-Hernández, M.; Arévalo, A.; Acosta-Ramírez, A.; García, J. J. *J. Am. Chem. Soc.* **2005**, *127*, 18066.
- (26) Li, T.; García, J. J.; Brennessel, W. W.; Jones, W. D. *Organometallics* **2010**, *29*, 2430.
- (27) Cornella, J.; Gómez-Bengoa, E.; Martin, R. *J. Am. Chem. Soc.* **2013**, *135*, 1997.
- (28) Pfirrmann, S.; Limberg, C.; Ziemer, B. *Dalton Trans.* **2008**, 6689.
- (29) Pfirrmann, S.; Limberg, C.; Herwig, C.; Knispel, C.; Braun, B.; Bill, E.; Stösser, R. *J. Am. Chem. Soc.* **2010**, *132*, 13684.
- (30) Matsumoto, T.; Nagahama, T.; Cho, J.; Hizume, T.; Suzuki, M.; Ogo, S. *Angew. Chem. Int. Ed.* **2011**, *50*, 10578.
- (31) Dong, Q.; Zhao, Y.; Su, Y.; Su, J.-H.; Wu, B.; Yang, X.-J. *Inorg. Chem.* **2012**, *51*, 13162.
- (32) Müller, J.; Dorner, H.; Huttner, G.; Lorenz, H. *Angew. Chem. Int. Ed.* **1973**, *12*, 1005.
- (33) Paquette, M. S.; Dahl, L. F. *J. Am. Chem. Soc.* **1980**, *102*, 6621.
- (34) Schneider, J. J.; Goddard, R.; Krüger, C.; Werner, S.; Metz, B. *Chem. Ber.* **1991**, *124*, 301.
- (35) Pasynkiewicz, S.; Buchowicz, W.; Pietrzykowski, A.; Głowiak, T. *J. Organomet. Chem.* **1997**, *536-537*, 249.
- (36) Sitzmann, H. *J. Organomet. Chem.* **1988**, *354*, 203.
- (37) Weismann, D.; Saurenz, D.; Boese, R.; Bläser, D.; Wolmershäuser, G.; Sun, Y.; Sitzmann, H. *Organometallics* **2011**, *30*, 6351.

- (38) Koenig, H.; Menu, M. J.; Dartiguenave, M.; Dartiguenave, Y.; Klein, H. F. *J. Am. Chem. Soc.* **1990**, *112*, 5351.
- (39) Xie, Y.; Schaefer, H. F.; King, R. B. *J. Am. Chem. Soc.* **2005**, *127*, 2818.
- (40) Kersten, J. L.; Rheingold, A. L.; Theopold, K. H.; Casey, C. P.; Widenhoefer, R. A.; Hop, C. E. C. A. *Angew. Chem. Int. Ed.* **1992**, *31*, 1341.
- (41) Sitzmann, H.; Saurenz, D.; Wolmershäuser, G.; Klein, A.; Boese, R. *Organometallics* **2001**, *20*, 700.
- (42) Yao, S. A.; Lancaster, K. M.; Götz, A. W.; DeBeer, S.; Berry, J. F. *Chem. Eur. J.* **2012**, *18*, 9179.
- (43) Yao, S. A.; Martin-Diaconescu, V.; Infante, I.; Lancaster, K. M.; Gotz, A. W.; DeBeer, S.; Berry, J. F. *J. Am. Chem. Soc.* **2015**, *137*, 4993.
- (44) Sitzmann, H.; Wolmershäuser, G. *Z. Naturforsch* **1995**, *50b*, 750.
- (45) Schär, M.; Saurenz, D.; Zimmer, F.; Schädlich, I.; Wolmershäuser, G.; Demeshko, S.; Meyer, F.; Sitzmann, H.; Heigl, O. M.; Köhler, F. H. *Organometallics* **2013**, *32*, 6298.
- (46) O'Connor, C. J. *Prog. Inorg. Chem.* **1982**, *29*, 203.
- (47) Baltzer, P.; Furrer, A.; Hulliger, J.; Stebler, A. *Inorg. Chem.* **1988**, *27*, 1543.
- (48) Brunker, T. J.; Green, J. C.; O'Hare, D. *Inorg. Chem.* **2003**, *42*, 4366.
- (49) Losi, S.; Rossi, F.; Laschi, F.; de Biani, F. F.; Zanello, P.; Buchalski, P.; Burakowska, K.; Piwowar, K.; Pasynkiewicz, S.; Pietrzykowski, A.; Suwińska, K.; Jerzykiewicz, L. *Inorg. Chem.* **2007**, *46*, 10659.
- (50) Trtica, S.; Meyer, E.; Prosenc, M. H.; Heck, J.; Böhnert, T.; Görlitz, D. *Eur. J. Inorg. Chem.* **2012**, *2012*, 4486.
- (51) Borrás-Almenar, J. J.; Clemente-Juan, J. M.; Coronado, E.; Tsukerblat, B. S. *Inorg. Chem.* **1999**, *38*, 6081.
- (52) Borrás-Almenar, J. J.; Clemente-Juan, J. M.; Coronado, E.; Tsukerblat, B. S. *J. Comput. Chem.* **2001**, *22*, 985.
- (53) Boča, R. *Coord. Chem. Rev.* **2004**, *248*, 757.
- (54) Miskowski, V. M.; Hopkins, M. D.; Winkler, J. R.; Gray, H. B. In *Inorganic Electronic Structure and Spectroscopy, Volume II: Applications and Case Studies*; Solomon, E. I., Lever, A. B. P., Eds.; John Wiley & Sons: 1999.

- (55) Cotton, F. A.; Murillo, C. A.; Walton, R. A. *Multiple Bonds Between Metal Atoms*; 3rd ed.; Springer Science and Business Media: New York, 2005.
- (56) Eckehard V. Dehmlow, C. B. *Z. Naturforsch* **1993**, 48b, 457.
- (57) Perdew, J. P.; Yue, W. *Phys. Rev. B* **1986**, 33, 8800.
- (58) Becke, A. D. *J. Chem. Phys.* **1993**, 98, 1372.
- (59) Schäfer, A.; Horn, H.; Ahlrichs, R. *J. Chem. Phys.* **1992**, 97, 2571.
- (60) Weigend, F.; Ahlrichs, R. *Phys. Chem. Chem. Phys.* **2005**, 7, 3297.
- (61) Seligson, A. L.; Cowan, R. L.; Trogler, W. C. *Inorg. Chem.* **1991**, 30, 3371.
- (62) Lee, C.; Yang, W.; Parr, R. G. *Phys. Rev. B* **1988**, 37, 785.
- (63) Becke, A. D. *Phys. Rev. A* **1988**, 38, 3098.
- (64) Becke, A. D. *J. Chem. Phys.* **1993**, 98, 5648.
- (65) ORCA: An ab Initio Density Functional and Semiempirical Program Package.
- (66) te Velde, G.; Bickelhaupt, F. M.; Baerends, E. J.; Fonseca Guerra, C.; van Gisbergen, S. J. A.; Snijders, J. G.; Ziegler, T. *J. Comput. Chem.* **2001**, 22, 931.
- (67) Roos, B. O.; Taylor, P. R.; Siegbahn, P. E. M. *Chem. Phys.* **1980**, 48, 157.
- (68) Siegbahn, P. E. M.; Heiberg, A.; Roos, B. O.; Levy, B. *Phys. Scr.* **1980**, 21, 323.
- (69) Siegbahn, P. E. M.; Almlöf, J.; Heiberg, A.; Roos, B. O. *J. Chem. Phys.* **1981**, 74, 2384.
- (70) Andersson, K.; Malmqvist, P.-Å.; Roos, B. O.; Sadlej, A. J.; Wolinski, K. *J. Phys. Chem.* **1990**, 94, 5483.
- (71) Andersson, K.; Malmqvist, P.-Å.; Roos, B. O. *J. Chem. Phys.* **1992**, 96, 1218-1226.
- (72) Douglas, M.; Kroll, N. M. *Ann. Phys.* **1974**, 82, 89.
- (73) Hess, B. A. *Phys. Rev. A* **1986**, 33, 3742.
- (74) Aquilante, F.; De Vico, L.; Ferré, N.; Ghigo, G.; Malmqvist, P.-Å.; Neogrády, P.; Pedersen, T. B.; Pitoňák, M.; Reiher, M.; Roos, B. O.; Serrano-Andrés, L.; Urban, M.; Veryazov, V.; Lindh, R. *J. Comput. Chem.* **2010**, 31, 224.
- (75) Malmqvist, P.-Å.; Roos, B. O.; Schimmelpfennig, B. *Chem. Phys. Lett.* **2002**, 357, 230.

- (76) Gagliardi, L.; Roos, B. O. *Nature* **2005**, 433, 848.
- (77) Brynda, M.; Gagliardi, L.; Widmark, P.-O.; Power, P. P.; Roos, B. O. *Angew. Chem. Int. Ed.* **2006**, 45, 3804.
- (78) Roos, B. O.; Borin, A. C.; Gagliardi, L. *Angew. Chem. Int. Ed.* **2007**, 46, 1469.
- (79) Ruipérez, F.; Ugalde, J. M.; Infante, I. *Inorg. Chem.* **2011**, 50, 9219.
- (80) Ruipérez, F.; Merino, G.; Ugalde, J. M.; Infante, I. *Inorg. Chem.* **2013**, 52, 2838.
- (81) Roos, B. O.; Lindh, R.; Malmqvist, P.-Å.; Veryazov, V.; Widmark, P.-O. *J. Phys. Chem. A* **2005**, 109, 6575.

Chapter 8

Oxygen Activation by Co(II) and a Redox Non-Innocent Ligand: Spectroscopic Characterization of a Radical – Co(II) – Superoxide Complex with Divergent Catalytic Reactivity

This chapter has been published:

Reprinted with permission from Amanda R. Corcos,^a Omar Villanueva,^b Richard C. Walroth,^c Savita K. Sharma,^b John Bacsá,^b Kyle M. Lancaster,^c Cora E. MacBeth,^b John F. Berry.^a *J. Am. Chem. Soc.* **2016**, *138*, 1796-1799. Copyright 2016 American Chemical Society

^a Department of Chemistry, University of Wisconsin–Madison, 1101 University Ave. Madison, WI 53706

^b Department of Chemistry, Emory University, 1515 Dickey Drive, Atlanta, GA 30322

^c Department of Chemistry and Chemical Biology, Baker Laboratory, Cornell University, Ithaca, NY 14853

Contributions: O. Villanueva performed catalytic studies with $[1]^{2-}$ and $[3]^{1-}$. S. K. Sharma synthesized and characterized $[2]^{2-}$. J. Bacsá provided crystallographic assistance. R. C. Walroth and K. M. Lancaster collected and modeled XAS data and provided SORCI calculations. All other work was performed by A. R. Corcos.

8.1 Abstract.

Bimetallic $(Et_4N)_2[Co_2(L)_2]$, $(Et_4N)_2[1]$ (where $(L)^{3-} = (N(o\text{-}PhNC(O)^iPr)_2)^{3-}$) reacts with 2 equiv of O_2 to form the monometallic species $(Et_4N)[Co(L)O_2]$, $(Et_4N)[3]$. A crystallographically characterized analog $(Et_4N)_2[Co(L)CN]$, $(Et_4N)_2[2]$, gives insight into the structure of $[3]^{1-}$. Magnetic measurements indicate $[2]^{2-}$ to be an unusual high-spin Co(II)-cyano species ($S = 3/2$) while IR, EXAFS, and EPR spectroscopies indicate $[3]^{1-}$ to be an end-on superoxide complex with an $S = 1/2$ ground spin state. By X-ray spectroscopy and calculations, $[3]^{1-}$ features a high-spin Co(II) center; the net $S = 1/2$ ground state arises after the Co electrons couple to both the $O_2^{\bullet-}$ and the aminyl radical on redox non-innocent $(L^{\bullet})^{2-}$. Dianion $[1]^{2-}$ shows

both nucleophilic and electrophilic catalytic reactivity upon activation of O₂ due to the presence of a high-energy, filled O₂⁻ π^* orbital and an empty low-lying O₂⁻ π^* orbital in [3]¹⁻.

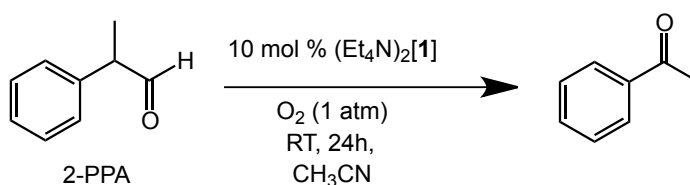
8.2 Introduction.

Synthetic cobalt complexes have been known to bind O₂ since the days of Werner.^{1,2} Upon O₂ addition, most Co(II) complexes form kinetically inert low-spin Co(III) terminal superoxide or μ -peroxide compounds that are inactive in catalysis.³⁻¹⁵ Catalytic reactivity can be coaxed from such molecules by addition of a co-reductant.^{11,16-19} In contrast, nature uses multiple metal centers²⁰⁻²² or redox non-innocent ligands²³⁻²⁸ to supply the requisite electrons when activating O₂ for catalysis with first-row transition metal complexes.

We recently reported²⁹ the dimeric pseudo-tetrahedral Co(II) complex (Et₄N)₂[Co₂(L)₂], (Et₄N)₂[1] (where L = (N(*o*-PhNC(O)^{*i*}Pr)₂)³⁻), which is unique among Co(II) compounds for its ability to activate O₂ toward electrophilic O-atom transfer without supplemental co-reductants. This O₂ activation proceeds with dioxygenase stoichiometry.²⁹ Here, we explore additional reactivity and offer insights into the O₂ activation step for this catalyst by characterizing the intermediate formed upon its interaction with O₂. Our discussion is facilitated by comparison to a stable compound formed using CN⁻ as an O₂ analog. Surprisingly, instead of forming a kinetically inert, low-spin Co(III) species, we show that the Co(II) centers remain high-spin when either substrate is added. Consequently, we argue that O₂ reduction occurs via one-electron oxidation of L rather than Co.

8.3 Results and Discussion.

In addition to its behavior as a catalyst for aerobic O-atom transfer,²⁹ we have now found $(\text{Et}_4\text{N})_2[\mathbf{1}]$ to be an excellent catalyst for the aerobic deformylation of 2-phenylpropionaldehyde (2-PPA), forming acetophenone in good yields (Scheme 8.1). While biological systems are known to carry out catalytic deformylation (nucleophilic) reactions using O_2 ,³⁰ synthetic aerobic deformylation catalysts have, to the best of our knowledge, not yet been reported.^{31-35,36-38} Metal-oxygen species typically show either electrophilic or nucleophilic character; this system merits study due to its electronically divergent reactivity.³⁹



Scheme 8.1 Catalytic aerobic deformylation of 2-PPA by $(\text{Et}_4\text{N})_2[\mathbf{1}]$.

To better understand this divergently-reactive species, 2 equiv of CN^- , an O_2 surrogate, was added to $[\mathbf{1}]^{2-}$. CN^- was found to disrupt the bimetallic core structure, yielding 2 equiv of monometallic $(\text{Et}_4\text{N})_2[\text{Co}(\text{L})\text{CN}]$, $(\text{Et}_4\text{N})_2[\mathbf{2}]$ (Figure 8.1, S8.1-S8.3), which has been crystallographically characterized as containing a four-coordinate Co(II) center, at the border between pseudosawhorse and pseudotetrahedral geometry ($\tau_8 = 0.59$).⁴⁰ The L ligand backbone undergoes a structural rearrangement upon reaction of $(\text{Et}_4\text{N})_2[\mathbf{1}]$ with CN^- such that each $(\text{L})^{3-}$ ligand coordinates to a single Co center in a novel tridentate pincer-like coordination mode.²⁹

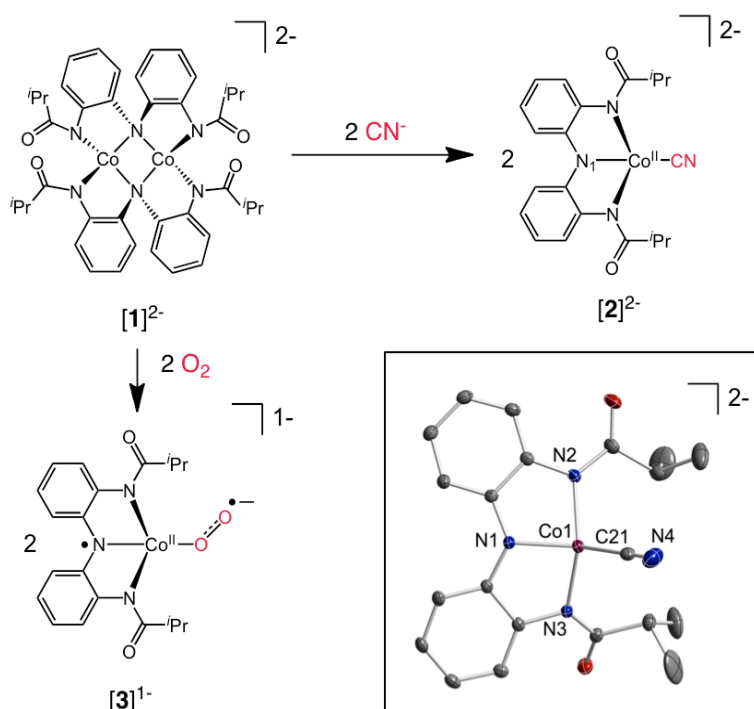


Figure 8.1 Preparation of $[2]^{2-}$ and $[3]^{1-}$ from $[1]^{2-}$. Thermal ellipsoid plot of $[2]^{2-}$ is shown at the 45% probability level, with H atoms and counter cations omitted for clarity.

Several spectroscopic techniques were employed to determine the first observable catalytically relevant intermediate responsible for the divergent reactivity of $[1]^{2-}$. Gas-uptake experiments indicate that $[1]^{2-}$ reacts with O_2 in a 1:2 stoichiometry (see SI), suggesting that one molecule of O_2 is taken up per Co center. UV-Vis spectroscopy shows isosbestic behavior indicating a clean conversion of $[1]^{2-}$ to $[3]^{1-}$ via a short-lived intermediate (Figure S8.4). The resulting burgundy species $[3]^{1-}$ can be isolated or used in situ to perform stoichiometric oxidations with PPh_3 and 2-PPA, generating the same products of catalytic oxidations using $[1]^{2-}$ (see SI). Along with the monometallic structure of $(\text{Et}_4\text{N})_2[2]$, this result suggests that $[1]^{2-}$ reacts with O_2 to form a monometallic Co– O_2 species, $[\text{Co}(\text{L})\text{O}_2]^{1-}$, $[3]^{1-}$. The monomeric nature of $[3]^{1-}$ is further supported by MALDI-TOF mass spectrometry, which shows that new ions with $m/z =$

410.49 or 412.47 amu are produced when $[1]^{2-}$ reacts with 2 equiv of $^{16}\text{O}_2$ or $^{18}\text{O}_2$, respectively (Figure S8.5). These mass values are consistent with formulations as $[3 - ^{16/18}\text{O}]^-$ species, similar to mass spectral data observed for a recently reported five-coordinate Co–O₂ complex capable of C–H bond activation via a postulated Co(IV)-oxo intermediate.⁴¹ Liquid-cell IR techniques show that $[3]^{1-}$ has an O₂ stretching feature at 1248 cm⁻¹, which shifts to 1203 cm⁻¹ upon $^{18}\text{O}_2$ labeling (Figure S8.6). These vibrational data are consistent with end-on Co–superoxide coordination.⁴²

This molecular geometry is further supported by analysis of extended X-ray absorption fine structure (EXAFS) in the Co K-edge XAS of $[2]^{2-}$ and $[3]^{1-}$ (Figure S8.7-8 and Table S8.1). The EXAFS of $[2]^{2-}$ and $[3]^{1-}$ are qualitatively similar, yielding a Co coordination number of four with average Co–L distances of 1.98 Å and 1.88 Å, respectively. These distances are in good agreement with the crystallographic and DFT-optimized average Co–L distances of 2.01 Å and 2.04 Å for $[2]^{2-}$, respectively, and are also in good agreement with the calculated average Co–L distance for $[3]^{1-}$ at 1.87 Å. These results suggest a similar coordination geometry for (L)³⁻ in $[2]^{2-}$ and $[3]^{1-}$, further indicating a monomeric Co(L) end-on superoxide structural unit for $[3]^{1-}$.

Ground-state electronic configurations of $[2]^{2-}$ and $[3]^{1-}$ were established from their magnetic properties. For $[2]^{2-}$, the μ_{eff} value of 4.27(3) μ_{B} at 298K in CDCl₃ is indicative of an $S = 3/2$ ground state. EPR data (Figure 8.2a) confirm this unusual high-spin state, with observed (effective) g values of $g_x = 4.53$, $g_y = 3.97$, and $g_z = 1.95$, indicating $D > h\nu$. Despite the clear indication of an $S = 3/2$ ground state for $[2]^{2-}$, the EPR spectrum for $[3]^{1-}$ is surprisingly characteristic of an $S = 1/2$ species, best simulated by $g_x = 2.20$, $g_y = 2.00$, $g_z = 1.975$ ($\mu_{\text{eff}} = 2.13 \mu_{\text{B}}$ at 298K in CH₃CN). The observation of a “high-spin” complex of cyanide, a strong-field ligand, is unusual^{43,44} but consistent with the low coordination number. Even more unusual is that the weaker field O₂⁻ complex, $[3]^{1-}$, appears low spin. Co K β X-ray emission spectra (XES)

of $[2]^{2-}$ and $[3]^{1-}$ were measured as a probe of the local spin at Co (Figure 8.2b). Splitting of $K\beta$ ($3p \rightarrow 1s$) main lines into $K\beta'$ and $K\beta_{1,3}$ features is a useful metric of spin population since electron delocalization out of metal 3d orbitals results in attenuation of the 3d–3p exchange energy.⁴⁵ $K\beta$ main line splitting is markedly decreased in $[3]^{1-}$ compared to $[1]^{2-}$ and $[2]^{2-}$, consistent with a decreased local Co spin population in $[3]^{1-}$.

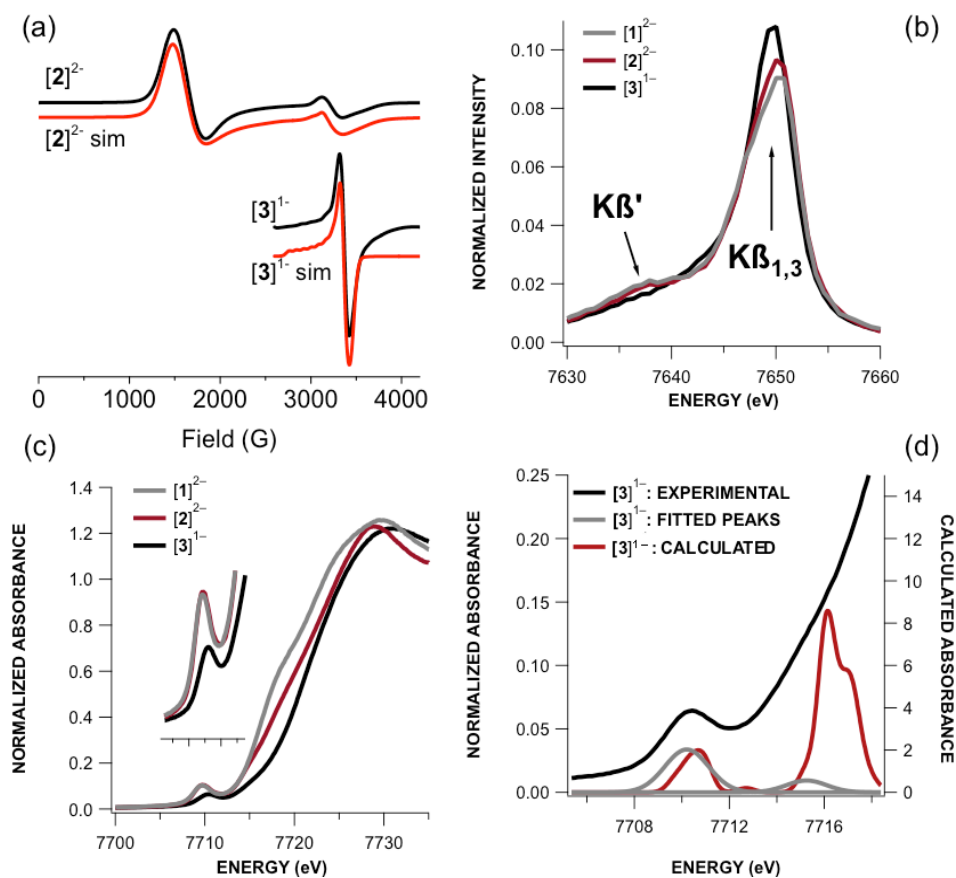


Figure 8.2 (a) Experimental EPR data and simulations for $[2]^{2-}$ and $[3]^{1-}$. (b) Co $K\beta$ XES main lines of $[1]^{2-}$ – $[3]^{1-}$. (c) Co K-edge XANES of $[1]^{2-}$ – $[3]^{1-}$. Inset: Magnification of the Co $1s \rightarrow$ (Co 3d + L) pre-edge features. (d) Overlay of calibrated TDDFT-calculated (B3LYP/def2-TZVP-ZORA) Co K-edge XANES pre-edge peaks for $[3]^{1-}$.

To defuse the spin state conundrum we carried out calculations using DFT in order to produce an electronic structure picture consistent with the aggregate structural and spectral data. To this end, we evaluated multiple electronic configurations for $[2]^{2-}$ and $[3]^{1-}$.⁴⁶ The quartet state for $[2]^{2-}$ was energetically favored over the doublet state by 26.7 kJ/mol, in agreement with the EPR data and the similarity of the Co X-ray absorption near-edge spectroscopy (XANES) pre-edge energy of $[2]^{2-}$ with that of $[1]^{2-}$, for the Co(II) centers in $[1]^{2-}$ are high-spin²⁹ (Figure 2c). The optimized geometry for $[2]^{2-}$ as a quartet is also a far superior match to the crystallographic data (Table S8.5). Additionally, the cyanide $C\equiv N$ stretch is predicted to occur at 2211 cm^{-1} and is experimentally measured at 2109 cm^{-1} , which is in decent agreement given the well-known tendency for DFT to overestimate vibrational frequencies.⁴⁷

For $[3]^{1-}$, DFT calculations support an $S = 1/2$ end-on superoxide species as the configuration with lowest energy (Table S8.6),⁴⁸ in accord with the experimental data. For this species, a spin-coupled electronic structure is obtained. There are two low-lying doubly occupied Co-centered e -type orbitals of the pseudotetrahedral Co d orbital manifold and three singly-occupied orbitals for the t_2 -derived set (Figure 8.3, S8.13). The superoxide ligand has two π^* valence orbitals—doubly-occupied π_1^* and singly-occupied π_2^* —that interact with the Co t_2 -derived orbitals. The π_1^* orbital engages in a 3-electron σ interaction with one Co orbital, while the π_2^* unpaired electron is coupled with another Co electron. A second antiferromagnetic interaction exists between the third Co t_2 -derived electron and a ligand-based orbital having significant character from the central N atom of L. Therefore, as with $[2]^{2-}$, the metal center in $[3]^{1-}$ contains a high-spin $S = 3/2$ Co(II) center. In this case, however, two of the three unpaired electrons of the Co(II) center couple with an L radical and a superoxide radical to yield an overall $S = 1/2$ ground state. This electronic structure explains the divergent reactivity of

(Et₄N)[**3**] (vide supra), for the half-filled O₂ π_2^* orbital can be either a donor orbital for nucleophilic reactivity or an acceptor orbital for electrophilic reactivity.

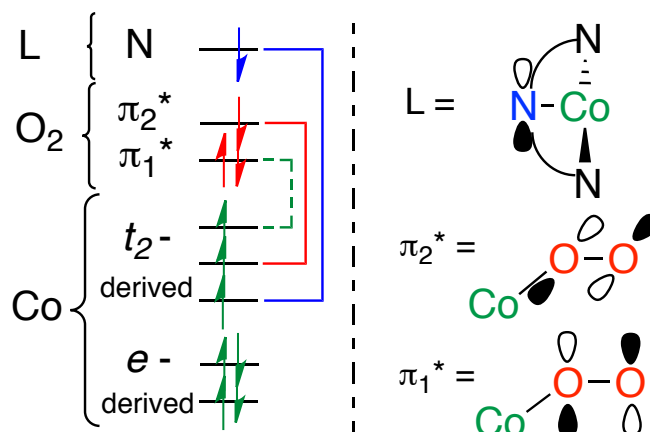


Figure 8.3 Molecular orbital interactions for [**3**]¹⁻. (Left) Green, red, and blue arrows represent electrons in Co-, O₂-, and ligand-based orbitals, respectively. The red and blue brackets show antiferromagnetic coupling between the O₂- and N-based ligands with Co d electrons. The green dashed bracket shows the 3-electron σ interaction between a Co electron and the π_1^* of the O₂⁻ ligand. (Right) Representation of ligand- and O₂-based orbitals.

The Co K-edge XANES of [**1**]²⁻–[**3**]¹⁻ (Figure 8.2.c) deserve further comment. All of the other experimental and computational data clearly indicate that the Co(II) oxidation state remains constant throughout this series, but the pre-edge features in the spectra of (Et₄N)₂[**1**] and (Et₄N)₂[**2**] effectively superimpose at 7709.7 eV, while that for [**3**]¹⁻ is shifted in energy to 7710.2 eV. Furthermore, rising edges distinguish all three compounds from one another, at 7716.4 eV, 7717.4 eV, and 7720.4 eV for [**1**]²⁻, [**2**]²⁻, and [**3**]¹⁻, respectively (Figure S8.9).

TD-DFT analysis of XANES pre-edge features, accomplished via calibration to a set of model compounds (Figure S8.10), was performed to reconcile the XANES features with the electronic structures of [**1**]²⁻–[**3**]¹⁻. For [**2**]²⁻, this led to a straightforward assignment of the pre-

edge transition as arising from the Co 1s to the valence “ t_2 ”-derived set. In the case of $[\mathbf{3}]^{1-}$ (Figure 8.2d), the acceptor orbitals participating in this excitation have substantial O–O π^* admixture. Comparison of the spin density plots of $[\mathbf{2}]^{2-}$ vs $[\mathbf{3}]^{1-}$ shows this effect quite clearly; while the spin density in $[\mathbf{2}]^{2-}$ is highly localized on the metal center with orbitals having roughly 70% metal character, the spin for $[\mathbf{3}]^{1-}$ is more delocalized and the orbitals are closer to 50% metal in character (Figure S8.11).

This delocalization of electron density manifests in the calculated Co atomic charges 0.47, 0.55, and 0.64 for $[\mathbf{1}]^{2-}$, $[\mathbf{2}]^{2-}$, and $[\mathbf{3}]^{1-}$, respectively. These values correlate to a reasonable degree ($R^2 = 0.94$) with the corresponding rising edge inflection points (Figure S8.9). Moreover, the trend line extrapolates to 7706 ± 3 eV at a charge of 0, consistent with the rising edge inflection of Co metal (7709 eV). Consequently, variations in the XANES of $[\mathbf{3}]^{1-}$ from the other compounds do not necessarily reflect a change in the physical oxidation state at Co after reaction with O₂. The difference in energy of the Co K-edge XANES pre-edge features is due to a difference in the nature of the acceptor orbital when comparing $[\mathbf{1}]^{2-}$ and $[\mathbf{2}]^{2-}$ to $[\mathbf{3}]^{1-}$, as has been seen previously for Cu complexes.^{49,50} The shift to higher energy of the rising edge inflection point in $[\mathbf{3}]^{1-}$ likely reflects the highly covalent interaction of Co with an electronegative O-donor. Although XANES is widely used as a metric of physical oxidation states of transition metal complexes, we emphasize here that the nature of the coordinated ligands also has a strong influence over the spectral profiles.

8.4 Conclusions.

In summary, the reaction of $[\mathbf{1}]^{2-}$ with 2 equiv of CN[−] yields the unusual, high-spin Co(II) complex $[\mathbf{2}]^{2-}$, which provides structural insight toward the catalytically relevant intermediate

[3]¹⁻. Compound [3]¹⁻ is determined to be a monometallic Co(II)-superoxide complex supported by the redox non-innocent ligand L in its singly-oxidized radical form. The local spin state of Co(II) is $S = 3/2$, but these electrons couple with unpaired electrons on L as well as the O₂⁻ ligand to yield an overall $S = 1/2$ state, as seen via EPR spectroscopy. The catalytic utility of [3]¹⁻ is therefore attributable to its redox non-innocent L supporting ligand, allowing Co to remain high-spin upon activation of O₂ and avoiding the kinetic quagmire that is a low-spin Co(III) complex.

8.5 Acknowledgements.

We thank NSF for support under CHE-1205646. J.F.B. thanks the DOE (DE-FG02-10ER16204). K.M.L acknowledges Cornell University for startup funding and NSF via CHE-1454455. A.R.C. thanks the NSF (DGE-0718123). R.C.W. thanks the NIH-NIGMS (T32GM008500). Computational and EPR facilities at UW-Madison are supported by NSF grants CHE-0840494 and CHE-0741901, respectively. We thank Dr. Elizabeth Blaesi for insightful discussions. This work is based on research conducted at the Cornell High Energy Synchrotron Source (CHESS), supported by NSF and NIH/NIGMS under NSF award DMR-1332208.

8.6 Supplementary Information.

Materials and Methods. All manipulations were carried out using standard Schlenk techniques or conducted in an MBraun Labmaster 130 drybox under a nitrogen atmosphere. All reagents used were purchased from commercial vendors and used as received unless otherwise noted. 2-phenylpropionaldehyde (2-PPA) was purchased from Sigma-Aldrich and the purity of this

substrates were checked by GC and ^1H NMR prior to use. Anhydrous solvents were purchased from Sigma-Aldrich and further purified by sparging with Ar gas followed by passage through activated alumina columns. Elemental analysis was performed by Atlantic Microlab, LLC.

^1H spectra were recorded on an Inova 400 MHz spectrometer at ambient temperature. ^1H chemical shifts were referenced to residual solvent peaks. Matrix-assisted laser desorption/ionization (MALDI) time-of-flight (TOF) mass spectrometry data was obtained using an anthracene matrix on a Bruker ULTRAFLEX[®] III mass spectrometer equipped with a SmartBeam[®] laser. Liquid IR data for $[\mathbf{3}]^{1-}$ was collected on a Bruker Tensor 27 FTIR spectrometer, and the samples were prepared in an NaCl amalgamated cell. Infrared spectra for $[\mathbf{2}]^{2-}$ were recorded as KBr pellets on a Varian Scimitar 800 Series FT-IR spectrophotometer. UV-visible absorption spectra were recorded on a Cary50 spectrophotometer using 1.0 cm quartz cuvettes. Solution-state magnetic moments were measured using the Evans' method.^{51,52} X-ray diffraction studies were carried out in the X-ray Crystallography Laboratory at Emory University on a Bruker Smart 1000 CCD diffractometer. Cyclic voltammetry experiments were carried out using a CH Instruments (Austin, TX) Model 660C potentiostat. All experiments were conducted in CH_2Cl_2 with 0.10 M tetrabutylammonium hexafluorophosphate as the supporting electrolyte. Electrochemical experiments were conducted in a three-component cell consisting of a Pt-wire auxiliary electrode, a non-aqueous reference electrode (Ag/AgNO_3), and a glassy carbon-working electrode.

EPR Spectroscopy. EPR data were acquired using a Bruker ELEXSYS E500 EPR spectrometer equipped with a Varian E102 microwave bridge interfaced with a Linux system. An Oxford Instruments ESR-900 continuous-flow helium flow cryostat and an Oxford Instruments 3120

temperature controller were used to set and maintain the sample temperature. A Hewlett-Packard 432A power meter was used for microwave power calibration, with measurement conditions as follows: for $[2]^{2-}$ in acetonitrile 9.3750 GHz, 100 MHz modulation frequency, 4.000 G modulation amplitude, 4000 G center field, 8000 G sweep width, 3.170 mW power, 30 dB gain, 327.68 ms time constant, and 10 K; for $[3]^{1-}$ in acetonitrile 9.3763 GHz, 100 MHz modulation frequency, 4.000 G modulation amplitude, 3400 G center field, 1600 G sweep width, 2.000 mW power, 55 dB gain, 655.36 ms time constant, and 10K. Simulations were performed using *EasySpin* software,⁵³ and the following parameters were used to model the data: for $[2]^{2-}$, $g_{\perp} = 2.13$, $g_{\parallel} = 1.92$, $HStrain_{\perp} = 1700$, $HStrain_{\parallel} = 1000$, $E/D = 0.04$, $S = 3/2$, weight = 100, with a minor impurity modeled as $g_{\perp} = 2.10$, $g_{\parallel} = 2.01$, $HStrain_{\perp} = 600$, $HStrain_{\parallel} = 500$, $S = 1/2$, weight = 3. Simulations for $[3]^{1-}$ are $g_x = 2.20$, $g_y = 2.00$, $g_z = 1.975$, $A_{x,Co} = 250$ MHz, $HStrain_x = 225$, $HStrain_y = 180$, $HStrain_z = 240$, $S = 1/2$.

X-ray Crystallography. A burgundy block-shaped crystal of $[2]^{2-}$ with dimensions $0.69 \times 0.43 \times 0.40$ mm was mounted on a loop with paratone oil. Data were collected using a Bruker APEX-II CCD diffractometer equipped with an Oxford Cryosystems low-temperature apparatus operating at $T = 173(2)$ K. Data were measured using ω scans using Mo- K_{α} radiation (fine-focus sealed tube, 45 kV, 35 mA). The total number of runs and images was based on the strategy calculation from the program APEX2.⁵⁴ The maximum resolution achieved was $Q = 31.50^{\circ}$. Unit cell indexing was performed by using the APEX2 software⁵⁴ and refined using SAINT⁵⁵ on 9948 reflections, 12% of the observed reflections. Data reduction, scaling and absorption corrections were performed using SAINT⁵⁵ and SADABS was used for absorption correction.⁵⁶ $wR_2(\text{int})$ was 0.0628 before and 0.0441 after correction. The ratio of minimum to

maximum transmission is 0.9188. The final completeness is 100.0% out to 31.50° in Q . The absorption coefficient (m) of this material is 0.480 mm^{-1} and the minimum and maximum transmissions are 0.6858 and 0.7464. The structure was solved with ShelXS⁵⁷ in the space group $P2_1/n$ (#14) by direct methods and using Olex2^{58,59} as the graphical interface. The structure was refined by least squares using ShelXL.⁶⁰ All non-hydrogen atoms were refined anisotropically. Hydrogen atom positions were calculated geometrically and refined using the riding model.

High Energy Resolution Fluorescence Detection X-ray Absorption Spectroscopy (HERFD-XAS). Co HERFD-XAS (Co $K\beta$ -detection) data were collected at the Cornell High Energy Synchrotron Source at C-line end station. The incident X-rays were monochromated using a double Si(111) crystal monochromator. Emitted x-rays were analyzed using a set of five spherically bent Si crystals (444 reflection) mounted on a Rowland circle in combination with a Pilatus Area Detector. He-filled plastic bags were used to displace air from the beam flight path to minimize attenuation of the fluorescence. The spectra were collected by monitoring the intensity of the $K\beta_{1,3}$ peak as a function of incident energy.

Samples were prepared as $\sim 10 \text{ mM}$ solutions in MiteGen MicroRT tubes and kept frozen in liquid N_2 until data collection. During data collection the samples were kept at a temperature of $\sim 170 \text{ K}$ using a stream of cold N_2 gas. Temperature was monitored with a diode at the base of the sample holder.

Experimental spectra were averaged and normalized using PyMCA. CoO was used as a calibrant, adjusting the energy axis to the reported values. Peaks were fit to the experimental spectra using the BlueprintXAS Matlab software package developed by Mario Delgado.⁶¹

DFT calculations were performed using the ORCA 3.00 software package.^{62,63} All spectra were calculated from geometry-optimized coordinates. Optimizations were carried out with the BP86 functional,^{64,65} zeroth order regular approximation (ZORA) for relativistic effects,^{66,67} and the scalar-relativistically recontracted def2-TZVP(-f) basis set.^{68,69} Solvation was modeled using the conductor like screening model (COSMO).^{70,71} XAS spectra were predicted using a TD-DFT approach as described previously.⁷² Spectral predictions were done using the B3LYP functional.⁷³⁻⁷⁶ The CP(PPP) basis set was used for Co with an integration accuracy of 7. The TZVP basis set was used for all other atoms. Solvation was again modeled using an appropriate COSMO correction.

DFT Computational Details. Three compounds $[\text{Co}(\text{L})(\text{CN})]^{2-}$ [**2**]²⁻, $[\text{Co}(\text{L})(\text{O}_2)]^-$ where O_2 is bound end-on [**3**]¹⁻, and $[\text{Co}(\text{L})(\text{O}_2)]^-$ where O_2 is bound side-on [**3b**]¹⁻, were investigated using spin-unrestricted DFT methods. All calculations were carried out with the Orca 2.9.1 program package using spin-unrestricted DFT methods.^{62,63} [**2**]²⁻, [**3**]¹⁻, and [**3b**]¹⁻ were optimized in both the doublet and quartet spin states. For [**2**]²⁻, the input geometry was obtained from crystallographic data and geometry optimizations were run using the B3LYP functional⁷³⁻⁷⁶ with the triple- ζ Default-3 (TZV on hydrogen, TZVP on main-group atoms, TZVPPP on transition metal) basis set.⁷⁷ Optimizations also included the diffuse basis set Diff aug_cc_VDZ_H,⁷⁸⁻⁸¹ increased integration grid (Grid4), tight optimization, tight SCF convergence criteria, the RIJCOSX approximation,⁸² and an appropriate⁸³ auxiliary basis set.

The input geometry for [**3**]¹⁻ was obtained from the crystallographic data for [**2**]²⁻ but the carbon and nitrogen atoms of the cyano ligand were exchanged for two oxygen atoms. Multiple geometry inputs for [**3b**]¹⁻ were performed in the same manner, with the additional step of

manually placing the oxygen atoms in a side-on configuration; the geometry that gave the lowest overall energy as calculated by the single-point calculation was used going forward. All geometries were verified as potential energy minima by numerical frequency calculations to not contain any negative frequencies. Unrestricted natural orbitals (UNOs) were used to study and plot the electronic structure of $[2]^{2-}$, and a combination of unrestricted corresponding orbitals (UCOs)⁸⁴ and spin-up/spin-down orbitals were used for $[3]^{1-}$ and $[3b]^{1-}$ due to the spin-coupling that exists in the frontier orbitals of these complexes that does not exist in $[2]^{2-}$. All images were generated using the UCSF Chimera package.⁸⁵ The Avogadro program⁸⁶ was used to edit the XYZ files for converting $[2]^{2-}$ to $[3]^{1-}$ and $[3b]^{1-}$.

SORCI Computational Details. Multireference character in the ground state of $[3]^{1-}$ was assessed with SORCI calculations.⁸⁷ SORCI was performed on a complete active space (CAS) for $[3]^{1-}$ comprising 17 electrons and 11 orbitals [CAS(17,11)]. The def2-TZVP(-f)-ZORA was used on all atoms, and relativistic effects were modeled using the ZORA relativistic correction. As described elsewhere,⁸⁷ individual selection was used to ease the computational burden. The size of the first-order interacting space was reduced with a threshold: $T_{sel} = 10^{-6} E_h$. A further approximation involved reducing the reference space through another selection: all initial references that contributed less than a second threshold ($T_{pre} = 10^{-5}$) to the zeroth-order states were rejected from the reference space. Starting orbitals were taken from localized, quasi-restricted orbitals.⁸⁸

$(Et_4N)_2[2]$: Under an inert atmosphere, a 20 mL scintillation vial was charged with $(Et_4N)_2[1]$ (0.120g, 0.114 mmol), a stir bar, and 10 mL of CH_3CN . To this homogenous dark green solution,

[Et₄N]CN (0.229 mmol, 0.359 g) was added as a solid and the dark green solution immediately changed to a deep burgundy color. The resulting homogenous solution was concentrated to dryness under reduced pressure to yield a dark burgundy solid. The solid was extracted into a CH₃CN and filtered through a plug of Celite®. Slow diffusion of diethyl ether into the burgundy filtrate yielded needle- and blocked-shaped dark burgundy crystals of the product (109 mg). This product oxidizes readily in air. ¹H NMR (δ, CD₃CN, 400 MHz): (ppm) -30.80 (s), -46.55 (s), -37.18 (s), -31.30 (s), -2.744 (s), 26.91 (s), 37.06 (s), 47.04 (s), 60.58 (s). FTIR (KBr, cm⁻¹): ν(CO) 1663, ν(CN) 2109. UV-Vis: λ_{max}, nm (ε, M⁻¹cm⁻¹) (CH₃CN): 502 (1070), 740 (390). HRESI-MS: for [2]²⁻: Calcd (m/z): 421.1075, Found 421.1096. Anal. Calcd for C₃₇H₆₂CoN₆O₂: C, 65.17; H, 9.17; N, 12.33. Found: C, 65.09; H, 8.90; 12.17.

Gas uptake experiments with (Et₄N)₂[1]: To determine the stoichiometry of dioxygen binding, a gas uptake experiment was conducted following a previously described manometric method using equipment described by Sorrell et al.⁸⁹ Under an inert atmosphere at 21°C, a 50 mL round bottom Schlenk flask was charged with a stir bar, (Et₄N)₂[1] (0.500 g, 0.4760 mmol), and 25.0 mL of CH₃CN. Once the cobalt complex was completely dissolved to form a deep green homogeneous solution, the flask was fitted with a septum, sealed, and removed from the dry box. The Schlenk flask was first connected to a Schlenk line and then connected to the manometric setup under a positive flow of nitrogen gas. Purified O₂ gas from the monometric glassware was then introduced to the flask through the septum. An immediate color change from deep green to dark burgundy took place within minutes (~ 4 min). The system was allowed to equilibrate and the amount of O₂ that was taken up during the reaction was measured directly from the displacement of the volume change of the manometer (23.25 mL, 0.963 mmol O₂).

(Et₄N)[3]. *Typical Procedure for reaction of (Et₄N)₂[1]. + 2.0 equivalents of O₂(g):* Under an inert atmosphere, a 25 mL round bottom Schlenk flask was charged with a stir bar, (Et₄N)₂[1] (0.200 g, 0.1904 mmol), and 10 mL of CH₃CN. The cobalt complex was stirred for approximately 10 minutes until completely dissolved. The flask was fitted with a septum and sealed, and removed from the dry box. While stirring at room temperature, O₂ gas (9.30 mL, 0.3808 mmol) was injected to the flask via a gas-tight, gas transfer syringe (inserted through the septum). The color of the solution changed from deep green to deep burgundy within minutes (~ 4 min). After stirring for 12 hours, the solvent was removed under vacuum, and the resulting solid was brought back into the dry box. The solid was washed with Et₂O (3 x 3 mL) and the crude solid was collected on a frit. λ_{max} (CH₃CN): 390 nm, 500 nm, and 785 nm. $\mu_{\text{eff}} = 2.13 \mu_{\text{B}}$ (Evan's Method, CH₃CN, 298K). Combustion analysis studies were conducted on [3]¹⁻ as its potassium salt. The potassium salt of [3]¹⁻ was isolated by reacting K₂[1] with dioxygen as described above for the Et₄N⁺ salt. This potassium complex (K[3]) displays similar spectroscopic signatures to those of the Et₄N[3] salt but it far less soluble in organic solvents. Anal. Calcd for K[3]·0.5(Et₂O)·0.5(CH₃CN): C₂₃H_{28.5}CoKN_{3.5}O_{4.5}: C 52.73, H 5.44, N 9.36. Found: C 52.56, H 5.81, N 9.42.

The final product of the oxygenation reaction is stable in acetonitrile for days. The product is stable in chlorinated solvents (CH₂Cl₂) for up to 12 hrs. The complex is also stable to vacuum and does not dissociate oxygen in solution when the solution is sparged with Ar or N₂ gas as evidenced by UV-Vis absorption spectroscopy. The oxygenation reaction of (Et₄N)₂[1] can be followed directly by UV-Visible absorption spectroscopy as shown in Figure S8.4. During the oxygenation reaction, we observe an intermediate species (orange trace below) grow

in that eventually fades to form the final stable species $(\text{Et}_4\text{N})[\mathbf{3}]$, represented in the burgundy trace below.

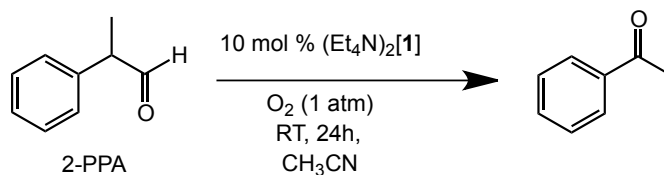
Stoichiometric Reaction of $(\text{Et}_4\text{N})[\mathbf{3}]$ with PPh_3 : Under an inert atmosphere, a 25 mL round bottom Schlenk flask was charged with a stir bar, $(\text{Et}_4\text{N})_2[\mathbf{1}]$ (0.150 g, 0.143 mmol), and 10 mL of CH_3CN . Once the solution was homogeneous, the flask was fitted with a septum, sealed and removed from the dry box. While stirring at room temperature, O_2 gas (7.00 mL, 0.143 mmol at 1 atm) was injected to the flask via a gas-transfer syringe (inserted through the septum). The solution color changed from deep green to deep burgundy within minutes (~ 4 min). After stirring for 12 hours, the solvent was removed under vacuum, and the resulting burgundy solid was brought back into the dry box. Triphenylphosphine (PPh_3) (0.150 g, 0.572 mmol) in 3 mL of CH_3CN was added to the dark burgundy solid. The solution was stirred for 4 hours. Over this time interval the color of the reaction mixture changed from deep burgundy to deep green. Solvent was removed under vacuum. The solid that remained was extracted multiple times with diethyl ether (4 X 10 mL), and the extracts were filtered through a silica plug to remove insoluble materials (i.e., cobalt complex). Evaporation of the ether yielded a solid (0.136 g) that was analyzed by ^1H and ^{31}P NMR spectroscopy [$(\delta, \text{CDCl}_3, 400 \text{ MHz})$: (ppm) 24.71 (s, OPPh_3)] that showed complete conversion of the PPh_3 to OPPh_3 (86% isolated yield) under these conditions.

Additional experiments indicated that $(\text{Et}_4\text{N})[\mathbf{3}]$ did not have to be isolated for these stoichiometric reactions. Instead, $(\text{Et}_4\text{N})[\mathbf{3}]$ could be generated in situ by the addition of dry oxygen gas to acetonitrile solutions of $(\text{Et}_4\text{N})_2[\mathbf{1}]$ with an O_2 (g) to $(\text{Et}_4\text{N})_2[\mathbf{1}]$ ratio of 2:1. After stirring for 30 minutes, substrate could be added directly to these reactions mixtures

anaerobically as acetonitrile solutions. This procedure gives identical product yields as observed when using isolated $(\text{Et}_4\text{N})[\mathbf{3}]$.

Stoichiometric Reaction of $(\text{Et}_4\text{N})[\mathbf{3}]$ with 2-PPA: Under an inert atmosphere, a 25 mL round bottom Schlenk flask was charged with a stir bar, $(\text{Et}_4\text{N})_2[\mathbf{1}]$ (0.046 g, 0.0438 mmol), and 6 mL of CH_3CN . Once the solution was homogeneous, the flask was fitted with a septum, sealed and removed from the dry box. While stirring at room temperature, O_2 gas (2.20 mL, 0.090 mmol at 1 atm) was injected to the flask using a gas-tight syringe and injecting through the septum. The solution color changed from deep green to deep burgundy almost immediately. The reaction mixture was allowed to stir for 2 hours and then 2-phenylpropionaldehyde (0.0120 g, 0.0896 mmol) was added to the reaction mixture as an acetonitrile solution (1 mL). The reaction was stirred for four hours and then concentrated under vacuum to yield a brownish solid. The resulting solid was extracted 3 times with a 1:1 hexanes/ethyl acetate solution and the extract filtered through a plug of silica gel to remove insoluble materials (i.e. cobalt complex). The filtrate was analyzed by GC and indicated that approximately 85% of the 2-PPA had been converted to acetophenone.

Catalytic Deformylation of 2-phenylpropionaldehyde (2-PPA) by $(\text{Et}_4\text{N})_2[\mathbf{1}]$:



Typical procedure for catalytic 2-PPA oxidation: The reaction was set up in a drybox under an inert atmosphere using freshly distilled 2-PPA purchased from Sigma-Aldrich. $(\text{Et}_4\text{N})_2[\mathbf{1}]$ (0.200 mg,

0.1904 mmol), 2-PPA (255 μ L, 1.904 mmol), and 20 mL of CH₃CN were added to a 50 mL round bottom flask that was charged with a stir bar and sealed with a septum. The flask was removed from the drybox and, while stirring, gently sparged with dry dioxygen gas. After 24 hours, the reaction was removed from the O₂ gas line and the acetonitrile was removed using a rotary evaporator to yield a thick reddish-brown residue. This residue was further dried on a vacuum line (30 minutes). The residue was then taken up in 20 mL of a 9:1 hexanes/ethyl acetate solution and passed through a plug of silica gel to remove the catalyst. The colorless filtrate was then concentrated again using a rotary evaporator and acetophenone was isolated as the organic product as a clear oily-liquid (83 % isolated yield, 190 mg). The acetophenone product was characterized by ¹H NMR spectroscopy and GC analysis and compared with a pure sample from commercial vendors. The other products of this reaction (i.e., formate or formic acid) were not isolated.

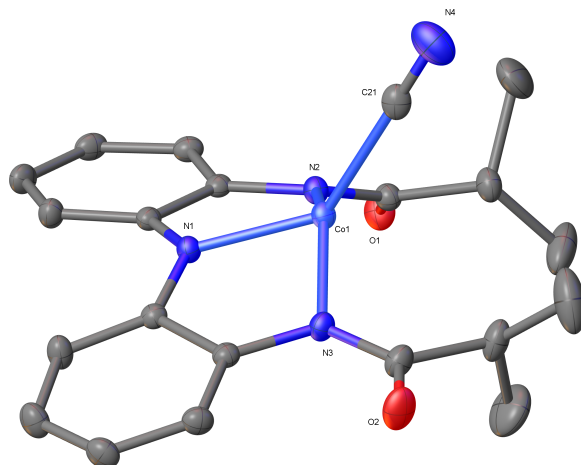


Figure S8.1 Plot of [Et₄N]₂[2] with counter cations and H atoms omitted for clarity.

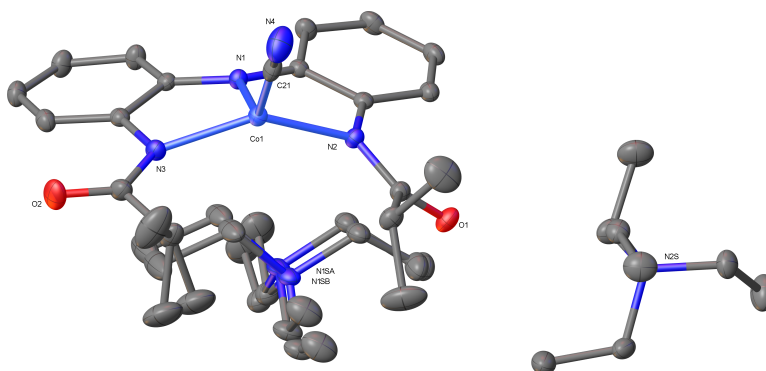


Figure S8.2 Plot of the asymmetric unit of [Et₄N]₂[2] showing two disordered components. H atoms omitted for clarity.

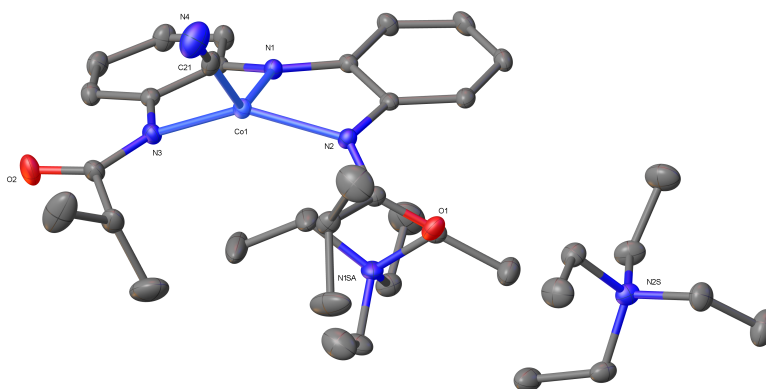


Figure S8.3 Plot of the asymmetric unit of [Et₄N]₂[2] with one of the two disorder components.

H atoms omitted for clarity.

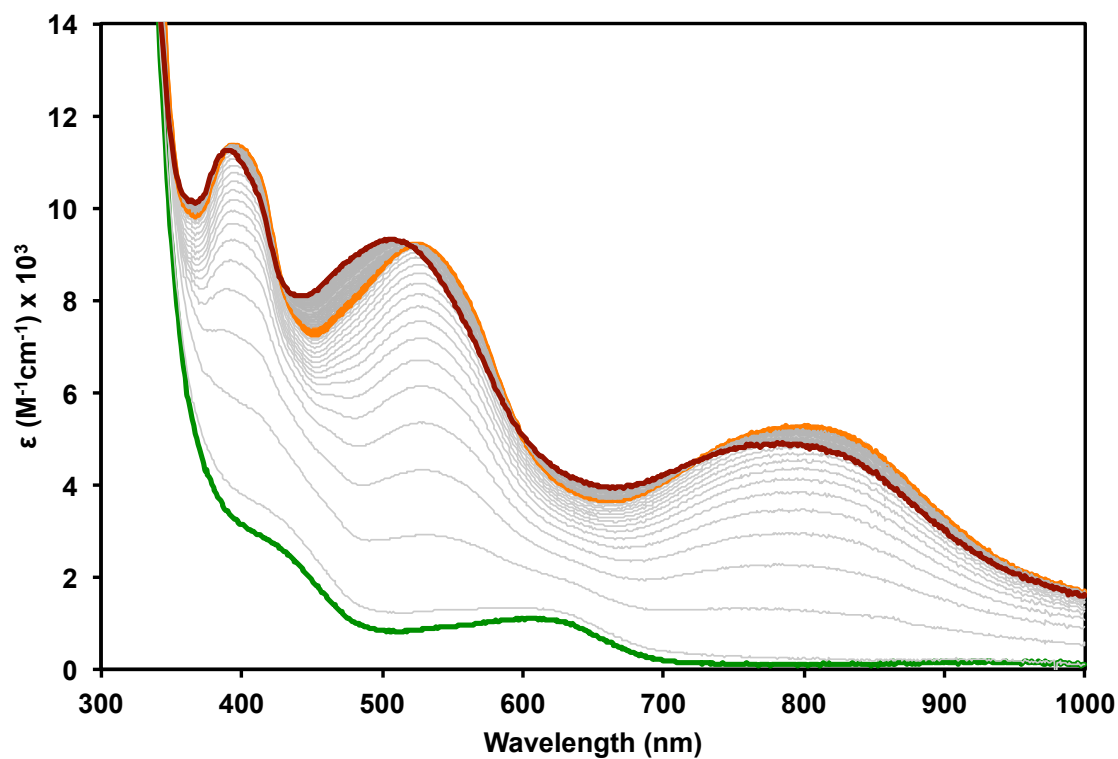


Figure S8.4 UV-visible absorption spectrum of $(\text{Et}_4\text{N})_2[\mathbf{1}]$, (green trace, prior to oxygenation) upon addition of dioxygen into the headspace above a solution of $(\text{Et}_4\text{N})_2[\mathbf{1}]$ in CH_3CN at 25 °C. Scan rate of 1 scan/min. Orange trace corresponds to a short-lived intermediate and burgundy trace corresponds to the final oxygenated species $(\text{Et}_4\text{N})[\mathbf{3}]$ upon reaction with dioxygen.

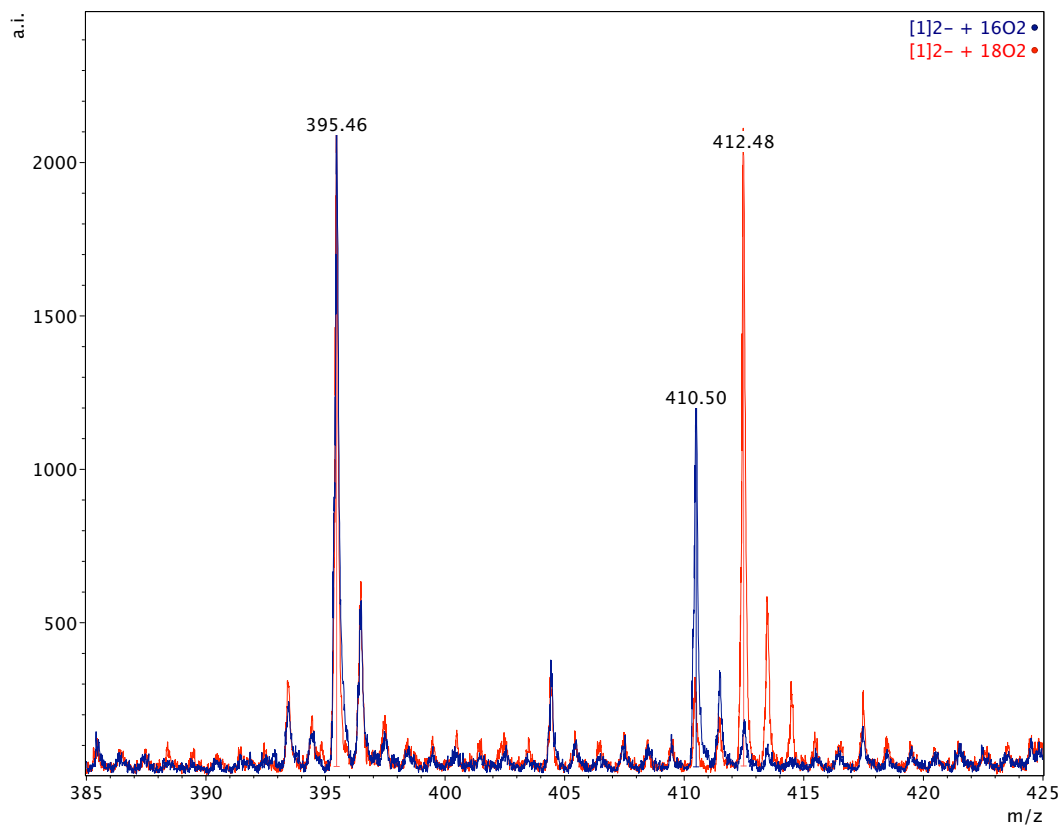


Figure S8.5 MALDI-TOF mass spectra for $[\text{Et}_4\text{N}][^{16/18}\mathbf{3}]$, resulting from reaction of $[\text{Et}_4\text{N}]_2[\mathbf{1}]$ with 2 equivalents of $^{16}\text{O}_2$ (blue) or $^{18}\text{O}_2$ (red). Masses correspond to $\text{L} + \text{Co}$ ($m/z = 395.46$), $\text{L} + \text{Co} + ^{16}\text{O}$ ($m/z = 410.50$), and $\text{L} + \text{Co} + ^{18}\text{O}$ ($m/z = 412.48$).

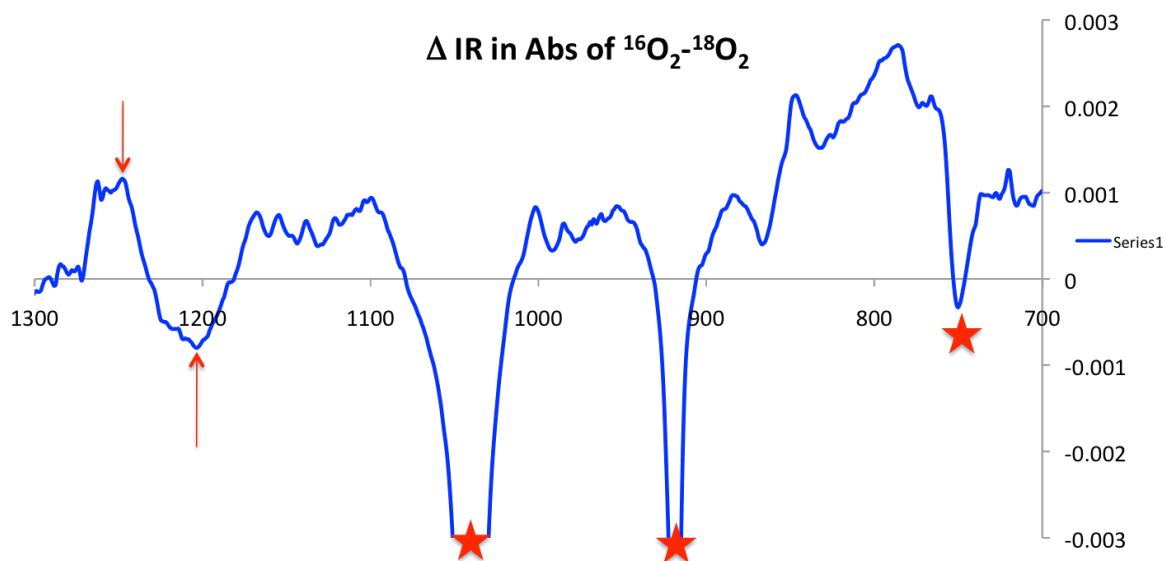


Figure S8.6 Liquid-cell IR difference spectrum, which shows O₂ vibrational shift from 1248 cm^{-1} to 1203 cm^{-1} (arrows) upon isotopic labeling of [Et₄N][**3**]. Stars indicate residual acetonitrile solvent peaks.

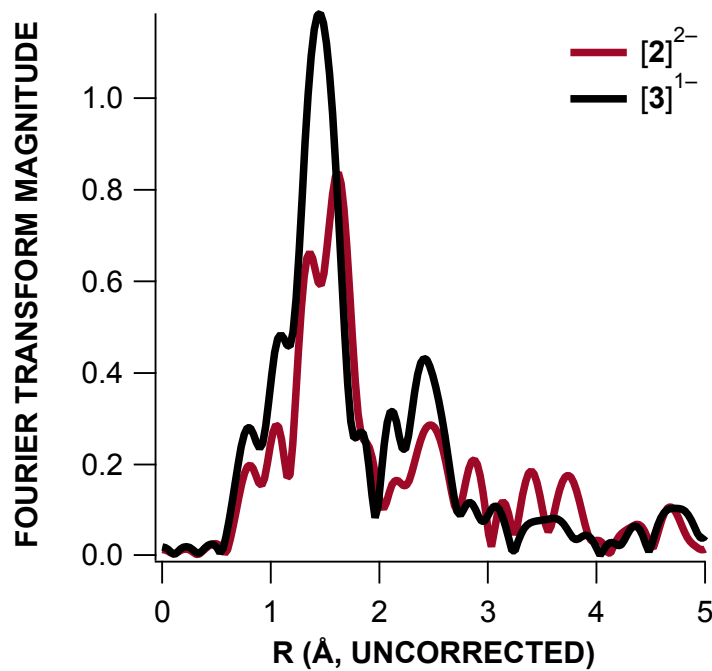


Figure S8.7 Overlay of Fourier-transformed EXAFS for $[2]^{2-}$ and $[3]^{1-}$. The Fourier transform amplitude of $[3]^{1-}$ is larger than that of $[2]^{2-}$ due to the proximity of the distal O atom in bent, end-on O_2^- coordination.

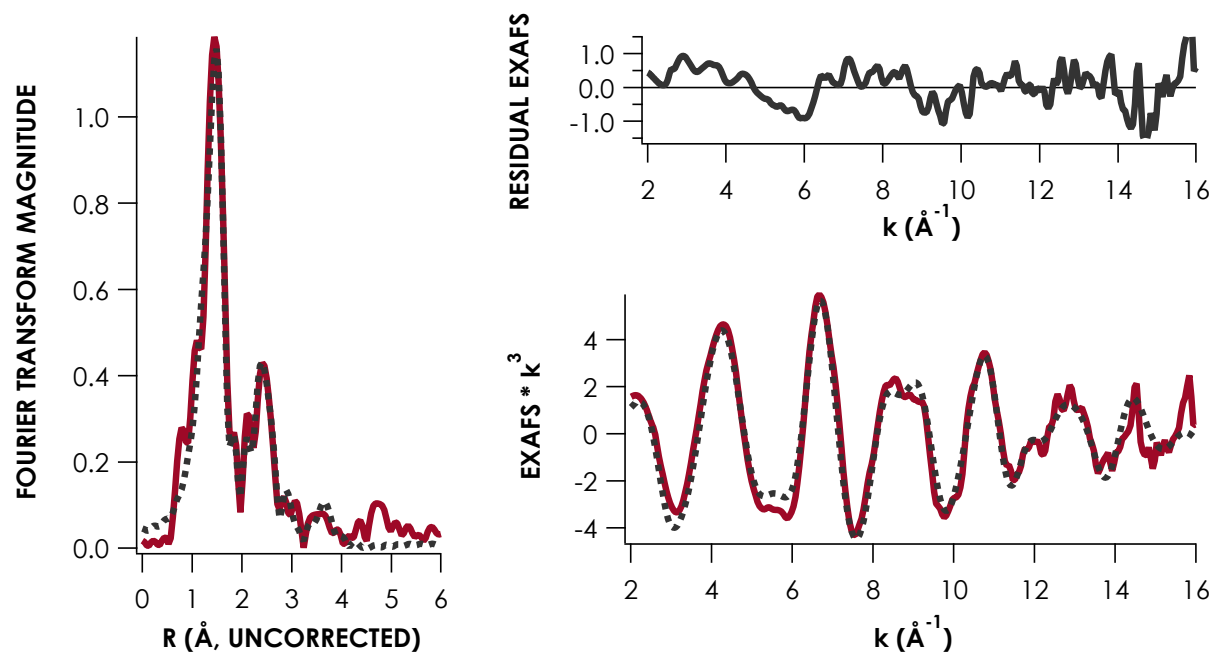


Figure S8.8 EXAFS and fits for $[3]^{1-}$. Experimental data are red, fits are dashed black. Inclusion of paths to model Co–C(isopropyl) scatter in both $[2]^{2-}$ and $[3]^{1-}$ improve fit quality. Similarity in extracted distances suggest that L binding is not significantly perturbed on going from the CN^- to the O_2 adducts, also in accord with calculated structures.

Table S8.1 EXAFS Fitting Parameters.

	Path	CN ^a	R (Å)	ΔR (Å)	σ (Å ²) ^b	$\Delta\sigma$ (Å ²) ^b	E ₀ (eV)	F (%) ^c
[2] ²⁻	Co–N/C	4	1.978	0.001	512	12	1.589	22.9
	Co–C	2	2.851	0.011	385	102		
	Co–N–C	14	3.069	0.017	636	282		
	Co–O/C	4	4.323	0.008	425	85		
	Co–C (isopropyl)	2	3.299	0.01	395	100		
	Co–C (isopropyl)	2	3.961	0.009	175	91		
	Co–C (isopropyl)	2	4.536	0.011	35	90		
[3] ¹⁻	Co–N/O	4	1.884	0.001	515	11	-4.29	24.41
	Co–C/O	3	2.779	0.003	301	22		
	Co–O/C (isopropyl)	4	4.082	0.009	445	87		
	Co–C (isopropyl)	2	3.196	0.02	915	269		
	Co–C (isopropyl)	2	3.596	0.013	451	133		

^aCoordination numbers (CN) were held constant during fits. Errors in CN are estimated to be on the order of 25%. ^bDebye-Waller factors (σ) are multiplied by 10⁵. ^cGoodness of fit is measured by F, defined as $F = [\sum k^6(\text{EXAFS}_{\text{expt}} - \text{EXAFS}_{\text{calc}})^2 / \sum k^6(\text{EXAFS}_{\text{expt}})^2]^{1/2}$.

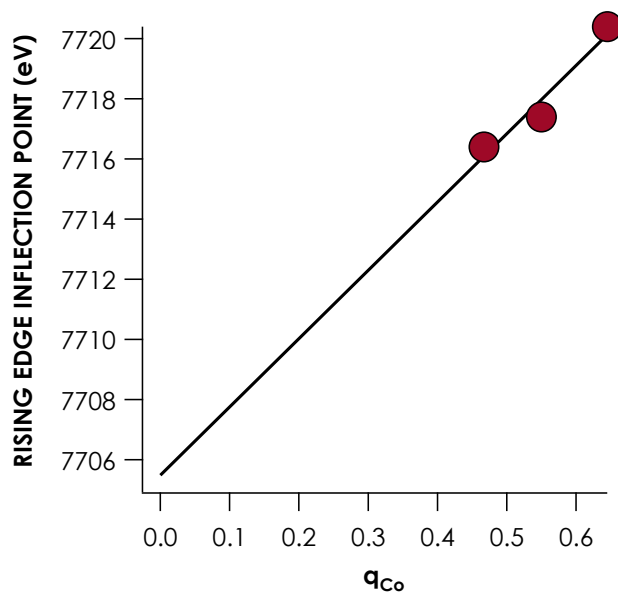


Figure S8.9 Experimental rising edge inflection point energies for the compounds under investigation correlate to Löwdin atomic charges for Co from B3LYP/def2-TZVP-ZORA calculations with $R^2 = 0.94$. The y-intercept is 7706 ± 3 eV, consistent with the rising edge inflection point energy for Co metal which is 7709 eV. Rising edges distinguish all three compounds from one another, at 7716.4 eV, 7717.4 eV, and 7720.4 eV for $[\mathbf{1}]^{2-}$, $[\mathbf{2}]^{2-}$, and $[\mathbf{3}]^{1-}$, respectively

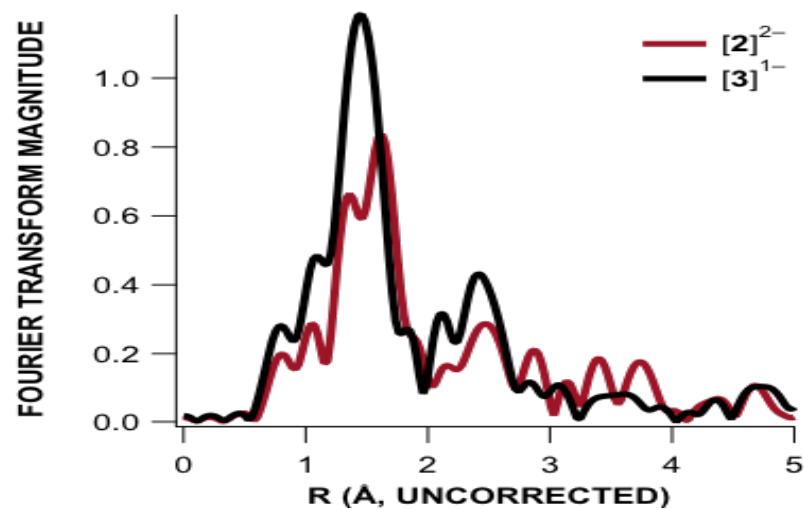


Figure S8.10 Correlation of experimental Co K pre-edge XAS energies to transition energies calculated by TDDFT. (B3LYP-def2-TZVP-ZORA).

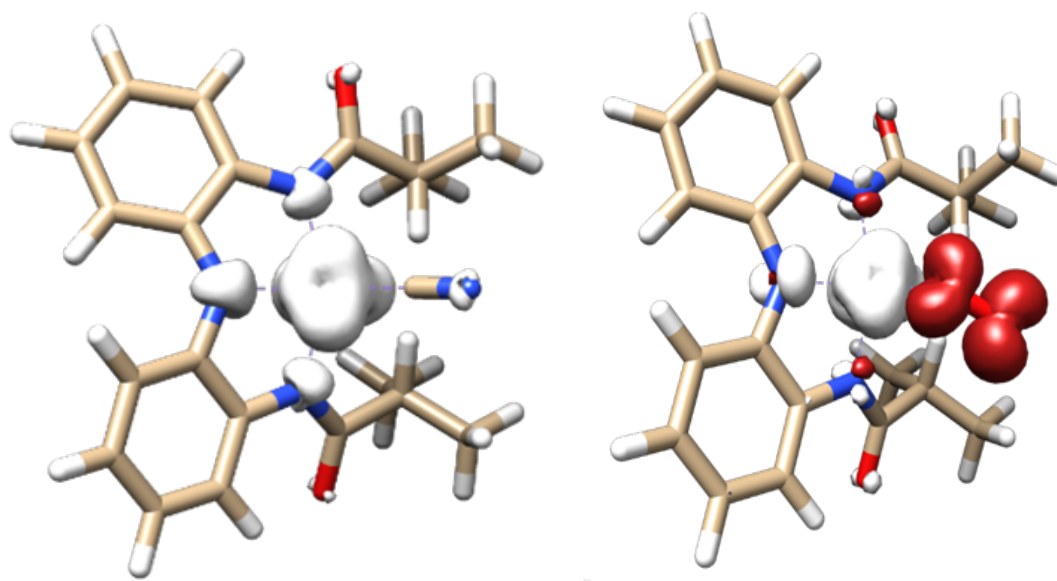


Figure S8.11 Spin densities of $[2]^{2-}$ (left) and $[3]^{1-}$ (right).

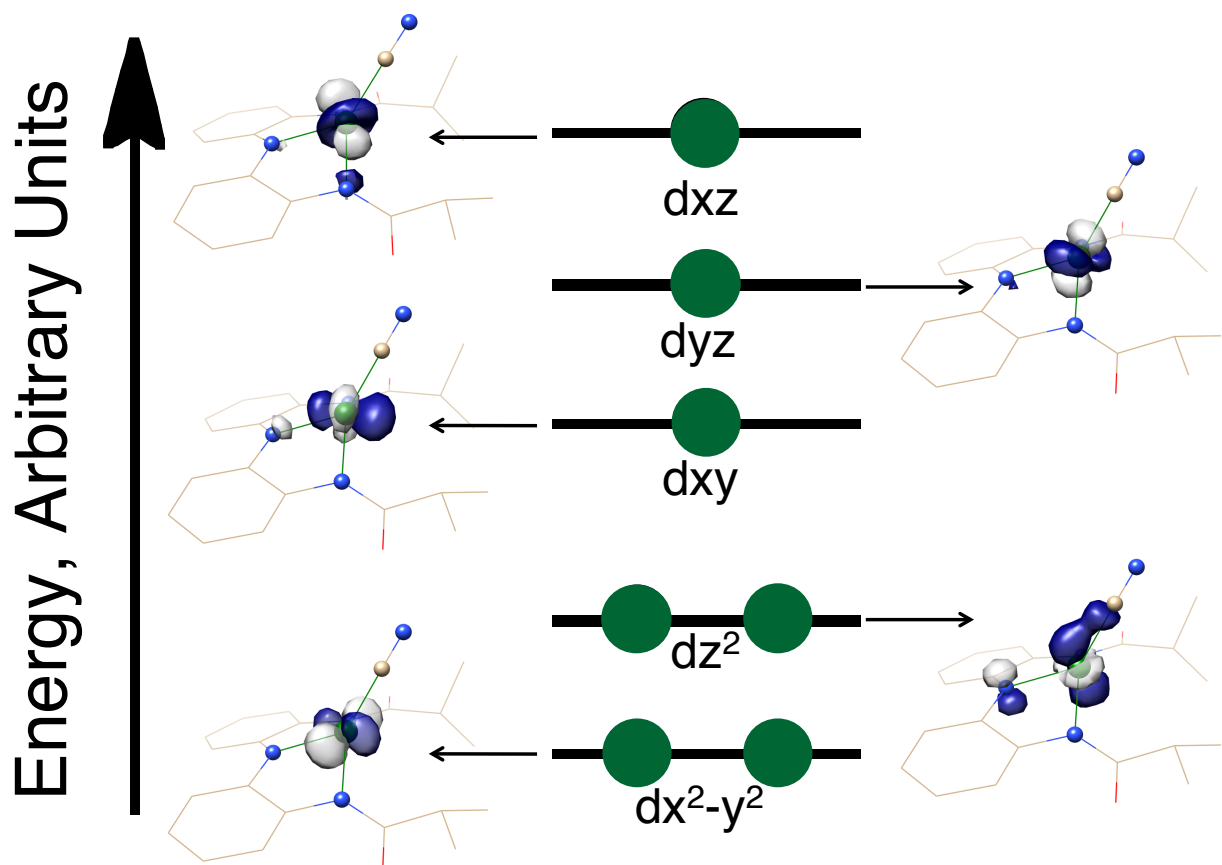


Figure S8.12 Molecular orbitals for $[2]^{2-}$.

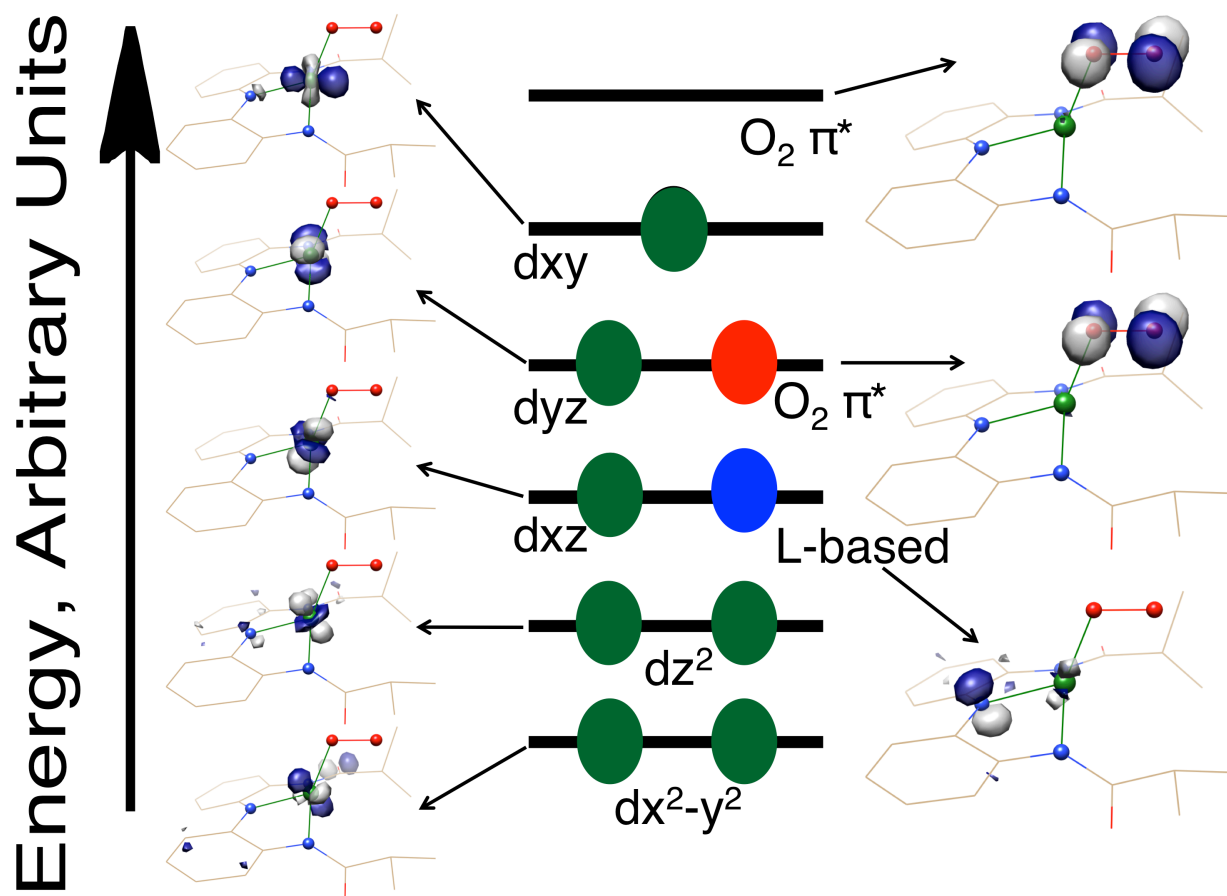


Figure S8.13 Molecular orbitals for $[3]^{1-}$. Green dots represent Co-based electrons, while the blue and red dots represent L-based and O_2 -based electrons, respectively.


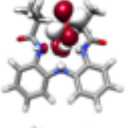
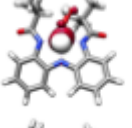
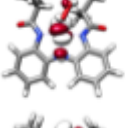
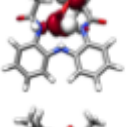
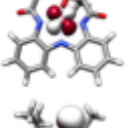
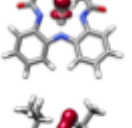
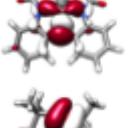
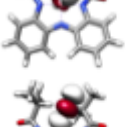
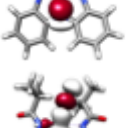
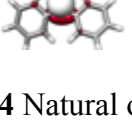
GROUND DOUBLET CONFIG WEIGHT, OCC #s				
	0.3973	0.3146	0.0863	
 56% Co d - [9% N p _x + 8.6% O ₂ π*]	0	0	0	
 19% Co d - 71% O ₂ π*	0	1	2	
 94% Co d	2	2	2	
 92% Co d	1	1	1	
 69% Co d + 30 % O ₂ π* 2		1	0	
 95% Co d	2	2	2	
 90% O ₂ π*	2	2	2	
 37% Co d + 29 % N π + 6% O ₂ π	2	2	2	
 80 % O ₂ π	2	2	2	
 20% N p _z - 60 % O ₂ σ	2	2	2	
 40% N p _z + 28 % O ₂ σ	2	2	2	

Figure S8.14 Natural orbitals from a SORCI calculation on $[3]^{1-}$. The weighted configurations for the lowest energy doublet state (the ground state of the ion) are shown.

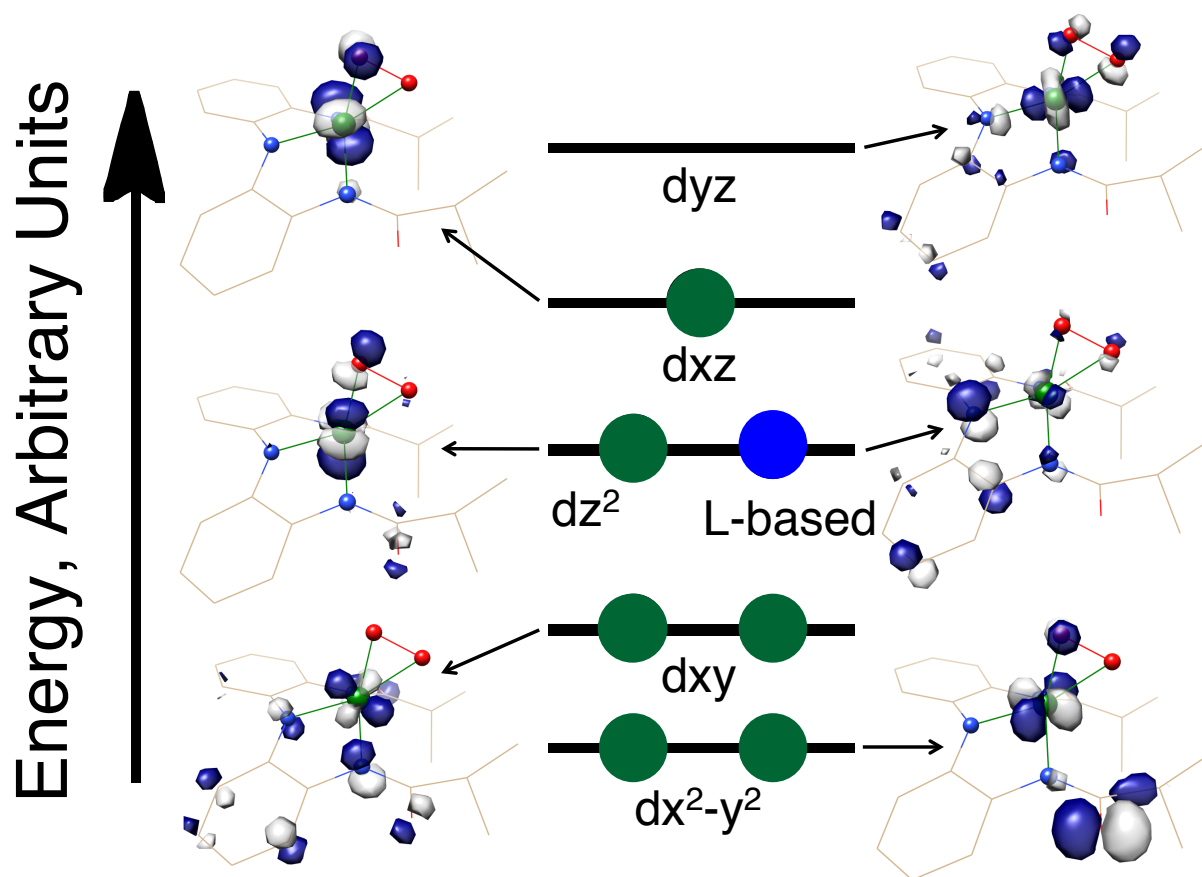


Figure S8.15 Molecular orbitals for $[3b]^{1-}$. Like $[3]^{1-}$, the ground state electron configuration of $[3b]^{1-}$ has one unpaired electron to give an overall spin state of $S = 1/2$. Upon examination of the frontier orbitals, the ground state is again a spin-coupled state in which the Co d_{z^2} orbital antiferromagnetically couples with a ligand-based orbital. There are no unpaired electrons on the O_2 -ligand, and the unpaired electron resides in the Co d_{yz} orbital. Therefore, $[3b]^{1-}$ is formally a peroxide complex with an unpaired electron on the L radical ($S = 1/2$) that couples to an intermediate-spin Co(III) center ($S = 1$) to form an overall $S = 1/2$ ground state.

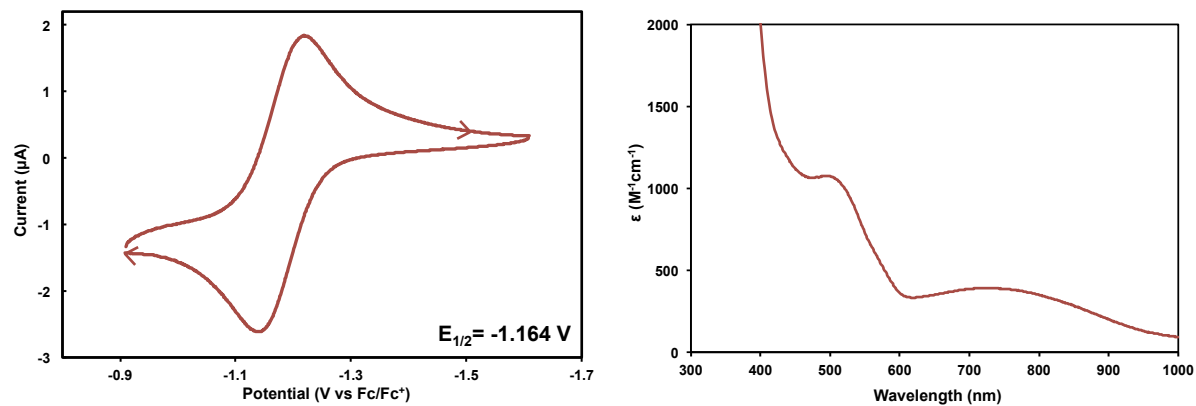


Figure S8.16 (Left) Cyclic voltammogram of $(\text{Et}_4\text{N})_2[\mathbf{2}]$ scan rate of 10 mV/s, with 0.1 M TBAPF₆ in CH₂Cl₂ as the supporting electrolyte, referenced vs. Fc/Fc⁺, with Ag/Ag⁺ as the reference electrode, using a glassy carbon working electrode. (Right) UV-visible absorption spectrum of $(\text{Et}_4\text{N})_2[\mathbf{2}]$ recorded in acetonitrile.

Table S8.2 Summary of X-ray crystallographic data for [Et₄N]₂[**2**]. [Et₄N]₂[**2**].

Compound	[Et ₄ N] ₂ [2]
Formula	C ₃₇ H ₆₂ CoN ₆ O ₂
Formula Weight g/mol	681.85
Temperature (K)	173(2)
Crystal system	Monoclinic
Space Group	<i>P</i> 2 ₁ / <i>n</i>
<i>a</i> , Å	11.150(5)
<i>b</i> , Å	16.151(7)
<i>c</i> , Å	22.24(1)
<i>α</i> °	90
<i>β</i> °	104.421(7)
<i>γ</i> °	90
<i>V</i> , Å ³	3879(3)
<i>Z</i>	4
Density (calculated)	1.168 g/cm ³
Crystal size	0.69 x 0.43 x 0.40 mm ³
Data / restraints / parameters	9540 / 88 / 466
Goodness-of-fit on <i>F</i> ²	1.075
<i>R</i> 1 ^a , <i>wR</i> 2 ^b (<i>I</i> < 2σ(<i>I</i>))	0.0482, 0.1210
<i>R</i> 1 ^a , <i>wR</i> 2 ^b (all data)	0.0721, 0.1353

^a*R*1 = Σ||*F*_o| - |*F*_c|| / Σ|*F*_o|. ^b*wR*2 = [Σ[*w*(*F*_o² - *F*_c²)²] / Σ[*w*(*F*_o²)²]]^{1/2}, *w* = 1/σ²(*F*_o²) + (*aP*)² + *bP*, where *P* = [max(0 or *F*_o²) + 2(*F*_c²)]/3.

Table S8.3 Selected experimental and calculated bond lengths (Å) and angles (°)for $[2]^{2-}$, $[3]^{1-}$, and $[3b]^{1-}$.

	2 (Experimental)	2 ($S = 1/2$)	2 ($S = 3/2$)	$[3]^{1-}$ ($S = 1/2$) [#]	$[3]^{1-}$ ($S = 3/2$)	$[3b]^{1-}$ ($S = 1/2$)	$[3b]^{1-}$ ($S = 3/2$)
Co–N1 (Å)	1.950(1)	1.905	1.965	1.849	1.972	1.91	1.949
Co–N2 / N3 (Å)	2.010(1) / 1.997(2)	1.959 / 1.965	2.067 / 2.074	1.900 / 1.922	2.003 / 2.015	2.014 / 2.021	2.014 / 2.100
Co–C21 (Å)	2.088(2)	1.962	2.058	---	---	---	---
Co–O1 / O2 (Å)	---	---	---	1.790	1.946	1.810 / 1.905	1.843 / 1.883
C21–N4 (Å)	1.073(3)	1.165	1.164	---	---	---	---
O1–O2 (Å)	---	---	---	1.327	1.322	1.399	1.393
N2–Co–N3 (°)	139.18(6)	159.8	134.4	149.3	138.0	131.4	127.9
N1–Co–C21(°)	134.86(6)	136.1	135.0	---	---	---	---
N1–Co–O1 / O2 (°)	---	---	---	132.7	126.4	117.9 / 162.0	111.7 / 150.4
Co–C21–N4(°)	179.5(2)	177.9	179.2	---	---	---	---
Co–O1–O2 (°)	---	---	---	123.7	115.4	64.3 / 71.5	66.5 / 69.6
N1–Co–N2 / N3 (°)	82.35(6) / 83.13(6)	84.1 / 84.2	81.9 / 82.2	84.7 / 83.5	81.8 / 82.6	81.6 / 82.8	80.0 / 80.1

[#] Optimization was performed with BP86. All other optimizations performed with B3LYP.

Table S8.4 Relative energies of ground states for $[\mathbf{3}]^{1-}$ and $[\mathbf{3b}]^{1-}$.[#]

	End-bound Superoxide [3]		Side-bound Peroxide [3b]	
	Doublet	Quartet	Doublet	Quartet
Gibbs Energy* (kJ/mol)	0	7.05	17.61	26.11
Favored Multiplicity?	Doublet ($\Delta G = 7.05$ kJ/mol)		Doublet ($\Delta G = 8.50$ kJ/mol)	
Favored Coordination?	End-bound Superoxide ($\Delta G = 17.61$ kJ/mol)			

* = Relative to End-bound doublet

[#] B3LYP was used for all of these calculations.

Note: Attempts were also made to optimize structures in which $[\mathbf{3}]^{1-}$ and $[\mathbf{3b}]^{1-}$ bind additional acetonitrile molecules to increase their coordination number. No such structures led to stable potential energy minima.

Table S8.5 Spin multiplicities and energies of 15 electronic states of $[\mathbf{3}]^{1-}$ calculated via SORCI using a CAS (17,11) reference.

State	Spin Multiplicity	Energy Relative to Ground State (cm^{-1})
0	2	0.0
1	4	4663.1
2	4	5168.5
3	2	5241.8
4	2	5327.9
5	2	5734.7
6	4	5917.2
7	4	6730.9
8	4	6972.3
9	2	7110.3
10	6	10150.5
11	6	10302.9
12	6	11896.1
13	6	12784.6
14	6	13176.0

XYZ Coordinates for quartet state $[\text{Co}(\text{L})\text{CN}]^{2-} [\mathbf{2}]^{2-}$

C -1.945046 0.588023 -2.011535
C -2.921736 0.532154 -3.026423
H -3.250848 -0.422644 -3.401363
C -3.491247 1.680319 -3.576690
H -4.246225 1.578838 -4.352625
C -3.092308 2.931187 -3.135772
H -3.541745 3.832826 -3.544024
C -2.101153 3.033661 -2.154217
H -1.758359 4.001396 -1.827261
C -1.490486 1.902726 -1.597771
C 0.202502 3.052727 -0.287250
C 1.437570 2.832684 0.608182
H 1.662698 1.766168 0.632583
C 2.655251 3.549875 0.019647
H 2.862393 3.206711 -0.997128
H 3.545047 3.353267 0.626893
H 2.481758 4.627435 -0.018057
C 1.153841 3.291463 2.041843
H 2.044112 3.169060 2.667996
H 0.357877 2.699215 2.490473
H 0.858188 4.344629 2.051089
C -1.208798 -1.788047 -1.779002
C -2.146454 -2.547982 -2.501684
H -3.092041 -2.106720 -2.775188
C -1.923254 -3.884987 -2.829755
H -2.679422 -4.429892 -3.389069
C -0.748557 -4.506725 -2.437580
H -0.557369 -5.544760 -2.696238
C 0.197936 -3.796084 -1.694890
H 1.112883 -4.270679 -1.379953
C 0.006968 -2.452193 -1.353550
C 2.167082 -2.049319 -0.324273
C 3.029174 -0.960392 0.347088
H 2.368236 -0.231061 0.817830
C 3.855895 -0.249828 -0.732481
H 4.485489 0.533302 -0.297083
H 3.209110 0.214426 -1.478882
H 4.504448 -0.967192 -1.243101
C 3.928183 -1.551227 1.430578
H 3.333136 -2.007563 2.224193
H 4.552759 -0.771243 1.879884
H 4.574052 -2.322007 1.005818
Co -0.098439 0.019308 0.065851
N -1.325235 -0.470021 -1.388456
N -0.414413 1.918745 -0.684872
N 0.908360 -1.661241 -0.614651
N -0.223639 -0.037537 3.284316
C -0.188543 -0.017325 2.121478
O -0.094648 4.231523 -0.562791
O 2.720288 -3.136771 -0.580455

XYZ Coordinates for doublet state end-on superoxide $[\text{Co}(\text{L})\text{O}_2]^{1-} [\mathbf{3}]^{1-}$

C	-1.773310211	0.627290480	-2.192512051
C	-2.700847022	0.561922200	-3.251877438
H	-2.921040313	-0.383427889	-3.739650616
C	-3.334281266	1.722148430	-3.700284709
H	-4.053900776	1.656567884	-4.518187328
C	-3.053056188	2.955320160	-3.102993290
H	-3.565966340	3.857899772	-3.439538302
C	-2.094248933	3.050587449	-2.088777154
H	-1.849676533	4.014642112	-1.654896977
C	-1.414373400	1.902144547	-1.649116258
C	0.310724593	2.954518484	-0.270379620
C	1.297753603	2.765066047	0.882315149
H	1.491558714	1.691219325	1.028066323
C	2.625602054	3.473271648	0.583928748
H	3.103123593	3.069475814	-0.320635160
H	3.320879559	3.341002966	1.425415956
H	2.463365709	4.549317204	0.431621886
C	0.653353505	3.302323005	2.175022170
H	1.343957590	3.175275868	3.021338899
H	-0.277480911	2.768121061	2.412588972
H	0.423873338	4.373328927	2.071512808
C	-1.147814666	-1.786078489	-1.826064507
C	-2.173195011	-2.518635667	-2.454366776
H	-3.057725182	-2.018012124	-2.838059993
C	-2.092352296	-3.911522876	-2.529985919
H	-2.900009095	-4.468039192	-3.008544184
C	-0.999694347	-4.588562952	-1.978553738
H	-0.943984011	-5.677020561	-2.036368196
C	0.021688691	-3.882381865	-1.333089128
H	0.864436031	-4.405952270	-0.891511001
C	-0.034488490	-2.482510330	-1.253720972
C	2.211205375	-1.953697053	-0.468541134
C	3.120589934	-0.844778938	0.060034111
H	2.486308247	-0.036950973	0.458425105
C	3.958466266	-0.294108596	-1.108940115
H	4.628214928	0.504630077	-0.757828232
H	3.319867444	0.119037746	-1.903255594
H	4.575582764	-1.093778868	-1.544305322
C	4.013575039	-1.364544446	1.193666082
H	3.410886601	-1.717401151	2.042225379
H	4.677271631	-0.564484327	1.553012871
H	4.636179581	-2.198158141	0.837889490
Co	0.033886774	0.042912184	-0.196880258
N	-1.089528016	-0.416767812	-1.592163449
N	-0.387360325	1.830785357	-0.681005208
N	0.885994426	-1.627238461	-0.618937358
O	0.916825313	-0.295674291	2.393781207
O	-0.114616442	-0.102404461	1.581293842
O	0.158071497	4.084671648	-0.764348381
O	2.700976972	-3.053118660	-0.795151629

XYZ Coordinates for doublet state side-on peroxide [Co(L)O₂]¹⁻ [**3b**]¹⁻

Co -0.171269 -0.081149 0.074362
O -1.367879 -0.619982 1.321098
O -0.232809 -0.132879 1.977451
N -0.667376 -0.234817 -1.764154
N -0.308974 1.881147 -0.358835
N 1.200164 -1.472074 -0.443229
C -1.428843 0.840780 -2.187319
C -2.352740 0.846974 -3.242977
H -2.535787 -0.059715 -3.801678
C -3.105715 1.979495 -3.509255
H -3.838030 1.965999 -4.308233
C -2.932018 3.123752 -2.729051
H -3.520728 4.010720 -2.937729
C -2.029682 3.144645 -1.674779
H -1.901133 4.032861 -1.079221
C -1.250890 2.011961 -1.375236
C 0.264939 2.960747 0.262283
C 1.372932 2.608873 1.263057
H 1.112629 1.659140 1.727605
C 2.696156 2.448504 0.494587
H 2.624611 1.667483 -0.263198
H 3.508670 2.181804 1.175469
H 2.965759 3.381617 -0.007490
C 1.499961 3.662443 2.359778
H 2.289476 3.377565 3.061367
H 0.570447 3.763533 2.923169
H 1.744685 4.638244 1.936938
C -0.005472 -1.172233 -2.483240
C -0.114919 -1.390855 -3.876770
H -0.750477 -0.749961 -4.467720
C 0.584943 -2.408024 -4.484443
H 0.476294 -2.575851 -5.550225
C 1.439581 -3.222561 -3.723503
H 1.985179 -4.025822 -4.206344
C 1.621201 -3.002156 -2.372850
H 2.294835 -3.622066 -1.806331
C 0.951895 -1.943857 -1.714688
C 2.044337 -2.141949 0.435818
C 2.666668 -1.284083 1.542163
H 2.239606 -0.287322 1.486200
C 4.177969 -1.190588 1.289797
H 4.645232 -0.546528 2.038808
H 4.400442 -0.771915 0.305399
H 4.638700 -2.178086 1.353364
C 2.385834 -1.864258 2.929671
H 1.318681 -1.833739 3.144776
H 2.902173 -1.276605 3.693664
H 2.741300 -2.895239 2.991210
O 0.020108 4.141627 0.009177
O 2.355922 -3.325452 0.347885

References.

- (1) Werner, A.; Mylius, A. *Z. Anorg. Chem.* **1898**, *16*, 245.
- (2) Tsumaki, T. *Bull. Chem. Soc. Jpn.* **1938**, *13*, 252.
- (3) Schaefer, W. P.; Marsh, R. E. *J. Am. Chem. Soc.* **1966**, *88*, 178.
- (4) Floriani, C.; Calderazzo, F. *J. Chem. Soc. A* **1969**, 946.
- (5) Rodley, G. A.; Robinson, W. T. *Nature* **1972**, *235*, 438.
- (6) Fritch, J. R.; Christoph, G. G.; Schaefer, W. P. *Inorg. Chem.* **1973**, *12*, 2170.
- (7) Collman, J. P.; Gagne, R. R.; Kouba, J.; Ljusberg-Wahren, H. *J. Am. Chem. Soc.* **1974**, *96*, 6800.
- (8) Gall, R. S.; Rogers, J. F.; Schaefer, W. P.; Christoph, G. G. *J. Am. Chem. Soc.* **1976**, *98*, 5135.
- (9) James, B. R. In *The Porphyrins*; Dolphin, D., Ed.; Academic Press: New York, 1979; Vol. 5, p 207.
- (10) Jones, R. D.; Summerville, D. A.; Basolo, F. *Chem. Rev.* **1979**, *79*, 139.
- (11) Bailey, C. L.; Drago, R. S. *Coord. Chem. Rev.* **1987**, *79*, 321.
- (12) Busch, D. H.; Alcock, N. W. *Chem. Rev.* **1994**, *94*, 585.
- (13) Hikichi, S.; Akita, M.; Moro-oka, Y. *Coord. Chem. Rev.* **2000**, *198*, 61.
- (14) Cho, J.-H.; Sarangi, R.; Kang, H.-Y.; Lee, J.-Y.; Kubo, M.; Ogura, T.; Solomon, E. I.; Nam, W.-W. *J. Am. Chem. Soc.* **2010**, *132*, 16977.
- (15) Tiné, M. R. *Coord. Chem. Rev.* **2012**, *256*, 316.
- (16) Smith, T. D.; Pilbrow, J. R. *Coord. Chem. Rev.* **1981**, *39*, 295.
- (17) Mandal, A. K.; Iqbal, J. *Tetrahedron* **1997**, *53*, 7641.
- (18) Sharma, V. B.; Jain, S. L.; Sain, B. *Tetrahedron Lett.* **2003**, *44*, 383.
- (19) Schultz, M. J.; Sigman, M. S. *Tetrahedron* **2006**, *62*, 8227.
- (20) Merkx, M.; Kopp, D. A.; Sazinsky, M. H.; Blazyk, J. L.; Müller, J.; Lippard, S. J. *Angew. Chem. Int. Ed.* **2001**, *40*, 2782.

- (21) Solomon, E. I.; Heppner, D. E.; Johnston, E. M.; Ginsbach, J. W.; Cirera, J.; Qayyum, M.; Kieber-Emmons, M. T.; Kjaergaard, C. H.; Hadt, R. G.; Tian, L. *Chem. Rev.* **2014**, *114*, 3659.
- (22) Wang, W.; Liang, A. D.; Lippard, S. J. *Acc. Chem. Res.* **2015**, *48*, 2632.
- (23) Jazdzewski, B. A.; Tolman, W. B. *Coord. Chem. Rev.* **2000**, *200-202*, 633.
- (24) Meunier, B.; de Visser, S. I. P.; Shaik, S. *Chem. Rev.* **2004**, *104*, 3947.
- (25) Denisov, I. G.; Makris, T. M.; Sligar, S. G.; Schlichting, I. *Chem. Rev.* **2005**, *105*, 2253.
- (26) *Cytochrome P450: Structure, Mechanism, and Biochemistry*; 3rd ed.; Ortiz de Montellano, P. R., Ed.; Kluwer/Plenum: New York, 2005.
- (27) Rose, E.; Andrioletti, B.; Zrig, S.; Quelquejeu-Etheve, M. *Chem. Soc. Rev.* **2005**, *34*, 573.
- (28) Chirik, P. J.; Wieghardt, K. *Science* **2010**, *327*, 794.
- (29) Sharma, S. K.; May, P. S.; Jones, M. B.; Lense, S.; Hardcastle, K. I.; MacBeth, C. E. *Chem. Commun.* **2011**, *47*, 1827.
- (30) Patra, T.; Manna, S.; Maiti, D. *Angew. Chem. Int. Ed.* **2011**, *50*, 12140.
- (31) Seo, M. S.; Kim, J. Y.; Annaraj, J.; Kim, Y.; Lee, Y.-M.; Kim, S.-J.; Kim, J.; Nam, W. *Angew. Chem., Int. Ed.* **2007**, *46*, 377.
- (32) Jo, Y.; Annaraj, J.; Seo, M. S.; Lee, Y.-M.; Kim, S. Y.; Cho, J.; Nam, W. *J. Inorg. Biochem.* **2008**, *102*, 2155.
- (33) Cho, J.; Sarangi, R.; Nam, W. *Acc. Chem. Res.* **2012**, *45*, 1321.
- (34) Cho, J.; Kang, H. Y.; Liu, L. V.; Sarangi, R.; Solomon, E. I.; Nam, W. *Chem. Sci.* **2013**, *4*, 1502.
- (35) Shokri, A.; Que, L. *J. Am. Chem. Soc.* **2015**, *137*, 7686.
- (36) Donoghue, P. J.; Gupta, A. K.; Boyce, D. W.; Cramer, C. J.; Tolman, W. B. *J. Am. Chem. Soc.* **2010**, *132*, 15869.
- (37) Pirovano, P.; Magherusan, A. M.; McGlynn, C.; Ure, A.; Lynes, A.; McDonald, A. R. *Angew. Chem. Int. Ed.* **2014**, *53*, 5946.
- (38) Ure, A. D.; McDonald, A. R. *Synlett* **2015**, *26*, 2060.

- (39) Classification of reactive metal-oxygen species as electrophilic impolies reactivity such as O-atom transfer, hydrogen atom abstraction, and electron transfer. Nucleophilic metal-oxygen species react with electron-deficient substrates such as 2-PPA to produce acetophenone.
- (40) The τ_8 value distinguishes between "pinched" tetrahedral and sawhorse geometries. τ_8 alues close to 1.0 indicate tetrahedral geometry, while τ_8 values between 0.45-0.63 are best described as distorted sawhorse geometries, see: Reineke, M. H.; Sampson, M. D.; Rheingold, A. L.; Kubiak, C. P. *Inorg. Chem.* **2015**, *54*, 3211.
- (41) Nguyen, A. I.; Hadt, R. G.; Solomon, E. I.; Tilley, T. D. *Chem. Sci.* **2014**, *5*, 2874.
- (42) Nakamoto, K. *Infrared and Raman Spectra of Inorganic and Coordination Compounds. Part B: Applications in Coordination, Organometallic, and Bioinorganic Chemistry*; Wiley: New York, 1997.
- (43) Nelson, K. J.; Giles, I. D.; Shum, W. W.; Arif, A. M.; Miller, J. S. *Angew. Chem. Int. Ed.* **2005**, *44*, 3129.
- (44) Scott, T. A.; Berlinguette, C. P.; Holm, R. H.; Zhou, H.-C. *Proc. Natl. Acad. Sci. U.S.A.* **2005**, *102*, 9741.
- (45) Pollock, C. J.; Delgado-Jaime, M. U.; Atanasov, M.; Neese, F.; DeBeer, S. *J. Am. Chem. Soc.* **2014**, *136*, 9453.
- (46) For calculations ruling out a possible Co(III) side-on peroxide assignment for $[3]^{1-}$, see SI.
- (47) Hehre, W. J. R., L.; Schleyer, P. V. R.; Pople, J. A. *Ab Initio Molecular Orbital Theory*; Wiley: New York, 1986.
- (48) The ground state of $[3]^{1-}$ was also assessed with SORCI calculations (see SI).
- (49) Tomson, N. C.; Williams, K. D.; Dai, X.; Sproules, S.; DeBeer, S.; Warren, T. H.; Wieghardt, K. *Chem. Sci.* **2015**, *6*, 2474.
- (50) Walroth, R. C.; Uebler, J. W. H.; Lancaster, K. M. *Chem. Commun.* **2015**, *51*, 9864.
- (51) Evans, D. F. *J. Chem. Soc.* **1959**, 2003.
- (52) Bain, G. A.; Berry, J. F. *J. Chem. Ed.* **2008**, *85*, 532.
- (53) Stoll, S.; Schweiger, A. *J. Magn. Reson.* **2006**, *178*, 42.
- (54) Bruker-AXS. *APEX2*. v. 2014.11-0.

- (55) Bruker-AXS. *SAINT*. v. 7.68A; 2009.
- (56) Krause, L.; Herbst-Irmer, R.; Sheldrick, G. M.; Stalke, D. *J. Appl. Cryst.* **2015**, *48*, 3.
- (57) Sheldrick, G. M. *XS*.; Georg-August-Universitat: Gottingen, Germany, 2008.
- (58) Sheldrick, G. M. *Acta Cryst. A* **2008**, *64*, 112.
- (59) Dolomanov, O. V., Bourhis, L. J., Gildea, R. J., Howard, J. A. K., Puschmann, H. *J. Appl. Cryst.* **2009**, *42*, 339.
- (60) Sheldrick, G. M. *Acta Cryst. C* **2015**, *71*, 3.
- (61) Delgado-Jaime, M. U.; Mewis, C. P.; Kennepohl, P. *J. Synchrotron Radiat.* **2010**, *17*, 132.
- (62) Neese, F. *WIREs Comput. Mol. Sci.* **2012**, *2*, 73.
- (63) Neese, F. *ORCA, An Ab Initio, Density Functional and Semi-empirical Program Package*; Max-Planck-Institute for Bioinorganic Chemistry: Ruhr, Germany, 2012.
- (64) Perdew, J. P. *Phys. Rev. B* **1986**, *33*, 8822.
- (65) Becke, A. D. *Phys. Rev. A* **1988**, *38*, 3098.
- (66) van Lenthe, E.; Snijders, J. G.; Baerends, E. J. *J. Chem. Phys.* **1993**, *99*, 4597.
- (67) van Wullen, C. *J. Chem. Phys.* **1998**, *109*, 392.
- (68) Schafer, A.; Horn, H.; Ahlrichs, R. *J. Chem. Phys.* **1992**, *97*, 2571.
- (69) Pantazis, D. A.; Chen, X.-Y.; Landis, C. R.; Neese, F. *J. Chem. Theory Comput.* **2008**, *4*, 908.
- (70) Klamt, A.; Schuurmann, G. *J. Chem. Soc., Perkin Trans. 2* **1993**, 799.
- (71) Sinnecker, S.; Rajendran, A.; Klamt, A.; Diedenhofen, M.; Neese, F. *J. Phys. Chem. A* **2006**, *110*, 2235.
- (72) DeBeer George, S.; Petrenko, T.; Neese, F. *J. Phys. Chem. A* **2008**, *112*, 12936.
- (73) Vosko, S. H.; Wilk, L.; Nusair, M. *Can. J. Phys.* **1980**, *58*, 1200.
- (74) Lee, C.; Yang, W.; Parr, R. G. *Phys. Rev. B* **1988**, *37*, 785.
- (75) Becke, A. D. *J. Chem. Phys.* **1993**, *98*, 1372.

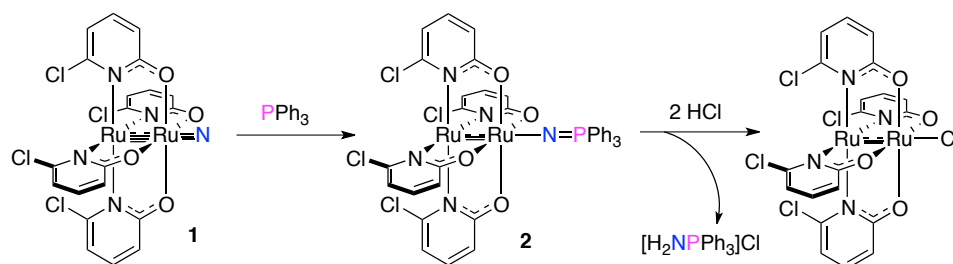
- (76) Stephens, P. J.; Devlin, F. J.; Chabalowski, C. F.; Frisch, M. J. *J. Chem. Phys.* **1994**, *98*, 11623.
- (77) Weigend, F.; Ahlrichs, R. *Phys. Chem. Chem. Phys.* **2005**, *7*, 3297.
- (78) Dunning, T. H. *J. Chem. Phys.* **1989**, *90*, 1007.
- (79) Kendall, R. A.; Dunning, T. H.; Harrison, R. J. *J. Chem. Phys.* **1992**, *96*, 6796.
- (80) Woon, D. E.; Dunning, T. H. *J. Chem. Phys.* **1993**, *98*, 1358.
- (81) Woon, D. E.; Dunning, T. H. *J. Chem. Phys.* **1994**, *100*, 2975.
- (82) Neese, F.; Wennmohs, F.; Hansen, A.; Becker, U. *Chem. Phys.* **2009**, *356*, 98.
- (83) Weigend, F. *Phys. Chem. Chem. Phys.* **2006**, *8*, 1057.
- (84) Neese, F. *J. Phys. Chem. Solids* **2004**, *65*, 781.
- (85) Pettersen, E. F.; Goddard, T. D.; Huang, C. C.; Couch, G. S.; Greenblatt, D. M.; Meng, E. C.; Ferrin, T. E. *J. Comput. Chem.* **2004**, *25*, 1605.
- (86) *Avogadro: An open-source molecular building and visualization tool*; 1.0.3.
<http://avogadro/openmolecules.net/>.
- (87) Neese, F. *J. Chem. Phys.* **2003**, *119*, 9428.
- (88) Neese, F. *J. Am. Chem. Soc.* **2006**, *128*, 10213.
- (89) Sorrell, T. N.; Malachowski, M. R. *Inorg. Chem.* **1983**, *22*, 1883.

Appendix 1

Attempts to Characterize the $\text{Ru}_2(\text{chp})_4\text{NPPH}_3$ Intermediate in the Synthetic Cycle of Chapter 3.

A1.1 Background.

Chapter 3 discussed our efforts to characterize a synthetic cycle for intermolecular nitrogen atom transfer.¹ While the starting material, products, and Ru_2 nitride intermediate $\text{Ru}_2(\text{chp})_4\text{N}$ (**1**) were successfully characterized for this reaction, we also speculated as to the existence of the phosphinimine intermediate $\text{Ru}_2(\text{chp})_4\text{NPPH}_3$ (**2**), which should exist after addition of PPh_3 to the nitride intermediate² and before cleavage of the $\text{Ru}_2\text{--N}$ bond by HCl (Scheme 1). Due to the difficulty in characterizing this species in-situ, attempts were made to purposefully synthesize this intermediate and then compare its spectroscopic features to those of the reaction mixture.

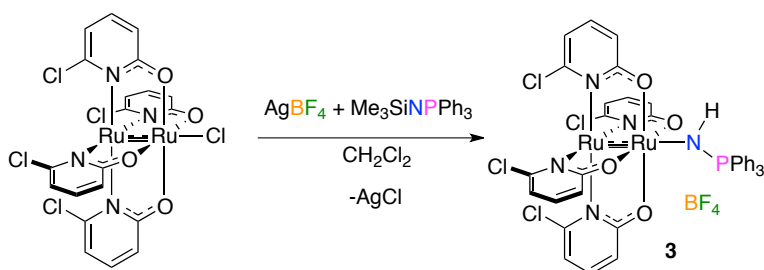


Scheme A1.1 Proposed formation of **2** from **1** and subsequent formation of $\text{Ru}_2(\text{chp})_4\text{Cl}$.

A1.2 Results and Discussion.

$\text{Ru}_2(\text{chp})_4\text{Cl}$ was exposed simultaneously to AgBF_4 (to remove the bound axial chloride) and $\text{Me}_3\text{SiNPPH}_3$, with the anticipation of generating $\text{Ru}_2(\text{chp})_4\text{NPPH}_3$ (**2**), Me_3SiF , BF_3 , and AgCl . After filtration to remove the white precipitate (presumably AgCl), concentration of the

filtrate, and layering with dry hexanes, crystals of this reaction mixture unexpectedly produced $[\text{Ru}_2(\text{chp})_4\text{NHPPH}_3][\text{BF}_4]$ (**3**) (Scheme A1.2, Figure A1.1).



Scheme A1.2 Synthetic formation of unexpected product **3** (instead of **2**).

Two distinct molecules are present in the asymmetric unit of **3**. The phosphinamine nitrogen atom is protonated, presumably from the dichloromethane solvent due to the basicity of the complex, and the Ru–N–P angle is bent (Table 1).

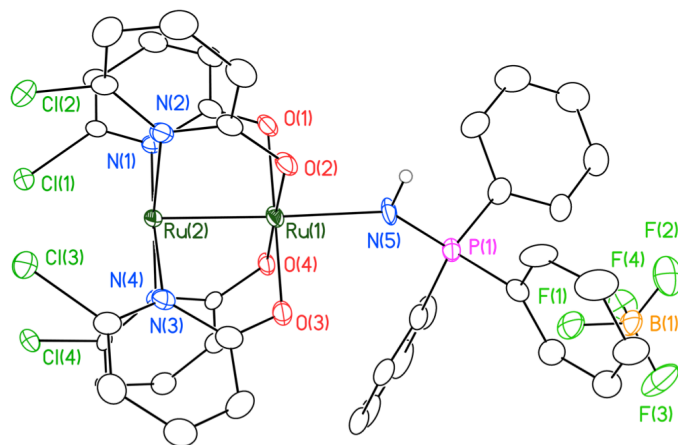


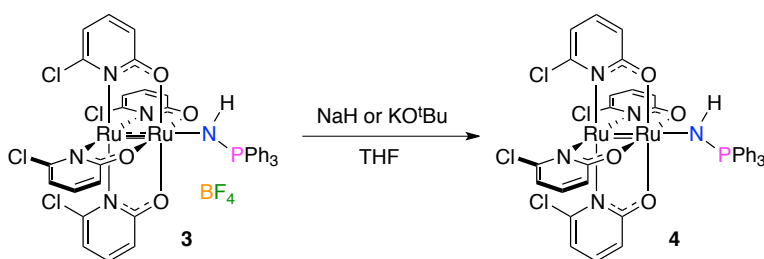
Figure A1.1 Thermal ellipsoid plot of $[\text{Ru}_2(\text{chp})_4\text{NHPPH}_3][\text{BF}_4]$ (**3**) with ellipsoids drawn at the 50% probability level. Hydrogen atoms (except on N(5)) and molecules of solvation omitted for clarity.

Subsequent attempts to deprotonate **3** to form **2** failed. **3** was dissolved in THF and exposed to either NaH or KO^tBu , allowed to stir overnight, and then filtered and layered with

hexanes (Scheme A1.3). In both cases, rather than deprotonating the Ru_2^{5+} species, the reagents reduced the metal center to Ru_2^{4+} , and the N_{axial} atom remained protonated (Figure A1.2).

Crystals for **4** are non-merohedral twins. As expected, upon reduction from **3** to **4**, the Ru–Ru bond distance slightly contracts (Table A1.1), although not by a statistically relevant amount.

Additionally the Ru– N_{axial} distance elongates. The N–P distance also slightly contracts here, while the angles do not change significantly. Deprotonation attempts of **3** with MeLi degraded the Ru_2 species. No other reagents were tested.



Scheme A1.3 Formation of **4** from **3**, rather than **2**.

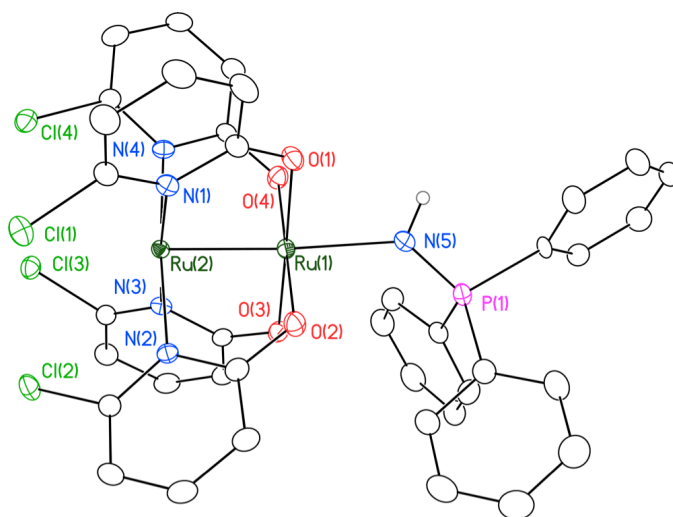


Figure A1.2 Thermal ellipsoid plot of $\text{Ru}_2(\text{chp})_4\text{NHPPH}_3$ (**4**) with ellipsoids drawn at the 50% probability level. Hydrogen atoms (except on N(5)) and molecules of solvation omitted for clarity.

Table A1.1 Selected bond lengths and angles for **3** and **4**.

Bond length or angle	[Ru ₂ (chp) ₄ NHPPPh ₃][BF ₄] (3)		Ru ₂ (chp) ₄ NHPPPh ₃ (4)
	Molecule 1	Molecule 2	
Ru(1)–Ru(2) [Å]	2.2797(6)	2.2870(6)	2.2750(6)
Ru(1)–N(5) [Å]	2.152(4)	2.143(4)	2.210(3)
N(5)–P(1) [Å]	1.590(4)	1.597(4)	1.581(3)
Ru(2)–Ru(1)–N(5) [°]	173.3(1)	176.9(1)	175.49(7)
Ru(1)–N(5)–P(1) [°]	139.6(2)	136.2(2)	134.8(2)

A1.3 Supplementary Information.

Materials and Methods. All syntheses and product workup/isolation were conducted under a dry N₂ atmosphere using Schlenk line or glovebox techniques. Dichloromethane (CH₂Cl₂) was distilled over CaH₂ prior to use. Hexanes and THF were obtained from a vacuum atmospheres solvent system, degassed, and passed through activated alumina prior to use. All materials were commercially available and used as received, unless otherwise noted. Ru₂(chp)₄Cl was prepared according to literature procedures.^{1,3} Crystals of **3** and **4** were grown from the reaction mixture by slow diffusion into dry hexanes.

[Ru₂(chp)₄NHPPPh₃][BF₄] (**3**). Ru₂(chp)₄Cl (36.9 mg, 0.049 mmol, 1 eq.), AgBF₄ (17.1 mg, 0.0878 mmol, 1.78 eq.), and Me₃SiNPPPh₃ (18.5 mg, 0.0529 mmol, 1.07 eq.) were dissolved in 15 mL of freshly distilled CH₂Cl₂ and allowed to stir for 24 h at RT under inert N₂. A white precipitate (AgCl) formed along with color change from green to brown. The reaction mixture was filtered through a fine sintered glass frit. The filtrate was removed under reduced pressure, and the resulting solid was washed with hexanes and collected. Crystals suitable for X-ray diffraction were grown by slow diffusion of a dry CH₂Cl₂ solution into hexanes at RT.

Ru₂(chp)₄NHPPPh₃ (**4**). [Ru₂(chp)₄NHPPPh₃][BF₄] (84.2 mg, 0.0779 mmol, 1 eq.) and NaH (10.7 mg, 0.445 mmol, 5.72 eq.) were dissolved in 10 mL of dry THF and allowed to stir for overnight at RT under inert N₂. Color change from purple to red. The reaction mixture was filtered through a fine sintered glass frit. The filtrate was reduced, and layered with dry hexanes to crystallize. Crystals suitable for X-ray diffraction were grown by slow diffusion of a dry THF solution into hexanes at RT.

Route #2: Ru₂(chp)₄NHPPPh₃ (**4**). [Ru₂(chp)₄NHPPPh₃][BF₄] (39.0 mg, 0.0361 mmol, 1 eq.) and KO^tBu (5.3 mg, 0.0472 mmol, 1.31 eq.) were dissolved in dry THF and allowed to stir overnight at RT under inert N₂. Color change from purple to brown. The reaction mixture was filtered through a fine sintered glass frit. The filtrate, which then appeared orange in color, was concentrated and layered with dry hexanes. Formation of **4** is confirmed by X-ray crystallography.

References.

- (1) Corcos, A. R.; Long, A. K. M.; Guzei, I. A.; Berry, J. F. *Eur. J. Inorg. Chem.* **2013**, 3808.
- (2) Scepaniak, J. J.; Fulton, M. D.; Bontchev, R. P.; Duesler, E. N.; Kirk, M. L.; Smith, J. M. *J. Am. Chem. Soc.* **2008**, *130*, 10515.
- (3) Chakravarty, A. R.; Cotton, F. A.; Tocher, D. A. *Inorg. Chem.* **1985**, *24*, 1263.

Appendix 2

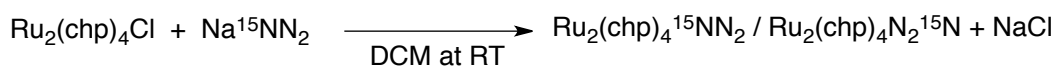
Attempts at Additional Stoichiometric and Catalytic Reactivity with a Proposed Ru₂ Nitride Intermediate.

A2.1 Background.

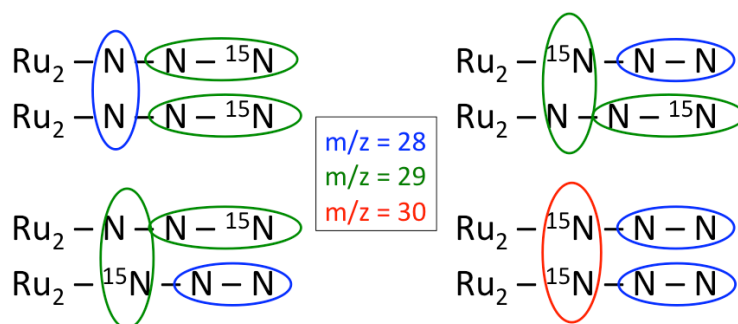
After successfully characterizing a synthetic cycle for intermolecular nitrogen atom transfer (Chapter 3),¹ attempts were made to broaden the substrate scope. However, none of the additional reagents tested, including cyclohexene, styrene, ethylbenzene, anthracene, triphenylmethane, adamantane, benzene, cyclohexane, triphenylsilane, and triethylsilane, reacted with Ru₂(chp)₄N₃ (**1**) to generate the corresponding activated product. We previously postulated that the relatively low conversion of PPh₃ to [H₂NPPH₃]Cl using **1** could be due to nitride dimerization and subsequent generation of N₂. If this is the case, then it could also explain the lack of reactivity between **1** and the reagents mentioned above.

A2.2 Results and Discussion.

To test this scenario, we used Na¹⁵NN₂ to synthesize the analogous Ru₂(chp)₄¹⁵NN₂ complex from Ru₂(chp)₄Cl (**2**) (Scheme 1), which binds the single ¹⁵N atom to the Ru center 50% of the time. After room temperature solution-phase photolysis, we then conducted GC-MS analysis of the headspace to look for *m/z* = 30 amu, corresponding to two Ru₂¹⁵N species reacting together to form ¹⁵N₂ (Scheme A2.2). As seen in Figure A2.1, we can confirm that ¹⁵N₂ is generated, so the limited intermolecular reactivity of **1** is in fact due to nitride dimerization.



Scheme A2.1 Formation of Ru₂(chp)₄¹⁵NN₂ from Ru₂(chp)₄Cl (**2**).



Scheme A2.2 Possible dimerization products and their corresponding masses. Only $m/z = 30$ amu is definitive for nitride dimerization.

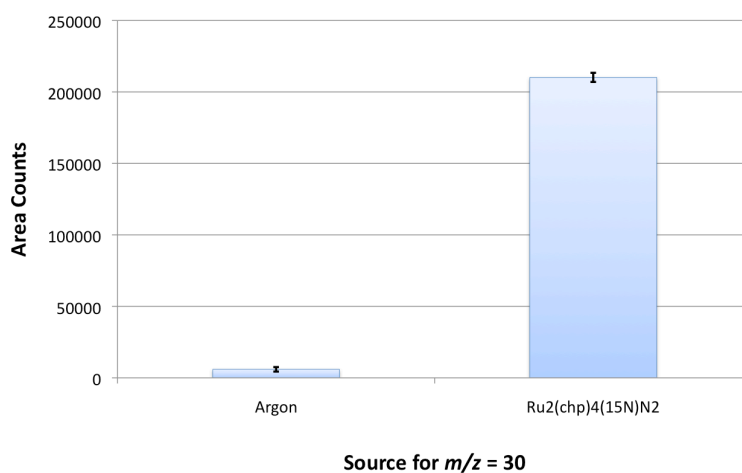
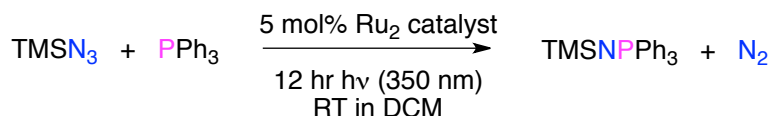


Figure A2.1 Headspace analysis by GC-MS after photolysis of $\text{Ru}_2(\text{chp})_4({}^{15}\text{N})\text{N}_2$ in solution at room temperature. ${}^{15}\text{N}_2$, corresponding to $m/z = 30$, is clearly generated.

Attempts were also made to turn the synthetic cycle (Chapter 3) into a catalytic cycle. The synthetic cycle utilized both NaN_3 and HCl , which when mixed together would generate explosive hydrazoic acid, and would therefore not be compatible reagents in a catalytic cycle. Instead, attempts moving forward utilized TMSN_3 as the new azide source. Multiple Ru_2 catalysts were tested, including known $\text{Ru}_2(\text{chp})_4\text{Cl}$ (**2**),² $\text{Ru}_2(\text{chp})_4\text{N}_3$ (**1**),¹ $\text{Ru}_2(\text{ap})_4\text{Cl}$ (**3**),³ and

new $\text{Ru}_2(\text{ap})_4\text{N}_3$ (**4**) (Scheme A2.3). Reactions were monitored by ^{31}P NMR spectroscopy and the results are shown in Figure A2.2. In all cases Ru_2 clearly catalyzed the conversion of PPh_3 , but the expected product of TMSNPPH_3 was not identified. Instead, the hydrolysis products $[\text{H}_2\text{NPPH}_3]\text{Cl}$ and OPPh_3 were generated. The best catalyst for this reaction was **2**, as it converted all of the PPh_3 to new products.



Scheme A2.3 Conditions and proposed products for complete catalytic nitrogen atom transfer.

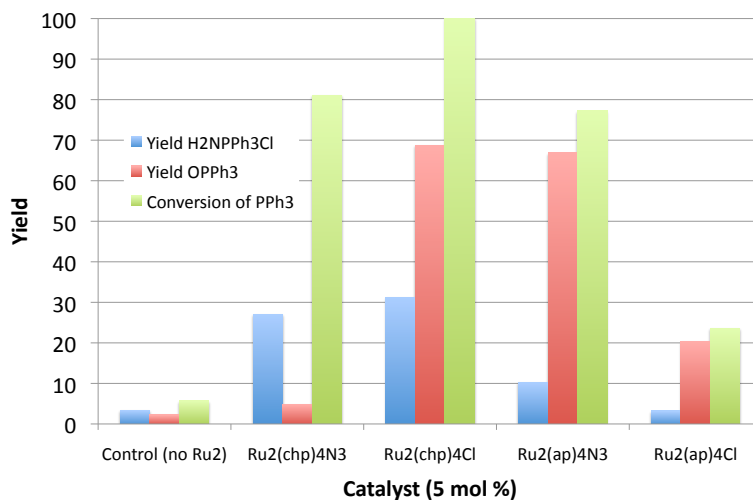


Figure A2.2 Yield and identification of products generated after performing catalytic reaction shown in Scheme A2.1. Unexpected products of $[\text{H}_2\text{NPPH}_3]\text{Cl}$ and OPPh_3 were characterized.

A2.3 Future Directions.

Many aspects of this reaction still need to be determined, including whether this reaction actually proceeds via an Ru_2 nitride (Figure A2.3, left), or if it actually occurs via a nitrene intermediate (Figure A2.3, right). One piece of evidence against the possible nitrene cycle is that **2** does not react with stoichiometric amounts PPh_3 – only **2** is recovered, rather than the proposed

reduced species. Additionally, the fate of the TMS group has not been determined, nor is it clear where the O atom in product OPPh_3 originates from, although we suspect both are hydrolyzed due to methodologies employed to work up the reaction.

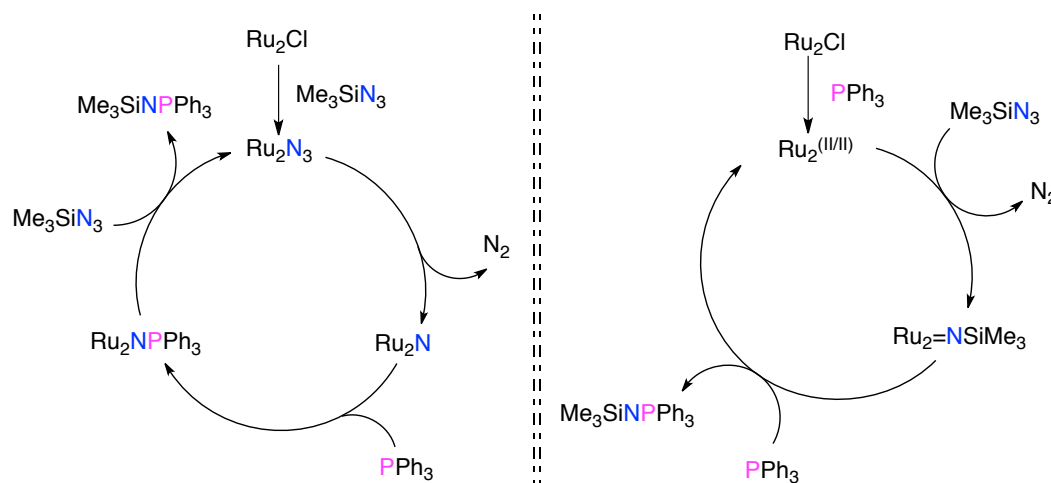


Figure A2.3 Proposed mechanisms for catalytic nitrogen atom transfer via a nitride (left) or nitrene (right) intermediate.

A2.4 Supplementary Information.

Materials and Methods. All syntheses and product workup/isolation were conducted under a dry N_2 atmosphere using Schlenk line or glovebox techniques. CH_2Cl_2 was distilled over CaH_2 prior to use. All materials were commercially available and used as received, unless otherwise noted. $\text{Ru}_2(\text{chp})_4\text{Cl}$ (**2**),² $\text{Ru}_2(\text{chp})_4\text{N}_3$ (**1**),¹ and $\text{Ru}_2(\text{ap})_4\text{Cl}$ (**3**)³ were prepared according to literature procedures.

Ru₂(ap)₄N₃ (**4**). $\text{Ru}_2(\text{ap})_4\text{Cl}$ (100.1 mg, 0.1094 mmol, 1 eq.) and NaN_3 (720.5 mg, 11.09 mmol, 101.3 eq.) were dissolved in 50 mL of freshly distilled CH_2Cl_2 and allowed to stir for 48 h at RT under inert N_2 . A white precipitate (AgCl) formed along with color change from green to dark

yellow-brown. The reaction mixture was filtered through a fine sintered glass frit, and DCM was used to dissolve the Ru₂ species, some of which had crashed out of solution. The filtrate was removed under reduced pressure, and the resulting purple solid was collected. Yield: 73.1 mg, 72.5%. MW: 921.98 g mol⁻¹. MALDI-TOF (m/z): ([M – N₂]⁺) 894, (M – N₃)⁺ 880. IR (ATR): 3058 (w), 3028 (w), 2091 (s) [ν (N₃)], 1599 (s), 1587 (s), 1534 (m), 1467 (s), 1434 (s), 1361 (s), 1286 (s), 1264 (w), 1225 (w), 1216 (s), 1155 (m), 1111 (w), 1069 (m), 1042 (w), 1019 (s), 948 (w), 922 (s), 895, 856 (s), 753 (s), 733 (m), 701 (s), 649 (w) cm⁻¹. UV-Vis (CH₂Cl₂): λ_{max}(ε) = 475 (6077), 770 (6313 mol⁻¹ L cm⁻¹). Combustion analysis for [4·0.5(CH₂Cl₂)] = C_{44.5}H₃₇Cl₁N₁₁Ru₂: calcd. C 55.48, H 3.87, N 15.99; found C 55.13, H 4.24, N 15.71.

Physical Measurements. Matrix-assisted laser desorption/ionization (MALDI) time-of-flight (TOF) mass spectrometry data were obtained using an anthracene matrix on a Bruker ULTRAFLEX® III mass spectrometer equipped with a SmartBeam® laser in positive ion detection mode. UV-Vis spectra were obtained using a StellarNet Miniature BLUE-wave UV-Vis dip probe with a Tungsten-Krypton light source and a 10 mm path length tip. IR spectra were taken on a Bruker Tensor 27 spectrometer using an ATR adapter (no matrix). Elemental analysis was performed by Midwest Microlab, LLC in Indianapolis, IN, USA.

References.

- (1) Corcos, A. R.; Long, A. K. M.; Guzei, I. A.; Berry, J. F. *Eur. J. Inorg. Chem.* **2013**, 3808.
- (2) Chakravarty, A. R.; Cotton, F. A.; Tocher, D. A. *Inorg. Chem.* **1985**, 24, 1263.
- (3) Chakravarty, A. R.; Cotton, F. A.; Tocher, D. A. *Inorg. Chem.* **1985**, 24, 172.

Appendix 3

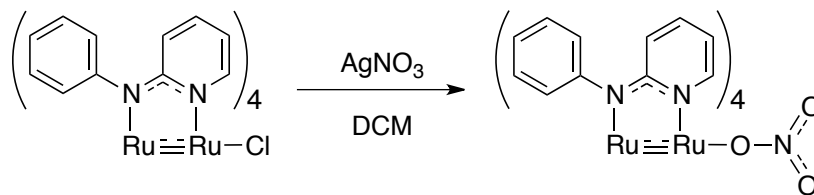
Additional Attempts to Generate Ru₂O by Photolysis of a Different Ru₂-Oxyanion Complex

A3.1 Background.

Chapter 4 discussed our efforts to generate and characterize an Ru₂-oxo species by photolyzing an oxyanion complex. Due to the poor conversion of Ru₂(chp)₄ONO₂ to Ru₂(chp)₄O with these methods,¹ we were interested to determine the role played by the supporting equatorial ligands: if we utilized a more donating ligand than chp to stabilize the oxo, then maybe we could attain more complete conversion to the oxo using this photolytic methodology. We turned to the ap (2-anilinopyridine) ligand for reasons discussed in Chapter 5, generated the new complex Ru₂(ap)₄ONO₂, and tested its ability to convert to Ru₂(ap)₄O.

A3.2 Results and Conclusions.

Ru₂(ap)₄ONO₂ (**2**) was synthesized from the chloride precursor Ru₂(ap)₄Cl (**1**) with 1 equivalent of AgNO₃ in dry CH₂Cl₂ under N₂ (Scheme 1). After workup, crystals were grown by slow evaporation from CH₂Cl₂ in air (Figure 1). The NO₃[−] group of **2** replaces the axial chloride of **1**. The Ru(1)–Ru(2) distance of 2.2679(4) Å is typical of Ru₂⁵⁺ species. The Ru(2)–Ru(1)–O(1) angle of 172.74(7)° is bent. The O(1)–N(9) distance of 1.305(4) Å is elongated as compared to the O(2)– and O(3)–N(9) distances of 1.224(4) Å and 1.222(4) Å, which indicates activation of the O(1) atom by Ru(1). The nitrate group, as with that in Ru₂(chp)₄ONO₂, is planar with combined O–N–O angles of 360°.



Scheme A3.1 Synthetic formation of **2** from **1**.

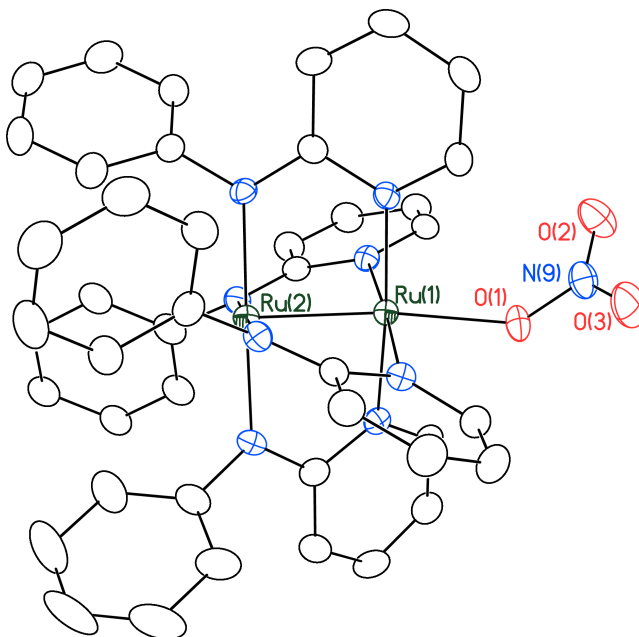


Figure A3.1 Thermal ellipsoid plot of $\text{Ru}_2(\text{ap})_4\text{ONO}_2$ (**2**) with ellipsoids drawn at the 50% probability level. Hydrogen atoms omitted for clarity. Selected bond distances and angles: $\text{Ru}(1)\text{--Ru}(2) = 2.2679(4) \text{ \AA}$, $\text{Ru}(1)\text{--O}(1) = 2.202(2) \text{ \AA}$, $\text{O}(1)\text{--N}(9) = 1.305(4) \text{ \AA}$, $\text{O}(2)\text{--N}(9) = 1.224(4) \text{ \AA}$, $\text{O}(3)\text{--N}(9) = 1.222(4) \text{ \AA}$, $\text{Ru}(2)\text{--Ru}(1)\text{--O}(1) = 172.74(7)^\circ$, $\text{Ru}(1)\text{--O}(1)\text{--N}(9) = 131.7(2)^\circ$, $\text{O}(1)\text{--N}(9)\text{--O}(2) = 118.4(3)^\circ$, $\text{O}(1)\text{--N}(9)\text{--O}(3) = 118.0(3)^\circ$, $\text{O}(2)\text{--N}(9)\text{--O}(3) = 123.6(3)^\circ$.

The main isotopic envelope for **2** in the MALDI-TOF mass spectral data corresponds to $[\text{Ru}_2(\text{ap})_4\text{O}]^+$ and is centered at $m/z = 896$ amu. **2** was therefore subjected to photolysis using 254

nm light while frozen in a CH_2Cl_2 matrix at 77 K with the intention of generating $\text{Ru}_2(\text{ap})_4\text{O}$ and the side-product NO_2^\bullet . Figure A3.2 shows the initial EPR signal for the $S = 3/2$ species, which decreases in intensity with irradiation while the sample changes color from green to brown. After 8 h the $S = 3/2$ signal does not continue to decrease, and instead the signal shape degrades. We also do not see a new $S = 1/2$ signal for NO_2^\bullet , as we did in Chapter 4. Therefore, while we see a more pronounced decrease in the signal for **2** after irradiating for 8 h than we did for that of $\text{Ru}_2(\text{chp})_4\text{ONO}_2$ after 16 h in Chapter 4, this methodology still cannot fully convert our Ru_2ONO_2 species into the desired Ru_2O species. We thus turned to chemical oxidation methodologies, as described in Chapter 5.

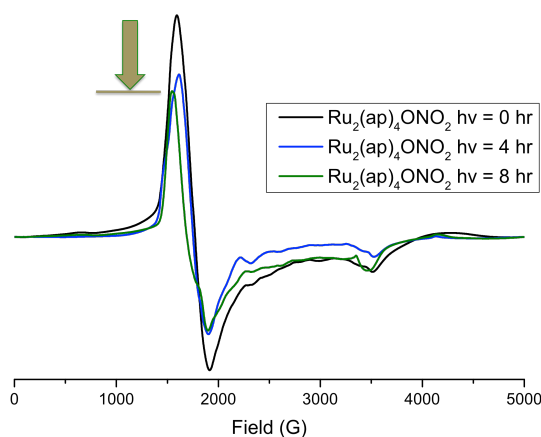


Figure A3.2 EPR data of **2** and subsequent signal taken at 10 K after prolonged photolysis of frozen (77 K) CH_2Cl_2 solution using 254 nm bulbs.

A3.3 Supplementary Information.

Materials and Methods. All syntheses were conducted under a dry N_2 atmosphere using Schlenk line techniques; product workup and isolation were achieved under ambient conditions. Dichloromethane (CH_2Cl_2) was dried with CaH_2 and distilled before use. All materials were commercially available and used as received, unless otherwise noted. $\text{Ru}_2(\text{ap})_4\text{Cl}$ (**1**) was

prepared according to literature procedure. Photolysis of frozen samples of **2** were performed in a Rayonet RPR-200 photochemical reactor with light from 254 and 350 nm mercury vapor bulbs.

Ru₂(ap)₄ONO₂ (2). Ru₂(ap)₄Cl (50.0 mg, 0.0547 mmol, 1 eq.) and AgNO₃ (9.4 mg, 0.0553 mmol, 1.01 eq.) were dissolved in 20 mL of freshly distilled CH₂Cl₂ and allowed to stir for 24 h at RT under inert N₂. A white precipitate (AgCl) formed along with color change from forest to kelly green. The reaction mixture was filtered through a fine sintered glass frit. The filtrate was removed under reduced pressure, and the resulting solid was washed with hexanes and collected. Yield: 49.7 mg, 96.6%. MW: 940.96 g mol⁻¹. MALDI-TOF (m/z): ([M – NO₂]⁺) 896, (M – ONO₂]⁺) 880. IR (ATR): 3064 (w), 2963 (w), 1592 (s), 1582 (s), 1531(m), 1448, 1436, 1360, 1304, 1289 (s), 1266 (s) [*v*_{asym} (ONO)], 1219 (s), 1155 (m), 1020 (s), 1001 (s), 996 (w), 967 (w), 924 (w), 916 (s), 862 (s), 764 (s), 737 (m), 697 (s), 674 (w), 651 (w) cm⁻¹. [**2**·H₂O = C₄₄H₃₈N₉O₄Ru₂]: calcd. C 55.11, H 3.99, N 13.15; found C 55.10, H 3.94, N 13.01. Crystals suitable for X-ray diffraction were grown by slow evaporation of a CH₂Cl₂ solution at RT.

References.

- (1) Corcos, A. R.; Pap, J. S.; Yang, T.; Berry, J. F. *In Preparation*.

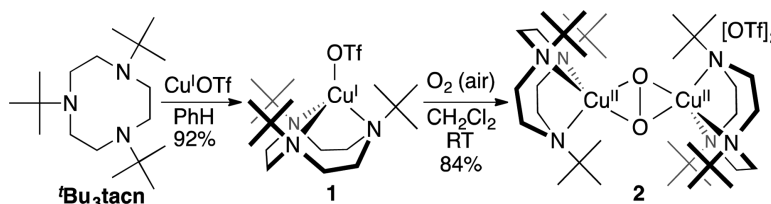
Appendix 4

Characterization of an Unusual Cu₂O₂ species.

Work recently published (*Inorg. Chem.* **2016**, 55, 1102-1107) is based on the data below.

A4.1 Background.

The Scarborough group at Emory University is interested in developing new, sustainable catalysts for selective aerobic oxidation. Inspired by Cu^I-containing metalloenzymes, they have recently developed a new Cu^I complex **1** that has the ability to activate O₂ and generate a Cu^{II}₂–(μ-η²:η²-O₂) species **2** (Scheme 1), which is the most solution-stable Cu_nO₂ species currently known apart of enzymatic systems.¹ The stability of the complex is due to the new supporting ligand ^tBu₃tacn (1,4,7-^tBu₃-1,4,7-triazacyclononane),² which does not undergo irreversible ligand oxidation like the previous Bn₃tacn and ^tPr₃tacn ligands.



Scheme A4.1 Synthetic scheme for Cu metalation of ^tBu₃tacn to form **1**, followed by oxygenation to form bridging peroxide species **2**. From *Inorg. Chem.* **2016**, 55, 1102-1107.

In their initial attempts to characterize a ^tBu₃tacn-supported Cu_nO₂ species, the Scarborough group designed the complex [(^tBu₃tacn)Cu^I(MeCN)][PF₆] (**1b**, an analog of **1** with PF₆[−] instead of OTf[−]) and asked that we acquire resonance Raman data on the oxygenated

product. Such data would indicate whether the species is a monomeric $\text{Cu}^{\text{III}}\text{-O}_2$ species, a bridging $\text{Cu}^{\text{III}}_2\text{-(}\mu\text{-O)}_2$, or a bridging $\text{Cu}^{\text{II}}_2\text{-(}\mu\text{-}\eta^2\text{:}\eta^2\text{-O}_2\text{)}$ species.³

A4.2 Results and Conclusions.

Initial resonance Raman data was collected on solid phase samples (including solution-phase samples frozen in liquid nitrogen and solid-state samples at room temperature), but these underwent photo-oxidation. After multiple attempts, we successfully attained resonance Raman data for the oxygenated Cu sample **2b** (an analog of **2** with PF_6^- instead of OTf) (Figure A4.1) by collecting on a room-temperature solution-phase sample. This allowed the sample to be in a state of free-flow and so avoid photo-oxidation at any one site. The signal in the sample data at 768 cm^{-1} indicates the species is a bridging $\text{Cu}^{\text{II}}_2\text{-(}\mu\text{-}\eta^2\text{:}\eta^2\text{-O}_2\text{)}$ complex.³ This is an especially unusual species, for most bridging peroxide species can isomerizes to the bridging $\mu\text{-oxo}$ analog.¹ The lack of isomerization in this specific complex is most likely due to the steric bulk and, therefore, stability of the supporting $t\text{Bu}_3\text{tacn}$ ligand, for the Cu^{II} atoms are not able to decrease their interatomic distance so as to isomerize between $\text{Cu}^{\text{II}}_2\text{-(}\mu\text{-}\eta^2\text{:}\eta^2\text{-O}_2\text{)}$ and $\text{Cu}^{\text{III}}_2\text{-(}\mu\text{-O)}_2$.¹

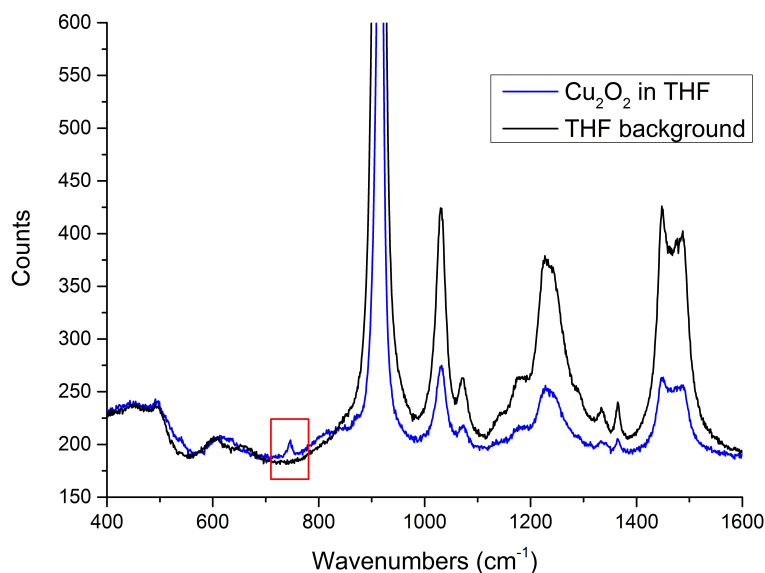


Figure A4.1 Resonance Raman data collected at room temperature in THF for complex $[(^t\text{Bu}_3\text{tacn})\text{Cu}^{\text{I}}(\text{MeCN})][\text{PF}_6]$ after exposure to O_2 . The signal at 768 cm^{-1} (red box) indicates the sample contains a bridging $\text{Cu}^{\text{II}}_2-(\mu-\eta^2:\eta^2-\text{O}_2)$ structure.

References.

- (1) Karahalios, G. J.; Thangavel, A.; Chica, B.; Bacsá, J.; Dyer, R. B.; Scarborough, C. C. *Inorg. Chem.* **2016**, 55, 1102.
- (2) Thangavel, A.; Wieliczko, M.; Bacsá, J.; Scarborough, C. C. *Inorg. Chem.* **2013**, 52, 13282.
- (3) Nakamoto, K. *Infrared and Raman Spectra of Inorganic and Coordination Compounds. Part B: Applications in Coordination, Organometallic, and Bioinorganic Chemistry*; 5th ed.; John Wiley & Sons: New York, 1997.

This page is intentionally left blank.